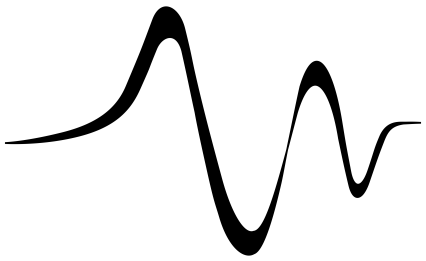
The Physical Origin of Reversible Surface Attachment in Insects

Imperial College London



Andrea Eli Luigi Attipoe, *MSc.*

Supervisor: Dr. David Labonte.

Department of Bioengineering,
Imperial College of Science, Technology and Medicine.
London, United Kingdom.

This dissertation is submitted for the degree of
Doctor of Philosophy (PhD).

February 2024

Abstract

Insects can attach themselves on surfaces under an impressive range of environmental conditions using adhesive pads. Earlier studies indicated the contact under the pad is mediated by a thin layer of liquid secretion, which could produce adhesive forces through capillary bridges and viscous effects. Previous work found another source of viscous dissipation in the viscoelastic properties of the pad. This lead to the formulation of two main supposed mechanisms of adhesion: "wet" and "dry" models, where temperature and rate, following distinct laws, act as crucial factors influencing these models.

The wetting properties of the liquid secreted by the stick insect *Carausius morosus* were determined through interference reflection microscopy, and found to be weakly affected by temperature. Dewetting experiments indicated that the secretion's viscosity is exponentially dependent on temperature.

The storage and loss moduli of the pad were determined through creep experiments, and were found to be weakly influenced by temperature when compared to typical amorphous polymers.

The resulting "wet" and "dry" models were compared to the adhesive forces produced by single pads during detachment at different temperatures and pulling rates. The measured forces were drastically affected by rate, while temperature had no significant effect.

The adhesive performance of insect pads can thus not be explained by "wet" models, due to the inconsistencies of capillary forces with rate dependence, and viscous forces with weak temperature influence. On the other hand, the rate dependence of the energy required to break adhesive bonds in viscoelastic fracture corresponded with the measured pull-off forces, and the weak temperature dependence of the viscoelastic properties of the pad was consistent with the similar performance of the pads. Hence,

I argue that fracture mechanics theories of viscous dissipation offer a viable answer to the question of reversible surface attachment in insects.

To Mamma,
My eternal inspiration, my earliest critic,
The bright star lost ships follow in the night sky, upon dark seas.
You reading these pages was never a given.
They were all written for you.
A te, che immutabile nel tempo, hai cambiato tutti noi.
Per sempre.
9th October 1967 – 5th February 2023

Declaration

Colophon

This thesis was typeset in LaTeX, using the CUED template by *Krishna Kumar*. Copyright 2013, *MIT* ©.

Statement of Originality

I hereby declare that all work presented in this thesis is my own, carried out during my time at *Imperial College London*, unless explicitly mentioned. All other references to previous or published work have been appropriately cited.

Copyright Declaration

The copyright of this thesis rests with the author. Unless otherwise indicated, its contents are licensed under a Creative Commons Attribution-Non Commercial 4.0 International Licence (CC BY-NC). Under this licence, others may copy and redistribute the material in any medium or format. They may also create and distribute modified versions of the work. This is on the condition that: the author is credited and the material, or any derivative works, are not used for a commercial purpose. When reusing or sharing this work, the licence terms must be made clear to others by naming the licence and linking to the licence text. Where a work has been adapted, there should be mention that the work has been changed and the changes must be described. Please seek permission from the copyright holder for uses of this work that are not included in this licence or permitted under UK Copyright Law.

Andrea Eli Luigi Attipoe, *MSc.*
February 2024

A Brief Statement of Great Importance

Before finding interest in the microscopic world, and long before my engineering studies, I was mesmerised by the immense world of astrophysics. I always had a particular fascination for dark matter. This intangible, mysterious, and inhumane form of matter never seems to interact with our world in the ways we expect it to. It is so strangely similar to racism, another dark and impalpable force whose true extent is difficult to quantify, but whose influence is always present. Even academia, a place where people and ideas come together, has undertones of systemic biases which can be ignored, but can not be denied. In the years I spent completing my PhD, I dedicated myself to the equally difficult struggle of challenging a *status quo* of discrimination. It is and often disappointing fight, but I am proud of *Imperial College* and its community for their commitment to creating a fairer and better environment for all. After the summer of 2020, many People of Colour felt like something had to be said, or rather, done. This wave of renewed determination inspired us to spearhead multiple events and campaigns across *Imperial College*. I take particular pride in the creation of the *Black Doctoral Network*, a community for Black students to come together and discuss their joys and struggles. I had the opportunity to discuss my views on Blackness in academia through multiple talks and careers events, and I got to collaborate with the people of *Imperial as One*, an organism working to promote inclusivity and diversity. Out of these many conversations, came the *James West* scholarship, which every year supports three PhD students of African descent to undertake their studies in the *Department of Bioengineering*. These initiatives only represent the beginning of a widespread change, but I am hopeful that many will recognise the need for diversity, and some will continue this fight after me, and for all of us.

I count on *you*, dear reader, and anyone involved in the thrill of discovery and science, to constantly challenge the boundaries of the unobservable.

Acknowledgements

This thesis represents a journey of mine, of which many people have been part. These few pages are dedicated to them and their own respective paths; I am infinitely grateful they got to cross mine.

To my mother, *Paola Moreno*, I owe the strength to never yield, and always keep my head up proud. She taught me the fine balance between constant introspection and unconditional identity, which I can safely say is my defining trait. You made me who I am, and you will always be a part of me.

To my father, *Alfred Attipoe*, I owe the roots I am anchored to. He fought his battles in his own way, and I am grateful I got to witness the unbending will of those who care for the liberties and livelihoods of others, as much as they care for their own.

To *Katherine Manshreck*, I owe the eternal bliss of feeling loved for who I am, and knowing I can love back as unconditionally. You are every second of every day.

Giulia de Lange, Claudia de Lange, and *Martina Moreno*, I am proud of you, and I hope I can inspire you to create your own paths. *Pino Moreno* and *Mary Moreno*, you are the giants whose shoulders we stand on. *Luigi Moreno*, *Titina Moreno*, and the rest of my wonderful family, you can be proud of us. I thank my big brother *Edem Agbodjan*, *Vivien Attipoe*, and *Kpoti Agbodjan*, for making *London* feel like I never left home.

I am grateful for *Dr. David Labonte*'s guidance, and for always enthusiastically showing me the way when I felt lost. I am also grateful for the teachings of *Julien Jeunechamps* and *Dr. Tristan Gilet*. One taught me to take pride in my work, the other gave me the opportunity to make it flourish. I thank my jury, *Prof. Walter Federle* and *Dr. Spyros Masouros*, for seeing this journey through the end.

I am proud of the *Evolutionary Biomechanics Lab*, and grateful for its kind and multiply talented people. I can never repay *Liv Walthaus*, who deserves the world, and asks for so little back. I thank *Fabian Plum* for the great extent of his empathy, and for his dedication to friendship, and everything he undertakes in life. *Dr. Freddie Püffel*, was from the beginning until the end, the most comforting person I could ever share this academic journey with. I thank *Hendrick Beck* for his joy, I feel comfortable leaving the social life of the lab in his capable hands. I am also grateful for *Haaris Asghar*'s perpetual good mood, radiant laughter, and mild manners. To *Dr. Victor Kang*, I express my deepest gratitude for not only having been a role model, but also a caring friend. I warmly thank *Simon Chen*, who was always ready to help and consistently prioritises the needs of others. I thank *Dilanka Deegala*, whose sense of humour has surprised me in unexpected ways. I thank *Dr. Domna-Maria Kaimaki*, *Dr. Sam Fabian*, *Dr. Natalie Imirzian*, *Eleni Papafilippou*, and *Myrta Stoukidi*, for the upbeat lab company, and the insightful discussions. I express my gratitude to *Dr. Martin Sprenger*, *Dr. Christopher Rowlands*, *Dr. Manlio Tassieri*, *Prof. Daniele Dini*, and *Prof. Carmine Putignano* for the enthusiastic help and the fruitful conversations.

I have been lucky to be surrounded by incredibly devoted people, who take inclusivity and diversity at heart as much as I do. I feel particularly grateful for *Dr. De-Shaine Murray*, *Kemi Aofolaju*, *Dr. Wayne Mitchell*, *Dr. Sunday Popo-Ola*, *Dr. Parastoo Hashemi*, and *Dr. Joseph van Batenburg-Sherwood*, as well as all the beautiful people of the *Black Doctoral Network*. May your kindness and empathy benefit many other students, and comfort them in the belief that they too, belong.

Maxine Nicolay, be your true self at all costs, you forever have a place in my heart. I thank *Dr. Antoine Wehenkel* for his level-headed calmness, and his never-ending sense of humour. *Marc Boubnovski*, you are a singularity, free yourself of expectations. *Martin Delrée*, you were there at the start and at the end, I am happy to finally see you shine. I am grateful for *Mustafa Altaha*, who no matter what had a smile and kind words to offer. The same goes for *Johan Cammaerts*, whose compassion is limitless. *Laura Thonnart* has known me for a long time, and I am grateful for having her by my side all these years. I thank *Ben Van Lierop* for his internal peace, and for making me feel welcome anywhere, anytime. I also thank *Nassèr Sept*, for never letting me forget where I am from, and for his thrill for life. I am grateful for *Benjamin Delvoye*, *Lara Joiret* and *Pauline Hannosset*, because going back home is never the same without them. I thank *Lea Bayer* with all my heart, because she always knew what to say to make everything better. I also thank *Delphine Spitaels*, who simply cares and does so with humility. I am grateful for *Pit Paetz*'s friendship, testimony of the secret understanding of those who have lived similar lives. I send my love to *Levi* and *Matti*. I thank *Vanessa Hamoir* and *Prof. Dominique Allart*, for their motherly benevolence. I am grateful for *M. Khurram Shaikh*, whose teachings go beyond the self.

I acknowledge the proud *Ewe* tribe, natives of the sovereign land now referred to as *Togo* and *Ghana*.

I am grateful to have called *Riccardo Pastrello* a friend. I will never forget him, for he was light. The kind of light all want to bask in, the kind of light that I will never let fade away.

Table of contents

Abstract iii

Dedication v

Declaration vii

A Brief Statement of Great Importance ix

Acknowledgement xi

List of figures xix

List of tables xxxi

General Introduction 1

The Need for Reversible Surface Attachment in Insectss 2

Human-made Adhesives and their Limitations 3

Morphology of Insect Pads 5

Wet Adhesion – Capillary and Viscous Contact 9

Dry Adhesion – Fracture Mechanics 15

1 The Physical Properties of the Adhesive Pad Secretion of Indian Stick Insects 19

1.1 Introduction 21

1.2 Methods 23

1.2.1 Contact Angles and Surface Tension 23

1.2.2 Silane Coating and Temperature Control 25

1.2.3 Study Animals and Droplet Deposition 28

1.2.4 General Principle of Contact Angle Measurements 28

1.2.5 Interference Reflection Microscopy 28
1.2.6 Image Processing and 3D Reconstruction 29
1.2.7 Statistical Methods 38
1.3 Results 39
1.3.1 Contact Angle and Surface Tension Measurements 39
1.3.2 Viscosity Measurements 45
1.4 Discussion 47
1.4.1 Surface Tension and Contact Angles 47
1.4.2 The Effect of Temperature on Contact Angles and Surface Tension 49
1.4.3 Spherical Cap Fitting 51
1.4.4 The Effect of Temperature on Viscosity 52
1.4.5 Do Insects Rely on "Wet" Adhesion? 54

2 The Viscoelastic Properties of Smooth Adhesive Pads of Indian Stick Insects 57
2.1 Introduction 58
2.2 Methods 62
2.2.1 Study Animals and Sample Preparation 62
2.2.2 Temperature Control 64
2.2.3 Indentation Experiments 64
2.3 Data Analysis and Validation 66
2.3.1 Viscoelastic Functions for Creep 66
2.3.2 Dynamic Modulus 70
2.3.3 Time-Temperature Superposition 71
2.3.4 Statistical Methods 73
2.4 Results 74
2.5 Discussion 78
2.5.1 The Effect of Stiffness 78
2.5.2 The Effect of Rate 80
2.5.3 The Effect of Temperature 82
2.5.4 Do Insects Rely on "Dry" Adhesion? 84

3 The Forces Produced by Single Smooth Pads of Indian stick Insects 85
3.1 Introduction 86
3.2 Methods 88
3.2.1 Study Animals and Sample Preparation 88

3.2.2 Force Sensor and Image Recording . . . 88
3.2.3 Temperature Control . . . 89
3.2.4 Experimental Protocol . . . 90
3.3 Data Analysis . . . 93
3.3.1 Image Analysis and Crack Speed Extraction . . . 93
3.3.2 Fracture Mechanics . . . 95
3.3.3 Statistical Methods . . . 99
3.4 Results . . . 100
3.4.1 Contact Radius and Adhesive Force . . . 100
3.4.2 A Simple Parametric Model . . . 102
3.4.3 Contact Theory . . . 103
3.4.4 Viscoelastic Tackiness . . . 106
3.5 Discussion . . . 107
3.5.1 Magnitude of the Measured Forces and Their Rate Dependence 107
3.5.2 The Effect of Temperature . . . 108
3.5.3 An Empirical Power Law is Consistent with Detachment Dynamics 109
3.5.4 Contact Theory Predicts the Pull-off Forces . . . 110
3.5.5 Viscoelastic Tackiness Predicts Rate and Temperature Effects . 110
3.5.6 Wet or Dry Adhesion? The Functional Significance of the Pad Secretion . . . 112

Concluding Remarks **117**

References **123**

Appendix A Contact Angles and IRM **143**
Spherical Cap Fitting . . . 144
Simulating Interference Patterns under IRM . . . 147
Electromagnetic Theory . . . 147
Wedge Geometry . . . 147
Spherical Cap Geometry . . . 153

Appendix B Nanoindentation Validation **155**
Validation with a Known Material . . . 156
Force and Displacement Profiles over Time . . . 158
Creep Compliance Function . . . 159

Appendix C Force Sensor Calibration **161**
Beam Theory and Calibration 162

List of figures

1 (A) The Indian stick insect (*Carausius morosus*) has a wide size variation over its different instars. (B) Insects can carry up to a hundred times their own body weight. Featured here: a 400 mg Indian stick insect clinging to a 4 g weight with the two adhesive pads on its front feet. . . 3

2 Two main pad morphologies exist for insects: hairy and smooth pads. Displayed here: (A) The front adhesive pads and claws of the beetle *Gastrophysa viridula*. (B) The hairy adhesive pad bears an array of *setae* ended in different tip shapes. (C) The front adhesive pad and claws of the stick insect *Carausius morosus*. (D) The *arolium* (smooth adhesive pad) is a soft and deformable bean-shaped structure. Images adapted from *Bullock et al.* (Bullock et al., 2008) 6

3 Schematic representation of the capillary and viscous forces (F_{wet}) produced by a wet pad, assumed to be a rigid disk of radius R_{pad}. The viscosity η, surface tension γ_{L}, and height h of the liquid film are represented on the figure, as well as the substrate's surface energy γ_{S}, and the pull-off velocity v_{r}. 12

4 Schematic representation of the equivalence between the pull-off of a sphere from a half space and a deformable sphere on a rigid surface. The pulling force F_{dry}, contact radius a, indentation depth d, crack speed v_{c}, and the material's complex modulus $E^{\star}(\omega)$ and strain energy release rate $\mathcal{G}(v_{\text{c}})$ are annotated on the figure. 17

1.1 (A) A side view of an adhesive pad of an Indian stick insect in contact with a glass substrate. Photo credit: *Fabian Plum*. (B) A schematic representation of the adhesive pad contact, mediated by a thin layer of secretion. The physical properties relevant to determine the forces of a squeezed layer of liquid between two surfaces are the surface tension γ_{L} and energy γ_{S}, viscosity η and contact angle θ. Detaching the pad (purple arrow) leads to the formation of small droplets of the secretion. (C) An Interference Reflection Microscopy (IRM) view of a deposited droplet. (D) The bright and dark fringes are the result of incident light rays (yellow) passing through the glass coverslip and interfering with the rays reflected (orange) at the droplet's interface. The resulting constructive and destructive interference contains quantitative information about the droplet's local height increment Δh, which is a function of the illuminating wavelength λ. The balance of forces between the three interfaces (arrows), as expressed in *Young-Dupre*'s equation, links the surface energy of the substrate, the surface tension of the pad secretion, and the contact angle of the droplet. 23

1.2 The secretion droplets are imaged with Interference Reflection Microscopy (IRM) at wavelength $\lambda = 445\,\mathrm{nm}$, so visualising fringes, resulting from destructive and constructive light interference. A series of radial intensity profiles are extracted and filtered with a third or fourth order *Butterworth* filter (yellow). The extrema were detected on the filtered profile with a neighbouring values algorithm (bright and dark purple disks). From their height determined by Equation (1.2) and their horizontal spacing along the radius, the height profile can be reconstructed. This process can be repeated along the droplet's circumference. Combining the height profiles along all radii leads to a 3D scatter of points along the droplet's surface. The resulting 3D coordinates can be fitted with a spherical cap (orange mesh). The contact angle follows as the tangent to the cap, determined from the geometry of the fitted sphere. Note the difference in scale between Z and XY coordinates. . . 31

1.3 A simulated fringe pattern (light purple disks) with outer and inner outliers (red triangles) in the XY plane. The corresponding 3D reconstruction of the droplet is shown below, where the inner outliers are misplaced by Δh or $2\Delta h$ above the droplet. The less frequent outer outliers shift all points on a radius by a height Δh. Nonetheless, the spherical cap fits the fringes well, and the contact angle obtained through the tangent to the spherical cap (θ_c) is almost identical to the real contact angle θ used to simulate the droplet. The contact angle using a linear fit on the outermost points of the droplet (θ_l) underestimates the original angle. Note the difference in scale between Z and XY coordinates. 33

1.4 (A) "Real" and "measured" angles differ for a wedge system. The correction function was calculated for a liquid of refractive index $n = 1.47$ observed under an optical system with $\lambda = 445\,\text{nm}$, INA = 0.8, and NA = 1.3. The dashed line represents the fitted correction function $\mathcal{F}(\beta_{UC})$. (B) Schematic representation of a discretised section of a spherical cap where the crosses are the uncorrected fringes and the dashed line represents the wedges with their respective local angles $\beta_{UC,i}$. (C) The corrected wedge with its displaced fringes (circles), based on the corrected angles $\beta_{C,i}$, and the incremental corrections δ_i, correct for the non-planar interfaces assumption. The newly fitted spherical cap is then fitted to the corrected data points, providing the correct angle θ_C. . . 35

1.5 Representative Interference Reflection Microscopy (IRM) images of droplets and their 3D reconstruction on surfaces with different wettability, before (Uncorrected Reconstruction) and after (Corrected Reconstruction) applying the contact angle correction method for non-parallel reflective interfaces. The detected fringes (minima and maxima in dark and light purple) are indicated on the left half of the droplets. The orange surface is the fitted spherical cap, and the black line represents the contact angle extracted for each droplet. The correction method leads to a systematic increase of the contact angle values. Note the difference in scale between Z and XY coordinates. 40

1.6 To quantify the surface tension of the secretion and its temperature dependence, the contact angles were measured on surfaces of different wettability at different temperatures. The surface energy of the silane coated coverslips had a significant effect on the contact angle values, but temperature only had a statistically significant effect through its interaction with surface energy. 41

1.7 The contact angle values on all surfaces were used to calculate γ_L^d and γ_L^p, the dispersive (triangles) and polar (circles) components of the surface tension, for every pair of silanised surfaces. The data points are shown for every temperature, which had no statistically significant effect. The dashed and dash-dotted lines represent the total average of the dispersive and polar component, for all temperatures and surface pairs. 43

1.8 (A) The dispersive (γ_L^d) and polar (γ_L^p) surface tension components can be inserted into the *OWRK* equation (1.1), in order to predict contact angle values on surfaces of known dispersive (γ_S^d) and polar (γ_S^p) surface energies. The bottom of the colour bar (on the right) indicates a fully wetting state, the dashed line marks the wetting limit ($\theta = 90°$), and the plain white area indicates a non-wetting state ($\theta > 90°$). (B) The *Eötvös* law can be used to predict the theoretical decrease in surface tension with increasing temperature (Equation (1.13), see Discussion). The wetting limit is almost unchanged by temperature variations in the observed range, signifying a minute change in the wetting capabilities of the secretion. 44

1.9 (A) Measuring the growth rate of nucleated holes in the secretion film at different temperatures gives insight into the the wetting and viscous dynamics of the secretion. The competition of capillary and viscous forces results in the dewetting speed, which increases with increasing temperature. (B) The viscosity, obtained as proportion between the dewetting velocity and the wetting properties of the secretion (Equation (1.10)), follows an exponential decay with temperature. Here, two estimates of the viscosity are obtained with extreme values of the proportionality constant (bright and dark purple), and fitted with exponential decay functions. The viscosity of the secretion hence likely falls within the range indicated in orange. The exponential fits and their 95% confidence intervals are indicated in dashed black lines and in grey, respectively. 45

1.10 (A) The dewetting speed measured on surfaces of different wettability at room temperature increases with decreasing surface energy. An additional measurement for OTS, for which the contact angle could not be estimated with IRM is also included (pink). (B) The relationship between the wettability of different surfaces and the dewetting velocity should follow a cubic dependence (Equation (1.10)). We verified this assumption by fitting a power law to the dewetting velocities of the four surfaces indicated in orange and their contact angles obtained through IRM, and found a power exponent of 3.52. This power law can be used to extrapolate the contact angle of OTS based on its dewetting velocity (pink), providing an approximate contact angle for OTS, close to the IRM limit discussed above at $\sim 40°$. The fit and its 95% confidence intervals are indicated in dashed black lines and in grey, respectively. . 46

2.1 (A) Schematic representation of the setup for indentation experiments at controlled temperatures. An isolated insect leg was clamped and fixed to the bottom of a glass *Petri* dish filled with Phosphate Buffered Saline (PBS). The temperature of the PBS was measured with a thermocouple and varied with a *Peltier* element via a Proportional–Integral–Derivative (PID) control run on a microcontroller. The nano-indenter probe was positioned over the pad with the help of a digital microscope. Figure not to scale, 3D scan of the insect's leg by *Fabian Plum*, using *scAnt* (Plum and Labonte, 2021). (B) Example of a Force-Displacement curve resulting from pad indentation, characterised by three segments: Loading (blue), creep (pink), unloading (yellow). The adhesion part of the unloading curve, characterised by a negative tensile load, is shown in dashed orange. The dashed and dotted lines show the fit of a simple power law compared to the prediction from *Hertz*'s contact theory. The mechanical behaviour of the pad cuticle is in reasonable agreement with *Hertz*'s theory, so that adhesion can be neglected. (C) Characteristic Displacement-Time data (solid) and theoretical fit (dashed) at the three investigated temperatures: 25°C (blue), 35°C (pink), and 45°C (yellow). (D) Schematic representation of Time-Temperature-Superposition (TTS) for the storage modulus $E'(\omega)$. A reference temperature T_{ref} is chosen, and data collected at higher (resp. lower) temperatures are shifted left (resp. right), according to the temperature-dependent shift factor $a_T(T)$. Here, $T_1 < T_{\text{ref}} < T_2$. 63

2.2 (A) The creep compliance function extracted via indentation (blue lines) can be used to predict the mechanical behaviour at a different peak load (pink lines) with reasonable accuracy, suggesting that the pad can be modelled as approximately linearly viscoelastic. (B) The effective elastic modulus of the insect cuticle, extracted via a simple Hertzian analysis of the loading curve, is independent of the leg clamping, leg autotomy, and location of the indent on the pad (n=3). 70

2.3 (A) The zero- and infinite-time elastic moduli of the stick insect adhesive pad cuticle decrease with temperature, but this decrease was only significant for E_0. (B) The ratio E_∞/E_0 is a measure for the extent of viscoelasticity, and shows a weak but insignificant trend to increase with temperature. (C) The time constants which determine the creep behaviour are independent of temperature ($N = 3$ indents for $n = 13$ insects at 3 temperatures for all data in this figure). 75

2.4 (A) The time-space creep compliance function can be used to extract the storage and loss moduli of the adhesive footpad cuticle through *Fourier* transforms. The storage modulus decreases in magnitude with increasing temperatures. The vertical orange lines represent the cut-off frequencies considered for the *WLF* shift, determined from the averages of the fitted time constants $\tau_1 = 5$s and $\tau_2 = 65$s. The temperatures are colour-coded for all four figures, as indicated on the first plot. (B) The variation of the storage modulus E' with frequency in the considered interval. The storage moduli (hollow circles) measured at temperatures above $T_{\text{ref}} = 25°$C are shifted to the left (solid disks) by their respective *WLF* shift factor a_T. (C) The shift factors were fitted with the *WLF* equation (dashed line; see Equation (2.9)). (D) The shifted storage and loss moduli can be used to construct a master curve, which I fitted with a *Prony* series (dashed, and dashed dotted orange). The fit is performed by including the shifted data points, as well as the low and high frequency asymptotic values of the lowest and highest temperatures (purple). 77

3.1 (A) Schematic representation of the force measurement setup. Insect pads were mounted on a wire in proximity of a glass coverslip. Two thin wires were cold soldered to the coverslip and connected to a thermocouple to control the surface temperature via a PID controller. The coverslip was mounted by means of a resin holder to a cantilever beam, whose deflection was measured with a fibre optic sensor. The whole apparatus was connected to a 3D motor stage represented by the arrows, and the contact area on the coverslip was visualised with a microscope and a high speed camera. (B) The force sensor allowed measuring the adhesive forces F produced by insect pads (orange) when the motor stages moved away from the pad in the Z direction perpendicular to the coverslip (purple). The camera recorded the contact area of the pad, which normalised by its perimeter gave a measure of the contact radius a (red). All curves were divided by their maximum and minimum values to reveal synchronicity, in reality the adhesion peak is in the negatives. Note the stress relaxation displayed on the force curves, and the corresponding increase of the contact radius, consistent with a viscoelastic material. (C) In terms of contact mechanics, a crack propagating at speed v_c through a material's bulk is equivalent to the same material being peeled off a rigid substrate. 92

3.2 The contact area videos underwent five steps of image processing. A *Gaussian* filter was applied to extract high contrast features, followed by a rolling ball algorithm to remove the background of the images. Outliers were removed, and a thresholding algorithm binarised the image. The crack speed was then extracted by measuring the change of the ratio between contact area and perimeter with time. The progressive peeling of the pad at different time points during detachment is indicated by the white topology-like lines. 94

3.3 (A) The contact radius was extracted from the video recordings and filtered with a LOWESS algorithm. At high retraction speeds v_r, the contact radius decreases in a faster manner than for low speeds. (B) The corresponding peak forces, filtered with a *Butterworth* filter, show an increase with increasing retraction speeds. The same colour coding is used for both figures, and the raw data was downsampled for visualisation purposes. 100

3.4 (A) The peak adhesive forces measured for insect pads increased with increasing retraction speeds, but temperature had no significant effect (See Tables 3.1 and 3.2). (B) The crack speed scaled with the retraction speeds and varied by two orders of magnitude (black disks). The corresponding relationship between retraction and crack speeds was shifted compared to the prediction from Equation (3.10) 101

3.5 (A) The peak adhesive forces were normalised by the median peak force for the lowest retraction speed at 25°, and converted to strain energy release rate ratio $\mathcal{G}/\mathcal{G}_0$ through Equation (3.4). This ratio was fitted with a power law for each temperature, yielding exponents n in the 0.46-0.83 range. (B) Since temperature did not have an effect on the peak adhesive forces, a power law was fitted through the ratio's average per retraction speed. The 95% confidence intervals are indicated in grey. 103

3.6 The theory established by *Barquins et al.* allowed predicting the tackiness of a sphere of modulus $E_0 = 30\,\mathrm{kPa}$, whose strain energy release rate follows a power law determined in Equation (3.17). (A) The normalised contact radius approximates (dashed lines) the data for insect pads (full lines) well. (B) The peak loads were well approximated by the theory towards low retraction speeds, and slightly underestimated at higher speeds. (C) The crack speed sharply increases for the *Barquins et al.* model, resulting in higher crack speeds at the time of peak force $v_\mathrm{c}(t_\mathrm{max})$, represented on the figure by the crosses and the dashed dotted line. (D) This resulted in a shifted strain energy release rate, where the peak loads are comparable for similar retraction speed, but the crack speeds exceed those anticipated by Equation (3.17). 105

3.7 (A) The dynamic modulus estimated in Chapter 2 (disks and triangles) was fitted with a one-term *Prony* series (dashed and dash dotted lines, Equation (3.14)), together with its associated temperature shift governed by the previously determined *WLF* factor a_T (3.15). (B) The resulting dynamic modulus at different temperatures was integrated according to Equation (3.12), choosing $v_0 = 4\,\mu$m/s. A prediction for the normalised strain energy release rate $\mathcal{G}/\mathcal{G}_0 - 1$ was obtained (full lines) and compared to the data collected for insect pads and their average (symbols). All force values were normalised by the lowest measured peak force, to ensure $\mathcal{G} \to \mathcal{G}_0$ for $v_c \to v_0$. An additional predictive law was calculated for high speeds (dash dotted black line), following Equation (3.16). . . 106

3.8 The viscous force (F_η) induced by the secretion and the viscoelastic tack induced by the pad (expressed through its strain energy release rate $\mathcal{G}$) should both decrease with increasing temperatures. I used *Persson*'s viscoelastic tack model (Equation (3.12)), and the *WLF* shift factor a_T established in Chapter 2 to estimate the magnitude of the decrease in the viscoelastic forces over the 25-45°C temperature range (dashed line) at a crack speed of $v_c = 129\,\mu$m/s. The viscous forces induced by the secretion follow a exponential decrease with temperature, as determined in Chapter 1. The extent of this decrease over the same temperature range (dash dotted line) is thus more consequential than the decrease in the viscoelastic tack. 114

A.1 (A) Schematic representation of the error introduced by the "line fit". This increases for shallower droplet geometries. (B) The percentage error of the "line" fit error can be as high as 62%. 144

A.2 The percentage error introduced by the spherical cap fitting procedure on simulated droplets for $P_{out} = 0.01$ and variable P_{in} is similar for different droplet geometries. The error remains below 15% in all cases. 145

A.3 The percentage error committed by the line fitting procedure on simulated droplets for $P_{out} = 0.01$ and variable P_{in} increases for small droplets. The error can be as high as 65%. 146

A.4 Schematic figure representing the light path of incident and reflected rays under IRM imaging, for a wedge geometry. 148

A.5 Schematic figure representing the light path of incident and reflected rays under IRM imaging, for a spherical geometry. 153

B.1 (A) Example of a force-displacement curve resulting from the indentation of collagen, characterised by three segments: Loading (blue), creep (pink), unloading (yellow). The dashed and dotted lines show the fit of a simple power law compared to the prediction from *Hertz* theory. (B) Characteristic Displacement-Time data (solid) and theoretical fit (dashed) for collagen. 157

B.2 Example curves of the force (P) and displacement h profiles obtained during the indentation of a stick insect's pad. The material's creep becomes apparent during the force profile's holding phase, followed by the probe's retraction and subsequent adhesion. 158

B.3 The time-space creep compliance function $J(t)$ is obtained by fitting *Prony* series to the creep data at different temperatures. The creep function increases in magnitude with increasing temperatures. 159

C.1 (A) The relationship between the deflection of the cantilever beam read by the sensors and the forces applied on the coverslips was determined by hanging different calibration weights in the 2-500 mg range at two lever arms a. (B) The difference in lever arms was adjusted using Equation (C.1). The slope of the resulting curve was used as the multi-lever arm calibration factor $\mathcal{C}$. 162

List of tables

1 Summary table of the physical properties of the secretion found under insects's pads. 14

1.1 Summary of the surface energies of the substrates utilised in this study. The coefficient of determination R^2 represent the goodness of fit of the *OWRK* method in determining the surface energies of the silanised coverslips. All values are given as mean ± std. 27

1.2 A two-way repeated measures ANOVA was performed to analyse the effect of surface energy and temperature on the contact angle of the secretion. The type of silane coating had a statistically significant effect, while the temperature of the coverslips had no significant effect. The interaction of the two independent variables had a significant effect. . . 42

1.3 Summary of the contact angle values of the secretion obtained through IRM, as well as water and diiodomethane as measured with a goniometer on all silanised surfaces utilised in this study. Measurements on OTS were not possible due to the spacing between fringes being reduced as a result of the high contact angle. 42

1.4 Summary of the polar and dispersive surface tension values at all temperatures, obtained applying the *OWRK* method to the contact angle values of the secretion on the four coatings used in this study. Temperature did not have a significant effect on the surface tension values. 43

2.1 A two-way repeated measures ANOVA was performed to analyse the effect of sectioning, clamping, and indent location on the effective elastic modulus of the pad. All variables had no statistically significant effect. 69

2.2 Summary table of the *Prony* series fitting constants extracted at all temperatures, used to reconstruct the viscoelastic creep function $J(t)$. All values are provided as a mean ± std. 75

3.1 A two-way repeated measures ANOVA was performed to analyse the effect of crack speed and temperature on the peak adhesive force. The forces significantly increased with the crack propagation velocity, while the temperature of the coverslips had no significant effect. The interaction of the two independent variables had no significant effect. 101

3.2 A two-way repeated measures ANOVA was performed to analyse the effect of retraction speed and temperature on the crack speed measured at the maximum adhesive force. The retraction velocity had a statistically significant effect, while the temperature of the coverslips had no significant effect. The interaction of the two independent variables had no significant effect. 102

3.3 Summary table of the measured crack speed v_c and the peak adhesive force F_{max} for different retraction speeds v_r. Both the adhesive force and the crack speed increase with the retraction speed. 103

3.4 Summary table of the Root Mean Squared Error (RMSE) comparing the strain energy release rate values for data at all temperatures and their average to the different predictive laws used in this work. 107

General Introduction

The Need for Reversible Surface Attachment in Insects

Why seek a solution to a problem, when time is the answer?



Biomimicry has become common practice in engineering and scientific fields. With any technical problem encountered in human-made technologies, there is a chance of it having already been addressed by millions of years of evolution. Natural selection in particular is a passive and extensive problem-solving mechanism related to biological necessities (Darwin, 1859). Our planet is filled with intricate designs that shaped living organisms throughout their evolution to better survive in, and interact with a range of different environments. Of those, insects are the most successful taxon, and inhabit almost every ecosystem under almost any condition (Grimaldi and Engel, 2005). A crucial aspect of the success of insects is their capacity to adhere to many types of surfaces, a feat partially accomplished by the footpads located on their legs.

Such a biological adhesive system needs to be versatile, since a key ability in the life of insects is to be able to adhere to a variety of different plants with variable roughness, wettability and stiffness (Drechsler and Federle, 2006; Federle et al., 2002). Adhesive strength is a key parameter of insect attachment, as they often find themselves carrying multiple times their own body weight; either bringing food back to shelter, as leaf cutter ants (*Atta vollenweideri*) do (Püffel et al., 2021), or working with conspecifics like army ants (*Eciton hamatum*), who overcome obstacles on their trails by creating bridges made up of many individuals clinging to one another (Reid et al., 2015). Another fascinating example is the nest building behaviour of weaver ants (*Oecophylla smaragdina*), which pull together fragments of leaves much larger than themselves, and weave them together with the silk produced by their larvae (Devarajan, 2016).

An insect's adhesive system must also be reversible, since insects are dynamic creatures, who often need to escape predators (Maginnis, 2008). Being relatively small, insects are predated upon by many mammals, birds, fish, plants, and other insects (Birkhead et al., 1987; Bohn et al., 2012; Maginnis, 2008). Due to their small size, insects also need to escape what at their scales could be considered natural disasters, such as wind, floods,

freeze, and dehydration under sunlight. As a result, insects need to be reactive and fast, and thus require an adhesive system that fits those criteria. Through approximately 400 million years of evolution, systems allowing these interactions have evolved for insects of all shapes and sizes (See Figure 1A, showing the size spectrum of different instars of the Indian stick insect *Carausius morosus* de Sinéty, 1901). Not only can their pads withstand hundreds of times their own body weight (See Figure 1B), they also allow them to do so while running at stride frequencies upwards of 30 Hz (Bohn et al., 2012; Federle et al., 2002). These numbers bare witness to an astonishing small-scale adhesive system.

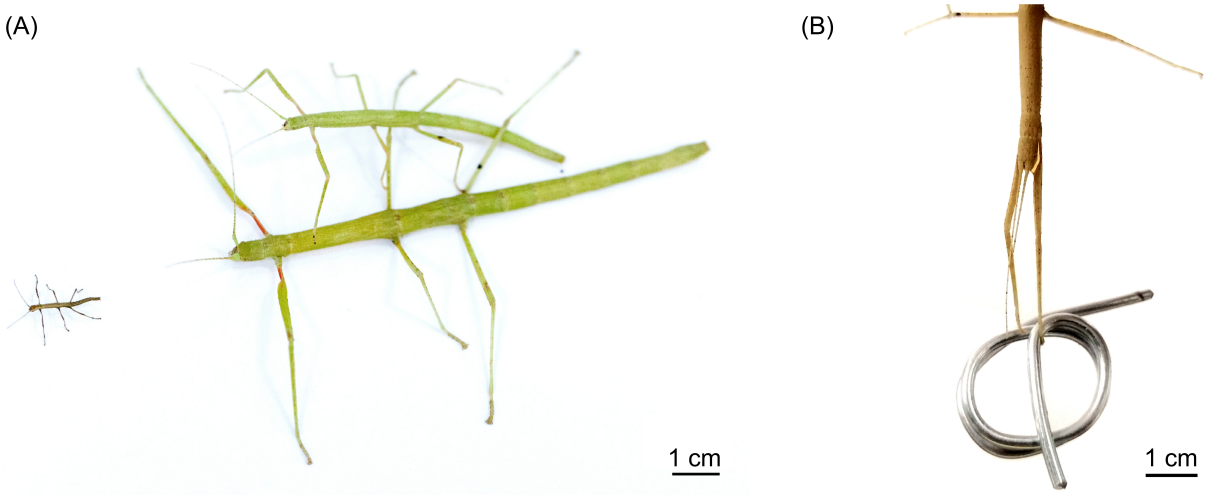


Figure 1 (A) The Indian stick insect (*Carausius morosus*) has a wide size variation over its different instars. (B) Insects can carry up to a hundred times their own body weight. Featured here: a 400 mg Indian stick insect clinging to a 4 g weight with the two adhesive pads on its front feet.

Human-made Adhesives and their Limitations

Adhesion refers to a binding contact between two surfaces (Adderley, 1984). Almost all engineering applications require material elements of different or similar nature to come into contact, whether permanently, or temporarily. A few examples can be found in construction, aerospace, biological, and medical fields (Adderley, 1984; Favi et al., 2014; Mann et al., 1985). Generally speaking, in many commercial applications requiring two surfaces to cling to one another, adhesion is favoured over mechanical fastening techniques such as bolts, screws, rivets, and spot welds (Adderley, 1984). Those intru-

sive binding methods often require perforation or local warping of the bound surfaces, compromising the structural integrity of an interface. In fact, these local anomalies in a material's continuum often introduce fatigue crack initiation points, which can result in catastrophic failure of buildings, aircraft or tools (Adderley, 1984; Mann et al., 1985). Instead of acting in local stress concentrated points, adhesive bonding acts over a surface area, which homogenises stress distributions (Adderley, 1984). Adhesives are typically strong in compression, tension, and shear, but weak in loading modes which concentrate stresses onto a line, such as peeling or cleavage (Adderley, 1984). This characteristic can provide controllability, and possibly reversibility to adhesive designs. The real difficulty most commercial adhesives face lies in that balance: strength versus reusability (Cho et al., 2019).

The adhesive mechanism insects employ, realised over microscopic contact areas, remains unparalleled by current commercial and synthetic adhesives (Favi et al., 2014). Modern electrostatic and pressure systems face critical difficulties at this length scale, where *van der Waals* forces are too strong to allow for easiness of detachment (Uran and Safaric, 2017). Whether for building better robots, designing more effective drugs, or improving manufacturing techniques, the industry is in constant need for better small-scale adhesives (Favi et al., 2014). For instance, care professionals are always seeking better wound dressings, which need to be reliable and bio-compatible, but not so invasive that healing processes are disrupted. Hydrogels have been considered for their attractive viscoelastic properties and tackiness (Liang et al., 2021), some of which were bio-inspired by binding proteins used by mussels (Han et al., 2017). Not only do such adhesives function as an excellent tissue glue, they also work under water and in wet conditions (Berger et al., 2022; Han et al., 2017; Pandey et al., 2020). While these chemically based bonds are highly effective, and sometimes exceed the performance of their natural inspiration (Berger et al., 2022), they are often permanent and thus suffer from limited reusability (Berger et al., 2022; Han et al., 2017; Pandey et al., 2020). On the other hand, synthetic adhesives inspired by dynamic animals such as geckos display high reusability, versatility, and the capacity to bear substantial loads (Hirano et al., 2020; Ruotolo et al., 2021). Gecko-inspired grippers do however often require a relatively large contact areas and high pull-off strengths, and thereby not well-suited to manipulating microscopic objects (Hirano et al., 2020; Ruotolo et al., 2021; Yoo et al., 2023).

Because of this need for systems that: *i.* strongly adhere to many types of substrates and can manipulate soft objects, *ii.* are capable of self-cleaning and can endure many cycles without a decline in performance, *iii.* Can be controlled rapidly, and *iv.* work in wet conditions, adhesion is one of the many examples where engineers might benefit from observing nature. Unlike geckos, insects require tiny contact areas, reducing the burden of large pads compared to their body size. Insect species encompass an immense diversity of shapes and forms, thereby offering a variety of adhesive morphologies to draw inspiration from (Beutel and Gorb, 2001; Stork, 2018). Insects have evolved their adhesive pads for millennia, making them functional on substrates of variable stiffness, wetness, and roughness. Many readily available polymers and modern adhesives do cover some of these sought-after properties, but few seem to be capable of such well-rounded, efficient, and versatile adhesion (Favi et al., 2014; Jagota and Hui, 2011).

Another pivotal aspect that captivated my attention regarding insects as an adhesive model is my conviction that technological advancement often emerges from "Blue Skies Science" —the pursuit of scientific research purely for the sake of understanding and the intrinsic value of knowledge. Insects's adhesive systems are amongst the unexplained natural wonders that seem so familiar, and yet bare the potential for much innovation. Aside from the general thrill of the unknown, there are thus both direct and indirect interests in understanding the mechanisms behind insect adhesion.

Morphology of Insect Pads

With one million species discovered to date, and an estimated five million yet to be found, insects are the most diverse taxon (Stork, 2018). Most insects bear claws on their legs, which provide safe attachment to rough surfaces whose asperities are large enough to grip to (Asbeck et al., 2006; Bullock and Federle, 2011a; Dai et al., 2002; Endlein and Federle, 2008; Gorb, 2001; Voigt et al., 2008). On smooth surfaces, such a wide variety of insects predominantly utilises two main morphologies of attachment pads: hairy pads (a fibrillar array, see Figure 2A and B Bullock et al., 2008; Federle et al., 2002), and smooth pads (a deformable bean-shaped structure, see Figure 2C and D Bullock and Federle, 2009; Gorb, 2001). This small variation in adhesive "pad type" may be surprising given the immense variety of insects, but the shapes and sizes of hairy and smooth pads in itself are also widely diverse (Betz, 2002; Beutel and Gorb, 2001; Büscher et al., 2018; Stork, 1980).

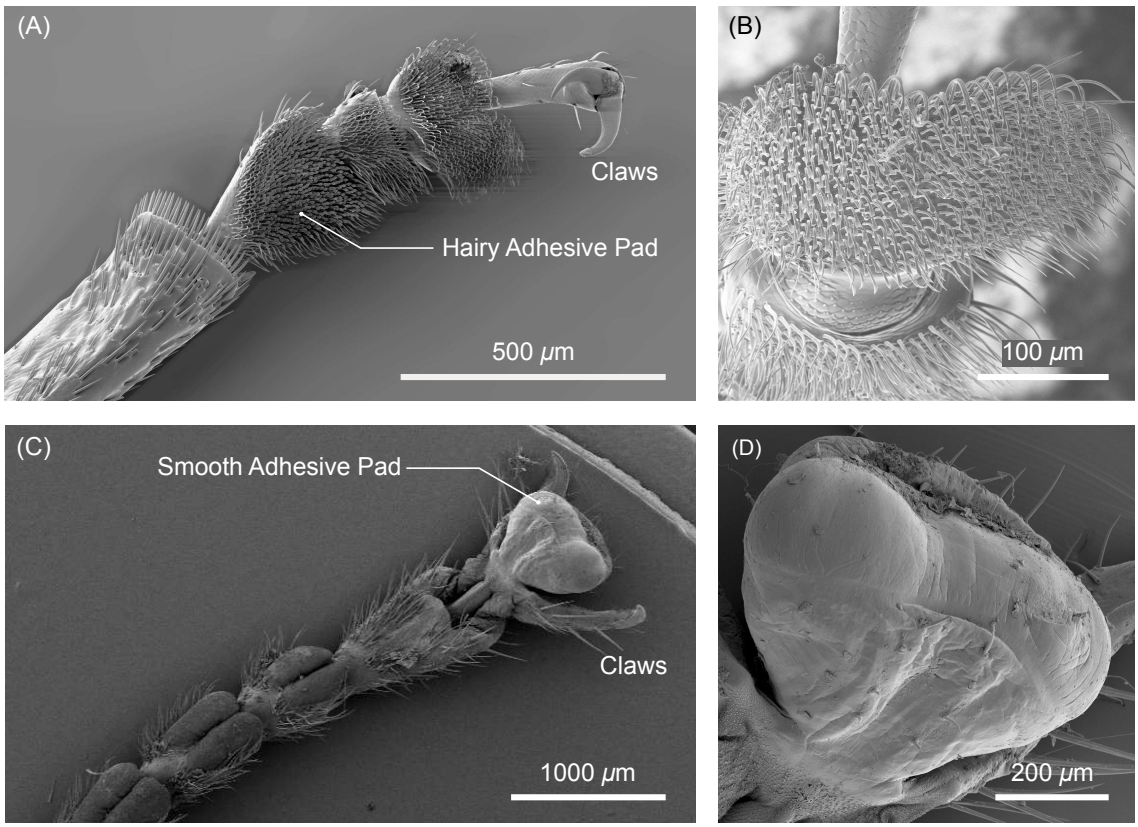


Figure 2 Two main pad morphologies exist for insects: hairy and smooth pads. Displayed here: (A) The front adhesive pads and claws of the beetle *Gastrophysa viridula*. (B) The hairy adhesive pad bears an array of *setae* ended in different tip shapes. (C) The front adhesive pad and claws of the stick insect *Carausius morosus*. (D) The *arolium* (smooth adhesive pad) is a soft and deformable bean-shaped structure. Images adapted from *Bullock et al.* (Bullock et al., 2008)

On the other hand, most insects have a strikingly similar leg structure. The leg of the Indian stick insect, for instance, is comprised of six segments. From proximal, the leg is attached to the *thorax* by the *coxa*, followed by a mobility-enhancing segment, the *trochanter*. The latter is then connected to the femur, followed by the *tibia*, the *tarsus* and the *pretarsus*, the terminating segment of the leg. The *tarsus* itself is subdivided into multiple *tarsomeres*, which can bear either hairy or smooth adhesive pads (Bullock et al., 2008; Gorb, 2001; Labonte and Federle, 2013). Some insects, such as phasmids and cockroaches, also have evolved additional pads on their *tarsi* called *eplantulae*, whose primary function is to generate forces in the proximal direction (Bennemann et al., 2011; Burack et al., 2022; Clemente and Federle, 2008).

Hairy Pads Hairy pads, found amongst others in beetles, earwigs and flies (Betz, 2002; Stork, 1980; Walker et al., 1985), consist in an array of stiff hairs (The elastic modulus of the hair in compression was found to be in the $5 - 16\,\mathrm{GPa}$ range. Bullock and Federle, 2009) called *setae*. The hair tips have different shapes; Amongst the most prevalent are spatula, discoidal and pointed shapes (Betz, 2002; Bullock and Federle, 2011b; Gernay et al., 2016; Stork, 1980). Of those three shapes, discoidal hairs were found to produce the highest adhesive forces and were only found in males (Bullock and Federle, 2011b; Eimüller et al., 2008). Benefiting from their array arrangement, hairs achieve intimate contact when pressed against a surface with minimal preload (Bullock et al., 2008; Bullock and Federle, 2009; Federle, 2006; Peisker et al., 2013). When pulled off, hairy pads leave behind patterns of secretion droplets corresponding to the locations of each hair tip's individual contacts (Betz, 2003; Federle, 2006; Iazzolino et al., 2020). Previous research has investigated the pathways through which this liquid is brought into the contact zone, and found that a pressure difference created during contact is likely to extract the secretion from nano-scale channels within the *setae* (Betz, 2003; Dirks and Federle, 2011b; Iazzolino et al., 2020).

Smooth Pads Smooth pads, found for instance between the claws of stick insects, grasshoppers, and cockroaches (Bennemann et al., 2011; Perez Goodwyn et al., 2006; Roth and Willis, 1952), are at first glance structurally simpler, as they consist in a bean-shaped structure. The surface topography of the cuticle can however be more complex. For the Indian stick insect *Carausius morosus*, it consists in an arranged succession of parallel folds with a $\sim 2\,\mu\mathrm{m}$ spacing (Bennemann et al., 2014, 2011). The internal ultrastructure of the pad margin consists in two layers; the epicuticle and the fibrous procuticle (Bennemann et al., 2014, 2011). The innermost region of the pad is a haemolymph* filled region delimited by the endocuticle (Bennemann et al., 2014, 2011). In other words, the pad is a thin-film terminated fibrillar surface composed of multiple layers, and effectively resembles a liquid-filled pouch. The material properties of the pad were investigated in previous studies, yielding an elastic modulus in compression around $10 - 100\,\mathrm{kPa}$ (Jiao et al., 2000; Perez Goodwyn et al., 2006; Scholz et al., 2008). Previous work by *Gorb et al.* however determined that the pad underwent stress relaxation under constant strain, demonstrating the pad is a viscoelastic material (Gorb et al., 2000). Note that many insects not only have adhesive pads such as described above (the *arolium*), but also additional pads located along their legs. The

*The insect equivalent of blood, to us vertebrates.

latter primarily produce friction forces in the plane of contact, and do not contribute to adhesion (Clemente and Federle, 2008; Labonte and Federle, 2013; Labonte et al., 2014). Smooth pads are also covered in a secretion, which was found to be an emulsion containing a hydrophilic disperse phase in a hydrophobic continuous phase (Dirks, 2009; Dirks et al., 2010; Federle et al., 2002). The secretion is presumably produced in the form of lipids by secretory vesicles in the epidermal cells of the pad, and subsequently stored in reservoirs within the cuticle (Dirks and Federle, 2011b; Gorb, 2007; Lees and Hardie, 1988; Scholz et al., 2008; Votsch et al., 2002). The pads contain nano-channels, through which the secretion likely crosses, and is ultimately delivered to the contact area (Lees and Hardie, 1988; Scholz et al., 2008).

I chose to carry out all experiments presented in this thesis on the Indian stick insect (*Carausius morosus*) for their relatively large pads, and the ease with which they can be kept in laboratory conditions, and manipulated during experiments. Indian stick insects have emerged as a model species in insect adhesion research, and a large body of work thus exist to contextualise the results presented here (Bennemann et al., 2014, 2011; Clemente et al., 2010; Clemente and Federle, 2012; Drechsler and Federle, 2006; Endlein and Federle, 2013; Labonte and Federle, 2015a, 2016; Labonte et al., 2019, 2014; Schmitt et al., 2018; Scholz et al., 2008).

Do Insects Rely on “Wet” or "Dry" Adhesion?

In order to provide new insights into the functional significance of the insect pad secretion, pondered for centuries, it is necessary to separate the two mechanisms that could potentially give rise to adhesive forces: The “wet” model, supposing the secretion induces adhesive capillary and viscous forces due to its surface tension and viscosity (Chan and Carlson, 2019; Dirks, 2014; Federle et al., 2002), or the “dry” model for which the insect pad itself may enhance adhesion through viscoelastic losses (Gorb et al., 2000; Labonte and Federle, 2015a; Perez Goodwyn et al., 2006; Scholz et al., 2008). This separation can only be accomplished by writing predictive models for the different interfaces at play. In fact, the complex interaction between these solid- and liquid-based forces has not been fully characterised, and a series of questions have been intriguing scientists in the recent years:

1. *Why do insects secrete a fluid, and what are its properties?*

2. *What are the relative contributions of "dry" adhesive forces?*

3. *How do insects achieve a rapidly controllable adhesive contact in the presence of a liquid?*

These questions are at the core of the work carried out during my PhD, in which I studied the physical origin of reversible surface attachment in insects, with a particular focus on the functional significance of the pad secretion and the contribution of the soft deformable footpad, by breaking down a complex adhesive system into its simpler components.

Wet Adhesion – Capillary and Viscous Contact

Due to the presence of a thin layer of liquid secretion, previous work has investigated its functional significance by means of "wet" models (Barnes et al., 2011; Betz, 2010; Bullock et al., 2008; Dirks and Federle, 2011a; Federle et al., 2004, 2002; Gillett and Wigglesworth, 1932; Gorb et al., 2000; Gorb, 1998; Koerner et al., 2012; Labonte and Federle, 2013; Niederegger and Gorb, 2003; Walker, 1993; Wigglesworth, 1987; Zhou et al., 2014). The thin secretion layer could act as a capillary bridge, leading to attraction between the two solid surfaces through capillary forces (Dirks and Federle, 2011a; Federle et al., 2002; Laplace, 1806). The magnitude of this attraction is partly the result of a pressure drop, determined by the curvature κ of the solid interfaces and the surface tension γ_{L} of the liquid as described by the *Young-Laplace* equation (de Gennes et al., 2003; Laplace, 1806):

$$\Delta P = \gamma_{\mathrm{L}} \kappa. \tag{1}$$

The contact angle θ of a liquid on a solid substrate is a combined measure of wettability, and the surface tension of the wetting liquid. The lower the contact angle, the better

the wetting, and the lower the surface tension (de Gennes et al., 2003). Equation (1) also depends on the surface energy of the solid interface γ_S and the solid-liquid interfacial energy γ_{SL}, and is expressed as a force balance through *Young-Dupre*'s equation (de Gennes et al., 2003; Young, 1805):

$$\gamma_S - \gamma_{SL} = \gamma_L \cos\theta. \tag{2}$$

Fowkes, *Owens* and *Wendt* extended this force balance by considering the specific and general attraction of molecules through the polar (p) and dispersive (d) components of the energy, for each interface (Fowkes, 1964; Owens and Wendt, 1969). These considerations lead to formulating the *Owens-Wendt-Rabel-Kaelble* (*OWRK*) method (Rudawska and Jacniacka, 2009; Zenkiewicz, 2007):

$$(1 + \cos\theta)\left(\gamma_L^p + \gamma_L^d\right) = 2\sqrt{\gamma_S^d \gamma_L^d} + 2\sqrt{\gamma_S^p \gamma_L^p}. \tag{3}$$

This set of equations is a powerful tool to determine the physical properties of a liquid, provided that the surface properties of the substrate on which it rests and the contact angle are known. In fact, writing Equation (3) with contact angles measured on two surfaces of different wettability provides a system of two equations for two unknowns (γ_L^p and γ_L^d), which can be determined for every pair of surfaces.

Once the contact angle and surface tension of a liquid are determined, the forces it can produce when squeezed between two rigid surfaces can be determined (See Figure 3). The capillary bridge created by a wet contact with a sphere of radius R_{pad} gives rise to a static capillary force (Federle et al., 2002; Fogden and White, 1990):

$$F_\gamma = 3\pi R_{pad} \gamma_L \cos\theta, \tag{4}$$

I mainly discussed here perpendicular adhesion to a substrate, but insect pads excel at producing friction forces as well (Büscher et al., 2020; Dai et al., 2002; Dirks et al., 2010; Federle et al., 2004, 2002; Labonte and Federle, 2015b, 2016). In fact, capillary forces can also act in the contact plane due to contact angle hysteresis: Most surfaces present physical or chemical defects, and contact angles typically do not have unique values, and are instead subject to hysteresis (de Gennes et al., 2003). The highest

and lowest contact angles are usually obtained as the triple contact line either moves outwards or inwards, and are referred to as the advancing (θ_a) and receding (θ_r) contact angles, respectively. As a liquid droplet is sheared across a surface, the contact angles at the advancing and receding edges will thus be higher and lower than the equilibrium contact angle θ, respectively. This hysteresis gives rise to a static friction force, proportional to the difference in the respective cosines of the advancing and receding angles: $F_\mathrm{a,r} \propto \gamma_\mathrm{L}(\cos\theta_\mathrm{r} - \cos\theta_\mathrm{a})$ (Federle et al., 2002). Thus, because of their molecular nature, the capillary forces a liquid can produce are inherently static in all directions (de Gennes et al., 2003).

Through their flow, liquid films can however also give rise to dynamic forces. Generally speaking, understanding the rate dependence of the forces fluids can produce requires making assumptions about the dynamics of flow. Given the typical tiny volumes of the secretion and assuming incompressibility, gravity can be neglected in the *Navier-Stokes* mass and momentum conservation laws (Landau and Lifshits, 1987):

$$\nabla \cdot \overline{u} = 0 \tag{5}$$

$$\frac{D\overline{u}}{Dt} = \frac{1}{\rho}\nabla \cdot \overline{\overline{\sigma}} + \overline{f}, \tag{6}$$

where $\overline{u}$ is the flow velocity vector, $\frac{D\overline{u}}{Dt}$ its material derivative, ρ the fluid's density, $\overline{f}$ are the externally applied forces (such as surface tension) and $\overline{\overline{\sigma}} = -p\overline{\overline{I}} + \overline{\overline{\tau}}$ is the *Cauchy* stress tensor, which comprises a pressure ($-p\overline{\overline{I}}$) and deviatoric component ($\overline{\overline{\tau}}$).

This last term is of particular interest, as it describes the rheological behaviour of the fluid. For *Newtonian* fluids, the deviatoric stress tensor reduces to $\overline{\overline{\tau}} = \eta\nabla\overline{u}$, where η is the viscosity coefficient (Landau and Lifshits, 1987). The dynamics of a simple viscous fluid are hence governed by this coefficient, which in essence represents a liquid's dynamic resistance to flow. As a result, if the fluid is at rest, it does not oppose viscous stresses. *Bingham* fluids (or *Bingham* plastics) on the other hand have an non-null component in their deviatoric stress tensor at zero velocity, often referred to as the yield stress tensor: $\overline{\overline{\tau}} = \overline{\overline{\sigma_\mathrm{y}}} + \eta\nabla\overline{u}$. Thus, in order to initiate flow in a *Bingham* fluid, the minimum yield stress must be overcome by the externally applied stresses (Yu and Wachs, 2007).

A simple *Newtonian* liquid film squeezed between two separating rigid plates hence produces viscous adhesive forces which are rate-dependent, as described by the *Stefan* adhesive force model (Barnes et al., 2006; Stefan, 1875):

$$F_\eta = \eta v_\mathrm{r} \left(\frac{3\pi R_\mathrm{pad}^4}{2h^3} \right), \tag{7}$$

where h is the film's thickness and v_r the rate of separation of the plates (See Figure 3).

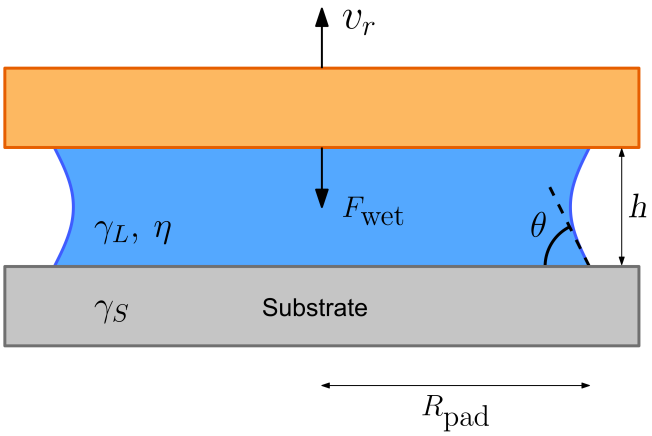


Figure 3 Schematic representation of the capillary and viscous forces (F_wet) produced by a wet pad, assumed to be a rigid disk of radius R_pad. The viscosity η, surface tension γ_L, and height h of the liquid film are represented on the figure, as well as the substrate's surface energy γ_S, and the pull-off velocity v_r.

Considering the above, previous work centrally discussed "wet" models, such as those described by Equations (4) and (7), attempting to predict the adhesive forces insects produce through capillary and viscous effects (Abou et al., 2010; Dirks, 2014; Dirks and Federle, 2011a; Federle et al., 2004, 2002; Gilet et al., 2018; Hosoda et al., 2021; Peisker et al., 2014; Stark et al., 2018; Stork, 1983; Votsch et al., 2002). Many of these efforts used diverse microscopy techniques to determine the physical properties of the secretion, a summary of which can be found in Table 1. A central issue in the determination of capillary and viscous predictive models, is that the interfaces at play are not rigid, mostly an effect of the demonstrated deformability of the pad (Gorb et al., 2000; Labonte and Federle, 2015a; Perez Goodwyn et al., 2006; Scholz et al., 2008). Recently, authors took interest in the potential synergy between the soft pad and the secretion, by writing predictive models for elasto-capillary adhesion, effectively

taking into account the elastic deformation of the pad while in contact with a capillary bridge (Butler et al., 2019; Butt et al., 2010). Despite thorough investigation, the evidence for "wet" models so far remains inconclusive (Dirks et al., 2010; Drechsler and Federle, 2006; Hosoda et al., 2021; Labonte and Federle, 2015a).

Method	Value	Comments	Temperature	Source
Surface tension [mN/m]				
Contact angle estimation	27			(Hasenfuss, 1999)
Contact angle estimation	30			(Federle et al., 2002)
Contact angle estimation	31.10 ± 9.98	Dispersive component		(Dirks, 2009)
	6.29 ± 5.34	Polar component		
Contact angle estimation	32.23 ± 13.63	Dispersive component		(Labonte, 2015)
	0.79 ± 1.10	Polar component		
Viscosity η [mPa·s]				
Dewetting speed estimation	40-150			(Federle et al., 2002)
Microrheology	100			(Abou et al., 2010)
Microrheology	11-22			(Peisker et al., 2014)
Microrheology	28-65		18-28°C	(Attipoe, 2018)
Microrheology	100-200	Whole body secretions		(Menzel et al., 2019)
Dewetting speed estimation	7-200	Across different sizes		(Kaimaki et al., 2022)
Dewetting speed estimation	20-10000	Whole body secretions	20-30°C	(Baumgart et al., 2022)

Table 1 Summary table of the physical properties of the secretion found under insects's pads.

Dry Adhesion – Fracture Mechanics

In recent years, authors have argued for "dry" models, considering the material properties of the pad to be in part or primarily responsible for the observed adhesive performance of insects (Federle et al., 2004; Hosoda et al., 2021; Labonte and Federle, 2015a; Langer et al., 2004). Such models assume that, similarly to geckos (Autumn et al., 2002), adhesive organs are highly deformable, and hence capable of achieving intimate contact with substrates, to a point where intermolecular forces become dominant (Labonte and Federle, 2015a; Langer et al., 2004). In writing a dry adhesive model, one must then determine how strong the bonds made between two (solid) interfaces are, and in particular how difficult it is – or equivalently, how much energy is required – to break them.

The adhesion between two surfaces can hence be viewed as a fracture problem, where instead of occurring in a material's bulk, a crack is progressing at the interface between the surfaces (Persson, 2021; Persson and Brener, 2005). The two situations (bulk vs interfacial crack propagation) are equivalent, as they both examine the easiness of bond breaking as a result of external stress (Persson, 2021).

Propagating a crack in a material requires energy, and results in a decrease in the contact area A with the substrate. Generally, materials will deform as they store or dissipate energy before separating. The strain energy release rate $\mathcal{G}$, a key quantity in fracture mechanics, assesses said amount of elastic (U_E) and potential (U_P) energy associated to the change in contact area between the newly released material and the substrate, and writes as (Labonte and Federle, 2015a):

$$\mathcal{G} = \frac{\partial U_\mathrm{E}}{\partial A} + \frac{\partial U_\mathrm{P}}{\partial A}. \tag{8}$$

When the strain energy release rate reaches a critical value $\mathcal{G}_\mathrm{c}$, crack propagation becomes energetically favourable (Labonte and Federle, 2015a; Persson, 2001; Persson et al., 2005). This quantity directly relates to the general concept of adhesion or tack, as they are defined as resistance to such separation (Barquins and Maugis, 1981).

In order to propagate a crack through the interface, elastic materials only require to overcome the thermodynamic work of adhesion $\mathcal{G}_0$, which is strictly the energy required to break the bonds at the interface. For a simple elastic material of modulus

E on a smooth substrate, the *Griffith*'s criterion predicts the adhesive strength of the contact by relating the elastic potential energy stored in the material to the energy required to propagate a crack at the interface (Griffith, 1921). This criterion is usually expressed through the fracture stress $\sigma_\mathrm{f} \propto \left(\frac{E\mathcal{G}_0}{l}\right)^{1/2}$, where E is the elastic modulus and l the crack length (Barquins and Maugis, 1981; Gao and Yao, 2004; Griffith, 1921; Shull, 2002). From this prediction, it is clear that the higher the elastic modulus, the more energy a material can store before fracture, and hence the stronger the adhesive. Although this criterion is very useful in predicting the fracture of materials such as glass (Griffith, 1921), it is based on the significant assumption of complete (atomic) contact between flat interfaces. Most materials found in nature are not smooth (Burack et al., 2022; Persson et al., 2005), and fit outside of these theoretical considerations. Materials that present surface roughness permit a larger adhesive area to be achieved, on the condition that intimate contact is reached, or in other words, that the material can deform and comply to the surface topology and increase the surface area in contact, allowing close-range *van der Waals* forces to act (Autumn et al., 2002; Bush et al., 1975; Creton and Leibler, 1996; Greenwood and Williamson, 1966; Persson, 2001; Persson et al., 2005; Scholz et al., 2008). Specifically, *Persson et al.* provided the energy required for an elastic material of modulus E to reach intimate contact with a substrate of roughness height h_r and width λ_r: $U_E = E\lambda_\mathrm{r}h_\mathrm{r}^2$ (Persson and Tosatti, 2001; Scholz et al., 2008). This potential was compared by *Scholz et al.* to the energy gained by initiating additional contact: $U_\mathrm{C} = -\mathcal{G}_0\lambda_\mathrm{r}^2$, providing an equilibrium at $\mathcal{G}_0 = Eh_\mathrm{r}^2/\lambda_\mathrm{r}$. Ergo, soft materials adhere better to rough materials, for which $\lambda_\mathrm{r} \approx h_\mathrm{r}$ (Persson and Tosatti, 2001; Scholz et al., 2008).

Viscoelastic materials can dissipate energy in addition to storing it, and the value of the strain energy release rate can hence exceed said work of adhesion. In fact, all solids dissipate energy at a characteristic timescale τ_c, as they adjust to sustained deformation and eventually flow, given a long enough observation timescale τ_o. A common rheological interpretation of the propensity of a material to dissipate energy is expressed through the *Deborah* number:

$$\mathrm{De} = \frac{\tau_\mathrm{c}}{\tau_\mathrm{o}}. \tag{9}$$

For such materials with $\mathrm{De} \ll 1$, $\mathcal{G}$ takes no unique value and is rather a function of the rate of propagation of the crack, expressed through the crack speed v_c. Fracture

mechanics models aim at predicting the forces arising from a material separating from a substrate as a function of the rate of propagation of such cracks. For instance, *Barquins* and *Maugis* wrote a system of equations which utilises a parametrisation of the strain energy release rate within the *Johnson-Kendall-Roberts* (*JKR*) contact theory describing a rigid sphere indenting an elastic half-space (Johnson, 1985; Johnson et al., 1971). Note that the pull-off required to detach a rigid sphere from a half space, and those experienced by a deformable sphere on a rigid surface are fully equivalent (See Figure 4).

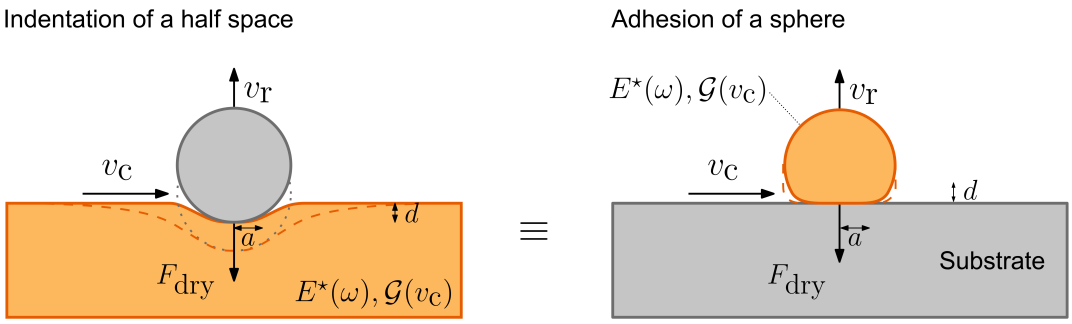


Figure 4 Schematic representation of the equivalence between the pull-off of a sphere from a half space and a deformable sphere on a rigid surface. The pulling force F_{dry}, contact radius a, indentation depth d, crack speed v_c, and the material's complex modulus $E^\star(\omega)$ and strain energy release rate $\mathcal{G}(v_c)$ are annotated on the figure.

However, this model is empirical and only reflects a parametrisation of a viscoelastic material, given experimental parameters which need fitting. Recent efforts have been aimed at writing a form of the strain energy release rate from first principles, using the characteristic viscoelastic functions of a material. Because of their frequency dependence (Lakes, 2009), viscoelastic materials do not have a single elastic modulus value, but rather a complex and frequency dependent dynamic modulus: $E^\star(\omega) = E' + iE''$ where i is the complex unity, and E' and E'' are the storage and loss moduli, respectively. Naturally, a key quantity in determining the magnitude of energy a viscoelastic material dissipates whilst being pulled off a substrate lies in the loss modulus E'', for which other viscoelastic tack theories have been developed and are presented further in this thesis.

Chapter 1

The Physical Properties of the Adhesive Pad Secretion of Indian Stick Insects

Disclaimer The methods and experiments described in sections 1.2.2, 1.2.6 and 1.3.2 were conducted as a collaboration between Andrea E.L. Attipoe (AELA), Dr. Domna-Maria Kaimaki[†] (DMK), and Eleni Papafilippou[‡] (EP). Dewetting measurements on glass were performed by DMK and AELA, and on silanes by DMK. The data analysis was performed by DMK using image analysis scripts written by AELA, DMK, and EP. The silane surfaces were produced and characterised by DMK. Given the high relevance of these results to the broader context of insect adhesion at different temperatures, I include a brief description of these measurements, with the permission of the authors mentioned above.

[†]Previously: Department of Bioengineering, Imperial College London, London, UK

[‡]Currently: Department of Chemical Engineering and Biotechnology, University of Cambridge, Cambridge, UK.

1.1 Introduction

Insects, one of the most prolific taxon on the planet, have adapted to their environment in multiple ways throughout their evolution. An important trait is their ability to cling to a variety of leaves and plant stems. In fact, insects manage to attach themselves and run on many surfaces, using adhesive pads and claws located at the end of their limbs (See Figure 1.1A). The exact physics of this feat has been a subject of interest to biologists, physicists and engineers alike. Studies on insect attachment on smooth substrates dating as far back as two centuries ago indicated the contact under the pad is mediated by a thin layer of liquid secretion (Barnes et al., 2011; Betz, 2010; Bullock et al., 2008; Dirks and Federle, 2011a; Federle et al., 2004, 2002; Gillett and Wigglesworth, 1932; Gorb et al., 2000; Gorb, 1998; Koerner et al., 2012; Labonte and Federle, 2013; Niederegger and Gorb, 2003; Walker, 1993; Wigglesworth, 1987; Zhou et al., 2014). Since squeezed layers of liquid produce adhesive forces through capillary bridges and viscous effects, a hypothesised function of the secretion is to create static and dynamic adhesive forces (Dirks, 2014; Federle et al., 2004, 2002; Hosoda et al., 2021; Peisker et al., 2014). Other studies have considered the function of the secretion as a release layer, easing substrate-pad separation during detachment (Labonte and Federle, 2015a; Speidel et al., 2017). Lastly, the secretion could prevent water losses through evaporation, a crucial issue for small animals with large surface-to-volume ratios (Abou et al., 2010; Betz, 2010).

The secretion could thus serve one or more of these functions, and a key aspect of studying the physics behind insect adhesion hence lies in determining its properties. Previous work investigated the chemical properties of this liquid, establishing that it is effectively a mixture of mostly apolar hydrocarbons (Dirks et al., 2010; Dirks and Federle, 2011a; Eisner and Aneshansley, 2000). Gas-Chromatography and Mass-Spectrometry (GCMS) analyses detected traces of C_{22} to C_{49} n-alkanes and n-alkenes, sometimes containing monomethyl and dimethyl functional groups. Many other branched components were found, making the secretion a complex mixture of long-chained hydrocarbons, fatty acids and amino acids. (Betz et al., 2016; Eisner and Aneshansley, 2000; Geiselhardt et al., 2009; Reitz et al., 2015; Speidel et al., 2017; Votsch et al., 2002). The composition of the secretion found on the pads did not however significantly differ from the liquids covering other parts of insects's bodies, such as *tarsi*, tibia, and wings, raising questions as to whether it is specialised to aid adhesion (Geiselhardt et al., 2011, 2010, 2009; Speidel et al., 2017; Votsch et al., 2002).

Analyses such GCMS are capable of detecting small traces of chemicals and therefore do not require macroscopic samples of the secretion to determine its composition. However, its physical properties such as surface tension and viscosity are difficult to infer from the chemical composition, and standard measurement techniques, such as the ring technique, goniometers, and rheometers are unavailable due to the scarce volume of liquid available (See Figure 1.1B). Knowledge of the physical properties of the secretion is however required to understand and predict its viscous and capillary contributions to the adhesion of pads. Specifically, since the forces produced by insects are rate and sometimes temperature dependent (Federle et al., 2002; Labonte and Federle, 2015a; Roth and Willis, 1952; Stark et al., 2018; Votsch et al., 2002), the temperature dependence of the surface tension and viscosity of the secretion must be established, to then compare them to the adhesive performance and mechanical properties of insect pads at different rates and temperatures. A comprehensive study of this complex interface, and its rate and temperature dependencies should clarify the function of the secretion and its contribution to the pad's adhesive forces. Here, I used and improved an existing microscopy technique to reconstruct 3D images of deposited secretion droplets (Contreras-naranjo et al., 2010; Federle et al., 2006, 2002; Wiegand et al., 1997, 1998), allowing me to investigate the contact angle and surface tension of the adhesive pad secretion and their temperature dependence.

1.2 Methods

1.2.1 Contact Angles and Surface Tension

The insect pad, the secretion covering it, and the surface to which it is attached, constitute a solid-liquid-solid interface (See Figure 1.1A and B) (Betz, 2010; Dirks and Federle, 2011a; Federle et al., 2002; Walker, 1993; West, 1862).

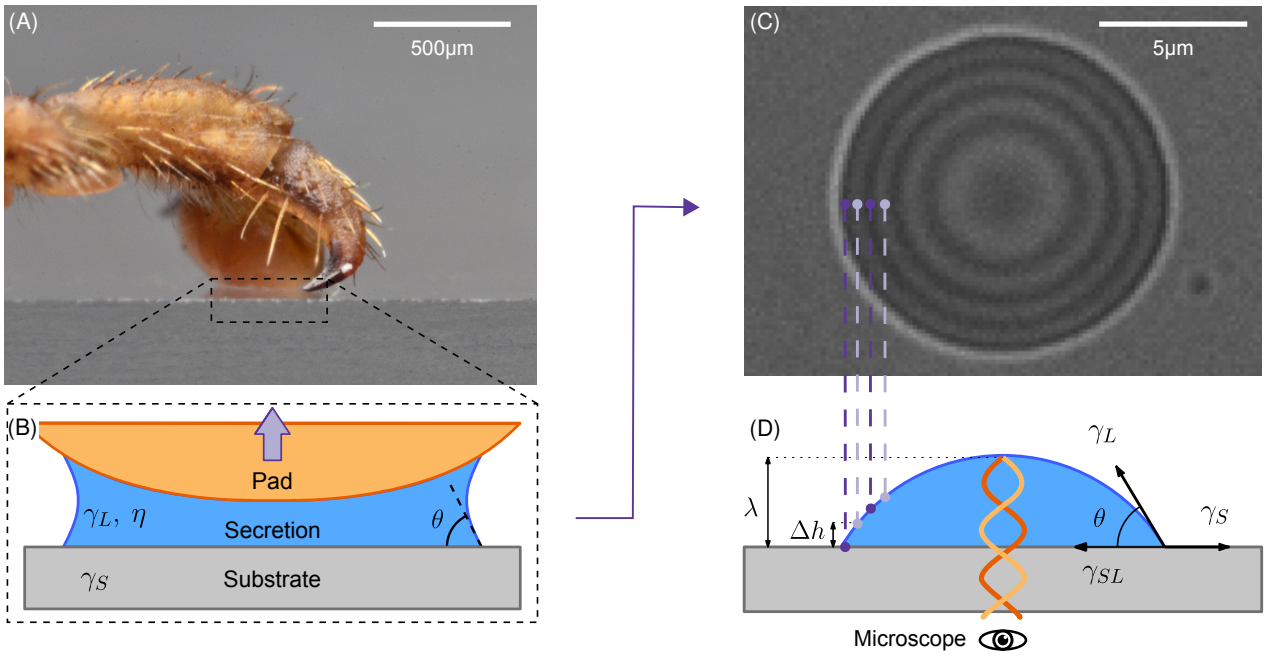


Figure 1.1 (A) A side view of an adhesive pad of an Indian stick insect in contact with a glass substrate. Photo credit: *Fabian Plum*. (B) A schematic representation of the adhesive pad contact, mediated by a thin layer of secretion. The physical properties relevant to determine the forces of a squeezed layer of liquid between two surfaces are the surface tension γ_L and energy γ_S, viscosity η and contact angle θ. Detaching the pad (purple arrow) leads to the formation of small droplets of the secretion. (C) An Interference Reflection Microscopy (IRM) view of a deposited droplet. (D) The bright and dark fringes are the result of incident light rays (yellow) passing through the glass coverslip and interfering with the rays reflected (orange) at the droplet's interface. The resulting constructive and destructive interference contains quantitative information about the droplet's local height increment Δh, which is a function of the illuminating wavelength λ. The balance of forces between the three interfaces (arrows), as expressed in *Young-Dupre*'s equation, links the surface energy of the substrate, the surface tension of the pad secretion, and the contact angle of the droplet.

The forces arising between each of these layers result in the adhesive force between the insect and the substrate to which it sticks. Wetting theory provides a balance between the interfacial forces between a liquid droplet, the surface it rests on, and the vapour phase they are both in. Considering the polar and dispersive components of this balance translates into the *Owens-Wendt-Rabel-Kaelble* (*OWRK*) equation (Fowkes, 1964; Owens and Wendt, 1969; Rudawska and Jacniacka, 2009; Zenkiewicz, 2007):

$$(1+\cos\theta)\left(\gamma_{\mathrm{L}}^{\mathrm{p}}+\gamma_{\mathrm{L}}^{\mathrm{d}}\right)=2\sqrt{\gamma_{\mathrm{S}}^{\mathrm{d}}\gamma_{\mathrm{L}}^{\mathrm{d}}}+2\sqrt{\gamma_{\mathrm{S}}^{\mathrm{p}}\gamma_{\mathrm{L}}^{\mathrm{p}}}, \tag{1.1}$$

where θ is the contact angle between the surface and the liquid, and γ_i^j is a surface energy (or surface tension); the subscript i denotes the interface it is relative to (S: solid, L: liquid), and the superscript j denotes the polarity (p: polar, d: dispersive), see General Introduction. The wetting properties of liquids are typically measured microscopically by observing the lateral profile of droplets with an optical device, such as a goniometer. Such direct optical measurements become impossible when the profiles of the observed drops become shallow, or when the volume of tested liquid is below about a millilitre (de Gennes et al., 2003). The secretion films covering insect pads are typically at most a few hundred nanometres thick (Dirks, 2009; Dirks et al., 2010; Dixon et al., 1990; Federle et al., 2002; Geiselhardt et al., 2009; Lees and Hardie, 1988; Stork, 1983; Walker et al., 1985), making standard optical techniques impractical. *Federle et al.* have previously utilised a microscopy technique developed by *Wiegand et al.* to determine the contact angle of liquid secretions from insects and frogs (Federle et al., 2006, 2004, 2002; Wiegand et al., 1997, 1998). Following this work, I here determine the contact angles of the Indian stick insect's pad secretion using Interference Reflection Microscopy (IRM) (Wiegand et al., 1997, 1998). This technique overcomes the difficulties mentioned above, by allowing the 3D reconstruction of thin films and droplets. Because estimating the surface tension with the *OWRK* method requires paired measurements on multiple surfaces (Rudawska and Jacniacka, 2009; Zenkiewicz, 2007), contact angles were estimated on surfaces functionalised with silanes to vary their surface energy and thus wettability. Insects can face drastic temperature changes in their environment, and an adhesive system which is robust to such variations may therefore be beneficial (Colinet et al., 2015). Herein, I investigate the temperature dependence of the contact angle and surface tension of the liquid, to ultimately determine its biological relevance. Moreover, assessing the influence of temperature on the surface tension and contact angle of the pad secretion is crucial to

determine other relevant physical properties of the liquid such as its viscosity. The temperature dependence of the surface tension and viscosity of the secretion then provide a basis for a quantitative comparison to the time and temperature dependent processes in the viscoelastic pad material (Gorb et al., 2000; Perez Goodwyn et al., 2006; Scholz et al., 2008), which are essential to determine the role of the liquid in the overall process of adhesion (Federle et al., 2006, 2004, 2002). Measurements of individual insects were hence repeated on four coated substrates, and at four temperatures over a naturally encountered temperature range of $20 - 50°C$ (Colinet et al., 2015; Stark et al., 2018).

1.2.2 Silane Coating and Temperature Control

Experiments were conducted with borosilicate glass coverslips coated with Indium-Tin-Oxide (ITO) on one side (18×18 mm, 0.18 mm thickness and $8 - 12\,\Omega$ resistance, SPI Supplies, USA). In order to produce surfaces of different wettability, the coverslips were coated with four different silanes: octadecyltrichlorosilane (OTS, $C_{18}H_{37}Cl_3Si$), trimethylchlorosilane (TMCS, C_3H_9ClSi), (3-dimethylaminopropyl)trimethoxysilane (DMAPTMS, $C_8H_{21}NO_3Si$) and (3-glycidoxypropyl)trimethoxysilane (GPTS, $C_9H_{20}O_5Si$), Sigma-Aldrich, Missouri, USA). Chemical Vapour Deposition (CVD) was employed to produce uniform silane coatings and to reduce co-deposition of polymeric silane particles, as well as hydrolytic degradation of the deposited layer (Jönsson et al., 1985; Yadav et al., 2014).

The glass coverslips were cleaned with a CO_2 jet stream using a custom-made snowjet gun, (*Loos* group, Zernike Institute of Advanced Materials, NL) (Yang et al., 2007) and activated with a UV Ozone cleaner (Novascan, Ames, USA) at 22° C for 10 minutes. The activated surfaces were placed above a glass *Petri* dish containing 3 mL of a silane solution, with the help of a custom-built stainless steel holder. The surfaces were placed inside a desiccator which had been flushed with argon to avoid side reactions of the silanes with air. The desiccator was connected to a vacuum pump, resulting in a 10^{-3} mbar vacuum. The Sigma-Aldrich Pressure-Temperature Nomograph Interactive Tool (Goodman et al., 2000; McQuarrie and Simon, 2008; Thomson, 1946) was utilised to determine the temperature and pressure conditions required to evaporate each silane (30° C for DMAPTMS and TMCS, 60° C for GPTS, and 110° C for OTS). These temperatures were reached by surrounding the desiccator with heat tape (MIL-HT-201,

Isoheat, Germany), and placing it on a hot plate (RT2 Plus Advanced, Thermo Fisher Scientific, Germany).

The functionalisation process was iteratively adjusted until the measured contact angles stabilised, and compared to literature values. All surfaces were exposed for five hours, after which the desiccator was flushed with argon and the heating stopped. The surfaces were rinsed with deionized water (GPTS and DMAPTMS) or tetrahydrofuran (TMCS and OTS) for 30 s, and blow dried with condensed air. The surfaces were stored in custom-built 3D printed boxes, which were sealed with paraffin film (Parafilm, Bemis Company, USA).

The surface energy of the functionalised coverslips was assessed by sessile drop contact angle measurements, using a custom-made goniometer based on a Dino-lite Edge digital microscope (AM7915MZTL, AnMo Electronics Corporation, Taiwan). Single 1 μL droplets were deposited onto every surface with a pipette (Finnpipette, Thermo Fisher Scientific, USA). The process was repeated for three to five droplets per surface and 10 surfaces per silane. A side image of each droplet was captured with the microscope. The resulting contact angle images were analysed in *Fiji* (version 1.53t Schindelin et al., 2012), using an ellipse fit implemented in the contact angle plug-in (Brugnara, 2004). Three liquids with different polar and dispersive surface tensions (formamide, diiodomethane and water) were utilised, in order to fit the *OWRK* equation (1.1) with the surface energies of the silanes as unknowns. A regression using the *statsmodels* module (Seabold and Perktold, 2010) in *Python* 3.8.10 was performed, providing the polar (γ_S^p) and dispersive (γ_S^d) components of the solid's surface energy (Rudawska and Jacniacka, 2009; Zenkiewicz, 2007). In order to further increase the assessed range of surface wettabilities, sonicated and plasma-treated glass surfaces (BD-20AC, Electro-Technic Products, USA) were also characterised and used in this work (See Table 1.1).

In order to characterise the surface roughness of the functionalised surfaces, they were scanned with an Atomic Force Microscope (EnviroScope III by Veeco, USA). Squares of $5 \times 5\,\mu$m were inspected in tapping mode with a 40 N/m stiffness and 300 kHz resonant frequency probe (RTESP-300, Bruker, USA) (Kaimaki et al., 2018), which confirmed that all monolayers were dense, smooth, and well-organised (Ajami and Aguey-Zinsou, 2011). The Root Mean Squared roughness was extracted in WSXM (Horcas et al., 2007); it was sub-nanometric, and comparable to clean non-functionalised coverslips.

Surface	γ_S [mN/m]	γ_S^p	γ_S^d	R^2 [-]
Glass	70.85 ± 17.58	34.75 ± 12.5	35.1 ± 12.36	0.97
GPTS	43.24 ± 5.59	7.48 ± 2.38	35.76 ± 5.06	0.98
DMAPTMS	36.81 ± 5.62	6.13 ± 2.35	30.68 ± 5.11	0.96
TMCS	29.3 ± 0.26	1.39 ± 0.06	27.91 ± 0.25	1.0
OTS	27.42 ± 0.62	0.08 ± 0.03	27.35 ± 0.61	0.95

Table 1.1 Summary of the surface energies of the substrates utilised in this study. The coefficient of determination R^2 represent the goodness of fit of the *OWRK* method in determining the surface energies of the silanised coverslips. All values are given as mean ± std.

All surfaces were cleaned prior to characterisation and experimental use with acetone and isopropanol in an ultrasonic bath, rinsed with DI water, and blow dried with compressed air, as described in *Kaimaki et al.* (Kaimaki et al., 2022). In order to assess its impact on the contact angles and surface tension of the secretion, temperature was varied with a custom-built setup (An earlier version of this setup was developped by *M. Stoukidi*, Stoukidi, 2019), making use of *Joule* heating in the conductive coverslips. The ITO (non-functionalised) side of the coverslips was brought in contact with copper tape on a custom 3D printed microscope mount. Low resistance was insured by pressing the coverslip between two 3D printed frames with paper clamps. Before every experiment, I verified that the combined resistance of the coverslips and the copper tape was below $50\,\Omega$. Local temperature was measured by fixating a thermocouple (K-type TP870, Extech, USA) on the coverslips with thermal grease (Kryonaut, Thermal Grizzly, Germany), and reading the temperature through an Arduino microcontroller (UNO, Arduino, Italy). The current output of a 9V DC power supply (2230, Keithley Instruments, USA) was driven through the coverslip and regulated by a MOSFET transistor (N-Type, 1N914, Infineon Technologies, Germany). The transistor was opened and closed according to a Pulse Width Modulated (PWM) signal regulated by a Proportional–Integral–Derivative (PID) controller implemented on the Arduino (Beauregard, 2021), in order to maintain the temperature read from the thermocouple at a chosen set point. The setup achieved temperature control over the $20 - 50°C$ range with an accuracy of $\pm 1°C$.

1.2.3 Study Animals and Droplet Deposition

A colony of Indian stick insects (*Carausius morosus*, *Sinéty* 1901) was kept in the laboratory at room temperature ($T = 23 \pm 3$°C), and fed water and bramble *ad libitum*. Adults, identified via the scarlet colouration on the femur of their front legs (MacBride and Jackson, 1915) (Body mass 560.0 ± 240.0 mg, mean ± standard deviation, $n = 10$) were inserted into glass tubes, and one of the two front legs was attached to a metal wire with dental impression material (Elite HD+, Zhermack, Germany), exposing the *arolium* (Bullock et al., 2008; Labonte and Federle, 2015a). Using a micro-manipulator (MM 33 right, Märzhäuser Wetzlar, Germany), the pads were brought in contact with a glass coverslip until a maximum in the contact area was observed, and were left in contact for about a minute. Subsequently, secretion droplets were deposited on the glass coverslips by concentrically peeling the pads from the substrate. Experiments were conducted at four biologically relevant temperatures: 20, 30, 40, and 50°C (Stark et al., 2018). I deposited three droplets on each substrate for each of the ten individuals, at every temperature, for a total of $n = 480$ droplets.

1.2.4 General Principle of Contact Angle Measurements

Interference Reflection Microscopy (IRM) allows the reconstruction of 3D profiles from 2D images. The method is based on light interference, and utilises intensity extrema arising from constructive and destructive interaction of incident and reflected rays. Each extrema can be linked to a fixed height increment, and the resulting height profile can be used to extract a contact angle. This process requires a series of steps: First, the resulting extrema must be detected. Second, their corresponding elevation with respect to the imaging plane must be quantified. Third, the contact angles must be extracted from the reconstructed 3D coordinates. Below, I describe the steps I undertook to quantify the contact angles of tiny droplets.

1.2.5 Interference Reflection Microscopy

IRM utilises interference of monochromatic light to quantify the thickness of different optical interfaces, allowing the reconstruction of a three-dimensional profile of liquid deposits (Contreras-naranjo et al., 2010; Federle et al., 2006, 2002; Theodoly et al., 2010; Wiegand et al., 1997, 1998). A monochromatic light beam of wavelength λ passes through the glass coverslip and through a deposited droplet. Assuming all these media are parallel and the incident light beam is strictly perpendicular, refraction and

reflection occur at each interface according to *Fresnel*'s law (Wiegand et al., 1997, 1998). The reflected waves from each interface undergo constructive and destructive interference. This results in bright and dark patterns, further referred to as fringes, on the 2D images of the secretion droplets (See Figure 1.1C). *Wiegand et al.* established an expression for the light intensity measured on a system with any number of interfaces, allowing to measure their thickness (Wiegand et al., 1997, 1998). In the specific context of a single wedge-shaped interface (i. e a constant inclination angle), each fringe can be mapped to a contour line with height offset:

$$\Delta h = \frac{\lambda}{4 n_{\mathrm{L}} \delta}, \tag{1.2}$$

where $n_{\mathrm{L}} = 1.47$ is the secretion's refractive index (Dirks, 2009; Federle et al., 2002). The term δ corrects for non-normal incidence introduced by a finite Illumination Numerical Aperture (INA) through (Federle et al., 2002; Wiegand et al., 1997, 1998):

$$\delta = 1 - \sin^2\left(\frac{\arcsin(\mathrm{INA}/n_{\mathrm{L}})}{2}\right). \tag{1.3}$$

Each fringe thus acts as a contour line for droplet height, and can be related to the local height increment Δh (See Figure 1.1D). Because this method is entirely based on microscope imaging, it is non-intrusive and can reconstruct the height profile of minute droplets with high accuracy.

Deposited droplets were observed under an inverted reflected light microscope with a 60× oil immersion objective (Microscope: DMi8. Oil: Type N immersion liquid, Leica, Germany), and a filtered monochromatic LED light source (445 nm peak 10 nm bandwidth, pE-300 ultra, CoolLED, UK). The INA was set to the lowest available value of 0.8 to ensure dominantly perpendicular light incidence.

1.2.6 Image Processing and 3D Reconstruction

Images of the droplets were captured with a 1.6 MP camera at 60 fps (Blackfly BFS-U3-16S2C-CS, FLIR, USA) and analysed with a *Python* script using *Fiji*'s toolboxes (Schindelin et al., 2012). Three consecutive images of each droplet were taken and averaged to reduce camera noise. The centre of mass, area, and perimeter of each drop was determined by binarising the images in *Fiji* using a thresholding algorithm. The

droplet's radius was then calculated as twice the ratio between area and perimeter of the droplet (Schindelin et al., 2012; Van Rossum and Drake, 2009; Virtanen et al., 2020).

Intensity profiles were captured by rotating a line $n = 300$ times. The line started at the centre of mass and had a length 1.4 times the droplet's radius, excluding points closer than 0.3 times the radius from the centre of the droplet, where the intensity profiles were typically noisy and devoid of fringes. Previous work considered a single radial cross-section to determine the contact angle of small droplets (Dirks, 2009; Federle et al., 2006, 2002; Labonte, 2010). Here, each individual intensity profile represents a radial cross-section of the analysed droplet, as represented in Figure 1.2. Each intensity profile was then filtered with a third or fourth order *Butterworth* filter of variable critical frequency. Such adaptable filtering is preferred, as droplets on surfaces with different wettabilities may form substantially different contact angles; the closer the fringe spacing (occurring for steeper angles), the fewer the pixels available to detect extrema. As a result, intensity profiles with closer fringe spacing require a higher filtering frequency, to avoid high frequency intensity variation being interpreted as noise, particularly towards the centre of the droplet, where the contrast between bright and dark fringes is significantly reduced (See Figure 1.2). Since preliminary experiments revealed that the droplet size is orders of magnitude below the capillary length (Assuming a surface tension $\gamma_\mathrm{L} =\approx 30\,\mathrm{mN/m}$ and a density $\rho \approx 1\,\mathrm{g/mL}$, the capillary length is: $\lambda_\mathrm{c} = (\gamma_\mathrm{L}/\rho g)^{1/2} = 1.75\,\mathrm{mm}$. Federle et al., 2002) and since the secretion is in a wetting state ($\theta < 90°$) on all surfaces investigated in this work, a spherical cap seemed to be a reasonable approximation of a droplet's shape. A least squares algorithm was used to fit a full sphere of radius R_s to the 3D coordinates of the detected fringes, and the offset of the sphere on the Z axis was subtracted from this radius, to determine the height of the cap, h_c. The contact angle was extracted by calculating the exact tangent to the cap at the triple contact line, making use of the simple geometry of spherical caps through: $\theta = \arccos(R_\mathrm{s} - h_\mathrm{c})/R_\mathrm{s}$ (See Figure 1.2). The relative extrema were detected with a neighbouring values algorithm, using *Python*'s *Scipy* library (Virtanen et al., 2020). Since the spherical cap fitting was performed with a linearised version of a sphere's equation, the goodness of fit was estimated with the coefficient of determination R^2.

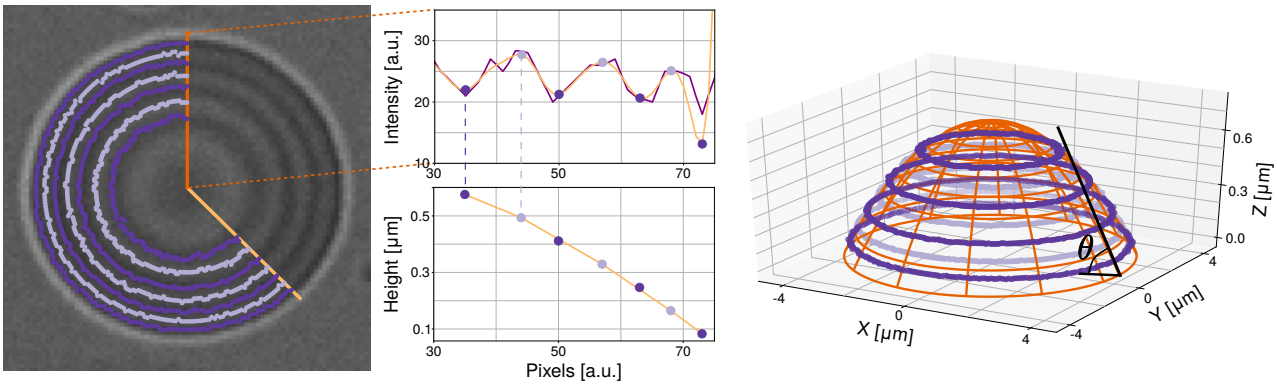


Figure 1.2 The secretion droplets are imaged with Interference Reflection Microscopy (IRM) at wavelength $\lambda = 445\,\text{nm}$, so visualising fringes, resulting from destructive and constructive light interference. A series of radial intensity profiles are extracted and filtered with a third or fourth order *Butterworth* filter (yellow). The extrema were detected on the filtered profile with a neighbouring values algorithm (bright and dark purple disks). From their height determined by Equation (1.2) and their horizontal spacing along the radius, the height profile can be reconstructed. This process can be repeated along the droplet's circumference. Combining the height profiles along all radii leads to a 3D scatter of points along the droplet's surface. The resulting 3D coordinates can be fitted with a spherical cap (orange mesh). The contact angle follows as the tangent to the cap, determined from the geometry of the fitted sphere. Note the difference in scale between Z and XY coordinates.

To verify the accuracy of IRM, a subset of droplets were imaged on all surfaces with both IRM and a White Light Interferometer (WLI; NewView NX2, ZYGO, USA) (Since they are based on the same imaging principle, I assume WLI suffers from the same difficulties as IRM for narrow fringe spacings, which is addressed below, Coupland and Lobera, 2010). The two methods are in good agreement, both qualitatively and quantitatively: there was no significant difference between both methods ($t_8 = 1.1$, $p = 0.30$), with an absolute contact angle error of $|\theta_{\text{IRM}} - \theta_{\text{WLI}}| = 3.3° \pm 1.4$, and an absolute fitted cap height error of $|h_{\text{IRM}} - h_{\text{WLI}}| = 326.7 \pm 232.8\,\text{nm}$ between the two setups (mean $\pm$ std, $n = 9$), with the average IRM cap height across all surfaces and temperatures being $h_{\text{IRM}} = 1252.2 \pm 458.6\,\text{nm}$ (mean $\pm$ std, $n = 160$).

Previous studies evaluated contact angles by measuring light intensity over a single radial section, extrapolating 2D height profiles, and fitting a line through the two or three outermost fringes to obtain the contact angle (Dirks, 2009; Federle et al., 2006, 2002; Labonte, 2010). This line fitting method however suffers from limitations for tiny

droplets, where the fitted line cuts through the droplet, rather than being tangential to it. I ran simulations to determine how significant this error is for $n = 10000$ droplets (Contact angles ranging from 10 to 30°, and droplet heights from 0.2 to 3.0 μm), and the maximum observed error may be as high as 62% (See Appendix A for details). The line fitting method has the advantage of estimating contact angles over specific diameters and avoiding droplet irregularities. Direct fitting of a spherical cap, on the other hand, uses all detected points to extract the 3D profile of droplets, and calculates the true tangent to the fitted spheres, instead of making use of a linear approximation of the profile at the edge.

The most common source of error stems from erroneously detected fringes, referred to as outliers in the following (See Figure 1.3). Outliers tended to occur near the edge or centre of droplets, both areas in which the contrast between neighbouring fringes tended to be weak. To test the cap fit method's robustness to errors, computer generated fringes were produced for a range of representative droplets (contact angles ranging from 10 to 30°, and droplet heights from 0.2 to 3.0 μm). Since the simulated droplets were extracted from perfect circles, the randomness of "real" droplets was simulated in three ways: First, random outliers were introduced around the innermost fringe, where the intensity profile is most sensitive to noise due to the low contrast in the light intensity. The probability of occurrence of these outliers was varied between 0 and 10% occurrence, which was representative of the experimentally observed droplets. Second, outliers were introduced around the outermost fringe. Because the out-of-plane (Z) spacing between fringes is calculated incrementally from the outermost to the innermost fringes, these outliers introduce larger errors by shifting a whole detected radius upwards (See Figure 1.3). Despite the fact that droplets with a high contact angle (and therefore tighter fringe spacing) exhibit more of these outliers, they were not frequently encountered, and their probability of occurrence was set to 1%. Third, the in-plane (X and Y) coordinates of the extrema were normally distributed over a standard deviation of half the spacing between fringes, introducing random noise.

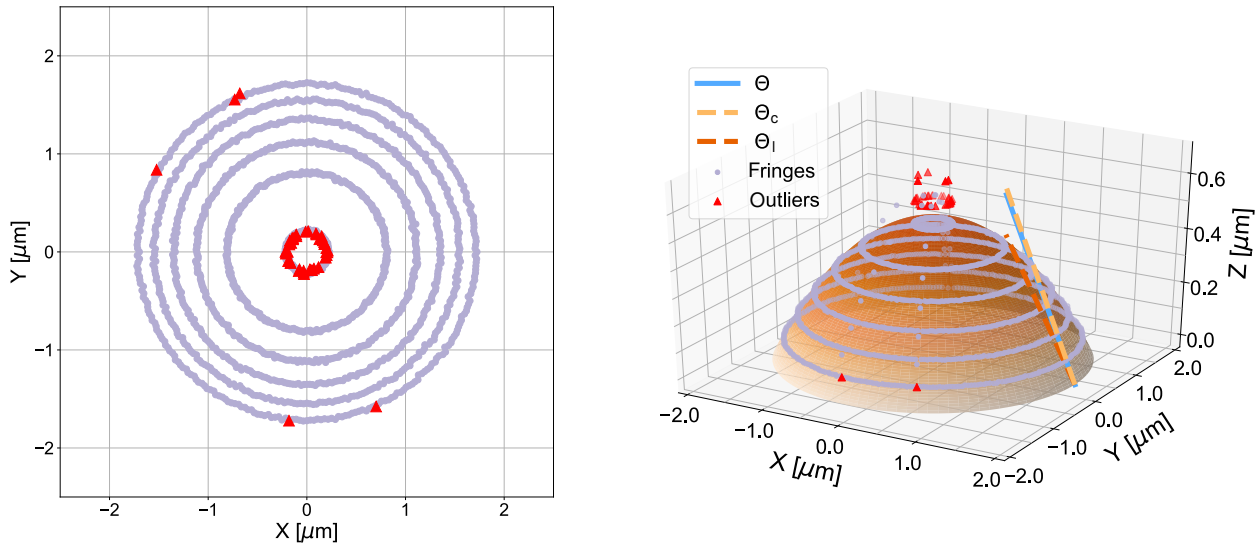


Figure 1.3 A simulated fringe pattern (light purple disks) with outer and inner outliers (red triangles) in the XY plane. The corresponding 3D reconstruction of the droplet is shown below, where the inner outliers are misplaced by Δh or $2\Delta h$ above the droplet. The less frequent outer outliers shift all points on a radius by a height Δh. Nonetheless, the spherical cap fits the fringes well, and the contact angle obtained through the tangent to the spherical cap (θ_c) is almost identical to the real contact angle θ used to simulate the droplet. The contact angle using a linear fit on the outermost points of the droplet (θ_l) underestimates the original angle. Note the difference in scale between Z and XY coordinates.

Simulated droplets were generated over the range of heights, angles and outlier probabilities ($n = 10000$). The cap fit method introduced a relative error ranging between 0.07 and 15% on the contact angle (the highest values occurring for the largest number of outliers at the innermost fringe), and is therefore more robust to experimental noise than the line fit, with an error of up to 65%, with a large majority of this error being a result of the line not being tangential to the droplet, as previously discussed (See Appendix A for details).

Physical limitations occur for contact angles greater than 40°, for which the light intensity dampens and the fringes overlap. Indeed, contact angle values for the OTS coated coverslip could not be obtained, as the spacing between the fringes became too narrow (Federle et al., 2006, 2004, 2002; Wiegand et al., 1997, 1998). In the case of intensity profiles that present observable fringes ($\theta < 40°$), a correction to the height profiles must be implemented, because the assumption that all interfaces are

parallel is violated (Wiegand et al., 1997, 1998). The formalism detailed by *Wiegand et al.* provides a method for reproducing expected intensity profiles for wedges of a certain angle, and a function: $\mathcal{F}$, relating the uncorrected "measured" angle β_{UC} to the corrected "real" angle β_{C} through:

$$\beta_{\mathrm{C}} = \beta_{\mathrm{UC}}\mathcal{F}(\beta_{\mathrm{UC}}). \tag{1.4}$$

Wiegand et al. also provide an empirical form for this function (Wiegand et al., 1998):

$$\mathcal{F}(\beta_{\mathrm{UC}}) = 1 + \frac{1}{c_1\left(c_2 - \beta_{\mathrm{UC}}\right)^{c_3}}, \tag{1.5}$$

where $c_{i=1,2,3}$ are fitted parameters. I hence simulated intensity profiles for wedges of different steepness, following the procedure described by *Weigand et al.* (Wiegand et al., 1997, 1998). Such simulations provide, given the optical parameters of the considered interfaces, pairs of "real" and "measured" angles, which differ due to the aforementioned limitations originating from the finite numerical aperture, and the non-planar interfaces considered here (See Appendix A for details).

I simulated the light intensity profiles resulting from wedges with uncorrected angles in the [0, 25°] range for the experimental parameters used in this study ($\lambda = 445\,\mathrm{nm}$, INA = 0.8, and NA = 1.3). The resulting correction function valid for wedges followed the shape expected from *Wiegand et al.*'s theory (See Figure 1.4A). To extend the applicability of said function to spherical caps, I considered individual radii of a droplet of uncorrected angle θ_{UC} and discretised each radial arc into a succession of wedges (See Figure 1.4B). Each wedge is defined as a segment joining two adjacent fringes separated by an horizontal and vertical distance r_i and z_i. Each of these angles makes an (uncorrected) angle $\beta_{\mathrm{UC},i} = \arctan(z_i/r_i)$ with the horizontal.

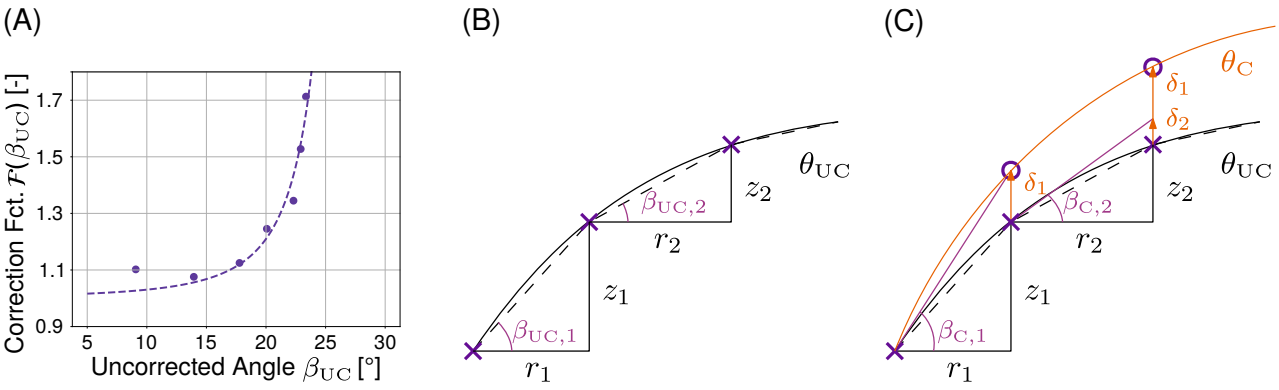


Figure 1.4 (A) "Real" and "measured" angles differ for a wedge system. The correction function was calculated for a liquid of refractive index $n = 1.47$ observed under an optical system with $\lambda = 445\,\text{nm}$, INA $= 0.8$, and NA $= 1.3$. The dashed line represents the fitted correction function $\mathcal{F}(\beta_{UC})$. (B) Schematic representation of a discretised section of a spherical cap where the crosses are the uncorrected fringes and the dashed line represents the wedges with their respective local angles $\beta_{UC,i}$. (C) The corrected wedge with its displaced fringes (circles), based on the corrected angles $\beta_{C,i}$, and the incremental corrections δ_i, correct for the non-planar interfaces assumption. The newly fitted spherical cap is then fitted to the corrected data points, providing the correct angle θ_C.

Each sub-section of the droplet can then be corrected as if it was a wedge. Starting from the first two fringes, the updated wedge angle is:

$$\beta_{C,1} = \arctan(z_1/r_1)\mathcal{F}(\arctan(z_1/r_1)), \tag{1.6}$$

leading to the height correction δ_1:

$$\delta_1 = r_1 \tan(\beta_{C,1}) - z_1. \tag{1.7}$$

This procedure can be repeated for every wedge i, providing the local correction factor δ_i for each wedge:

$$\begin{cases} \beta_{C,i} = \beta_{UC,i}\mathcal{F}(\beta_{UC,i}) \\ \delta_i = r_i \tan(\beta_{C,i}) - z_i \end{cases} \tag{1.8}$$

Since every wedge correction shifts the whole droplet profile upwards, the total correction Δ_i follows as the iterative sum of all previous corrections:

$$\Delta_i = \sum_{j=1}^{i} \delta_i = \sum_{j=1}^{i} r_j \tan(\beta_{C,j}) - z_j \tag{1.9}$$

This procedure is repeated for all radial arcs of the droplet, until the full 3D reconstructed droplet is recovered (See Figure 1.4C). To tackle the presence of outliers, and particularly their high correction coefficient (See Equation (1.9)) due to their steep angles with real fringes, I limited the corrections to angles below 95% of the asymptotic coefficient c_3. Furthermore, since no fringes are detected in the centre of the droplets, 3D coordinates should always be located below the highest point on the droplet. Hence, points with a Z coordinate higher than the spherical cap's height h_c were removed as outliers, and a new spherical cap was fitted to the remainder of the detected fringes. This procedure was iterated until all detected points were below the cap's height, finally providing the correct contact angle: θ_C.

The temperature and surface energy dependencies of the contact angle were assessed on the corrected angles. In order to apply the *OWRK* method (Equation (1.1)), the corrected contact angles from every Individual-Surface-Temperature combination were considered to be an independent measurement, and the values of the three contact angles measurements in each set were averaged during the estimation of the surface tension.

General Principle of Viscosity Measurements

Akin to surface tension measurements, standard rheology techniques are limited by the scarce volume of the secretion. Previous work has determined the viscosity of the secretion found under beetles's and stick insects's pads using microrheology (Abou et al., 2010; Attipoe, 2018; Peisker et al., 2014), which utilises the *Brownian* motion of one or multiple tracers in a liquid sample to determine its diffusion coefficient, and in turn its viscosity (Abou et al., 2010; Peisker et al., 2014). These studies reported a viscosity coefficient in the $10 - 110\,\mathrm{mPas}$ range (Abou et al., 2010; Attipoe, 2018; Peisker et al., 2014). Microrheology however requires extensive amounts of the secretion to be deposited from insects's feet and collected with glass capillaries over multiple hours (Abou et al., 2010; Attipoe, 2018; Peisker et al., 2014). The microscopic secretion droplets have a large surface area to volume ratio, and components within them are hence susceptible to evaporation over such large time scales. In order to overcome these difficulties, we adopted an *in-vivo* methodology, as described by *Federle et al.*,

where pads are slid across a glass coverslip, allowing the observation of the secretion's dewetting (Federle et al., 2004, 2002). Using this methodology, *Federle et al.* reported a viscosity estimate in the $40 - 50\,\mathrm{mPas}$ range.

Dewetting Theory

Dewetting refers to the thermodynamic process through which metastable thin films break down. When a liquid is spread below a critical thickness, thermal instabilities create dry patches within it (Redon et al., 1991; Reiter, 1993). These holes then grow over time, a process driven by the surface tension of the liquid γ_L and its affinity to the surface it is spread on, usually measured through the contact angle θ. The viscosity η of the liquid however opposes resistance to this growth, and the resulting radial velocity of a dry patch is governed by an empirical law (Redon et al., 1991; Reiter, 1993):

$$v_\mathrm{d} = k_\mathrm{d}\,\theta^3 \frac{\gamma_\mathrm{L}}{\eta}, \tag{1.10}$$

where k_d is an experimental constant (for which we chose a lower ($k_\mathrm{d}^\mathrm{low} = 1.9 \times 10^{-8}$) and upper ($k_\mathrm{d}^\mathrm{high} = 5.3 \times 10^{-8}$) bounds, found in literature Reiter, 1993), and $v_\mathrm{d} = \frac{\mathrm{d}R_h}{\mathrm{d}t}$ is the rate of change of a hole's radius R_h, and θ is the contact angle in degrees.

If the surface tension and contact angle of the secretion are determined, observing the growth rate of dry patches allows for a direct measurement of the secretion's viscosity. This measurement is valid when the metastable film is spread within a range of thicknesses that allows the spontaneous formation of holes, a condition met in all experiments conducted in this study. Moreover, by using the temperature control setup described above (Further detailed in our publication. Kaimaki et al., 2022), we were able to control the temperature of the glass coverslips on which the pads were being slid, allowing us to assess the temperature dependence of the secretion's viscosity. Typically, the viscosity of a *Newtonian* liquid follows an exponential law of type (Haj-kacem et al., 2014):

$$\eta(T_K) = a \exp\left(b/RT_K\right), \tag{1.11}$$

where T_K is the temperature in *Kelvin*, a and b are fitted constants, and $R = 8.31\,\mathrm{J/(mol{\cdot}K)}$ is the universal gas constant. Temperature is hence a key param-

eter in distinguishing the viscous and capillary contributions of the secretion; we expect a relatively weak temperature dependence of the surface tension, and an exponential relationship of viscosity with temperature (Fasina et al., 2006; Haj-kacem et al., 2014; Sahasrabudhe et al., 2017). Additionally, from Equation (1.10), we expect the dewetting speed on a surface to be dependent on its associated contact angle. A measurement of the viscosity at a fixed temperature combined with the dewetting speed on a surface can thus provide a measurement of the contact angle on said surface. This method is particularly helpful to determine the affinity of the secretion to surfaces whose energy is low, and on which contact angles are so large that they can no longer be determined with IRM (See above).

Study Animals and Dewetting Experiments

We recorded the dewetting of the pad secretion for $n = 10$ insects, on the five surfaces listed in Table 1.1, at 20, 30, 40, and 50°C. Insects were mounted in glass tubes, and their pads were slid across the coverslips with the help of a micromanipulator (MM 33 right, Märzhäuser Wetzlar, Germany, and MMO-220A, Narishige, Japan), connected to a custom-built DC motor circuit (UNO, Arduino, Italy). Videos of the dewetting film after pad sliding were recorded with two high-speed cameras, depending on the dewetting speed, dictated by the contact angle (Blackfly S BFS-U3-16S2C-CS, FLIR, USA and CR5000x2, Optronis GmbH, Germany). The size of the dry patches was tracked using a custom-written *Fiji* (Schindelin et al., 2012) macro and the average velocity over $N = 3$ dry patches per video was recorded as an independent measurement, in a procedure identical to that described in *Kaimaki et al.* (Kaimaki et al., 2022).

1.2.7 Statistical Methods

All numbers are represented as mean ± standard deviation (std) unless otherwise indicated. Effects of temperature, and surface energy on contact angles were analysed via a two-way repeated measures analysis of variance (ANOVA) in *R* (version 3.6.3 R Core Team, 2020). The effect of temperature on dewetting velocities was assessed with a repeated measures one-way ANOVA. All curves were fitted using a least squares procedure, as part of *Python*'s *Scipy* toolbox, utilising a trust region reflective algorithm (*Python* version 3.8.10 Van Rossum and Drake, 2009; Virtanen et al., 2020).

1.3 Results

1.3.1 Contact Angle and Surface Tension Measurements

The droplets analysed in this study had an average radius and height of $5.5 \pm 1.7\,\mu$m and $1.3 \pm 0.5\,\mu$m, respectively, corresponding to an average volume of $84.7 \pm 84.7\,$fL (mean $\pm$ std. $n = 480$). The droplet's rims, as viewed from the microscope were round, particularly on coverslips with low surface energy (DMAPTMS, TMCS), where the droplets achieved a circular contact line, the most energy efficient configuration. On such surfaces, fringes were numerous and closely spaced. The light intensity, and in particular the contrast between minima and maxima, were expectedly low given the overlapping of fringes discussed above. On the higher surface energy coatings (Glass, GPTS), the fringe spacing increased and the droplets occasionally were pinned on short sections of the contact line, demonstrating contact angle hysteresis (de Gennes et al., 2003). The contact angle values increased after applying the correction method accounting for non-parallel interfaces, particularly on low energy surfaces (See Figure 1.5).

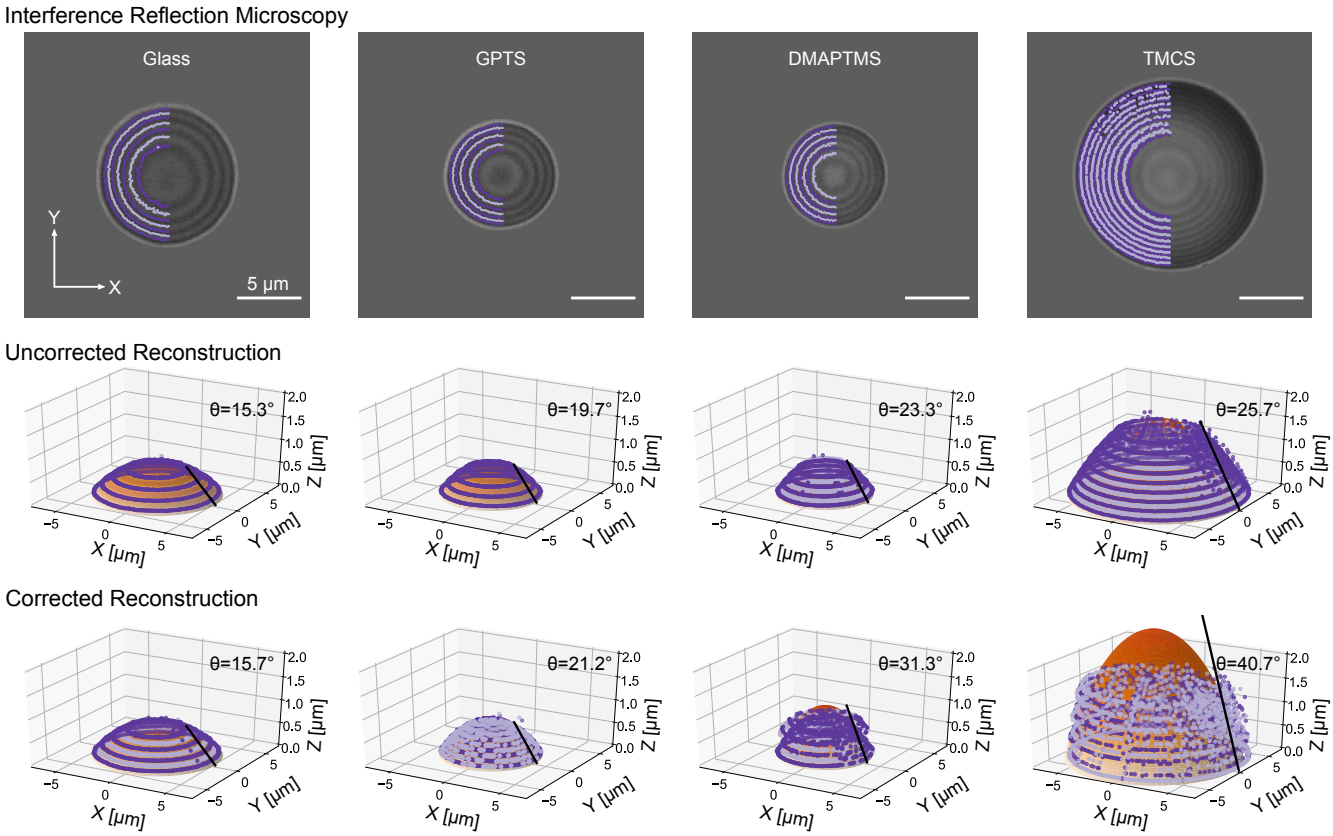


Figure 1.5 Representative Interference Reflection Microscopy (IRM) images of droplets and their 3D reconstruction on surfaces with different wettability, before (Uncorrected Reconstruction) and after (Corrected Reconstruction) applying the contact angle correction method for non-parallel reflective interfaces. The detected fringes (minima and maxima in dark and light purple) are indicated on the left half of the droplets. The orange surface is the fitted spherical cap, and the black line represents the contact angle extracted for each droplet. The correction method leads to a systematic increase of the contact angle values. Note the difference in scale between Z and XY coordinates.

Uncorrected contact angles of the insect pad secretion ranged from 10 to 30° across temperatures and surfaces. After correction, the higher end of the range increased to 55°, and the lower end remained almost unchanged, as the correction factor is effectively unity (See Figure 1.6). The outlier fringes were numerous for steep contact angles, but the filtering techniques employed here lead to plausible values according to previous literature (Dirks, 2009; Federle et al., 2004, 2002; Labonte, 2015). Additionally, due to the number of points used for each spherical cap fitting, these outliers did not seem to affect the spherical cap fitting, as the average coefficient of determination over all reconstructed droplets was $R^2 = 0.7 \pm 0.2$ (mean $\pm$ std, $n = 480$).

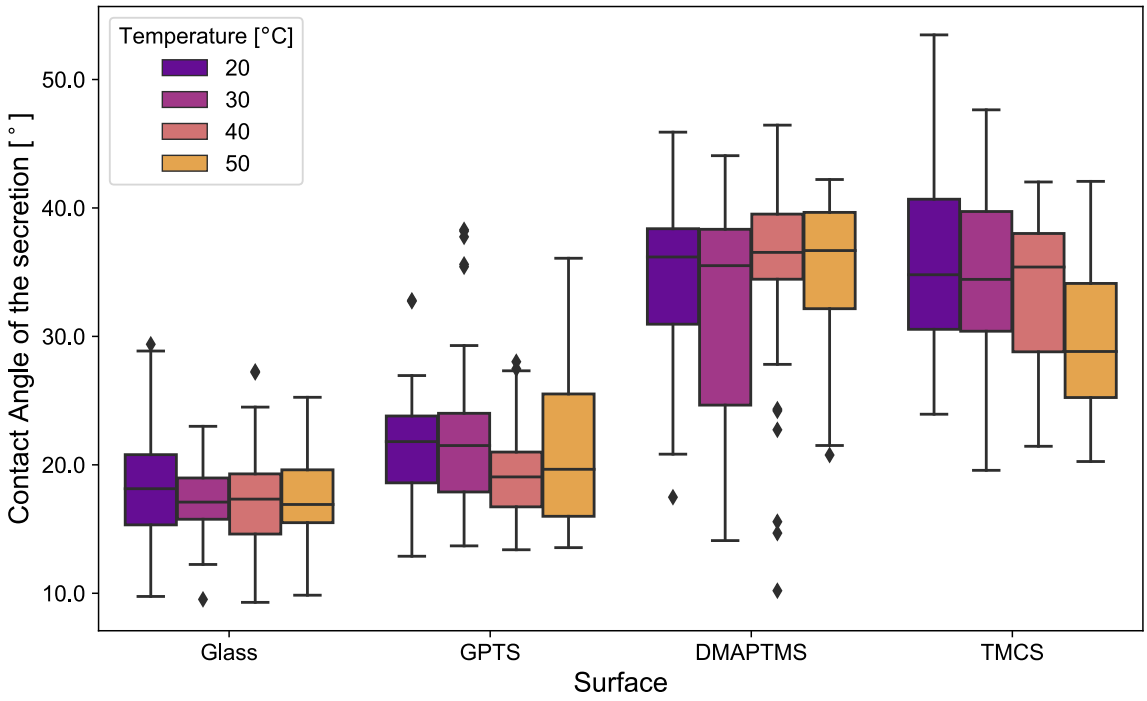


Figure 1.6 To quantify the surface tension of the secretion and its temperature dependence, the contact angles were measured on surfaces of different wettability at different temperatures. The surface energy of the silane coated coverslips had a significant effect on the contact angle values, but temperature only had a statistically significant effect through its interaction with surface energy.

The contact angles significantly increased with decreasing surface energy, but did not vary significantly with temperature (See Table 1.2). Most droplets imaged in this work were close to being perfectly circular in the imaging plane, and hence had a consistent contact angle across all radial sections. Because the droplets were deposited by pulling the pads away from the surface, the contact angles do however represent receding contact angles, and not equilibrium angles. Moreover, heterogeneities of the surface and possibly within the secretion (Dirks et al., 2010; Federle et al., 2002; Votsch et al., 2002), did sometimes locally deform the three-phase line. I decided to include such droplets in my analysis, because they were few, and the pinning was localised. Furthermore, the large number of data points around a droplet's perimeter still dominated the fitting of the spherical caps, so that pinning rarely had a significant influence. In fact, the variability within droplets was found to be low, as the within-subjects mean squared

error (residuals) associated specifically with the stick insect factor was $MS_{sticks} = 299.9$, substantially lower than the factor-related errors found in Table 1.2.

Predictor	d.f.	Sum Sq.	Mean Sq.	F	p
Surface	3	24481	8160	251.6	< 0.001***
Temperature	3	109	36	1.1	0.6
Surface * Temperature	9	751	83	2.6	0.007**
Residuals	455	14769	32		

Table 1.2 A two-way repeated measures ANOVA was performed to analyse the effect of surface energy and temperature on the contact angle of the secretion. The type of silane coating had a statistically significant effect, while the temperature of the coverslips had no significant effect. The interaction of the two independent variables had a significant effect.

Because contact angles were not significantly affected by temperature, I averaged them per surface. On most surfaces, the contact angles of the secretion were lower than those for water, which is mostly polar ($\gamma^{p}_{water} = 51.0$, $\gamma^{d}_{water} = 21.8\,mN/m$ (Janczuk et al., 1993)) and diiodomethane, a mostly dispersive liquid ($\gamma^{p}_{diiodomethane} = 0.0$, $\gamma^{d}_{diiodomethane} = 50.8\,mN/m$ (Janczuk et al., 1993), see Table 1.3).

Surface	$\theta_{secretion}$ [°]	θ_{water} [°]	$\theta_{diiodomethane}$ [°]
Glass	17.7	12.0	31.8
GPTS	21.2	71	41.3
DMAPTMS	33.8	77.2	48.3
TMCS	33.2	95.3	65.2
OTS	/	105.8	64.1

Table 1.3 Summary of the contact angle values of the secretion obtained through IRM, as well as water and diiodomethane as measured with a goniometer on all silanised surfaces utilised in this study. Measurements on OTS were not possible due to the spacing between fringes being reduced as a result of the high contact angle.

The dispersive, polar, and total surface tension were estimated for each pair of different surfaces with the *OWRK* method (See Figure 1.7). Temperature had no significant effect on either γ^{d}_{L} (ANOVA, $F_{3,20} = 0.10$, $p = 0.96$) or γ^{p}_{L} ($F_{3,20} = 0.18$, $p = 0.91$).

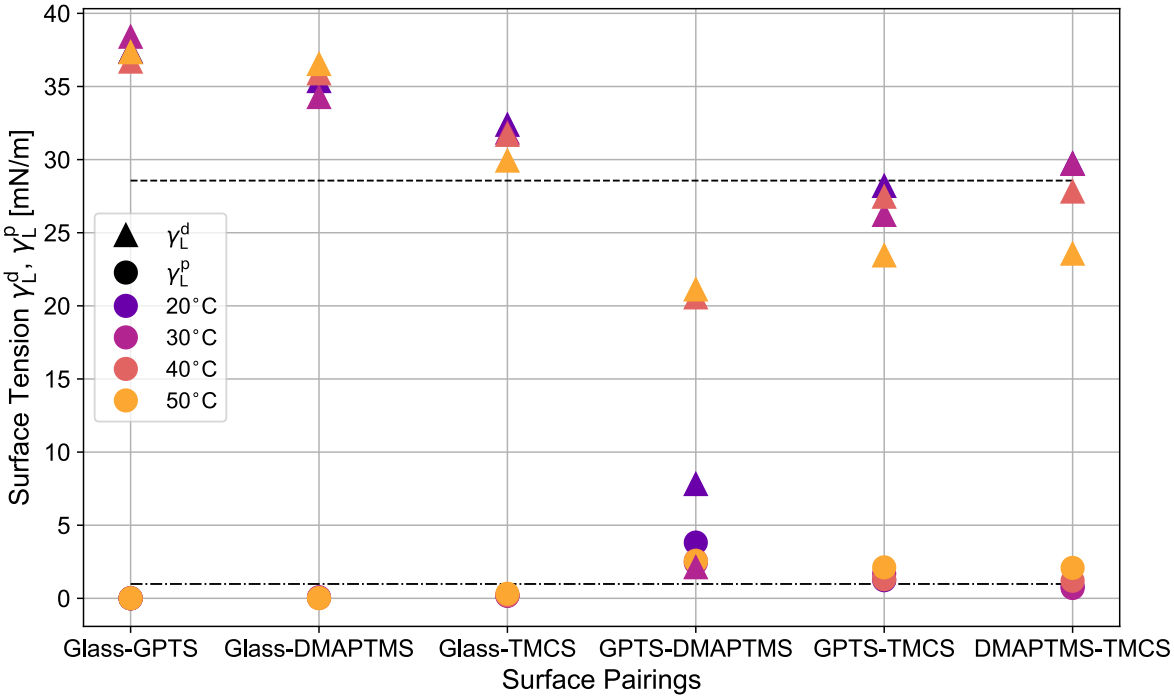


Figure 1.7 The contact angle values on all surfaces were used to calculate γ_L^d and γ_L^p, the dispersive (triangles) and polar (circles) components of the surface tension, for every pair of silanised surfaces. The data points are shown for every temperature, which had no statistically significant effect. The dashed and dash-dotted lines represent the total average of the dispersive and polar component, for all temperatures and surface pairs.

To provide a unique surface tension measurement for all surface pairs, the values extracted through the *OWRK* method were averaged for every temperature (See Table 1.4).

Temperature [°C]	γ_L^d [mN/m]	γ_L^p [mN/m]	$\gamma_L = \gamma_L^d + \gamma_L^p$ [mN/m]
20	28.5 ± 9.8	1.0 ± 1.3	29.5 ± 8.4
30	27.1 ± 11.8	0.9 ± 0.9	27.9 ± 11.0
40	30.0 ± 5.5	0.9 ± 0.9	30.9 ± 4.6
50	28.7 ± 6.4	1.2 ± 1.1	29.8 ± 5.4

Table 1.4 Summary of the polar and dispersive surface tension values at all temperatures, obtained applying the *OWRK* method to the contact angle values of the secretion on the four coatings used in this study. Temperature did not have a significant effect on the surface tension values.

The total average surface tension across all temperatures was $\gamma_L = 29.5 \pm 7.4\,\mathrm{mN/m}$. The surface tension was strongly dominated by its dispersive component; with $\gamma_L^p = 1.0 \pm 1.1\,\mathrm{mN/m}$ and $\gamma_L^d = 28.6 \pm 8.4\,\mathrm{mN/m}$ (mean $\pm$ std, $n = 24$), respectively.

These surface tension values can be inserted back into the *OWRK* equation, as it can also function as a predictor for contact angle values on any surface of known polar and dispersive surface energies. In the case of total wetting, the arccos function computed in Equation (1.1) becomes undetermined, and the contact angles are effectively zero; the fluid fully wets the surface, and spontaneously spreads to molecular thickness. When the contact angles are greater than 90°, the liquid is no longer wetting the surface (See Figure 1.8, in which both situations are represented in dark blue and white, respectively).

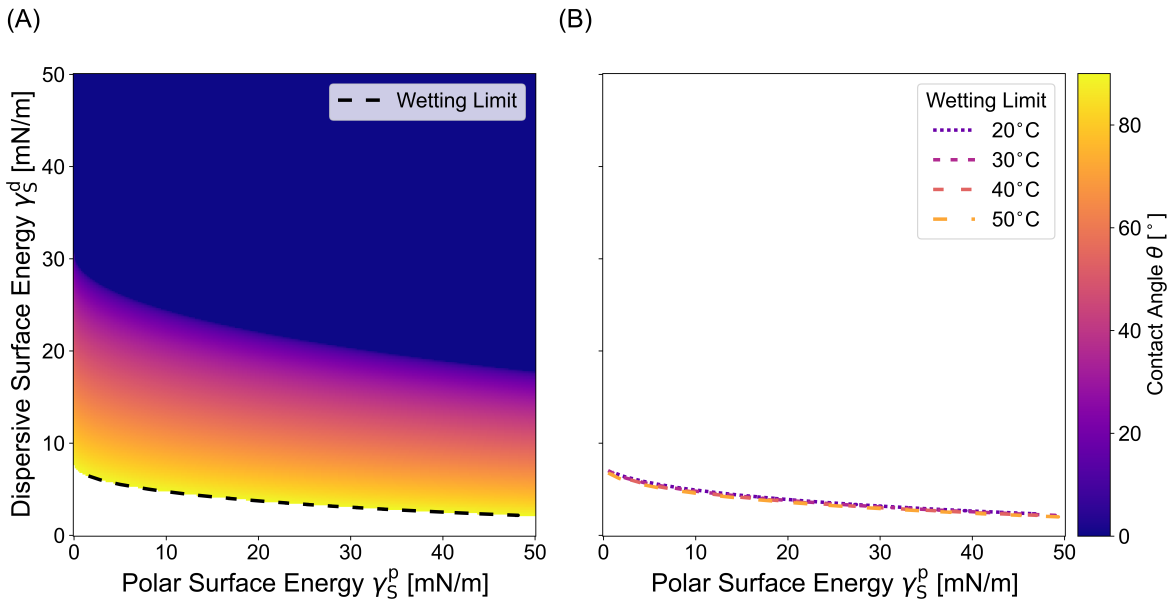


Figure 1.8 (A) The dispersive (γ_L^d) and polar (γ_L^p) surface tension components can be inserted into the *OWRK* equation (1.1), in order to predict contact angle values on surfaces of known dispersive (γ_S^d) and polar (γ_S^p) surface energies. The bottom of the colour bar (on the right) indicates a fully wetting state, the dashed line marks the wetting limit ($\theta = 90°$), and the plain white area indicates a non-wetting state ($\theta > 90°$). (B) The *Eötvös* law can be used to predict the theoretical decrease in surface tension with increasing temperature (Equation (1.13), see Discussion). The wetting limit is almost unchanged by temperature variations in the observed range, signifying a minute change in the wetting capabilities of the secretion.

1.3.2 Viscosity Measurements

As expected, the growth rate of nucleated holes increased with increasing temperature (ANOVA: $F_{3,14} = 30.83$, $p < 0.001$, See Figure 1.9A). The within-subject mean squared error (residuals) was $\mathrm{MS}_{\mathrm{sticks}} = 601\,\mu\mathrm{m}^2/\mathrm{s}^2$, much lower than the error associated with temperature changes $\mathrm{MS}_{\mathrm{sticks}} = 8394\,\mu\mathrm{m}^2/\mathrm{s}^2$. The viscosity of the secretion was calculated using Equation (1.10), and we found values between 20 and 500 mPa·s. Two exponential laws were fitted to the viscosity values at different temperatures, according to Equation (1.11), and provided low and high bounds for the temperature dependence of the viscosity as: $\eta_{\mathrm{low}}(T) = 5.22 \times 10^{-10} \exp(64.79/RT_K)$ ($[-3.15 \times 10^{-9}, 4.2 \times 10^{-9}]$ and [56.82, 72.76], 95% CI) and $\eta_{\mathrm{high}}(T) = 1.45 \times 10^{-9} \exp(64.79/RT_K)$ ($[-3.27 \times 10^{9}$, $6.18 \times 10^{9}]$ and [56.82, 72.76], 95% CI). The viscosity of the secretion at different temperatures hence likely falls between those two limits (See Figure 1.9B).

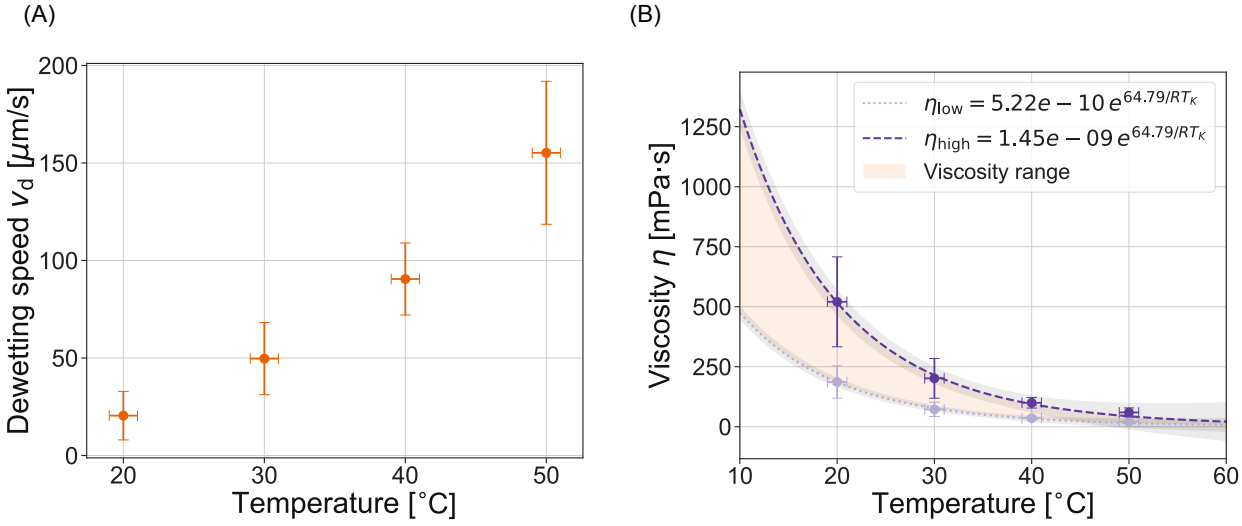


Figure 1.9 (A) Measuring the growth rate of nucleated holes in the secretion film at different temperatures gives insight into the the wetting and viscous dynamics of the secretion. The competition of capillary and viscous forces results in the dewetting speed, which increases with increasing temperature. (B) The viscosity, obtained as proportion between the dewetting velocity and the wetting properties of the secretion (Equation (1.10)), follows an exponential decay with temperature. Here, two estimates of the viscosity are obtained with extreme values of the proportionality constant (bright and dark purple), and fitted with exponential decay functions. The viscosity of the secretion hence likely falls within the range indicated in orange. The exponential fits and their 95% confidence intervals are indicated in dashed black lines and in grey, respectively.

At room temperature and on substrates with different coatings, the dewetting speed also increases with decreasing surface energies (See Figure 1.10A). This result is in line with the cubic dependence on the contact angle in Equation (1.10), and consistent with the range of contact angle values determined in this study (See Table 1.3). In order to test if the relationship between contact angle and dewetting velocity is cubic as predicted by theory, we fitted a power law $v_d = v_0\,\theta^n$ with an undetermined exponent to those data (See Figure 1.10B). The resulting fit had a power exponent of $n = 3.52$ ([2.74, 4.29], $v_0 = 0.88\,\mathrm{nm/s}$ [0.07, 11.06], 95% CI), not significantly different from the expected value of three. From the dewetting velocity on OTS substrates and the fitted power law, we extracted a contact angle value for OTS and found $\theta_{OTS} = [v_{OTS}/(0.88\,\mathrm{nm/s})]^{1/3.52} = 39.7°$ for the average dewetting speed for OTS $v_{OTS} = 373.1\,\mu\mathrm{m/s}$, close to the IRM limit discussed above.

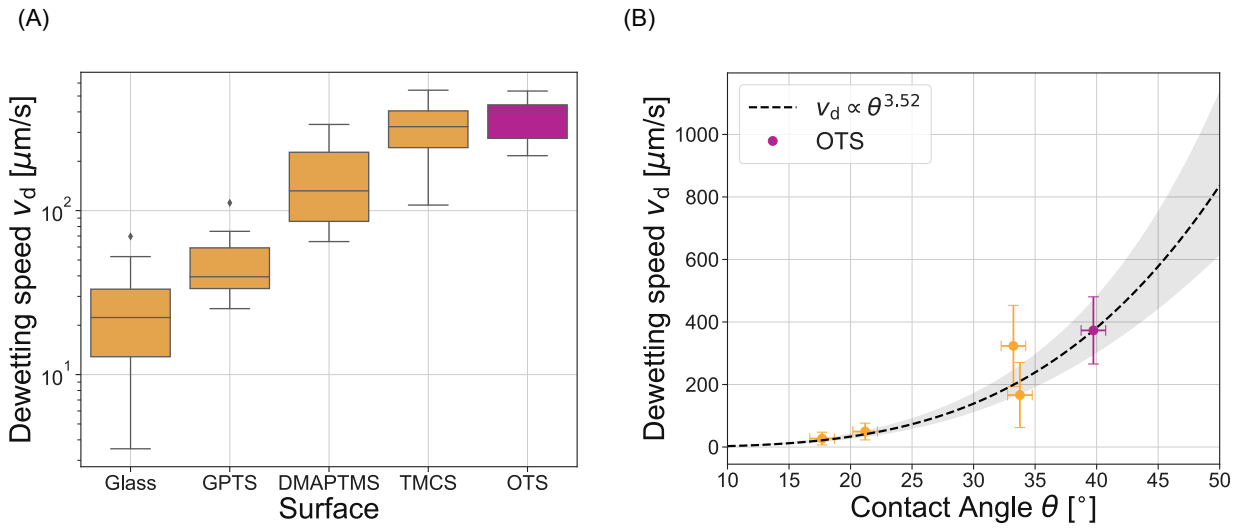


Figure 1.10 (A) The dewetting speed measured on surfaces of different wettability at room temperature increases with decreasing surface energy. An additional measurement for OTS, for which the contact angle could not be estimated with IRM is also included (pink). (B) The relationship between the wettability of different surfaces and the dewetting velocity should follow a cubic dependence (Equation (1.10)). We verified this assumption by fitting a power law to the dewetting velocities of the four surfaces indicated in orange and their contact angles obtained through IRM, and found a power exponent of 3.52. This power law can be used to extrapolate the contact angle of OTS based on its dewetting velocity (pink), providing an approximate contact angle for OTS, close to the IRM limit discussed above at $\sim 40°$. The fit and its 95% confidence intervals are indicated in dashed black lines and in grey, respectively.

1.4 Discussion

1.4.1 Surface Tension and Contact Angles

The discussion surrounding the physical origin of insect adhesion involves the study of a complex interface. The most common interpretation for the adhesion of smooth pads is perhaps closely tied to the capillary effects of the secretion found under hairy pads (Dirks and Federle, 2011a; Federle et al., 2002; Gilet et al., 2018; Sudersan et al., 2021). In this chapter, I investigated the physical properties of the secretion and their temperature dependence, with the aim of determining their relative importance to the adhesive forces produced by insects's pads.

My study confirmed that the surface tension and contact angles of the insects's adhesive secretion are characteristic of those of a low surface tension oil with $\gamma_L = 29\,\mathrm{mN/m}$, in good agreement with previous literature values (See Table 1 Dirks, 2009; Federle et al., 2004, 2002; Hasenfuss, 1999; Labonte, 2010). Most studies investigating the chemical composition of the secretion found that it contains long-chained hydrocarbons (C_{22} to C_{49} n-alkanes and n-alkenes Betz et al., 2016; Eisner and Aneshansley, 2000; Geiselhardt et al., 2010, 2009; Kosaki and Yamaoka, 1996; Reitz et al., 2015; Speidel et al., 2017; Votsch et al., 2002). Previous literature on the surface tension of hydrocarbons found that for alkanes, it increases with the number of carbon atoms (Janczuk et al., 1993; Romero-Martínez and Trejo, 1998; Yang et al., 2021). For a fixed number of carbon atoms, branched-chains hydrocarbons however tend to have a lower surface tension than their linear counterparts (Yang et al., 2021). Most linear hydrocarbons exhibit a low polar component, if existent at all (Janczuk et al., 1993; Kaelble, 1970). Overall, linear and branched hydrocarbons with a number of carbon atoms between 16 (n-hexadecane) and 28 (octacosane) have surface tension values between 15 and 30 mN/m at 20°C (Janczuk et al., 1993; Kaelble, 1970; Yang et al., 2021). These values are in good agreement with my measurements, and in accordance with the chemical nature of the secretion. It must be noted that due to their composition, and the melting point of some of its components, it is not uncommon to find solid particles in deposited secretion droplets. While these solid lipids might have a physical relevance to the adhesion of insects, their interaction with the liquid phase of the secretion is likely complex, and goes beyond the scope of this analysis. Droplets which contained large solid particles were thus excluded, and the secretion was treated as a purely liquid

phase. Similarly, if insects were to make use of the liquid secretion to produce adhesive forces, it must remain partly liquid over the temperature range insects are exposed to.

It was typically assumed that the surface tension of the secretion could give rise to capillary forces (Dirks, 2014; Dirks and Federle, 2011a; Federle et al., 2002). Accordingly, the low contact angles on all surfaces investigated in this study are representative of a high versatility of the secretion. In fact, the contact angle stays below 55° and can be as low as 10°, which corresponds to a wetting state ($\theta < 90°$) (de Gennes et al., 2003). These values are much lower than those of water (See Table 1.3), for which contact angles are indicative of a non-wetting state on the most hydrophobic surfaces tested in this study. The reason for the secretion's impressive wettability on all surfaces utilised here lies in the polar and dispersive components of the surface tension. Since the secretion has a mostly dispersive component, it is likely to wet surfaces whose variation in surface energy mostly lies in their polar component, akin to most plant and leaves on which diiodomethane typically exhibits better wetting than water (Wang et al., 2014). The surfaces tested in this study follow such a trend, where the dispersive component of the surface energy remains fairly low and constant (See Table 1.4). Such a low dispersive component gives rise to the advantageous behaviour depicted in Figure 1.8, where a wetting state is achieved for surfaces with a relatively small dispersive surface energy. Authors have in the past argued that since the secretion contains both a hydrophobic and a hydrophilic phase (Previous studies revealed the secretion is an emulsion containing a hydrophilic disperse phase in a hydrophobic continuous phase Dirks et al., 2010; Federle et al., 2004, 2002; Geiselhardt et al., 2010; Votsch et al., 2002), it might be capable of providing strong attachment to both hydrophobic and hydrophilic surfaces (Gorb, 2007; Koerner et al., 2012; Reitz et al., 2015; Speidel et al., 2017; Votsch et al., 2002). Following *Dirks et al.*'s line of thought, I argue that a dominant dispersive (hydrophobic) fraction of the secretion is sufficient to demonstrate high affinity to most surfaces (Dirks et al., 2010). As an example, the prediction in Figure 1.8 indicates the secretion will wet a surface with a polar energy of 20 mN/m (A typical value found in literature for many plants and leaves Fernández and Khayet, 2015; Wang et al., 2014) provided that its dispersive surface energy is above 5 mN/m. Most studies investigating the surface energy of plants and leaves revealed that their dispersive components are an order of magnitude higher than the polar ones (Fernández and Khayet, 2015; Wang et al., 2014), a situation favourable to insects, were they to rely on the wetting properties of the secretion to produce adhesive capillary forces. Nonetheless, literature focused on determining the polar and dispersive components

of plant surfaces is lacking. In fact, most studies used sessile droplet techniques on rough leaf surfaces, including the *OWKR* method utilised in this work. Such studies do not consider the effect of roughness, and hence do not measure the true molecular surface energies of plant surfaces, but are rather measuring effective angles and surface energies, most likely resulting from *Cassie-Baxter* (Cassie and Baxter, 1944) or *Wenzel* (Wenzel, 1936) states (de Gennes et al., 2003). Thus, surface energies are most likely underestimated, leading to polar components being estimated to be close to zero for many plants (Fernández and Khayet, 2015; Wang et al., 2014). However, the secretion even wets a highly hydrophobic human-made substrate such as *Teflon AF*, which most likely is more hydrophobic than plant surfaces, with a dispersive and polar surface energy of 18 and 0.5 mN/m respectively (Dirks, 2009).

1.4.2 The Effect of Temperature on Contact Angles and Surface Tension

The secretion's surface tension and contact angles on all surfaces did not change significantly with temperature over the 20-50°C range. This result is particularly relevant to the ecology of insects, as many species navigate environments which undergo drastic temperature changes over a day/night cycle (Colinet et al., 2015). Hence, a sound adhesive system should be versatile and adaptable to surfaces of different roughness and energies, at different temperatures. In fact, if insects indeed relied on capillary forces to cling to surfaces, a weak temperature dependence of the surface tension is favourable as insects would benefit from the same adhesive performance, no matter what temperatures they face. Nonetheless, by the very nature of surface tension, weak (linear) temperature dependence is always expected, and typically governed by the *Eötvös* law (Eötvös, 1886; Palit, 1956):

$$\gamma_{\mathrm{L}}(T) = k_{\mathrm{E}} V^{-2/3} \left(T - T_{\mathrm{c}}\right), \tag{1.12}$$

where V is the molar volume, k_{E} is an empirical proportionality constant, and T_{c} is the critical temperature of the liquid. From this law, and assuming the surface tension of the secretion is 30 mN/m at 20°C, the critical temperature is comparable to that of octacosane ($T_{\mathrm{c}} = 836$ K, alkanes with a number of carbon atoms between 20 and 40 have critical temperatures in the 769-904 K range. Nikitin and Popov, 2014), and that

the molar volume does not vary with temperature (Koller et al., 2017), one can write a predictive equation for the surface tension of the secretion at different temperatures as:

$$\gamma_{\mathrm{L}}(T) = \frac{30\,\mathrm{mN/m}}{542.85\,\mathrm{K}}\,(T - 836\,\mathrm{K})\,. \tag{1.13}$$

At the maximum temperature investigated in this study (50°C), the surface tension would decrease to $\gamma_{\mathrm{L}}(323{,}15\,\mathrm{K}) = 28.34\,\mathrm{mN/m}$, a reduction by a factor four times lower than the standard deviation obtained in this work. In fact, over the 20 to 50°C temperature range a $\sim 2\,\mathrm{mN/m}$ change in surface tension is typical for fatty acids (Sahasrabudhe et al., 2017) and long-chained hydrocarbons such as octacosane (Koller et al., 2017; Yang et al., 2021). This change in surface tension does not drastically influence the wetting properties of the secretion over the investigated temperature change, as the wetting limit – computed for different values of $\gamma_{\mathrm{L}}^{\mathrm{p}}(T)$ and $\gamma_{\mathrm{L}}^{\mathrm{d}}(T)$, assuming they both follow a linear decrease dictated by Equation (1.13) – is almost invariant with temperature (See Figure 1.8B). Although a temperature dependence is expected and most likely present for the secretion, it is hidden by the natural variation and measurement accuracy of these data.

Accordingly, contact angles of long-chained hydrocarbons typically decrease with increasing temperature (Diaz et al., 2017). However – for unbranched alkanes – the higher the number of carbon atoms, the less this trend is pronounced. For instance, previous work measured the contact angle of C_{8-16} *n*-alkanes on polytetrafluoroethylene (PTFE) ($\gamma_{\mathrm{S}}^{\mathrm{d}} = 8.8$ and $\gamma_{\mathrm{S}}^{\mathrm{p}} = 0.4\,\mathrm{mN/m}$ Dirks, 2009). For octane, the contact angle decreased from 26.5 to 23.4°, while for hexadecane, it remained unchanged at 41.8° over the $25 - 50$°C temperature range (Diaz et al., 2017). Our results indeed indicated that, depending on the surface, temperature has a significant effect through their interaction. In particular, on TMCS, the contact angle decreases from 35.2° at 20°C to 28.9° at 50°C. The magnitude of this change is comparable to octane, but on all other surfaces investigated in this work (See Figure 1.7), the contact angle does not change significantly and is thus comparable to the behaviour of hexadecane. It is hence likely that the errors associated with the contact angle measurements and the *OWRK* method prevent from resolving the expected contact angle and surface tension changes induced by temperature. Nonetheless, from literature values and the calculations presented above, I expect those variations to be low, and insignificant in the context of capillary bridges and insect adhesion.

1.4.3 Spherical Cap Fitting

The spherical cap fitting provided contact angle estimations that were slightly higher when compared to angles found in previous studies on surfaces of similar energies (Dirks, 2009; Federle et al., 2002; Hasenfuss, 1999; Labonte, 2010). For instance, *Dirks* reported contact angles between 1.7 and 25° on surfaces ranging from polysterene ($\gamma_S^d = 55.6$ and $\gamma_S^p = 0.4\,\mathrm{mN/m}$) to Teflon ($\gamma_S^d = 8.8$ and $\gamma_S^p = 0.4\,\mathrm{mN/m}$) (Dirks, 2009). However, the surface tension determined in this study is in good agreement with literature values, with a slightly lower error, even though a definitive "ground truth" value is difficult to assess (See Table 1). More strikingly and despite the good agreement of the data from different studies, it is clear from a theoretical perspective that the spherical cap method allows for a substantial error reduction, dependent on droplet geometry. In fact, the error associated with interpreting the contact angle of a drop by fitting a line through the first few fringes increases with a decreasing number of fringes, typically observed for small droplets of any contact angle (See Appendix A, for details on the theoretical error committed for line and cap fits).

There is perhaps one disadvantage of the spherical cap fitting method, related to the occurrence of outliers, which can introduce quite noticeable noise to the imaged droplets (See Figure 1.5, for TMCS). Such falsely detected fringes are however not present on all radial sections of a droplet, which gives an advantage to a line fitting method, for which radii can be carefully selected in order to avoid anomalies. I anticipated this issue, and confirmed that different occurrence probabilities of outliers detected at the centre and edge of a droplet do not drastically affect the evaluation of the contact angle (See Appendix A). In fact, contrary to a line fitting procedure which utilises a few points (Typical line fitting methods consider 2 to 5 points at the droplet's edge Dirks, 2009; Federle et al., 2002; Labonte, 2010), the spherical cap fitting method developed here uses $n = 300$ times the number of extrema detected on each radius, often resulting in thousands of 3D data points. Fitting a whole sphere* to the X, Y, and Z coordinates of the detected fringes on all radii is thus advantageous over fitting n circles to individual radii, because the error associated with multiple fitting procedures is absorbed into one linear model, which is less sensitive to noise than the average of many. The fitting procedure is hence considerably more robust to noise, and suitable to interpret droplets of variable radius, circularity, and contact angle, within the IRM limitations discussed above.

*Fitting a whole sphere or a spherical cap is mathematically equivalent.

Those IRM limitations however do exist, and are worthy of consideration. The non-planar interfaces correction method implemented here, based on wedge corrections determined by *Wiegand et al.*, considers discretised droplets, and is hence an approximation of the true relationship between "real" and "measured" intensity profiles of spherical caps (Wiegand et al., 1997, 1998). *Contreras-Naranjo et al.* suggested this form of IRM theory is ill-suited to convex interfaces, because it neglects interference between *p*- and *s*-polarised light, which has been demonstrated to become significant at high INA (Contreras-naranjo et al., 2010; Theodoly et al., 2010). The authors hence presented an alternative theory which includes such interference, and the effect of multiple incident light rays originating from convex interfaces (Contreras-naranjo et al., 2010). Despite my best efforts, and particularly simulations produced by our collaborator *Dr. Martin Sprenger*[‡], simulated light intensity profiles for spherical caps using both theories developed by *Wiegand et al.* and *Contreras-Naranjo et al.* did not provide a satisfactory match when compared to droplet intensity profiles extracted experimentally with IRM. Given the scope of this thesis and the good agreement between the physical properties of the secretion determined in this study and literature values, I thought it best to limit our analysis to the hereby presented discretised wedge correction. The difficulties we encountered however evidenced a clear gap in IRM theory literature, in the particular context of convex spherical caps. My hopes are for future developments, beyond the scope of this work, to shed *light* on this particular issue.

1.4.4 The Effect of Temperature on Viscosity

As previously done by *Federle et al.* (Federle et al., 2004, 2002), we suggested that dewetting measurements are an excellent candidate for investigating the viscosity of the liquid. Having determined the surface tension of the secretion at different temperatures we could examine the temperature dependence of the viscosity coefficient. Our results indicate that the secretion is 20 to 400 times more viscous than water, in good agreement with previous literature values obtained using microrheology (Previous authors found viscosity values at room temperature in the 10-100 mPa· s range, see Table 1 Abou et al., 2010; Attipoe, 2018; Baumgart et al., 2022; Peisker et al., 2014). Given the rapid and *quasi-in vivo* nature of our measurements, the viscosity values presented here are presumably close to the real rheological behaviour of the secretion

[‡]Previously: Eidgenössische Technische Hochschule Zürich, Zürich, CH.

during attachment and detachment. Indeed, the good agreement with microrheology techniques which requires hours of droplet collection (Abou et al., 2010; Peisker et al., 2014) indicates that viscosity might not substantially change over prolonged intervals of time.

The dewetting velocity increases with temperature (See Figure 1.9A), and since the contact angle and surface tension are invariant with temperature, the change in dynamics must be a consequence of a change in the secretion's viscosity (Equation (1.10)). The secretion's viscosity in fact follows typical exponential models, providing an estimate for the viscosity coefficient at any temperature. The uncovered exponential trend is in good agreement with a previous study, where I used microrheology to find a similar decay in the secretion's viscosity ($\eta(T_\mathrm{K}) = 9.3 \times 10^{-7}$ exp$(43.3/RT_\mathrm{K})$ Attipoe, 2018). The fitted constant b in the exponential in Equation (1.11) is typically interpreted as an activation energy E_a, and is representative of a state transition occurring in the liquid (Haj-kacem et al., 2014; Messaâdi et al., 2015). The exponential coefficients found in this study resemble those of glycerol ($E_\mathrm{a} = 59.61\,\mathrm{kJ/mol}$) and propylene glycol ($E_\mathrm{a} = 47.7\,\mathrm{kJ/mol}$), but this resemblance is tied to the energy dynamics within a compound, rather than to its chemical composition (Haj-kacem et al., 2014; Messaâdi et al., 2015). Long-chained hydrocarbons also display an exponential decrease in their viscosity with increasing temperatures, although the magnitude of the viscosity coefficient is typically lower than our measurements for the pad secretion (The visosity for hexadecane decays from 3.5 to 1.5 mPas over the 20-50° temperature range. Klein et al., 2019).

Since dewetting measurements do not suffer from the same limitation of high angles on low energy surfaces such as OTS, the contact angles on any surface could be extrapolated from the combined knowledge of the surface tension and viscosity of the liquid. We found for OTS a contact angle value close to the 40° limit imposed by IRM, for which fringes begin overlapping and extrema are no longer representative of the droplet's topography. We suggest dewetting experiments, complemented with the hereby determined wetting properties of the secretion, are hence capable of measuring contact angles on any surface, provided that a metastable film forms and breaks down on the substrate. Another important benefit emerging from dewetting theory is that it is only applicable for *Newtonian* liquids (Redon et al., 1991; Reiter, 1993). We found that the dewetting speed followed the trend predicted by empirical dewetting laws. This, combined with previous microrheology results (Abou et al., 2010; Baumgart

et al., 2022; Peisker et al., 2014), suggest that the liquid might not deviate from typical viscous (*Newtonian*) behaviour (Kaimaki et al., 2022; Reiter, 1993).

1.4.5 Do Insects Rely on "Wet" Adhesion?

Two clear trends emerged from our results: *i.* Contact angles and surface tension are weakly affected by temperature. *ii.* Viscosity decreases exponentially with increasing temperature. Those two behaviours with temperature offer insight into supposed capillary and viscous force contributions to insect adhesion, as stipulated by wet adhesion models (Federle et al., 2004, 2002; Gorb, 2001; Stork, 1983). The former is a result of intermolecular energy imbalances, and is hence a static force, while the latter requires relative motion between molecules in the fluid, and is thus a dynamic force. Insects could make use of both contributions since they are able to stand still or locomote on both horizontal and vertical surfaces, producing adhesive or frictional forces. By observing the effect of rate and temperature on insects's adhesive capabilities, it is possible to infer which of these two modes of attraction (if any at all) is most likely to explain the changes in adhesive forces produced by insect pads *in vivo*. The capillary bridge created by the secretion can only give rise to static forces through its adhesive component, which in the case of a wet contact with a sphere is modelled as (Federle et al., 2002; Fogden and White, 1990):

$$F_\gamma = 3\pi R_{\mathrm{pad}} \gamma_{\mathrm{L}} \cos\theta, \tag{1.14}$$

where R_{pad} is the radius of the pad in contact. The dynamic adhesive force resulting from the viscosity of the secretion only acts if the rate of separation between the pad and the substrate is non-zero, and is written for a spherical pad as the *Stefan* adhesive force (Barnes et al., 2006; Stefan, 1875):

$$F_\eta = F_{Stefan} = \frac{3\pi}{2h^3} R_{\mathrm{pad}}^4 \eta v_{\mathrm{r}}, \tag{1.15}$$

where h is the film's thickness, and v_{r} the separation velocity of the plates. (Federle et al., 2004). It is however important to note that *Stefan* forces assume parallel undeformable plates, and a continuous mediating liquid film, which is arguably not representative of the adhesive pad of insects (Bennemann et al., 2011; Dirks, 2009; Gorb et al., 2000; Jiao et al., 2000; Perez Goodwyn et al., 2006; Scholz et al., 2008). Another key assumption of this force model is centripetal flow, a likely violated assumption

for many biological adhesive interfaces (Dirks, 2009; Smith, 2002). Despite the low contact angles and high viscosity of the secretion, the two force models presented here fail to account for the adhesive forces measured for insects's pads, as previous literature has already demonstrated with similar estimates of the wetting and viscous properties of the secretion (Dirks, 2014; Federle et al., 2004, 2002). Our work on the other hand, not only demonstrated the viscous nature of the secretion, casting doubt over the hypothesised *Bingham* nature and frictional resistance, it also introduces a new variable: temperature. In fact, Equation (1.14) supposes, given our results, a capillary force that is both independent of rate and weakly affected by temperature. On the other hand, Equation (1.15) does depend on rate, but also on temperature through the determined exponential decay in viscosity. The rate dependence of insects's adhesive forces has been established in the literature (Federle et al., 2004; Labonte and Federle, 2015a), but previous work by *Federle et al.* indicated that adhesive pull-off forces did not vary with temperature, in the absence of shear forces (Federle et al., 2004). This "wet" model hence does not yet provide a satisfactory answer to the mystery of insect adhesion. In particular, the rate dependence and the energy dissipation resulting from the secretion's viscosity, must be compared to the energy losses induces by the viscoelastic footpad (Gorb et al., 2000), and to *in vivo* adhesive forces before any further conclusions can be drawn.

Chapter 2

The Viscoelastic Properties of Smooth Adhesive Pads of Indian Stick Insects

2.1 Introduction

Many insects rely on the ability to cling to plant surfaces, which can vary widely in their stiffness, roughness, and wetness (Burack et al., 2022; Büscher et al., 2020; Endlein and Federle, 2015; Labonte et al., 2014; Zhou et al., 2014). Insects achieve this feat by using specialised adhesive pads located on their feet, which they can attach and detach within fractions of a second, and at varying temperature and humidity (Barnes et al., 2011; Betz, 2010; Bullock et al., 2008; Dirks and Federle, 2011a; Federle et al., 2004; Federle and Labonte, 2019; Federle et al., 2002; Gillett and Wigglesworth, 1932; Gorb et al., 2000; Gorb, 1998; Koerner et al., 2012; Labonte and Federle, 2013, 2016; Niederegger and Gorb, 2003; Stark et al., 2018; Stark and Yanoviak, 2018; Walker, 1993; Wigglesworth, 1987; Zhou et al., 2014). In fact, the need for a versatile, strong, and controllable adhesive system is paramount for insects in order to escape predators, and to live and feed on plants. A combination of these desirable properties is as uncommon as it is sought after (Byern and Grunwald, 2010; Gorb et al., 2007), particularly in commercial applications where many adhesives are either strong but permanent, or reversible but weak. In all insects studied to date, the adhesive pads are covered by a thin layer of an oily secretion (Dirks and Federle, 2011a; Gillett and Wigglesworth, 1932; Gorb, 1998; Walker, 1993). Accordingly, a large body of literature has sought to quantify the contribution of this mediating liquid to the adhesive performance of insect feet (Betz, 2010; Blackwall, 1833; Dirks, 2014; Dirks and Federle, 2011a; Eisner and Aneshansley, 2000; Federle et al., 2004, 2002; Gillett and Wigglesworth, 1932; Gorb et al., 2000; Gorb, 1998; Peisker et al., 2014; Walker, 1993; West, 1862; Wigglesworth, 1987). A quantitative assessment of the role of liquid requires knowledge of its physical properties, and previous work has thus quantified the surface tension and viscosity of the secretion (Abou et al., 2010; Betz, 2010; Dirks, 2014; Dirks and Federle, 2011a; Eisner and Aneshansley, 2000; Federle et al., 2004, 2002; Gorb et al., 2000; Gorb, 1998; Kaimaki et al., 2022; Peisker et al., 2014). However, despite the agreement on the liquid's properties between different authors and techniques, evidence remains inconclusive as to whether a "wet" adhesive model, invoking capillary and viscous forces, explains the attachment performance of insect pads (Dirks et al., 2010; Drechsler and Federle, 2006; Hosoda et al., 2021; Labonte and Federle, 2015a). For instance, the adhesive performance of some insects has been observed to decrease with increasing temperature (Federle et al., 2002; Roth and Willis, 1952; Stark et al., 2018; Votsch et al., 2002). This trend was however not exponential, as one would expect if the

forces stemmed dominantly from the viscosity of a *Newtonian* liquid (Haj-kacem et al., 2014). Although single-pad adhesive forces have a magnitude comparable to predicted capillary forces at low detachment speeds(Barnes, 2007; Dirks, 2014; Federle et al., 2002; Labonte and Federle, 2015a), shear forces strongly modulate adhesion, much above the level expected for capillary adhesion (Labonte and Federle, 2015a). Surface tension based models do not provide an explanation for the observed rate dependence of the adhesive forces either (Federle et al., 2004, 2002; Labonte and Federle, 2015a; Langer et al., 2004). Recent work has suggested that capillary and viscous models also fail to account for the scaling of single pad force measurements with insect body size: the secretion's physical properties are invariant with size across instars of Indian stick insects, but the apparent adhesive strength of the pads increases with size in the presence of shear forces (Kaimaki et al., 2022; Labonte et al., 2019). Accordingly, some have argued that the secretion's consistency might be closer to that of a grease, due to the possible melting point depression in the long-chained hydrocarbon mixture (Gerhardt et al., 2016; Speidel et al., 2017). This observation calls into question the very assumption of a *Newtonian* liquid bridge (Dirks et al., 2010; Drechsler and Federle, 2006; Federle et al., 2004, 2002). Upon closer consideration, it may indeed appear that the presence of a liquid bridge and its associated capillary and viscous forces may be detrimental for some of the key functional requirements of controllable adhesives, for at least two reasons. Firstly, continuous liquid films typically act as lubricants and should thus cause insects to slide (Dirks, 2014). However, peak shear forces of animal attachment pads typically exceed adhesive forces by orders of magnitude (Dirks et al., 2010; Labonte and Federle, 2015a; Labonte et al., 2019). Previous work has attempted to resolve this conundrum by arguing that the secretion may be a non-*Newtonian Bingham* fluid (Betz, 2010; Dirks et al., 2010; Drechsler and Federle, 2006; Federle et al., 2004, 2002; Koerner et al., 2012; Speidel et al., 2017), but no direct evidence for a shear-rate dependency of the pad secretion viscosity has been found (Abou et al., 2010; Kaimaki et al., 2022; Peisker et al., 2014). Secondly, it remains unclear how a capillary and viscous adhesive can be switched "on" and "off" on short time scales, an essential requirement for small animals which are often preyed upon, and thus need to escape threats rapidly. Insects live in challenging environments, in which the temperature may vary significantly over a day/night cycle (Colinet et al., 2015), suggesting that reliance on a strongly temperature-dependent adhesive mechanism may be a key limitation to the ability to escape rapidly.

In light of these difficulties, others have recently argued for "dry" adhesion models, which consider contributions from viscous fluid flow and capillary forces negligible, and attribute attachment performance to solid-surface interactions instead. The presence of a liquid film could be reconciled with dry adhesion models: For example, solid-solid interactions could play a significant role if the liquid film is so thin (Dirks, 2009; Dirks et al., 2010; Dixon et al., 1990; Federle et al., 2002; Geiselhardt et al., 2009; Lees and Hardie, 1988; Stork, 1983; Walker et al., 1985), that it is clamped by its viscosity (Labonte and Federle, 2015a). In a “dry” adhesion framework, rate dependence arises from deformation of the soft footpad, and the viscoelasticity of the footpad thus replaces the viscosity of the pad secretion as the origin of the dissipative process that induces rate dependence (Labonte and Federle, 2015a). In fact, viscoelastic materials are both time and temperature dependent (Lakes, 2009), and could thus potentially explain both the rate and temperature dependence of adhesive forces produced by insects (Federle et al., 2002; Labonte and Federle, 2015a; Stark et al., 2018).

Most studies investigating the material properties of insects's pads have used purely elastic constitutive models, and so report a single-valued elastic modulus for the pad cuticle. For example, *Goodwyn et al.* determined the elastic properties of bush crickets with nanoindentation, and found an effective elastic modulus E_{eff} of 50 kPa (Perez Goodwyn et al., 2006), in good agreement with similar work by *Jiao et al.* (Jiao et al., 2000), and well below the *Dahlquist* criterion, which predicts that a material is tacky when its elastic modulus is below 100kPa (Dahlquist, 1966). *Scholz et al.* investigated the elastic modulus of Indian stick insects's pads using atomic force microscopy, and found that the stiffness varied depending on the indentation depth (Scholz et al., 2008). The outer layer ($100 - 300$ nm) had an effective elastic modulus of 12 kPa, while the inner layer ($300 - 50000$ nm) had a higher stiffness of up to 625 kPa. This variation in modulus from the outer to the inner layers may improve the performance on surfaces with multiple roughness length scales, combining the softness required to deform around asperities with the stiffness required to generate strong adhesion (Scholz et al., 2008). However, other studies have suggested that the outermost membrane is much stiffer when deformed in tension, with an elastic modulus of about 100 MPa (Bennemann et al., 2011). With the exception of this last study, most of the measured elastic moduli fall within a close range, and it hence might be crucial for insects to maintain a relative softness to their pads in order to produce strong and controllable adhesive forces. In particular, in the absence of any biological adaptations (such as a protective secretion), small animals with a large surface area to volume ratio are prone to dehydration, which

can reduce the compliance of the pad cuticle (Klocke and Schmitz, 2011; Labonte et al., 2017; Vincent and Wegst, 2004).

Only a small number of studies have reported the viscoelastic properties of animal attachment pads. *Gorb et al.* modelled bush crickets pad as a *Kelvin* viscoelastic solid with two time constants (Gorb et al., 2000). Furthermore, detailed work on geckos has demonstrated a key role of viscoelastic deformation, even though the modulus of gecko *setae* is orders of magnitude higher (Prowse et al., 2011; Puthoff et al., 2010). In particular, viscous dissipation in gecko *setae* explains the sensitivity of gecko adhesion to humidity (Prowse et al., 2011; Puthoff et al., 2010), an observation that was, in remarkable similarity to insect adhesion, originally thought to hint at a contribution of capillary forces (Huber et al., 2005). Other parameters than hydration might influence the material properties of the pads, and given the previously discussed rate dependence of the adhesive forces, "dry" models must consider the effect of rate and temperature on the pad's mechanical properties. In an effort to provide the quantitative information required to evaluate such "dry" adhesion models, I here quantify the viscoelastic properties of the adhesive pads of Indian stick insects through creep experiments across a range of biologically relevant temperatures.

2.2 Methods

2.2.1 Study Animals and Sample Preparation

A colony of Indian stick insects (*Carausius morosus, Sinéty* 1901) was kept in a climate chamber at 25°C, 60% relative humidity, 12/12 hours light cycle (FitoClima 12.000 PH, Aralab, Portugal), and fed water and bramble *ad libitum*. All experiments were conducted with adults, identified via the scarlet colouration on the femur of their front legs (Body mass 673.0 ± 241.3 mg, mean ± standard deviation, $n = 13$) (MacBride and Jackson, 1915). In order to avoid interference of haemolymph pressure variation on indentation measurements, I conducted experiments on pads of isolated legs. To this end, I clamped front legs at the femur (Tubing clamp, Hoffmann Type, Eisco, USA), triggering autotomy at the *coxa-trochanter* joint (Maginnis, 2008). In addition to facilitating the leg's precise severance, the clamp maintained the pad's integrity by keeping it inflated. Legs were sealed immediately at the site of detachment to avoid fluid leakage and pad deflation, using UV glue (AA 3525, Loctite, USA). The clamped leg was inserted into a glass *Petri* dish (5 cm diameter), and the adhesive footpad on the *pre-tarsus* (the *arolium*) was attached to the glass using dental impression silicone (Elite HD+, Zhermack, Germany), such that the adhesive contact area was exposed (See Figure 2.1A). In order to avoid dehydration over the time course of the indentation experiments, the *Petri* dish was filled with Phosphate Buffered Saline (PBS, 1X) at pH 7.4 until the leg was fully immersed (MilliporeSigma, USA). The entire process from clamping to full immersion took no longer than 15 minutes.

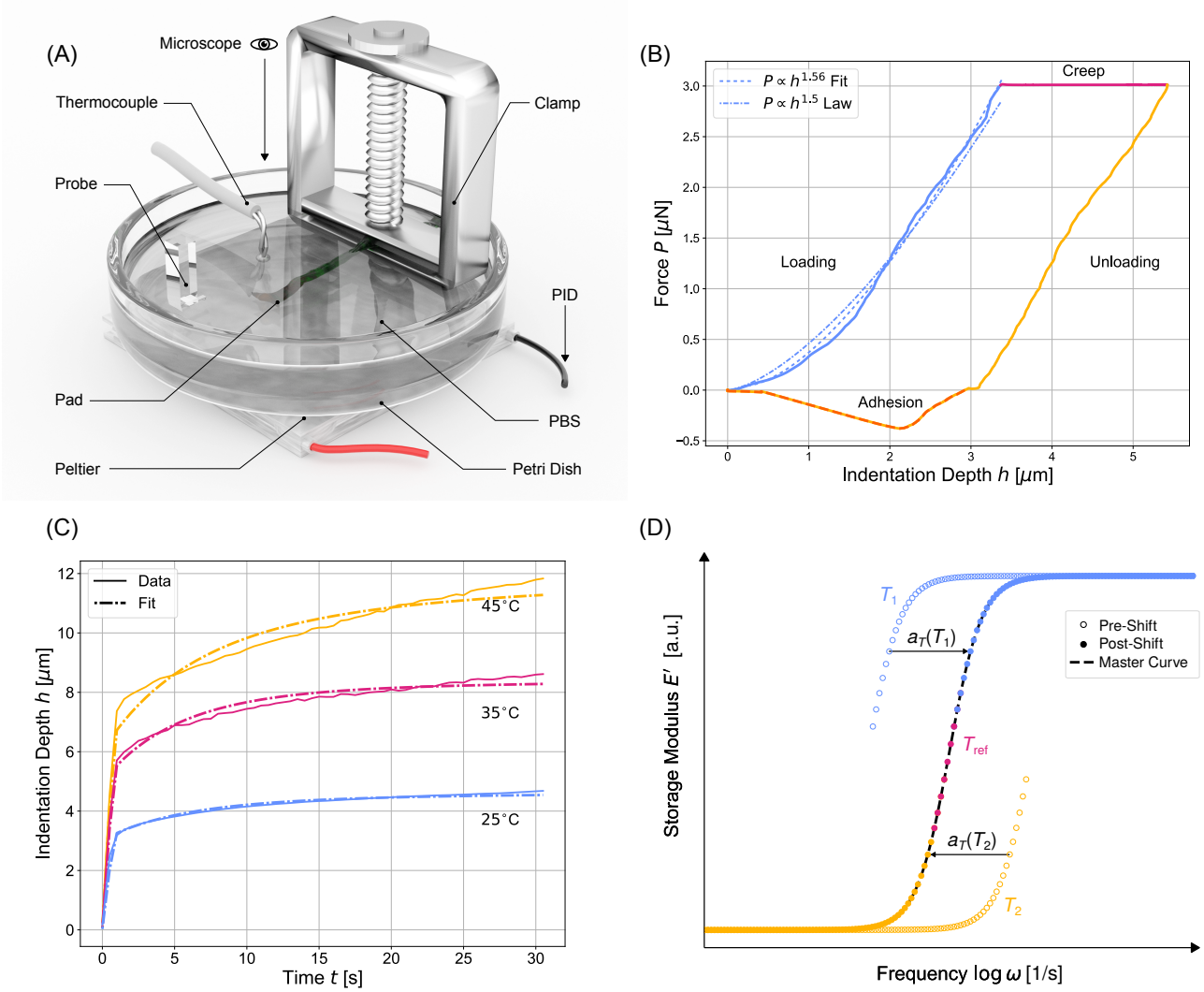


Figure 2.1 (A) Schematic representation of the setup for indentation experiments at controlled temperatures. An isolated insect leg was clamped and fixed to the bottom of a glass *Petri* dish filled with Phosphate Buffered Saline (PBS). The temperature of the PBS was measured with a thermocouple and varied with a *Peltier* element via a Proportional–Integral–Derivative (PID) control run on a microcontroller. The nano-indenter probe was positioned over the pad with the help of a digital microscope. Figure not to scale, 3D scan of the insect's leg by *Fabian Plum*, using *scAnt* (Plum and Labonte, 2021). (B) Example of a Force-Displacement curve resulting from pad indentation, characterised by three segments: Loading (blue), creep (pink), unloading (yellow). The adhesion part of the unloading curve, characterised by a negative tensile load, is shown in dashed orange. The dashed and dotted lines show the fit of a simple power law compared to the prediction from *Hertz*'s contact theory. The mechanical behaviour of the pad cuticle is in reasonable agreement with *Hertz*'s theory, so that adhesion can be neglected. (C) Characteristic Displacement-Time data (solid) and theoretical fit (dashed) at the three investigated temperatures: 25°C (blue), 35°C (pink), and 45°C (yellow). (D) Schematic representation of Time-Temperature-Superposition (TTS) for the storage modulus $E'(\omega)$. A reference temperature T_{ref} is chosen, and data collected at higher (resp. lower) temperatures are shifted left (resp. right), according to the temperature-dependent shift factor $a_T(T)$. Here, $T_1 < T_{\text{ref}} < T_2$.

2.2.2 Temperature Control

In order to characterise the temperature dependence of the viscoelastic pad properties, a *Peltier* heat pump (TEC1-12706, Diymore, Hong Kong) was connected to the bottom of the glass *Petri* dish with thermal grease (Kryonaut, Thermal Grizzly, Germany. See Figure 2.1A). The temperature of the PBS solution was monitored with a thermocouple placed close to the pad (K-type TP870, Extech, USA), and closed-loop temperature control was achieved via a custom-built proportional–integral–derivative (PID) controller, implemented on a microcontroller. The setup was powered by a 9V DC power supply (2230, Keithley Instruments, USA) through a MOSFET transistor (N-Type, 1N914, Infineon Technologies, Germany). The setup is conceptually similar to the one described in Chapter 1).

2.2.3 Indentation Experiments

The theory of nanoindentation has advanced significantly in the recent years, particularly in the study of time dependent and biological materials (Cohen and Kalfon-Cohen, 2013; Oyen, 2005). A nanoindentation experiment consists in driving a tip of known dimensions and shape inside a material, either controlling the amount of force applied, or the depth to which the tip indents the material (Cohen and Kalfon-Cohen, 2013; Oyen, 2005, 2006). The relationship between force and displacement may be interpreted as stress-strain curves, through which the material properties can be extracted. In order to choose suitable experimental parameters for instrumented indentation, prior knowledge of the approximate mechanical properties and structure of the sample is required. The Indian stick insect pad is bean-shaped, with a contact area in the plane of indentation similar to an ellipse with a minor and major axis of about $300\,\mu$m and $700\,\mu$m, respectively (Bennemann et al., 2014, 2011; Labonte and Federle, 2013; Scholz et al., 2008). The two outermost layers of the pad itself, the *epicuticle* and *procuticle* are approximately 200 nm and $50\,\mu$m thick, respectively (Bennemann et al., 2014, 2011; Scholz et al., 2008). The first is akin to a solid membrane, the latter to a fibrous structure (Bennemann et al., 2014). Hence, one can expect that indentations with a depth of 1 to $10\,\mu$m measure dominantly the "effective" mechanical properties of the procuticle (Scholz et al., 2008). Creep experiments were performed with a commercial indenter (Chiaro, Optics11 Life, Netherlands), using probes with spherical tips made from glass (radius $R = 50 \pm 5\,\mu$m), connected to a cantilever with a stiffness of 0.2 ± 0.01 N/m, as specified by the manufacturer. The probe radius was chosen to be

large enough to ensure small indentation strains, while providing sufficient sensitivity at small indentation depths relative to the probe radius. I estimated the indentation depth using Hertz-theory and an approximate modulus of $\sim 100\,k$Pa (Scholz et al., 2008). The arolia are curved, with a radius of curvature of about $500\,\mu$m (Labonte and Federle, 2015a). The "effective" radius is thus $R_{\text{eff}} = (1/500 + 1/50)^{-1} \approx 45\mu$m, or within 10% of the probe radius; I hence make the first order approximation to treat the pad as planar. The probes were calibrated at each experimental temperature following manufacturer guidelines. Each *arolium* was indented at three locations, at least $25\,\mu$m apart, on central parts of the adhesive pad contact area. Probe positioning was aided by a digital microscope (Edge, Dino-Lite, Netherlands). In order to allow for material recovery between indentations, the time between two consecutive measurements was at least one minute, a period of time larger than the duration of an insect's stride (Gernay et al., 2017; Tóth and Daun, 2019). In addition, the spacing between indents was chosen such that it exceeds the Hertzian indentation radius, $a = \sqrt{hR} = 17\,\mu$m, based on a mean probe radius of $50\,\mu$m and a mean indentation depth of $6\,\mu$m (Hertz and Lenard, 1896). Preliminary experiments indicated that a trapezoidal loading profile with a peak load of $3\,\mu$N provided consistent results, and resulted in indentation depths close to $6\,\mu$m as determined above. In all tests, displacements remained below 30% of the probe diameter, resulting in small representative *Tabor* indentation strains $\epsilon = 0.1\,h/R = 3\%$ for the maximum observed displacement of $h = 15\mu$m, so minimising the risk of permanent deformation or stress concentrations (Hutchings, 2009; Tabor, 1951). I used a trapezoidal loading profile with a ramp loading and unloading time of $t_{\text{r}} = 1\,$s, a peak load of $P_{\text{max}} = 3\,\mu$N, and a hold time of $t_{\text{h}} = 30\,$s, sufficient for the material to have undergone most of its time dependent deformation as determined in preliminary experiments. Force P and displacement d were recorded at 1kHz. In total N=3 indentations were conducted on pads of $n = 13$ insects, all at 25, 35, and 45°C. These temperatures were chosen because they are biologically relevant, and reach from room temperature to peak surface temperatures experienced by tropical insects, near 50°C (Stark et al., 2018). Because the *Peltier* element enabled active heating but not active cooling, I conducted all experiments in order of increasing temperature. I verified that the infinite- and zero-time moduli E_0 and E_∞ (See below for their definition), measured at 25° C did not differ significantly according to t-tests between moduli before and after the temperature treatment ($N = 3$ indentations on $n = 4$ insects. E_0: $t_{11} = -0.77$, $p = 0.46$. E_∞: $t_{11} = -0.16$, $p = 0.88$).

2.3 Data Analysis and Validation

2.3.1 Viscoelastic Functions for Creep

The load-displacement data was analysed with *Hertz* theory, modified with a *Boltzmann* viscoelastic integral to take into account the time dependence of the modulus (Johnson, 1985; Lee and Radok, 1960; Mattice et al., 2006; Oyen, 2005, 2006; Qian and Zhao, 2018; Sakai, 2002). The *Hertz* equation relates the load P and displacement h for a spherical probe of radius R, indenting an elastic half-space of *Poisson*'s ratio $\nu = 0.5$ (assuming incompressibility), with the effective, *Young*'s, or shear moduli E_{eff}, E, and G (Hertz and Lenard, 1896):

$$P = \frac{4}{3} R^{1/2} h^{3/2} E_{\text{eff}}, \tag{2.1}$$

or:

$$h^{3/2} = \frac{3}{4\sqrt{R}} P \frac{(1-\nu^2)}{E} = \frac{3}{8\sqrt{R}} \frac{P}{2G}. \tag{2.2}$$

In using *Hertzian* analysis, I consider adhesive forces to be negligible, which I achieve via the immersion of the pad in liquid; indeed, adhesive peaks during the retraction phase were miniscule (See Results), and the relation between force and displacement during loading followed the power-law predicted by *Hertz* theory (fitted in linear space with a power law exponent of 1.58 ± 0.84, mean ± std, $n = 117$, compared to the theoretical expectation of 1.5, see Equation (2.1)). To account for the time dependence of the elastic modulus, the time independent elastic operators in Equation (2.1) can be replaced with a *Boltzmann* hereditary integral, which also allows us to account for the time-history of deformation (Johnson, 1985; Lee and Radok, 1960; Mattice et al., 2006; Oyen, 2005, 2006; Qian and Zhao, 2018; Sakai, 2002):

$$h^{3/2}(t) = \frac{3}{8\sqrt{R}} \int_0^t J_{\text{s}}(t-u) \frac{\mathrm{d}P}{\mathrm{d}u} du. \tag{2.3}$$

Here, $J_{\text{s}}(t)$ is the shear creep function and u is a dummy integration variable for time. $J_{\text{s}}(t)$ is time and material dependent and has no accepted first-principle form. A common approximation is to write it as a weighted sum of decaying exponentials; a *Prony* series (Lakes, 2009; Mattice et al., 2006; Oyen, 2005, 2006; Qian and Zhao, 2018; Sakai, 2002):

$$J_{\text{s}}(t) = J_{\text{s},\,0} - \sum_{i=1}^{n} J_{\text{s},\,i} \exp(-t/\tau_i), \tag{2.4}$$

which mathematically resembles classic spring-dashpot models of viscoelasticity (Lakes, 2009). For creep, this expression involves $2n + 1$ constants $J_{\mathrm{s},0}$, $J_{\mathrm{s},i}$ and τ_i, which can be determined by numerical fitting of experimental data; I implemented such a fitting routine in *Python* (version 3.8.10 Van Rossum and Drake, 2009; Virtanen et al., 2020). The *Prony* series model was chosen over the previously used spring and dashpot model in order to better represent the complex nature of the material by characterising its creep function rather than parametrising stress or strain explicitly (Gorb et al., 2000). In fact, springs and dashpots used explicitly do not convey physical quantitative information regarding the pad's material (López-Guerra and Solares, 2014). On the other hand, *Prony* series reduce the risk of misinterpreting the material behaviour of the pad, and allow for a more adaptable viscoelastic curve fitting, capable of representing the time-history of the material, rather than its instantaneous response (Lakes, 2009; Oyen, 2005, 2006). Additionally, the model detailed here considers the material's entire deformation time frame under an integral (See Equation (2.3)), and thus also accounts for the initial material creep, caused by the instantaneous loading phase time t_r. Because a *Prony* series is versatile, appropriate initial guesses and bounds must be imposed on each fitted constant to constrain the fitting procedure to physical values (e. g. only positive elastic moduli). The initial guess for $J_{0,i}$ was determined by calculating an approximate value of G_0 from *Hertz*'s theory (2.2). Using the maximum observed displacement h_max, it follows that $J^{(\mathrm{g})}_{\mathrm{s},0} = 2\dfrac{8R^{1/2}h^{3/2}_\mathrm{max}}{3P}$, with bounds of $[0, 1]\mathrm{Pa}^{-1}$. For any additional $J_{\mathrm{s},i\neq 0}$, the initial guesses were a fraction of $J_{\mathrm{s},0}$: $J^{\mathrm{g}}_{\mathrm{s},i\neq 0} = \dfrac{J^{(\mathrm{g})}_{\mathrm{s},0}}{2 \times 10^{i-1}}$, with bounds of $\left[0, 0.95 \times J^{(\mathrm{g})}_{\mathrm{s},0}\right]\mathrm{Pa}^{-1}$. The number of terms in the *Prony* series, n, is usually related to the experimental time (Lakes, 2009; Oyen, 2005, 2006). I fitted two time constants, as a third exponential term provided time constants of the same order of magnitude as the second, with intervals $\tau_i \in 10\,[(i-1), i]\mathrm{s}$, with the exception of the last time constant which was left unbounded on its right-hand limit. In practice, this allows for capturing long-term creep beyond the timescale of the experiment; the behaviour at these long time scales (or low deformation frequencies) is likely of little biological relevance in light of the fast attachment and detachment cycles of insect pads during natural locomotion, which are typically in the sub-second range (Cruse and Bartling, 1995). In analogy to the charge and discharge of a resistor-capacitor circuit (Horowitz and Hill, 2015), the initial guesses for each time constant were estimated by examining the creep curve after loading ($t > t_\mathrm{r}$), and determining the time at which the additional creep displacement reached $1 - 1/e = 63.2\%$ of its

maximal value within each interval for τ_i. The fitted constants, $J_{\mathrm{s},\,i}$ and τ_i, determine the shear creep function for the material. The instantaneous and long-term response of the material can be examined by defining a zero- and infinite-time shear moduli $G_0 = \lim_{t\to 0} G(t) = \frac{1}{J_{\mathrm{s},\,0} - \sum J_{\mathrm{s},\,i}}$ and $G_\infty = \lim_{t\to\infty} G(t) = \frac{1}{J_{\mathrm{s},\,0}}$, respectively. The ratio of these two limiting moduli, $G_\infty/G_0 \leq 1$, is a suitable proxy for the extent of a material's viscoelasticity (Mattice et al., 2006; Oyen, 2006; Qian and Zhao, 2018); a perfectly elastic material has $G_\infty/G_0 = 1$. The equivalent quantities in terms of elastic moduli E_0 and E_∞ are obtained via the classic relation $E = 2(1+\nu)G$. Similarly, the bulk creep function is $J(t) = \frac{1}{2(1+\nu)} J_{\mathrm{s}}(t)$, and the *Prony* series for the bulk creep compliance can be written as: $J_i = \frac{J_{\mathrm{s},\,i}}{2(1+\nu)}$.

The theory developed above is valid under the assumption of linear viscoelasticity. In order to test if this assumption is a reasonable approximation, I directly compared predictions from the *Prony* series viscoelastic model, fitted to experimental data, to independent experimental data obtained with identical loading times but varying peak force (Oyen, 2006). Indentation experiments were conducted with load and hold times as described above, but for three different peak forces: 2, 3, and 4 μN. If the pad cuticle can be reasonably approximated as a linear viscoelastic solid, the mechanical response at different peak forces but constant displacement is described by one single creep compliance function, defined by the fitted constants J_i and τ_i. I assessed the quality of the predictions by comparing the Root Mean Square Error (RMSE) to the general RMSE obtained from fitting creep curves to repeats of the same experimental conditions (that is, the same peak load on the same individual). In other words, I compared the error associated with load-variation to the error in repeated measurements with the same conditions and the same individual. In general, the predicted force-displacement data are in robust agreement with the experimental data (See Figure 2.2A for an example). Indeed, the average RMSE of the predicted curves is $0.60 \pm 0.53\,\mu$m compared to an average RMSE for repeated measurements of $1.22 \pm 0.99\,\mu$m. On the basis of this result, I consider the assumption of linear viscoelastic behaviour reasonable for the scope of this study.

In order to verify whether the autotomy and clamping of the legs affected the estimated pad material properties, open-loop indentation experiments were conducted on a small sample size of three insect pads under three conditions: *i.* Live and unclamped; *ii.* Live and clamped; *iii.* Clamped and freshly autotomised. The open-loop protocol allowed rapid measurements of a single-valued effective elastic modulus, evaluated

by a Hertzian fit to the loading section of the force-displacement data. Closed-loop control, in contrast, would respond to temporal fluctuations in haemolymph pressure for unclamped pads, resulting in a systematic bias. The effective elastic modulus of the pad was independent of position, unaffected by sectioning and clamping, and their interaction (See Table 2.1).

Predictor	d.f.	Sum Sq.	Mean Sq.	F	p
Condition	2	5321	2261	0.971	0.4
Location	2	2037	1018	0.371	0.7
Condition * Location	4	8264	2066	0.754	0.6
Residuals	16	43856	2741		

Table 2.1 A two-way repeated measures ANOVA was performed to analyse the effect of sectioning, clamping, and indent location on the effective elastic modulus of the pad. All variables had no statistically significant effect.

In addition, the estimated elastic modulus was comparable to the range obtained from creep experiments (See Figure 2.2B). I conclude from the combination of both results that neither leg autotomy nor clamping have a significant effect on mechanical properties on the timescale of the conducted experiments.

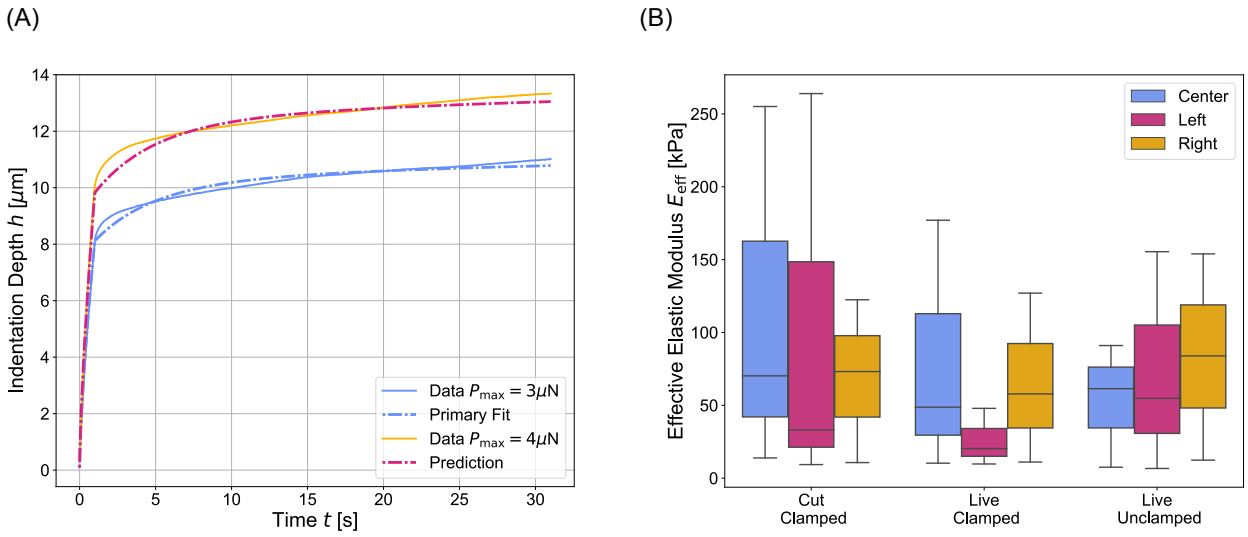


Figure 2.2 (A) The creep compliance function extracted via indentation (blue lines) can be used to predict the mechanical behaviour at a different peak load (pink lines) with reasonable accuracy, suggesting that the pad can be modelled as approximately linearly viscoelastic. (B) The effective elastic modulus of the insect cuticle, extracted via a simple Hertzian analysis of the loading curve, is independent of the leg clamping, leg autotomy, and location of the indent on the pad (n=3).

The nanoindentation procedure described above was validated by creep experiments on collagen samples, whose stiffness was comparable to the preliminary data presented here (See Appendix B).

2.3.2 Dynamic Modulus

The tackiness of polymers is strongly influenced by the thermodynamic losses occurring in the material when deformed at different frequencies (Hui et al., 2000; Müser and Persson, 2022; Persson, 2021). The viscoelastic behaviour of most solids can be characterised via a storage ($E'(\omega)$) and loss moduli ($E''(\omega)$), defined as the real and imaginary part of the dynamic modulus, respectively, $E^\star(\omega) = E'(\omega) + iE''(\omega)$, where i is the complex unity. The equivalent function for the creep modulus is $J^\star(\omega) = J'(\omega) - iJ''(\omega)$. In the frequency domain, the creep function and the dynamic modulus are simply the complex inverse of each other (Lakes, 2009):

$$E^\star = \frac{1}{J^\star}. \tag{2.5}$$

The frequency space definition can be recovered from the time domain creep function via *Fourier* transforms (Lakes, 2009). Introducing $J_\infty = \lim_{t\to\infty} J(t)$ and u, a dummy integration variable for time, yields (Lakes, 2009):

$$\begin{aligned} J'(\omega) &= J_\infty - \omega \int_0^\infty (J_\infty - J(u)) \sin \omega u \, du \text{ and} \\ J''(\omega) &= \omega \int_0^\infty (J_\infty - J(u)) \cos \omega u \, du. \end{aligned} \tag{2.6}$$

Via Equations (2.5) and (2.6) it follows that (Lakes, 2009):

$$\begin{aligned} E'(\omega) &= \frac{1}{|J^\star|^2} \left[J_\infty - \omega \int_0^\infty (J_\infty - J(u)) \sin \omega u \, du \right] \text{ and} \\ E''(\omega) &= \frac{1}{|J^\star|^2} \left[\omega \int_0^\infty (J_\infty - J(u)) \cos \omega u \, du \right]. \end{aligned} \tag{2.7}$$

where I used the definition of the dynamic modulus. Theoretically, these equations predict the storage and loss moduli at any frequency. However, these creep experiments only provide information about a finite range of deformation time scales; the average time constants at all temperatures $\tau_1 \approx 5\,\mathrm{s}$ and $\tau_2 \approx 65\,\mathrm{s}$ were thus chosen as upper and lower bounds for the frequency spectrum via: $\omega_1 = 2\pi/t_1$ and $\omega_2 = 2\pi/t_2$.

2.3.3 Time-Temperature Superposition

The time range over which experiments can be conducted via spherical indentation is bound. To overcome this limitation, I expanded the assessed frequency range by varying temperature instead. The dissipation of energy in viscoelastic materials depends not only on the deformation frequency, but also on temperature. For amorphous polymers, a change in temperature is equivalent to a shift in the deformation frequency: an increase in temperature corresponds to an increase in the deformation frequency of the material; the general shape of the viscoelastic functions, however, is preserved (See Figure 2.1D). Varying deformation frequency is thus equivalent to varying temperature, and this concept is referred to as Time-Temperature Superposition (TTS). The advantage of TTS is that it allows the exploration of the mechanical properties over a wide frequency range merely by varying temperature, and that it in principle enables prediction of the mechanical behaviour at arbitrary temperatures and deformation frequencies (Lakes, 2009). The storage and loss moduli determined at different ambient temperatures can be combined into a "master curve". To construct this master curve, a reference temperature is chosen, and results from other temperatures are shifted along the

frequency axis, until the curves overlap (See Figure 2.1D). To this end, the fitting coefficients J_i and τ_i were averaged for all repeats and individuals, in order to produce unique viscoelastic curves ($J(t)$, $E'(\omega)$, and $E''(\omega)$) for each temperature. The shift is typically performed by finding intervals over which either the storage modulus or its derivative have common values at different temperatures. I performed the shift directly on the moduli, through a nearest neighbour algorithm (Arzoumanidis and Liechti, 2003; Chan, 2001; Rajan et al., 2018). The multiplying factor a_T by which time or frequency need to be adjusted, is temperature-dependent and equally applicable to all viscoelastic functions. For instance, if the storage and loss moduli are known at a reference temperature T_{ref}, one can obtain their value at any experimental temperature T_{exp} through:

$$\begin{aligned} E'\left(T_{\text{exp}},\, \omega\right) &= E'\left(T_{\text{ref}},\, a_T\left(T_{\text{exp}}\right)\omega\right) \text{ and} \\ E''\left(T_{\text{exp}},\, \omega\right) &= E''\left(T_{\text{ref}},\, a_T\left(T_{\text{exp}}\right)\omega\right). \end{aligned} \tag{2.8}$$

The temperature dependence of the shift factor a_T is typically written as an empirical logarithmic law, first introduced by *Williams*, *Landel*, and *Ferry* (*WLF*) (Bae et al., 2011; Lakes, 2009; Rajan et al., 2018; Shangguan et al., 2017; Williams et al., 1955):

$$\log_{10} a_T = \frac{-C_1\left(T - T_{\text{ref}}\right)}{C_2 + T - T_{\text{ref}}}, \tag{2.9}$$

where C_1 and C_2 are experimental constants. Typical values for amorphous polymers are $C_1 = 17.44$ and $C_2 = 51.6K$ when T_{ref} is the glass transition temperature of the material (Shangguan et al., 2017). Once data obtained at different temperatures have been appropriately shifted, some overlap might still exist. In order to reconstruct a master curve with unique values, I fitted a *Prony* series model for the storage and loss moduli to the shifted data (Arzoumanidis and Liechti, 2003; Bae et al., 2011; Costa and Ribeiro, 2011):

$$\begin{aligned} E'\left(\omega\right) &= D_0 + \sum_{k=1}^{n} D_k \frac{\left(\omega\tau_k^{(\text{m})}\right)^2}{1 + \left(\omega\tau_k^{(\text{m})}\right)^2}, \text{ and:} \\ E''\left(\omega\right) &= \sum_{k=1}^{n} D_k \frac{\omega\tau_k^{(\text{m})}}{1 + \left(\omega\tau_k^{(\text{m})}\right)^2}. \end{aligned} \tag{2.10}$$

Since two time constants τ_i were previously used for each of the three temperatures utilised here, I chose $k = 1, \ldots 6$ "master" time coefficients as $\tau_k^{(\text{m})} = \tau_i / a_T(T_j)$, and fitted the D_k coefficient to the shifted storage modulus. The resulting master curve

provides a full representation of the dynamic modulus; shifting the storage and loss moduli along the frequency axis provides the mechanical response at any temperature or frequency, provided the material remains linearly viscoelastic. It must be noted that TTS's applicability is typically limited to amorphous polymers, and its pertinence is not guaranteed for biological and aqueous systems (Krajina et al., 2017; Tassieri et al., 2016). Since the object of this study is to determine the extent of values the dynamic modulus reaches at different temperatures and frequencies, I apply TTS with caution, and with no expectation of direct similarities with amorphous polymer blends.

2.3.4 Statistical Methods

All numbers are represented as mean ± standard deviation (std) unless otherwise indicated. Effects of temperature, indentation position, and clamping/sectioning condition, were analysed via one- or two-way repeated measure analysis of variance (ANOVA) in *R* (version 3.6.3 R Core Team, 2020). The influence of temperature on E_0 and E_∞ was assessed with a paired t-test. The goodness of fit for viscoelastic functions was determined by calculating the Root Mean Squared Error (RMSE), because alternative metrics such as R^2 cannot be used for non-linear relations. The disadvantage of using the RMSE is that it provides an absolute error metric. In order to judge the quality of fit, I thus compared the RMSE for predictions to the RMSE for repeated measurements, hence excluding intra-individual differences. All curves were fitted using a least squares procedure, implemented in *Python*'s *scipy* toolbox, utilising a Trust Region Reflective algorithm (Van Rossum and Drake, 2009; Virtanen et al., 2020).

2.4 Results

The force-displacement curves display creep and (minimal) adhesion, typical characteristics of a soft viscoelastic material (See Figure 2.1B). The pad cuticle creeps under constant load at all temperatures (See Figure 2.1C for the displacement profile over time, Appendix B for the corresponding applied force, and Gorb et al., 2000, for similar results for the pads of *Tettigonia viridissima* bush crickets).

The zero- and infinite-time elastic moduli for the insect pad averaged across all temperatures were 50.1 ± 43.1 and $23.9 \pm 19.1\,\mathrm{kPa}$, in good agreement with literature values ($n = 13$, see Figure 2.3A). The maximum adhesive force of the pad to the indentation probe was of $P_{\mathrm{adh}} = 0.18 \pm 0.26\,\mu\mathrm{N}$. Interpreting this result through Johnson-Kendall-Robertson (JKR) contact theory (Johnson et al., 1971; Nalam et al., 2015) yields an adhesive energy per area of $G_{\mathrm{JKR}} = \frac{2}{3}\frac{P_{\mathrm{adh}}}{\pi R_{\mathrm{pad}}} \approx 0.75\,\mathrm{mJ/m^2}$ (Johnson et al., 1971; Nalam et al., 2015), which is considerably lower than that of the pad in air (around $50\,\mathrm{mJ/m^2}$, see Labonte and Federle, 2015a), rendering adhesion of the probe to the pad negligible.

The zero-time modulus E_0 decreased significantly with temperature (ANOVA, $F_{2,102} = 3.169$, $p = 0.046$). A similar trend was observed for the infinite-time modulus E_∞; however this trend was not significant ($F_{2,102} = 1.49$, $p = 0.22$, see Figure 2.3A). The ratio between both moduli was also independent of temperature ($F_{2,102} = 2.853$, $p = 0.06$, see Figure 2.3B), with an across-temperature average of $E_\infty/E_0 = 0.5 \pm 0.1$, indicating substantial viscoelasticity of the pad cuticle. In addition to E_0 and E_∞, the time constants τ_1 and τ_2, also govern the *Prony* series representation of the shear creep function, and were found to be independent of temperature ($F_{2,102} = 0.21$, $p = 0.812$ and $F_{2,102} = 1.30$, $p = 0.277$, see Figure 2.3C).

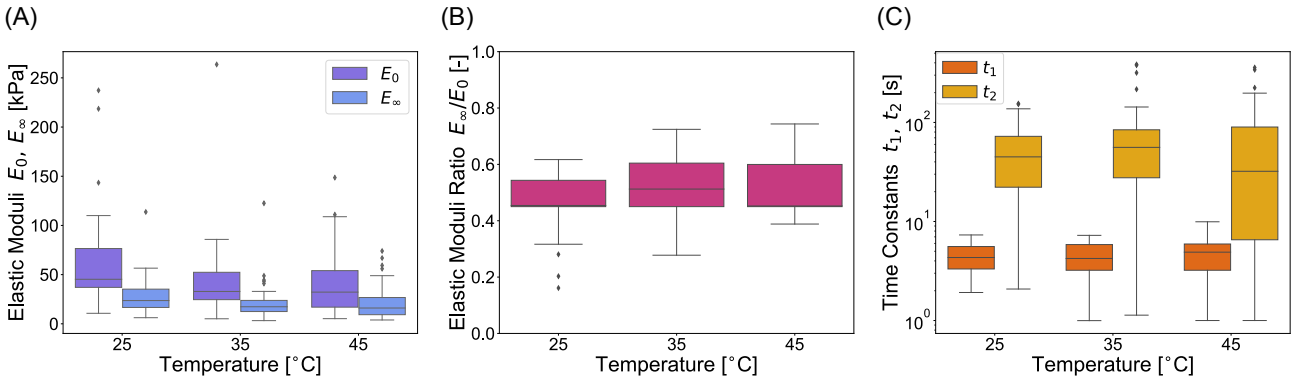


Figure 2.3 (A) The zero- and infinite-time elastic moduli of the stick insect adhesive pad cuticle decrease with temperature, but this decrease was only significant for E_0. (B) The ratio E_∞/E_0 is a measure for the extent of viscoelasticity, and shows a weak but insignificant trend to increase with temperature. (C) The time constants which determine the creep behaviour are independent of temperature ($N = 3$ indents for $n = 13$ insects at 3 temperatures for all data in this figure).

The time-space creep compliance function was used to extract the storage and loss moduli via *Fourier* transforms (See Figure 2.4A). The *Prony* series fitting coefficients are provided in Table 2.2 (See Appendix B for the time dependent creep function $J(t)$). At 25° C, the pad cuticle transitions from a soft, rubbery material to a glassy and stiff material at a low deformation frequency of 0.5 Hz (See Figure 2.4D). The material's dynamic modulus varies over four decades, and displays a peak in the viscoelastic loss modulus $E''(\omega)$, also around 0.5 Hz.

Temperature [°C]	J_0 [kPa^{-1}]	J_1 [kPa^{-1}]	J_2 [kPa^{-1}]	τ_1 [s]	τ_2 [s]
25	0.054 ± 0.039	0.023 ± 0.016	0.005 ± 0.006	4.4 ± 1.5	53.9 ± 38.5
35	0.072 ± 0.055	0.027 ± 0.019	0.007 ± 0.007	4.5 ± 1.7	81.0 ± 92.9
45	0.083 ± 0.063	0.032 ± 0.026	0.007 ± 0.009	4.6 ± 2.1	63.8 ± 86.7

Table 2.2 Summary table of the *Prony* series fitting constants extracted at all temperatures, used to reconstruct the viscoelastic creep function $J(t)$. All values are provided as a mean ± std.

The storage modulus data was shifted for each temperature above the reference of 25° C, and the respective shift factor a_T was computed (See Figure 2.4B). The shift

factors serve as frequency dilation coefficients in the *WLF* model, and were fitted via Equation (2.9) (See Figure 2.4C), yielding $C_1 = 1.37$ and $C_2 = 18.12\,\mathrm{K}$, for $T_{\mathrm{ref}} = 25°\mathrm{C}$.

The variation of the storage modulus with frequency and thus with temperature is represented on the master curve (See Figure 2.4D), which was fitted to the shifted data with the addition of the low and high frequency behaviour of the material. In order to capture the zero- and infinite-time behaviour of the material, I assumed that the behaviour at high or low frequencies for the master curve is approximately equal to that measured for the lowest or highest temperature, respectively. The master curve therefore provides a full characterisation of the effective mechanical properties of the pad cuticle over the investigated temperature and frequency range. For instance, determining the material behaviour of the pad for all stimulation frequencies at 30°C merely requires shifting the master curve by a multiplication factor determined by Equation (2.9):

$$a_T(30°\mathrm{C}) = 10^{\left(\frac{-1.37\times 5}{18.12+5}\right)} = 0.5, \tag{2.11}$$

which is smaller than unity, indicating the viscoelastic functions are shifted to the right of the frequency axis.

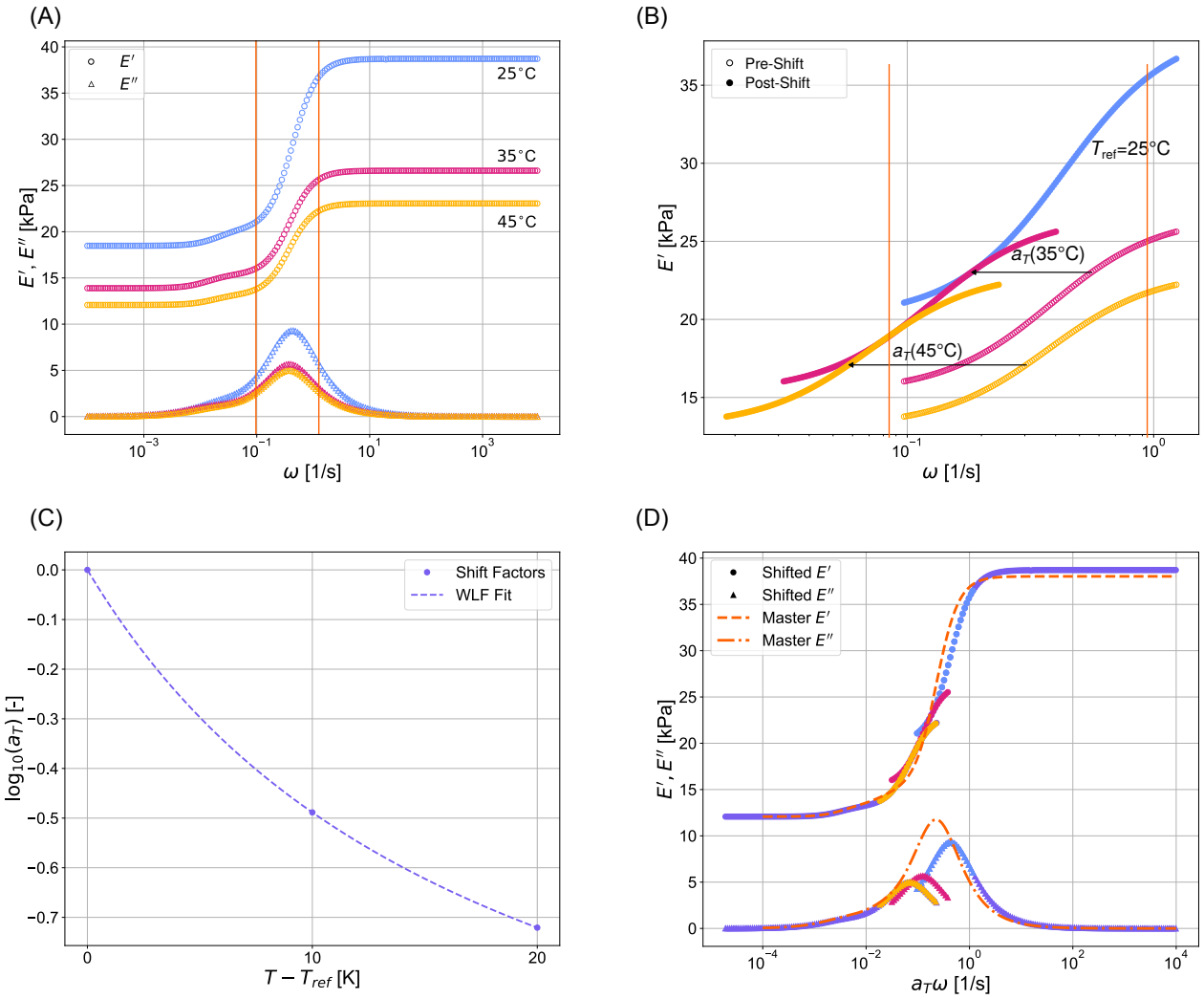


Figure 2.4 (A) The time-space creep compliance function can be used to extract the storage and loss moduli of the adhesive footpad cuticle through *Fourier* transforms. The storage modulus decreases in magnitude with increasing temperatures. The vertical orange lines represent the cut-off frequencies considered for the *WLF* shift, determined from the averages of the fitted time constants $\tau_1 = 5$s and $\tau_2 = 65$s. The temperatures are colour-coded for all four figures, as indicated on the first plot. (B) The variation of the storage modulus E' with frequency in the considered interval. The storage moduli (hollow circles) measured at temperatures above $T_{\text{ref}} = 25°\text{C}$ are shifted to the left (solid disks) by their respective *WLF* shift factor a_T. (C) The shift factors were fitted with the *WLF* equation (dashed line; see Equation (2.9)). (D) The shifted storage and loss moduli can be used to construct a master curve, which I fitted with a *Prony* series (dashed, and dashed dotted orange). The fit is performed by including the shifted data points, as well as the low and high frequency asymptotic values of the lowest and highest temperatures (purple).

2.5 Discussion

Insects use their adhesive system to navigate complex environments. The interaction between this system and the environment may be characterised as an interface composed of the solid pad, its liquid secretion, and the surface it is attached to. The interaction of these interfaces leads to strong but nevertheless controllable adhesive forces. This controllability implies a variability in at least one of the components of this system. The physical properties of the secretion have been characterised in the past, but a complete study of the viscoelastic functions of the pad cuticle itself was missing. I used viscoelastic analysis to quantify the material properties of the footpads of Indian stick insects, including the variation of the storage and loss moduli with temperature and deformation frequency. The pad is a soft viscoelastic material, with an instantaneous (E_0) and relaxed (E_∞) moduli in range with previous literature values (Gorb et al., 2000). I reconstructed the dynamic moduli of the material, and obtained a master curve providing the viscoelastic behaviour of the material at all temperatures and frequencies.

In order to better understand the influence of the pad's material properties on adhesive performance, it is instructive to separate the effects of elasticity, surface roughness, and rate dependence, and to use appropriate theories to study each of those factors. Fracture mechanics is a common theoretical framework to study the adhesion or tack of soft materials; the separation of a solid adhesive from a surface is interpreted as a crack propagating through their interface. As the materials are pulled apart, the potential energy within the material changes, defining the strain energy release rate $\mathcal{G}$. Associated with the propagation of the crack is the creation of "new" surface, which occurs when the strain energy release rate reaches a critical value $\mathcal{G}_c$ (Labonte and Federle, 2015a; Persson, 2001; Persson et al., 2005).

2.5.1 The Effect of Stiffness

Rough substrates offer more adhesive area to an insect's pad on the condition that intimate contact is reached, allowing close-range *van der Waals* forces to act (Autumn et al., 2002; Bush et al., 1975; Creton and Leibler, 1996; Greenwood and Williamson, 1966; Persson, 2001; Persson et al., 2005; Scholz et al., 2008). This consideration hence benefits soft pads, which can reach down to the asperities of a surface and create weak bonds. Our findings are consistent with this requirement, as E_0 and E_∞ are in the

10-40 kPa range, characteristic of a soft and deformable material. As a comparison, *Martina et al.* found that soft Polydimethylsiloxane (PDMS) substrates (E_0 and E_∞ in the 10-80 kPa range) demonstrated enhanced adhesion on rough substrates compared to smooth surfaces for the lowest moduli investigated in their study ($E_0 \approx 10\,\text{kPa}$) (Martina et al., 2012). These results, together with the viscoelastic time constants determined above are in excellent agreement with a previous study investigating the viscoelasticity of insect pads, in which *Gorb et al.* found similar elastic moduli ranges and time constants in the same order of magnitude (Gorb et al., 2000). This observation validates the *Prony* series methodology employed here, with which the dynamic moduli of the pad could be reconstructed.

The insect pad's instantaneous (E_0) and relaxed (E_∞) moduli stay within the $10-40\,\text{kPa}$ range at all temperatures, and so does the magnitude of the storage moduli E' at all frequencies, indicating that the material remains capable of intimate contact on surface asperities under all conditions investigated in this study. A perhaps unifying understanding of adhesion on smooth and rough substrates consists in the dual behaviour of the elastic pads: For most experiments, the loading part of the load-displacement curve appears to be governed by two power laws, as observed also by *Scholz et al.* (Scholz et al., 2008), suggesting that the two outermost layers of the pad may have different stiffness. This observation bodes well with the ultrastructure of the pads, which present a thin outer layer, and a fibrillar internal structure (Bennemann et al., 2014, 2011; Scholz et al., 2008). Such a system might be capable of complying to small asperities the claws can not cling to (Dirks and Federle, 2011a; Endlein and Federle, 2008; Féat et al., 2019; Gorb, 2001; Song et al., 2016), while providing a base layer capable of hardening during detachment (Krahn et al., 2011; Scholz et al., 2008).

The adhesive organs of other climbing animals have also been demonstrated to exhibit viscoelastic properties. Studies by *Puthoff et al.* and *Prowse et al.* showed that the hair (*setae*) covering the pads of geckos, characterized by a dynamic moduli in the GPa range, become tackier at higher Relative Humidity (RH). This change was significant, showcasing a three to four-fold drop in the complex modulus over the 10-80% RH range. These observations led the authors to speculate that the viscoelastic losses incurred by the *setae* may strengthen their bonding abilities (Prowse et al., 2011; Puthoff et al., 2010).

2.5.2 The Effect of Rate

The viscoelasticity of the material, and more specifically the frequency dependence of the storage and loss moduli, introduces another aspect to the fracture mechanics models presented here. In fact, viscoelastic materials on rough substrates are not only able to comply even further to asperities the longer they are kept in contact (Hui et al., 2000; Persson et al., 2004, 2005), they also dissipate energy close to the crack tip during separation (Greenwood and Johnson, 1981; Müser and Persson, 2022; Persson, 2021; Persson and Brener, 2005). This energetic loss thus requires an energetic surplus to induce crack propagation. Hence, $\mathcal{G}$ does not have a unique value for viscoelastic materials, and can be higher than $\mathcal{G}_0$. Since the magnitude of that excess is modulated by the dissipation of elastic energy into heat, it is tied to the loss modulus $E''(\omega)$, and is thus rate-dependent (Lakes, 2009), allowing the strain energy release rate to be written as $\mathcal{G}(v_c)$, a function of the crack speed v_c. My work revealed a significant rate dependence of the pad, through a master dynamic modulus that changes by a factor of 3.2 over the $10^{-4} - 10^{4}$ Hz frequency range. This result expands the individual viscoelastic ratios obtained at individual temperatures (See Figure 2.3B), where TTS enables the exploration of the full range of deformation of the investigated material. Nonetheless, most Pressure Sensitive Adhesives (PSA) capable of adhering to rough surfaces have a significantly higher viscoelastic ratio, often closer to $E_0/E_\infty \approx 10^3$ (Chang, 1997; Creton, 2003; Persson, 2021), with notable exceptions such as collagen hydrogels, for which $E_0/E_\infty \approx 1.4$ (Islam and Oyen, 2021). An elevated viscoelastic ratio is often considered to be a requirement for a highly tacky PSA (Chang, 1997; Leong et al., 2003). In comparison, the material insect pads are made of seem to have a much lower rate dependence. One can speculate regarding the function of such reduced rate sensitivity: While insects may benefit from a level of tack controllability through rate changes, they must minimise rate dependence to allow rapid attachment during fast locomotion. It may seem as though such an adhesive system might be inefficient in situations in which insects require high tack in a short period of time (when being pulled off a surface by a predator, for instance), but previous authors have shown insects mitigate this problem through "pre-flexes" in their limbs and the shear-sensitivity of the adhesive forces their pads produce (Endlein and Federle, 2013; Labonte and Federle, 2015a).

The frequency or time dependence of the modulus is marked by the time constants determined during fitting of the *Prony* series, adjusted by their *WLF* factor. This

confirms that the adhesive pad exhibits different material responses as a function of the crack speed, which is in turn related to the pull-off speed of the pad (Labonte and Federle, 2015a). This observation confers controllability to insect pads: since insects have control over the pull-off speeds of their pads, they can also control the force required to detach it. Typically, the relationship between $\mathcal{G}$ and the crack propagation velocity v_c is an empirical law written as: $\mathcal{G}/\mathcal{G}_0 - 1 = (v_c/v^\star)^n$, where $v^\star$ is a characteristic crack speed (Labonte and Federle, 2015a; Müser and Persson, 2022; Persson, 2021; Persson and Brener, 2005). The viscoelastic ratio is directly linked to the strain energy release rate at infinite speed: $\mathcal{G}_0/\mathcal{G}(v_c \to \infty) = E_\infty/E_0$ (Persson, 2021; Persson and Brener, 2005). The maximum pull-off force $F_{\max}(v)$ required to detach a viscoelastic solid with a crack velocity v_c writes as a power law (Fogden and White, 1990; Labonte and Federle, 2015a; Müser and Persson, 2022; Persson, 2021; Persson and Brener, 2005):

$$F_{\max}(v_c)/F_{\max}(0) = (\mathcal{G}(v_c)/\mathcal{G}(0))^m, \tag{2.12}$$

where m is a geometric coefficient (For a sphere on a flat substrate $m = 1$, for a cylinder $m = 2/3$ Fogden and White, 1990; Müser and Persson, 2022). Thus, the maximum expected difference between peak adhesive forces for an insect pad (modelled as a sphere) is bound by the ratio between the low and high frequency storage modulus, $F_{\max}(v)/F_{\max}(0) = E_0/E_\infty = 3.2$. This ratio is in excellent agreement with the forces measured by *Labonte et al.*, where the ratio between the peak adhesive forces for the slowest and fastest detachment speeds was 3.3 ± 1.9 (Labonte and Federle, 2015a). It may sometimes be favourable for insects to control adhesion through the rate dependence of their pads. In particular, higher pull-off forces at rapid speeds are useful, because they bring increased resistance to sudden events such as predator attacks, sudden rain or wind gusts. Nonetheless, such mechanism of control could also be detrimental, because it may limit the running speed insects are able to achieve before getting stuck.

Available evidence seems to suggest that minimising rate dependence is actually beneficial: the adhesive performance of pads is controlled via shear forces instead, the influence of which largely exceeds that of crack speed (Federle et al., 2004, 2002; Labonte and Federle, 2015a; Labonte et al., 2019). Interestingly, *Endlein et al.* argued that the morphology of insect legs is such that shear forces are suitably activated by sudden detachment impulses, triggering passive "preflexes" which result in a rapid

doubling of the pad's contact area (Endlein and Federle, 2008, 2013). Such mechanism is favourable to rate dependence which is most likely controlled by an insect's movements, firstly because this passive "reaction" is faster than any neurological impulse (Endlein and Federle, 2008, 2013), and secondly because it imposes no limit on the running speed of insects, but rather on the biomechanics of their movements. Additionally, if it experiences any sliding, a shear-sensitive adhesive is hence passively engaged during horizontal climbing.

2.5.3 The Effect of Temperature

Previous authors have assessed the influence of temperature on the adhesive and frictional forces produced by insects's pads. *Roth et al.* first noted the inability of roaches to climb up a glass wall when the temperature was raised above 40°C. They also noted that the adhesive pads seemed to collapse and deflate when kept at an elevated temperature for too long (Roth and Willis, 1952). Similarly, *Federle et al.* measured the shear stresses produced by ant pads at different sliding velocities at 15 and 30°C, and found that higher temperatures reduced the shear stress-velocity regression slope by half. In contrast, they did not find the static shear stress to be affected by temperature (Federle et al., 2002). These findings were confirmed in their follow-up work, in which the static and dynamic shear stresses were independent and strongly dependent on temperature, respectively (Federle et al., 2004). Additionally, the perpendicular detachment (adhesive) forces of ants were temperature independent, and significantly lower than the frictional forces (Federle et al., 2004). Recent work by *Stark et al.* measured the frictional forces produced by eleven species of ants on substrates heated up to 55°C, and identified three trends: a linear decrease, a hump-shaped relationship, and no variation of the shear forces with increasing temperature (Stark et al., 2018). From these results, it seems shear stresses are most affected by temperature changes. The authors cited here related these changes to the expected change in the secretion's viscosity with temperature, but to my knowledge, there exist no studies investigating the effect of temperature on the viscoelastic properties of the pad, and its potential effect on adhesion and friction.

At any given temperature, it is not trivial to investigate the absolute upper and lower bounds of the viscoelastic functions of the pad, because our experiments might not glean information from the entirety of the material's viscoelastic spectrum. In fact, E_0 and E_∞ both change with temperature even if only weakly for the latter. I

circumvented that problem by applying TTS, thus investigating the upper and lower limits of the pad's deformation over a biologically relevant temperature range. Our findings revealed that the dynamic modulus of the insect pad follows a *WLF* model, with constants $C_1 = 1.37$ and $C_2 = 18.12\,\mathrm{K}$ that result in a relatively weak temperature dependence when compared to typical amorphous polymers, for which $C_1 = 17.44$ and $C_2 = 51.6K$ (Bae et al., 2011; Curro and Salazar, 1975; Herrmann et al., 2002; Lakes, 2009; Rajan et al., 2018; Shangguan et al., 2017; Williams et al., 1955). The low value of C_1 suggests that the time constants may only show a weak temperature dependence, even after adjusting them with their respective a_T factors. It is important to note these values are comparable to those for amorphous polymers only if the reference temperature is chosen as the glass transition temperature of the material (Bae et al., 2011; Lakes, 2009; Rajan et al., 2018; Shangguan et al., 2017; Williams et al., 1955). This transition temperature has to our knowledge not been determined for insect pads, and its investigation goes beyond the scope of this work. While E_0 and E_∞ decrease with increasing temperatures, indicating a softening of the material, their viscoelastic ratio E_∞/E_0 is agnostic to temperature. Thus, the relative relaxation of the material over time is similar over the investigated temperature range.

The very creation of the master curve bears witness to the temperature dependence of the pad's material, however the insights presented here indicate that it is relatively weak when compared to typical elastomers, which often have a heightened temperature dependence due to their increased molecular mobility and cross-link densities (Curro and Salazar, 1975; Herrmann et al., 2002). In fact, according to Equation (2.12), which relates the viscoelastic ratio to the adhesive performance of a viscoelastic material, the adhesive forces should also be only weakly influenced by temperature, in good agreement with the results presented by *Federle et al.* (Federle et al., 2004). In a biological context where habitat temperatures can be highly variable (Colinet et al., 2015; Halsch et al., 2021; Huey et al., 1992; Sinclair et al., 2003; Stark et al., 2018), it is favourable for insects's feet not to be greatly affected by temperature. Insects are hence not limited by their environment, as they make use of their actively or passively controlled body mechanics to control rate and possibly shear, and navigate surfaces of variable temperature.

While the analysis here adheres to TTS principles, it is noteworthy that TTS is typically employed for polymers over larger temperature ranges, for which the overlap of the shifted storage or loss moduli is obvious over wide frequency intervals. Another possible

analysis of the data presented above consists in applying TTS to the displacement curves at different temperatures, and reconstituting a single creep curve over time, to which the *Prony* series model described above can be fitted. This method circumvents applying TTS to data already fitted by a *Prony* model and offers a more direct understanding of the temperature dependence of the studied material. This methodology will certainly be a part of the future work I intend to carry out as a continuation of this research, preliminary trials have indicated the magnitude of the storage and loss moduli, as well as their time-dependence, are equivalent to those presented in this work.

2.5.4 Do Insects Rely on "Dry" Adhesion?

The evidence presented here depicts the pad as a viscoelastic material whose viscoelastic ratio E_0/E_∞ provides the upper and lower bounds of the "dry" adhesive forces it can produce, as predicted by fracture mechanics. The temperature dependence of the viscoelastic functions investigated here follows a *WLF* model which is relatively weak, compared to typical elastomers (Ciavarella and Papangelo, 2021; Persson, 2021; Williams et al., 1955).

In the above, I have assumed the primary origin of adhesion to be a solid-solid interaction. However, surface contact is mediated by a liquid, whose viscosity we found to be highly temperature dependent (See Chapter 1). The study presented here has the advantage of providing quantitative changes in the viscoelastic functions according to temperature, which allows predictions of the solid-solid friction and adhesive properties of the pads and their change with temperature, or lack thereof. These predictions can hence be compared to "wet" models and –due to the two modes of variation of the physical properties of the liquid and solid with temperature– allow determining which mechanism dominates the adhesive forces produced by insects's pads.

Clearly, identifying which of the two models, "wet" or "dry", is most significant for insect's abilities requires further investigation into the adhesive performance of insect pads at different temperatures and retraction rates. With such measurements, predictions can be extracted in line with the fracture mechanics model described here, and compared to the measured forces, providing clarity on the exact mechanisms of insect adhesion, in the hopes of resolving this two centuries old question.

Chapter 3

The Forces Produced by Single Smooth Pads of Indian stick Insects

3.1 Introduction

The debate regarding the physical origin of the adhesive performance of insect pads has been ongoing for two centuries. In particular, the presence of a secretion mediating the contact between pad and substrate has lead to different interpretations of the functional significance of this thin liquid layer (Barnes et al., 2011; Betz, 2010; Bullock et al., 2008; Dirks and Federle, 2011a; Federle et al., 2004; Federle and Labonte, 2019; Federle et al., 2002; Gillett and Wigglesworth, 1932; Gorb et al., 2000; Gorb, 1998; Koerner et al., 2012; Labonte and Federle, 2013, 2016; Niederegger and Gorb, 2003; Stark et al., 2018; Stark and Yanoviak, 2018; Walker, 1993; Wigglesworth, 1987; Zhou et al., 2014). For many years, the investigation of the adhesive capabilities of insects was purely observational. Multiple reports described the different ways in which insects such as flies and cockroaches attach themselves effortlessly on smooth substrates such as glass, and previous authors determined conditions – such as temperature – that either facilitate or impede adhesion (Gillett and Wigglesworth, 1932; Kendall, 1970; West, 1862; Wigglesworth, 1987). Only after significant advances in microtechnology fields, did scientists and engineers get the opportunity to investigate the physical phenomena potentially giving rise to such impressive adhesive feats.

My first chapter was dedicated to examining the physical properties of the secretion, and expanding the state of knowledge by assessing their temperature dependence. I then investigated, in my second chapter, the ways in which rate and temperature affected the material properties of the soft pad material. Those two chapters centrally discussed two potential origins of reversible surface attachment in insects, each oriented towards the properties of either the secretion layer or the solid pad: "wet" and "dry" adhesion. Previous studies have brought forward evidence in support of either mechanism. For instance, *Jiao et al.* conducted adhesion measurements with and without the secretion, and argued that the liquid layer is necessary but not sufficient to produce strong adhesive forces, for which the deformation of the pad plays a key role (Jiao et al., 2000). *Federle et al* and others raised the question of frictional forces, which are strikingly higher than adhesive forces in insects (Federle et al., 2004, 2002; Labonte and Federle, 2015b; Labonte et al., 2019). A non-*Newtonian* nature of the secretion was hypothesised in order to reconcile the presence of a liquid with friction (rather than lubrication) (Drechsler and Federle, 2006; Federle et al., 2004, 2002; Speidel et al., 2017). However, previous microrheology experiments revealed no evidence for a departure from viscous (*Netwonian*) behaviour (Abou et al., 2010; Attipoe, 2018;

Baumgart et al., 2022; Peisker et al., 2014). *Labonte et al.* used fracture mechanics models to predict the rate dependence of insects's pads pull-off forces, suggesting that "dry" contacts provide controllability to the adhesive forces, since the energy required to detach a viscoelastic material from a surface can be close to the energy of the adhesive bonds themselves, also called the work of adhesion (Labonte and Federle, 2015a). The authors estimated this adhesive strength for dry (*van der Waals*) and wet (capillary) systems based on estimates of the physical properties of both interfaces, but did not find conclusive evidence for either of the two mechanisms (Labonte and Federle, 2015a).

In practice, differentiating "wet" and "dry" adhesion is challenging since both adhesive systems behave qualitatively similarly. For instance, geckos (Autumn et al., 2002; Gravish et al., 2008; Huber et al., 2005; Prowse et al., 2011; Puthoff et al., 2013, 2010; Stark et al., 2013), which have been thought to utilise "dry" adhesive mechanisms, whereas spiders (Peattie et al., 2011; Wolff and Gorb, 2011), as well as insects (Attipoe, 2018; Bullock et al., 2008; Drechsler and Federle, 2006; Federle et al., 2004, 2002; Jiao et al., 2000; Kaimaki et al., 2022; Labonte and Federle, 2015a,b; Stark et al., 2018; Stark and Yanoviak, 2018; Voigt et al., 2010), and frogs (Emerson and Diehl, 1980; Endlein et al., 2013; Federle et al., 2006; Hanna and Barnes, 1991), which have been primarily thought to rely on "wet" adhesion, have demonstrated similar performance through the dependence of their attachment forces on temperature, rate, and humidity. Because "wet" and "dry" adhesive models can depend on these environmental variables in a similar way (Labonte and Federle, 2015a), consistent experiments with controlled parameters are required in order to compare the resulting adhesive forces with physical interpretative models.

The rate dependence of the adhesive forces of insects is well established, and is consistent with both the secretion's viscosity and the pad's viscoelasticity (Federle et al., 2004, 2002; Labonte and Federle, 2015a; Langer et al., 2004). Other studies have also demonstrated that temperature can affect an insect's attachment performance (Federle et al., 2004, 2002; Roth and Willis, 1952; Stark et al., 2018), an observation equally consistent with dissipative processes in either the fluid or the solid, but this variation was neither consistent across species (Stark et al., 2018), nor across adhesive versus frictional performance.

The first two chapters of my thesis focused on determining the physical parameters governing insect adhesion, whether it be "wet" or "dry", and assessing their temperature dependencies. This final chapter now attempts to bring together the knowledge gained

from the previous two chapters, and comparing their respective predictive laws to live measurements on insects. Specifically, I plan to use the interaction between temperature and rate effects to disentangle the secretion's contribution from the contribution of the pad, benefiting from the different modes (or absence) of variation of viscous, capillary and viscoelastic forces. I suggest that the adhesive forces produced by a single pad, without the influence of an insect's body mechanics at different retraction rates and temperatures are a good candidate for assessing the relative importance of the secretion and the pad's contributions. Similarly to *Labonte et al.*, I make use of fracture mechanics (Labonte and Federle, 2015a), briefly outlined in the General Introduction, and further detailed below, interpreting the detachment process of a pad to a crack propagating at the interface between an insect's foot and the surface it sticks to.

3.2 Methods

3.2.1 Study Animals and Sample Preparation

A colony of Indian stick insects (*Carausius morosus, Sinéty* 1901) was kept in a climate chamber at 25C 60% relative humidity, 12/12 hours light cycle (FitoClima 12.000 PH, Aralab, Portugal), and fed water and bramble *ad libitum*. All experiments were conducted with adults, identified via the scarlet colouration on the femur of their front legs (Body mass 676.4 ± 39.1 mg, mean ± standard deviation, $n = 10$) (MacBride and Jackson, 1915). The live insects were inserted in glass tubes, and one of their protruding front legs was attached to a metal wire with dental impression silicone (Elite HD+, Zhermack, Germany), following the procedure detailed in Section 1.2.3.

3.2.2 Force Sensor and Image Recording

The adhesive forces produced by a single pad were measured using a custom-built force transducer (Similar to previous work Drechsler and Federle, 2006; Federle et al., 2004, 2002; Labonte and Federle, 2015a; Labonte et al., 2019, see Figure 3.1A). This setup was composed of a fibre optic sensor (MU 2DMS-RC32-T1/T4, Philtec, USA) mounted in proximity of a brass cantilever beam (width: 11 mm, thickness: 0.1mm). The beam was clamped at one end by a steel plate. The free-standing length of the beam was 25 mm, and the fibre optic sensor was mounted 16 mm from the steel support. The sensor has a nominal resolution of 20 nm, which, when correlated to the calibration constant of the beam, corresponded to a $\sim 1\,\mu$N force, about 1% of the

smallest adhesive forces previously measured for insect pads (Labonte and Federle, 2015a). The geometric spring constant of the beam was $5 - 10\,\mathrm{N/m}$ and its resonant frequency was estimated to be around $30 - 60\,\mathrm{Hz}$ (faster than the shortest detachment events found in this study $\sim 0.25\,\mathrm{s}$), depending on the lever arm ranging from 35 to 40 mm. The force sensor was calibrated by placing known weights on a $1\,\mathrm{mm}^2$ area on the coverslip, with the help of resin 3D printed holder. The corresponding force exerted by each weight over a $0.02 - 5\,\mathrm{mN}$ range was matched to the fibre optic distance reading at two lever arms, and the calibration curves were adjusted in order to account for a change in the distance at which force measurements were performed (See Appendix C). The coverslip was positioned and aligned with the location of the pad contact and the control weight holder prior to every calibration, which were performed at each coverslip change. The force transducer was mounted on a three-axes motor stage (X: M-404.1PD, Y: M-403.42S, Z: M-404.6PD, maximum resolution $0.16\,\mu\mathrm{m}$, Physik Instrumente, Germany) connected to three controllers (C-863, C-663, C-863, respectively, Physik Instrumente, Germany), allowing translation of the cantilever beam in all directions (See Figure 3.1).

3.2.3 Temperature Control

An ITO coated glass coverslip ($18 \times 18\,\mathrm{mm}$, 0.18 mm thickness and resistance of $8 - 12\,\Omega$, SPI Supplies, USA) was attached to the free end of the cantilever beam, by tightening a resin 3D printed holder with two plastic screws. The glass coverslips were cleaned in an ultrasonic bath with acetone and isopropanol for 10 minutes each, rinsed for 30 s with DI water and blow-dried with compressed air. While not in use, the coverslips were stored in a 3D printed box, sealed with paraffin film (Parafilm, Bemis Company, USA). To achieve temperature control, two thin wires ($0.03\,\mathrm{mm}^2$ cross-section, ThermoThin, Alpha Wire, UK) were cold soldered (Electric Paint, Bare Conductive, UK) to the ITO side of each coverslip, and connected to a temperature control setup identical to that described in Chapter 1. The thermocouple was attached to the conductive side of the coverslip with thermal grease, providing electrical insulation (Kryonaut, Thermal Grizzly, Germany). Experiments were conducted at three biologically relevant temperatures: 25, 35, and 45°C. The mounting of the temperature control components was designed such as to add minimal weight to the end of the cantilever beam (See Figure 3.1).

3.2.4 Experimental Protocol

Prior to experiments, an insect pad was positioned under the glass coverslip using a three axis micro-manipulator (MM 33, Märzhäuser Wetzlar, Germany) with the help of a camera (1.6 MP, Blackfly S BFS-U3-16S2C-CS, FLIR, USA) mounted on a custom-built 1.3× microscope (Optem Zoom 100, Qioptiq. USA) with LED illumination (M530L4, $\lambda = 530\,\text{nm}$, Thorlabs, USA). The pad was successively brought in contact with the coverslip with the micro-manipulator until a $\sim 2\,\text{mN}$ preload was registered (Previous experiments by *Labonte et al.* determined that in pure adhesion experiments, the pull-off forces are independent of the preload in the $0.5 - 4\,\text{mN}$ range Labonte and Federle, 2013) with the fibre optic sensor's proprietary *Labview* software (National Instruments, USA (Bitter et al., 2007)). It must be noted that the setup was controlled by displacement and not force, so the preload values tended to vary around the $1.94 \pm 0.31\,\text{mN}$ average. The coverslip was then moved away from the pad at a control speed v_r, by displacing the Z motor stage 1 mm away from the loading point. In order to reduce experimental noise, the whole setup, including the force transducer, motor stages, and microscope, was placed on a vibration-free table platform (BenchMate, Kinetic Systems, USA).

During experiments, the motor stages were controlled using a custom-written macro-script (PIMikroMove, Physik Instrumente, Germany), to implement the following loading/unloading cycle: *i.* The pad is brought in contact with the coverslip at a 1 mm/s velocity, breaching the 1 mm gap between the coverslip and the 2 mN loading point. *ii.* Static contact is maintained for a period of $t_\text{h} = 30\,\text{s}$ —Assuming the pad has the same thermal diffusivity as water $\alpha_\text{water} = 0.143\,\text{mm}^2/\text{s}$ (Blumm and Lindemann, 2013), the $L = 500\,\mu\text{m}$ thick pad (Bennemann et al., 2014) should heat up in about $L^2/\alpha_\text{water} \approx 1.7\,\text{s}$. *iii.* The pad is detached, by moving the Z stage at one of four logarithmically spaced velocities: $v_\text{r} = 0.01$, 0.06, 0.34, and 2.0 mm/s. The motor stage's controller in the Z axis was connected to a 9-pin I/O cable, capable of providing a trigger pulse at the beginning of step *i.* This pulse was received by a microcontroller (Arduino DUE, Arduino, Italy), and sent to the camera and the force sensor interface. This way, the contact area of the pad during pull-off could be recorded at 200 fps and matched to its corresponding force reading at a sampling rate of 1.3 kHz. Experiments were conducted at four different lever arms at $500\,\mu\text{m}$ spacing, one for each pull-off velocity, in order to avoid the systematic effect of fluid accumulation in one location (Labonte and Federle, 2015a), and to maximise the usable area of each coverslip. At

least 40 s elapsed between measurements at different speeds, and a 20 minutes rest time was allowed between each temperature (Previous experiments by *Dirks et al.* indicated the volume of adhesive secretion is fully restored over that time Clemente and Federle, 2012; Dirks and Federle, 2011b). The experiments described here were carried out for $n = 10$ insects, for $N = 4$ retraction speeds at 25, 35, and 45°C. The temperature and pull-off velocity orders were randomised.

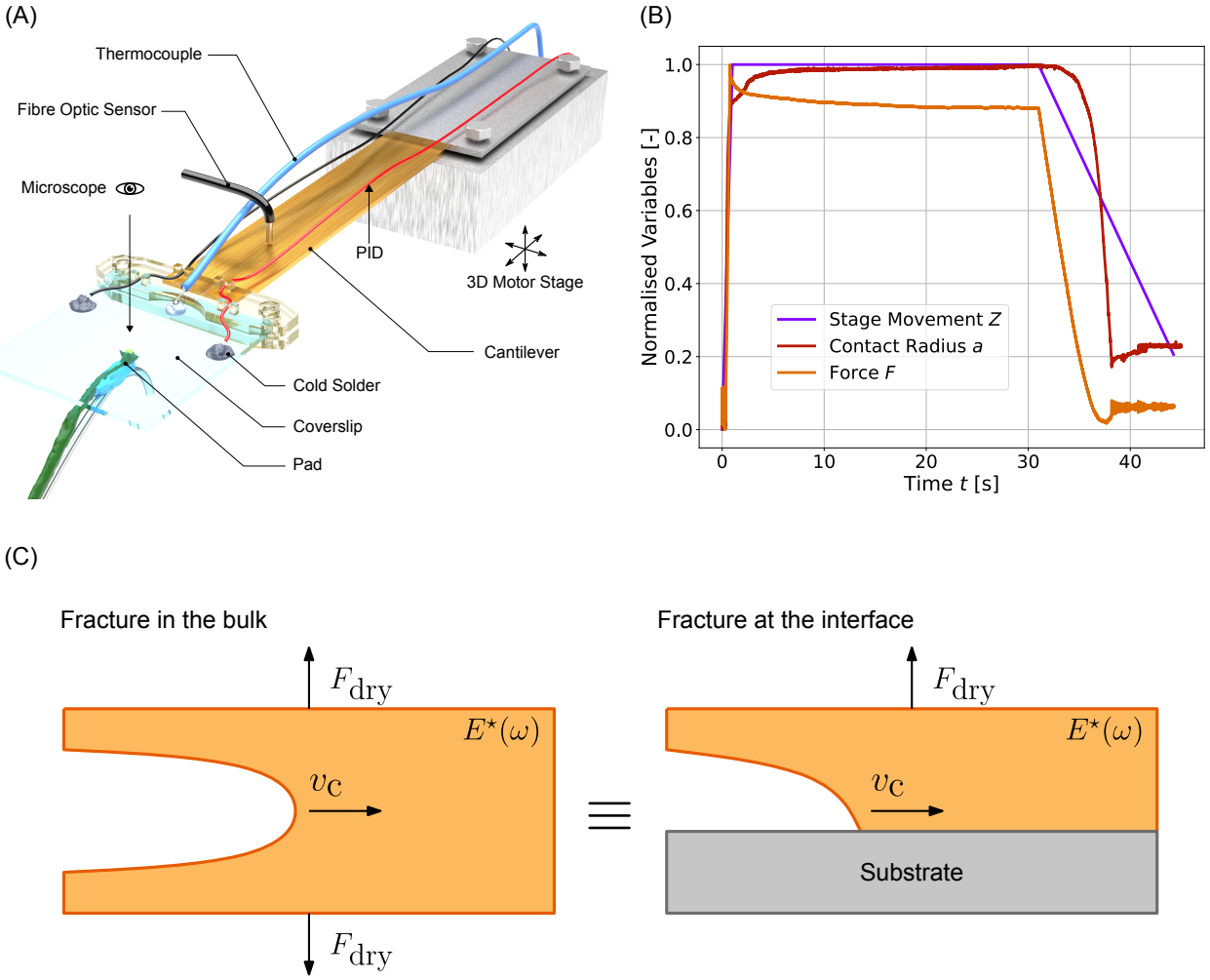


Figure 3.1 (A) Schematic representation of the force measurement setup. Insect pads were mounted on a wire in proximity of a glass coverslip. Two thin wires were cold soldered to the coverslip and connected to a thermocouple to control the surface temperature via a PID controller. The coverslip was mounted by means of a resin holder to a cantilever beam, whose deflection was measured with a fibre optic sensor. The whole apparatus was connected to a 3D motor stage represented by the arrows, and the contact area on the coverslip was visualised with a microscope and a high speed camera. (B) The force sensor allowed measuring the adhesive forces F produced by insect pads (orange) when the motor stages moved away from the pad in the Z direction perpendicular to the coverslip (purple). The camera recorded the contact area of the pad, which normalised by its perimeter gave a measure of the contact radius a (red). All curves were divided by their maximum and minimum values to reveal synchronicity, in reality the adhesion peak is in the negatives. Note the stress relaxation displayed on the force curves, and the corresponding increase of the contact radius, consistent with a viscoelastic material. (C) In terms of contact mechanics, a crack propagating at speed v_{c} through a material's bulk is equivalent to the same material being peeled off a rigid substrate.

3.3 Data Analysis

3.3.1 Image Analysis and Crack Speed Extraction

The recorded videos were post-processed using a custom-made *Fiji- Python* hybrid macro (*Python* version 3.8.10, *Fiji* version 1.53t Van Rossum and Drake, 2009; Virtanen et al., 2020). In order to reduce the impact of noise in the analysis of the videos, the contact area images were filtered with a *Gaussian* blur filter with a standard deviation close to $\sim 10\,\mu$m – the size of typical image noise. In many of the recorded videos, the glass coverslip tended to have a weak contrast with respect to the pad's contact area, and binarisation algorithms thus failed to distinguish the two. To extract the pad as a predominant feature of the image, a rolling ball background subtraction algorithm was successively applied with a cut-off radius close to the pad's contact radius $\sim 500\,\mu$m. Finally, I used an outliers removal algorithm which replaces pixel values by a local median with the same cut-off radius as the *Gaussian* filter, and binarised the resulting images with a thresholding algorithm native to *Fiji*. The maximum area particle detected in the final images was identified as the pad in contact with the coverslip, and its perimeter (Π) and area (A) were measured via *Fiji*'s native particle analysis routine for the entire video sequence from contact initiation to complete detachment (See Figure 3.2). All of the above was implemented using native *Fiji* functions (Schindelin et al., 2012).

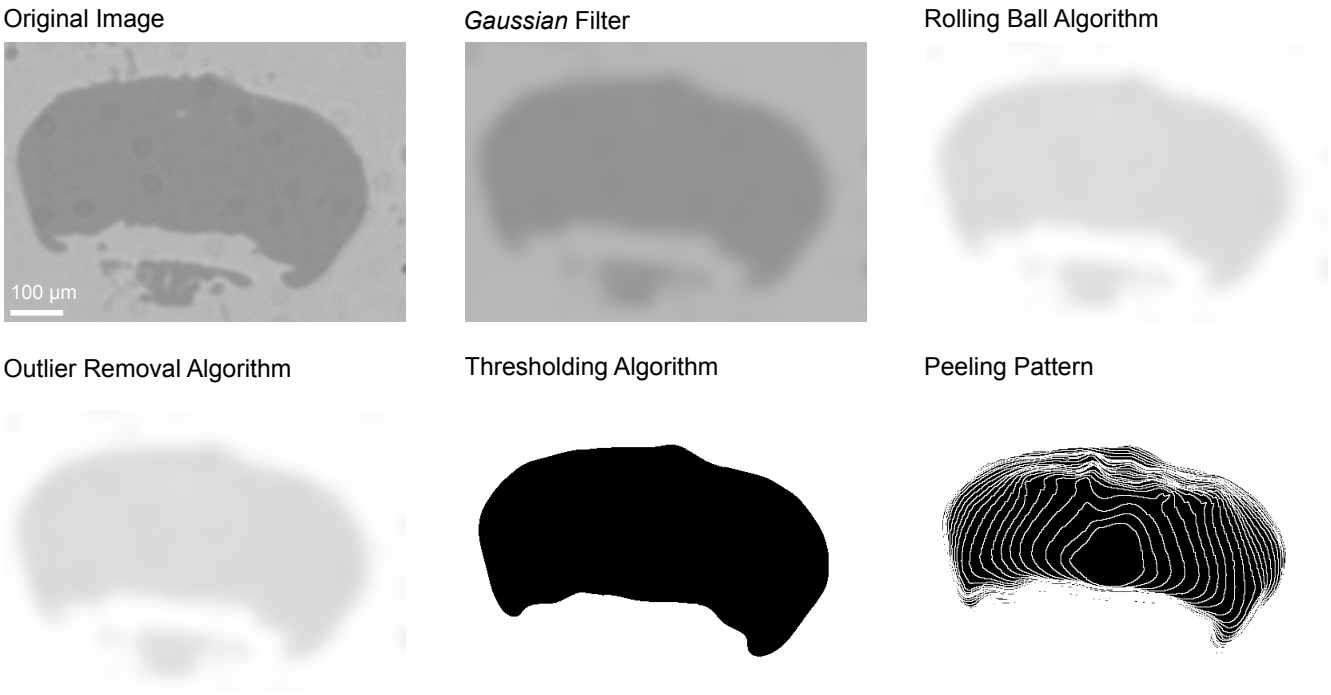


Figure 3.2 The contact area videos underwent five steps of image processing. A *Gaussian* filter was applied to extract high contrast features, followed by a rolling ball algorithm to remove the background of the images. Outliers were removed, and a thresholding algorithm binarised the image. The crack speed was then extracted by measuring the change of the ratio between contact area and perimeter with time. The progressive peeling of the pad at different time points during detachment is indicated by the white topology-like lines.

The time-dependent contact radius $a(t) = A/\Pi$ was then extracted in *Python*. Its time-derivative was interpreted as the crack propagation velocity (Labonte and Federle, 2015a):

$$v_c(t) = -\frac{da}{dt}. \tag{3.1}$$

The contact radius data were filtered with a Locally Weighted Scatterplot Smoothing (LOWESS) algorithm (span = 0.05), and any delay resulting from asynchronicity between the camera and the force sensor was corrected by matching the timestamps at which contact was initiated on the contact radius and force curves (this delay never exceeded 0.2 ± 0.02s). In order to minimise the noise of the fibre optic sensor signal, the force data were corrected by averaging the readings before and after contact and subtracting the resulting drift, assuming a linear drift rate. The curves were then

smoothed with an order three *Butterworth* filter (frequency: 0.01 rad/s), and the peak adhesive force ($F_{\max}$) was extracted by finding the maximum force reading within the in-contact interval (step *iii.* of the motor stages). Once the time at which the maximum peak force occurred ($t_{\max}$) was determined, the corresponding crack speed was extracted from the video recordings as $v_c(t_{\max})$, by performing a least-squares linear regression of the contact radius at $t_{\max}$, together with two points before and after $t_{\max}$ (as described by *Labonte et al.* Labonte, 2015; Labonte and Federle, 2015a). All analyses was performed using a custom-made *Python* script (Van Rossum and Drake, 2009), using the *statsmodels* Seabold and Perktold (2010) and *scipy* libraries (Virtanen et al., 2020).

3.3.2 Fracture Mechanics

Fracture mechanics is a powerful tool to interpret adhesive problems: the separation of a material from a substrate is viewed as a crack propagating through their interface (See Figure 3.1) (Labonte, 2015; Labonte and Federle, 2015a; Persson and Brener, 2005). A key quantity in determining the resistance a material opposes to such separation is the strain energy release rate. Determining a model that takes into account its variation with rate and temperature is equally crucial. I present in this work two main theories: One which uses a parametric approach of the strain energy release rate developed by *Barquins and Maugis* (Barquins and Maugis, 1981; Maugis and Barquins, 1980), and a second one which is based on first principles of viscoelastic dissipation, detailed by *Persson et al.* (Müser and Persson, 2022; Persson, 2021; Persson and Brener, 2005). The two theories rely on the same basic assumptions of linear viscoelasticity, and differ in the expression of the strain energy release rate, which can be determined considering the relevant material and geometrical parameters, further detailed in this section.

Barquins and Maugis assume that the strain energy release rate follows a law of type (Barquins and Maugis, 1981; Lakes, 2009; Maugis and Barquins, 1980; Persson and Brener, 2005):

$$\mathcal{G}(v_c) = \mathcal{G}_0 \left[1 + \phi(v_c)\right]. \tag{3.2}$$

The temperature dependence of $\mathcal{G}$ can be accounted for by multiplying the crack speed by a *Williams-Landel-Ferry* (*WLF*) shift factor a_T. A common formulation for the arbitrary function ϕ is an empirical power law (Ahn and Shull, 1998; Barquins and Maugis, 1981; Feng et al., 2007; Maugis and Barquins, 1980; Shull, 2002):

$$\mathcal{G}(v_\mathrm{c}) = \mathcal{G}_0 \left[1 + \left(\frac{v_\mathrm{c}}{v^\star}\right)^n\right], \tag{3.3}$$

where $v^\star$ is a characteristic crack speed for which $\mathcal{G}$ becomes double the value of $\mathcal{G}_0$, and n is a fitted power exponent which gives origin to viscous dissipation.

The viscoelastic ratio is directly linked to the strain energy release rate at infinite speed: $\mathcal{G}(v_\mathrm{c} \to \infty)/\mathcal{G}_0 = E_0/E_\infty$ (Persson, 2021; Persson and Brener, 2005). The maximum pull-off force $F_\mathrm{max}(v)$ required to detach a viscoelastic solid with a pull-off velocity v follows as a power law (Fogden and White, 1990; Labonte and Federle, 2015a; Müser and Persson, 2022; Persson, 2021; Persson and Brener, 2005):

$$\frac{F_\mathrm{max}(v)}{F_\mathrm{max}(v_\mathrm{c} \to 0)} = \left(\frac{\mathcal{G}(v)}{\mathcal{G}_0}\right)^m = \left(\frac{E_0}{E_\infty}\right)^m, \tag{3.4}$$

where m is a geometric coefficient. Assuming the pad is a sphere (Fogden and White, 1990; Müser and Persson, 2022, so that $m = 1$), it is hence possible to estimate the normalised strain energy release rate by measuring the normalised pull-off forces.

Accordingly, the relationship between crack speed and peak load was interpreted for each temperature by normalising the peak load by the median adhesive force at the lowest retraction speed $F_0 = 0.085\,\mathrm{mN}$, measured at the slowest retraction speed of $10\,\mu\mathrm{m/s}$ at 25°C. This ensured that the first data point was above unity, so that it could be fitted by a power law on the logarithmic scale.

Barquins et al. related the force F and displacement d for a spherical indenter of radius R and loading system of stiffness k_m retracting at speed v_r from a vicsoelastic material whose strain energy release rate is parametrised as a function of type (3.3). Using the *Johnson-Kendall-Roberts* (*JKR*) theory of contact for elastic solids (Barquins and Maugis, 1981; Johnson, 1985), relating the load and displacement of a sphere in contact with an elastic half-space as:

$$\delta = \frac{a^2}{3R} + \frac{2F}{3aK}, \tag{3.5}$$

where a is the contact radius between the indenter and the material and $K = \frac{4E}{3(1-\nu^2)}$ is a constant for an elastic material of *Young*'s modulus E and *Poisson* ratio ν. The associated strain energy release rate, or simply work of adhesion in the case of an

elastic material is (Barquins and Maugis, 1981; Johnson, 1985):

$$\mathcal{G} = \frac{(a^3K/R - F)^2}{6\pi a^3 K} \tag{3.6}$$

At equilibrium and under an applied force F_0, the contact radius a_0 takes the shape (Barquins and Maugis, 1981; Johnson et al., 1971):

$$a_0 = \left\{ \frac{F_0 R}{K} \left[1 + \frac{3\pi \mathcal{G}_0 R}{F_0} + \left(\frac{6\pi \mathcal{G}_0 R}{F_0} + \left(\frac{3\pi \mathcal{G}_0 R}{F_0} \right)^2 \right)^{1/2} \right] \right\}^{1/3} \tag{3.7}$$

Inserting Equation (3.3) into (3.6) provides a contact theory for viscoelastic solids following the power law described above. The time derivatives of Equations (3.5), (3.6), and (3.7) therefore link the contact force F to the strain energy release rate and the crack speed through:

$$\frac{\mathrm{d}F}{\mathrm{d}t} = \frac{3K}{2} \left(\delta \frac{\mathrm{d}a}{\mathrm{d}t} + a \frac{\mathrm{d}\delta}{\mathrm{d}t} - \frac{a^2}{R} \frac{\mathrm{d}a}{\mathrm{d}t} \right), \tag{3.8}$$

$$\frac{\mathrm{d}\delta}{\mathrm{d}t} = \frac{2k_m}{2k_m + 3aK} \left[v_\mathrm{r} - \frac{3K}{2k_m} \left(\delta - \frac{a^2}{R} \right) \frac{\mathrm{d}a}{\mathrm{d}t} \right], \tag{3.9}$$

$$\frac{\mathrm{d}a}{\mathrm{d}t} = -v^\star \left(\frac{3a^3 K}{8\pi R^2 a_T \mathcal{G}_0} \left[1 - \frac{\delta R}{a^2} \right]^2 - \frac{1}{a_T} \right)^{1/n}. \tag{3.10}$$

This system of equations can be solved numerically, and provides a prediction for the relationship between force, displacement and contact area during the detachment of a viscoelastic material (Barquins and Maugis, 1981; Maugis and Barquins, 1980). Predictions based on the four retraction speeds utilised in this study and a 2 mN preload were calculated for a material whose properties are similar to that of an insect pad ($G_0 = 30\,\mathrm{mJ/m}$, (Labonte and Federle, 2015a), $E_0 = 30\,\mathrm{kPa}$), and a testing machine of stiffness $k_\mathrm{m} = 10\,\mathrm{N/m}$ comparable to our setup and of indenter radius of $R = 500\,\mu\mathrm{m}$. The peak force values obtained with the system of equations described above were normalised by the force obtained at the lowest simulated retraction speed of $10\,\mu\mathrm{m/s}$.

To utilise the full information on insect pads' viscoelastic spectrum, and particularly its temperature dependence, I used a model for viscoelastic tack developed by *Persson*. The latter estimates the viscous losses from first principles, using a quantity representing the source of dissipation of a viscoelastic material: the loss moduli, and particularly

its frequency dependence which I determined in Chapter 2. The dissipative processes in viscoelastic materials have two origins: the first is the local region around the crack tip, which undergoes bond breaking, captured by $\mathcal{G}_0$ (Müser and Persson, 2022; Persson, 2021; Persson et al., 2004; Persson and Brener, 2005). The second relates to the viscous nature of the material, which can dissipate energy far ahead from the crack tip. *Persson* considers an energy balance, equating the energy stored in the material far from the crack tip to the energy required to break bonds near the crack tip (See Müser and Persson, 2022; Persson, 2021; Persson et al., 2004; Persson and Brener, 2005, for detailed calculations). They find:

$$\mathcal{G}(v_\mathrm{c}) = \mathcal{G}_0 \left[1 - \frac{E_0 \frac{2}{\pi} \int_0^{+\infty} \mathcal{R}(\omega) \frac{1}{\omega} \frac{1}{E''(\omega)} \mathrm{d}\omega}{1 + E_0 \frac{2}{\pi} \int_0^{+\infty} \frac{1}{\omega} \frac{1}{E''(\omega)} \mathrm{d}\omega} \right]^{-1}, \tag{3.11}$$

$$\mathcal{R}(\omega) = \frac{\sin(\omega\tau^\star)^2}{\omega\tau^\star}. \tag{3.12}$$

Here, $E_0 = \lim_{\omega\to\infty} E'(\omega)$ is the instantaneous storage modulus, $\tau^\star$ is a characteristic time, approximated as $\tau^\star \approx r/v_\mathrm{c}$, and r is the crack tip radius. Equation (3.12) is an implicit equation for the strain energy release rate, which can be evaluated by assuming that the stress at the crack tip is of the same order as a characteristic yield stress σ_c (Müser and Persson, 2022; Persson, 2021; Persson and Brener, 2005):

$$r = \frac{E_\infty \mathcal{G}}{2\pi\sigma_\mathrm{c}^2}, \tag{3.13}$$

where $E_\infty = \lim_{\omega\to 0} E'(\omega)$ is the equilibrium storage modulus. These equations hence depend on a dimensional parameter σ_c. Since the integrals in Equation (3.12) are highly sensitive to frequency variations, I used a least squares procedures to fit the dynamic modulus of the pads with a one-term *Prony* series of moduli $E_0 = 12.1\,\mathrm{kPa}$, $E_\infty = 38.7\,\mathrm{kPa}$, and time constant $\tau = 13.9\,\mathrm{s}$, together with the *WLF* model temperature dependence determined by the previously calculated factor a_T, yielding (Müser and Persson, 2022; Persson, 2021):

$$E^\star(a_T\omega) = \frac{E_\infty E_0 (1 - i a_T \omega\tau)}{E_0 - i a_T \omega\tau E_\infty} \tag{3.14}$$

and

$$\log_{10} a_T = \frac{-C_1 (T - T_\mathrm{ref})}{C2 + T - T_\mathrm{ref}}, \tag{3.15}$$

for which $C_1 = 1.37$ and $C_2 = 18.12\,\mathrm{K}$. In a previous paper, *Persson et al.* describe a similar model based on the relaxation spectrum of a material rather than its dynamic modulus (Persson and Brener, 2005). They provide an interpolation function for the strain energy release rate at high crack speeds (Persson and Brener, 2005):

$$\mathcal{G}(v_\mathrm{c}) = \mathcal{G}_0 \left(1 + \frac{v_\mathrm{c}}{v_0}\right)^{1/3}. \tag{3.16}$$

The equations described by *Persson et al.* are dependent on a length scale r_0, which is related to the vanishing velocity $v_0 = r_0/(2\pi\tau)$ for which $\mathcal{G} = \mathcal{G}_0$ (Müser and Persson, 2022; Persson, 2021; Persson and Brener, 2005). The distance r_0 is of order 1 nm according to *Persson et al.* (Persson and Tosatti, 2001), but depends strongly on the physical properties of the interface through Equation (3.13). *Ciavarella et al.* estimate this vanishing crack radius to be anywhere between 8 nm and 0.4 mm, depending on the adhesive system (Ciavarella and Papangelo, 2021). I used a vanishing crack propagation speed $v_0 = 4\,\mu\mathrm{m/s}$, lower than the lowest crack speed measured with our data (See Table 3.3). Given the relaxation time of the *Prony* series investigated here, the crack radius becomes $r_0 \approx 350\mu\mathrm{m}$. Assuming $\mathcal{G}_0 \approx 200\,\mathrm{mJ/m}$ for a flat punch (Labonte and Federle, 2015a), the yield stress for this adhesive system becomes $\sigma_\mathrm{c} \approx 1\,\mathrm{kPa}$. These values were arbitrarily determined to ensure that the lowest crack speed encountered in this study tended towards the lowest strain energy release rate $\mathcal{G}(v_0) \to \mathcal{G}_0$.

The average peak forces were normalised by the minimum average peak force found in this study $F_0 = 0.11\,\mathrm{mN}$ for (See Table 3.4). Similarly, data points at different temperatures were normalised by their minimum value. The laws described in Equations (3.12) and (3.13) thus provide powerful and versatile predictive tools for "dry" adhesion, which can be directly compared to the adhesion measurements presented in this work.

3.3.3 Statistical Methods

All numbers are represented as mean ± standard deviation (std) unless otherwise indicated. Effects of temperature, crack speed and retraction speed were analysed via a two-way repeated measure analysis of variance (ANOVA) in *R* (version 3.6.3 R Core Team, 2020). The goodness of fit for viscoelastic tackiness models was determined by calculating the Root Mean Squared Error (RMSE), because alternative metrics such as R^2 cannot be used as goodness of fit metrics for non-linear relations. All curves were fitted using a least squares procedure, as part of *Python*'s *scipy* toolbox, utilising

a Trust Region Reflective algorithm (Van Rossum and Drake, 2009; Virtanen et al., 2020).

3.4 Results

3.4.1 Contact Radius and Adhesive Force

During detachment, the contact radius a extracted from the processed contact area videos decreased from its maximum value $a_{\max}$, until it reached a minimum value $a_{\min}$ at which pull-off has occurred (See Figure 3.3A). The corresponding force curves followed an inverse trend; the force F increased from the imposed preload (measured in the negatives) until it crossed the zero line. It then reaches a peak, after which detachment proceeds increasingly rapidly, at which point forces switched from compressive to tensile. The rate of change of both the force and contact radius scaled with the retraction speed (See Figure 3.3B, and Table 3.2).

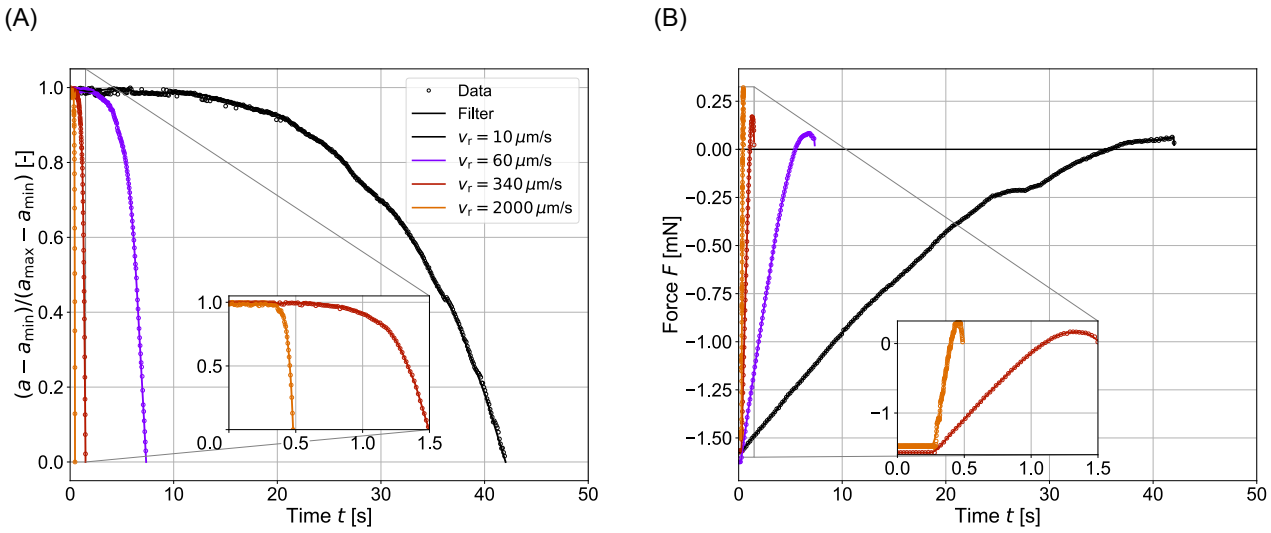


Figure 3.3 (A) The contact radius was extracted from the video recordings and filtered with a LOWESS algorithm. At high retraction speeds v_r, the contact radius decreases in a faster manner than for low speeds. (B) The corresponding peak forces, filtered with a *Butterworth* filter, show an increase with increasing retraction speeds. The same colour coding is used for both figures, and the raw data was downsampled for visualisation purposes.

The peak adhesive forces $F_{\max}$ increased significantly with the retraction speed at all temperatures, with no significant effect of temperature or its interaction with

the retraction speed (See Figure 3.4A and Table 3.1). The crack speed increased significantly with retraction speed, from a minimum value of 7, to a maximum of 500 μm/s, but temperature and its interaction with the retraction velocity were not found to be significant (See Figure 3.4B and Table 3.2).

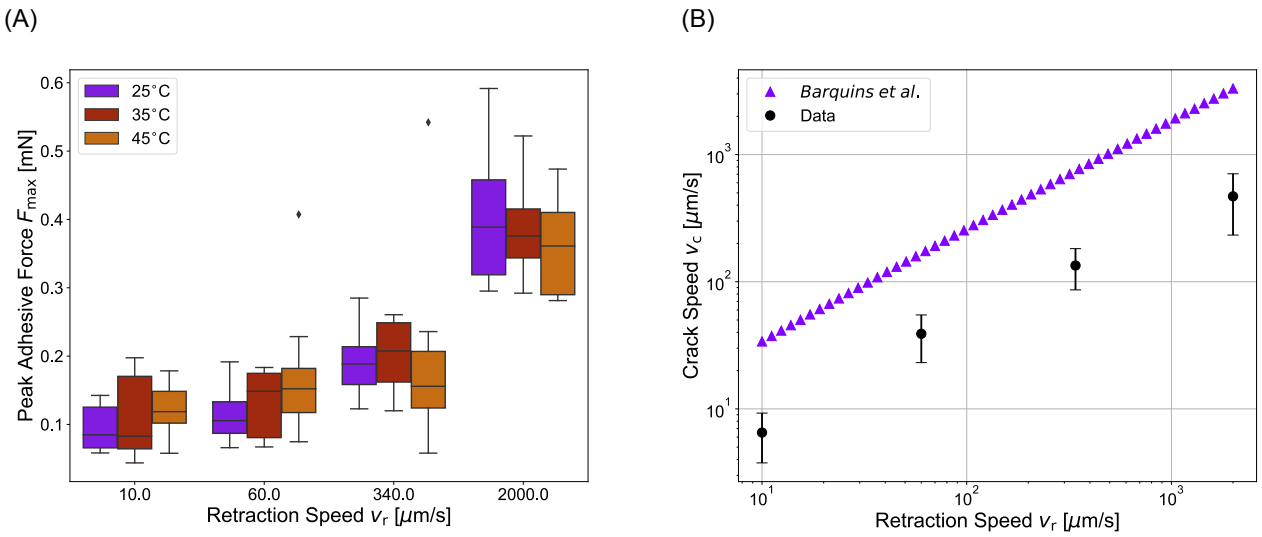


Figure 3.4 (A) The peak adhesive forces measured for insect pads increased with increasing retraction speeds, but temperature had no significant effect (See Tables 3.1 and 3.2). (B) The crack speed scaled with the retraction speeds and varied by two orders of magnitude (black disks). The corresponding relationship between retraction and crack speeds was shifted compared to the prediction from Equation (3.10)

Predictor	d.f.	Sum Sq.	Mean Sq.	F	p
Crack Speed	1	0.8954	0.8854	110.85	$< 0.001^{***}$
Temperature	2	0.0012	0.0006	0.07	0.93
Crack Speed * Temperature	2	0.0159	0.0079	0.99	0.37
Residuals	105	0.8387	0.008		

Table 3.1 A two-way repeated measures ANOVA was performed to analyse the effect of crack speed and temperature on the peak adhesive force. The forces significantly increased with the crack propagation velocity, while the temperature of the coverslips had no significant effect. The interaction of the two independent variables had no significant effect.

Predictor	d.f.	Sum Sq.	Mean Sq.	F	p
Retraction Speed	3	4041946	1347315	100.597	< 0.001***
Temperature	2	4831	2416	0.180	0.835
Retraction Speed * Temperature	6	4626	771	0.058	0.999
Residuals	99	1325923	13393		

Table 3.2 A two-way repeated measures ANOVA was performed to analyse the effect of retraction speed and temperature on the crack speed measured at the maximum adhesive force. The retraction velocity had a statistically significant effect, while the temperature of the coverslips had no significant effect. The interaction of the two independent variables had no significant effect.

3.4.2 A Simple Parametric Model

The resulting maximum force ratio from Equation (3.4) was 4.5 ± 0.93. At all temperatures, the maximum adhesive force followed a power law (Equation (3.3)) with coefficients in the $0.46 - 0.83$ range (See Figure 3.5). Since temperature had no significant effect, the peak adhesive forces and the crack velocities were averaged to obtain unique values per retraction speed (See Table 3.3). The same power law was fitted to the averaged data (See Table 3.4 for the Root Mean Squared Error), providing the relationship between the strain energy release rate and the crack speed as:

$$\mathcal{G}(v_\mathrm{c}) = \mathcal{G}_0 \left[1 + \left(\frac{v_\mathrm{c}}{69.7\,\mu\mathrm{m/s}}\right)^{0.58}\right]. \tag{3.17}$$

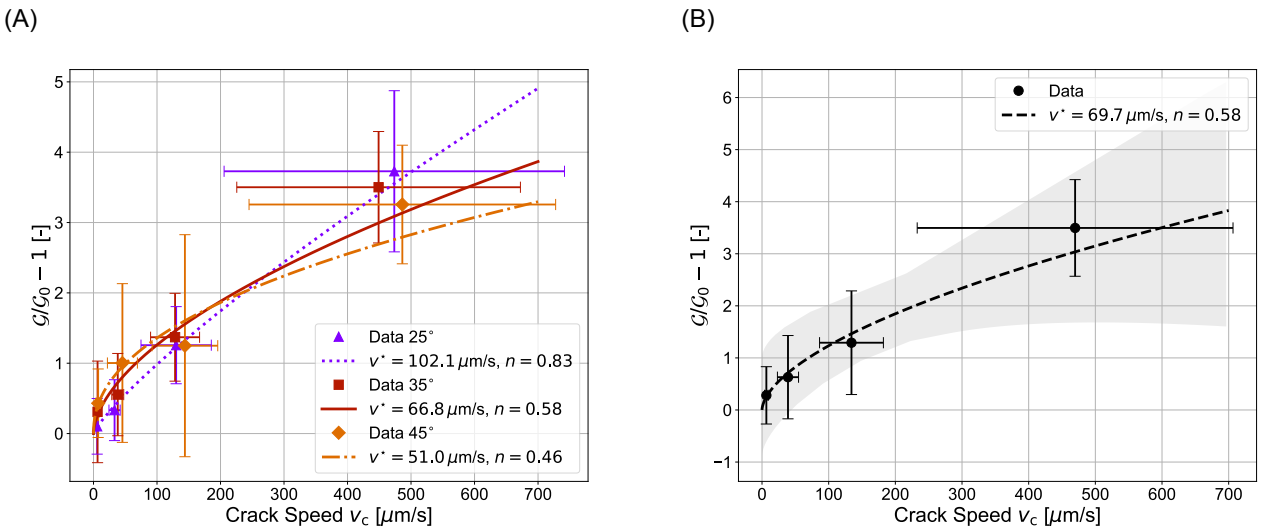


Figure 3.5 (A) The peak adhesive forces were normalised by the median peak force for the lowest retraction speed at 25°, and converted to strain energy release rate ratio $\mathcal{G}/\mathcal{G}_0$ through Equation (3.4). This ratio was fitted with a power law for each temperature, yielding exponents n in the 0.46-0.83 range. (B) Since temperature did not have an effect on the peak adhesive forces, a power law was fitted through the ratio's average per retraction speed. The 95% confidence intervals are indicated in grey.

Retraction Speed v_r [μm/s]	Crack Speed v_c [μm/s]	Peak Adhesive Force F_{max} [mN]
10	6.51 ± 2.75	0.11 ± 0.05
60	38.96 ± 15.85	0.13 ± 0.07
340	134.19 ± 47.88	0.19 ± 0.08
2000	469.64 ± 236.86	0.38 ± 0.08

Table 3.3 Summary table of the measured crack speed v_c and the peak adhesive force F_{max} for different retraction speeds v_r. Both the adhesive force and the crack speed increase with the retraction speed.

3.4.3 Contact Theory

The relation expressed in Equation (3.17) was inserted into a predictive model for the load profiles provided by *Barquins et al.* (See Equation (3.10) and *Barquins et al.* for complete derivations Barquins and Maugis, 1981). The force and contact radius predictions were compared to data collected for insect pads (See Figure 3.6A and B). Predicted peak forces were in close agreement for low crack speeds, but tended to be overestimated at the higher speeds. To further clarify this difference, I extracted

the crack speed corresponding to the maximum retraction speed, and found it to be consistently higher than that measured for insect pads at the time of maximum adhesive force $t_{\max}$ (See Figure 3.6C). This difference results in a shifted strain energy release rate, for which the crack speeds are overestimated, especially at high retraction speed (See Figure 3.4B and Figure 3.6D).

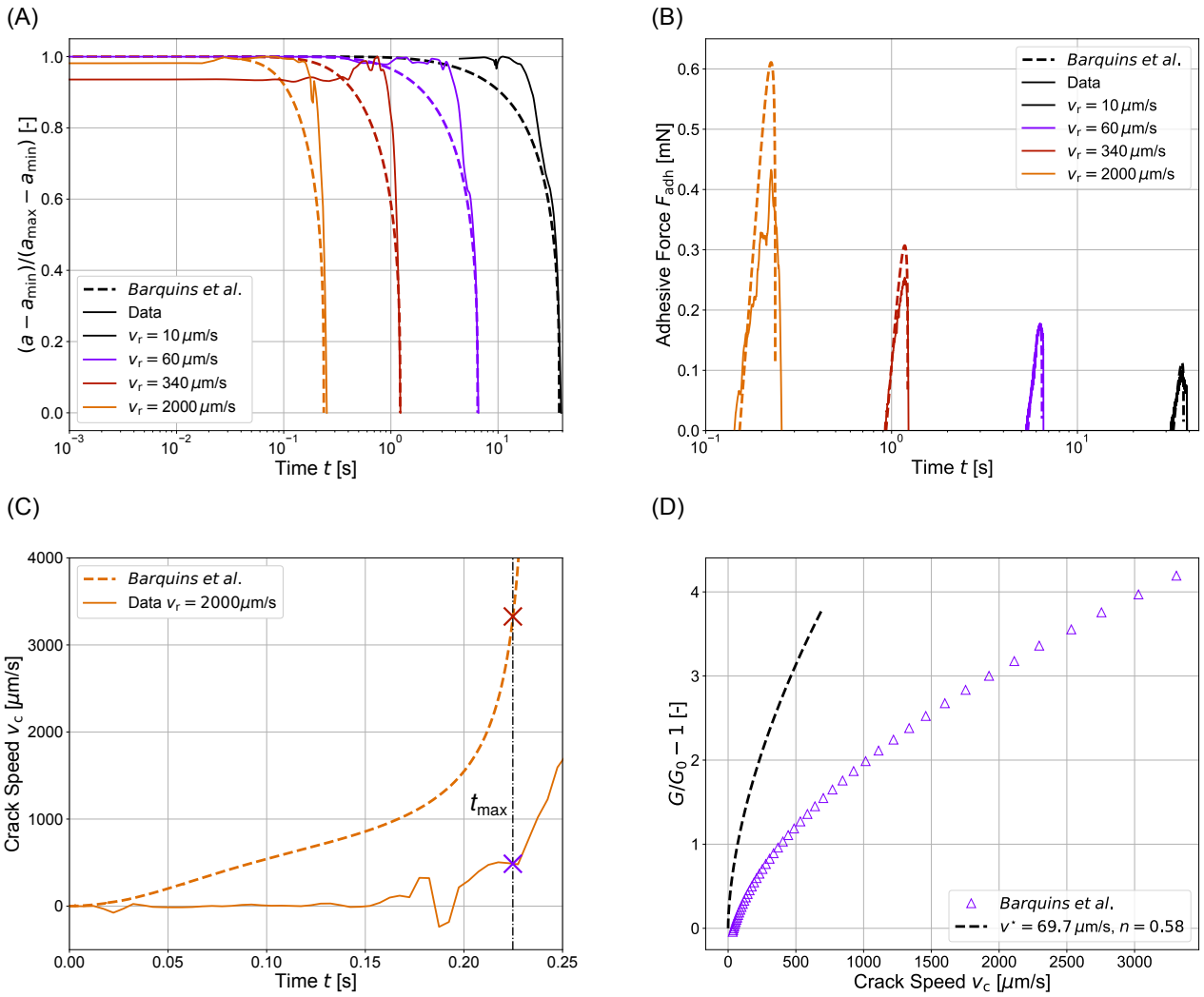


Figure 3.6 The theory established by *Barquins et al.* allowed predicting the tackiness of a sphere of modulus $E_0 = 30\,\text{kPa}$, whose strain energy release rate follows a power law determined in Equation (3.17). (A) The normalised contact radius approximates (dashed lines) the data for insect pads (full lines) well. (B) The peak loads were well approximated by the theory towards low retraction speeds, and slightly underestimated at higher speeds. (C) The crack speed sharply increases for the *Barquins et al.* model, resulting in higher crack speeds at the time of peak force $v_c(t_{max})$, represented on the figure by the crosses and the dashed dotted line. (D) This resulted in a shifted strain energy release rate, where the peak loads are comparable for similar retraction speed, but the crack speeds exceed those anticipated by Equation (3.17).

3.4.4 Viscoelastic Tackiness

The viscoelastic tackiness model by *Persson* was used to calculate the dependence of the strain energy release rate on crack velocity and temperature, using a one-term *Prony* series, fitted on the dynamic modulus identified in Chapter 2 (See Figure 3.7A). The strain energy release rate was thus calculated for crack speeds in the 10^{-4}-$10^{6}\mu$m/s range, for three temperatures 25, 35 and 45°C. The predictive curves are close to the normalised data points, for which the maximum force ratio from Equation (3.4) was 3.51 ± 0.72. The strain energy release rate is underestimated for the highest velocity measured in this study (See Figure 3.7B). The scaling law for high crack speeds from Equation (3.16) is in fact considerably closer to the high speed data (See Table for the RMSE of all models 3.4).

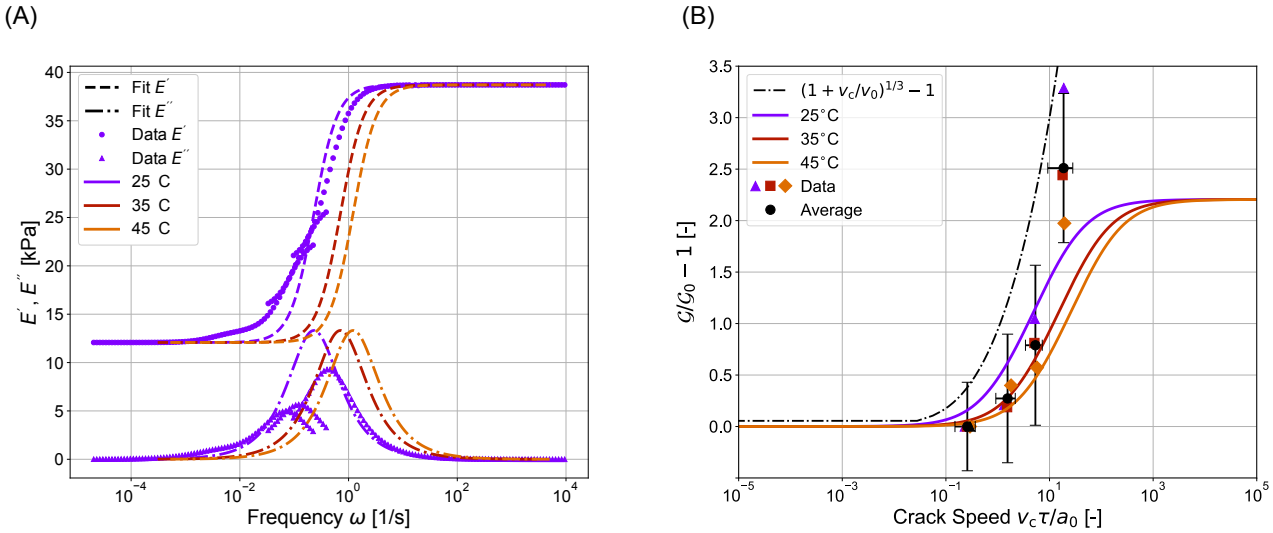


Figure 3.7 (A) The dynamic modulus estimated in Chapter 2 (disks and triangles) was fitted with a one-term *Prony* series (dashed and dash dotted lines, Equation (3.14)), together with its associated temperature shift governed by the previously determined *WLF* factor a_T (3.15). (B) The resulting dynamic modulus at different temperatures was integrated according to Equation (3.12), choosing $v_0 = 4\,\mu$m/s. A prediction for the normalised strain energy release rate $\mathcal{G}/\mathcal{G}_0 - 1$ was obtained (full lines) and compared to the data collected for insect pads and their average (symbols). All force values were normalised by the lowest measured peak force, to ensure $\mathcal{G} \to \mathcal{G}_0$ for $v_c \to v_0$. An additional predictive law was calculated for high speeds (dash dotted black line), following Equation (3.16).

Law	Parameters	Data	RMSE [-]
$\mathcal{G} = \mathcal{G}_0 \left[1 + \left(\frac{v_c}{v^\star}\right)^n\right]$	$v^\star$ =69.7 μm/s n =0.58	• Averaged	0.25
Persson model – Equation (3.12)	a_T(25°C)	▲ 25°C	0.83
		• Averaged	0.49
	a_T(35°C)	■ 35°C	0.63
		• Averaged	0.65
	a_T(45°C)	◆ 45°C	0.51
		• Averaged	0.79
$\mathcal{G} = \mathcal{G}_0 \left(1 + \frac{v_c}{v_0}\right)^{1/3}$	$v_0 = 7\,\mu$m/s	• Averaged	1.13

Table 3.4 Summary table of the Root Mean Squared Error (RMSE) comparing the strain energy release rate values for data at all temperatures and their average to the different predictive laws used in this work.

3.5 Discussion

The determination of the physical properties of the secretion and the pad in Chapters 1 and 2 allowed the writing of "wet" and "dry" adhesion models, together with their variation with rate and temperature. In this final chapter, I measured the forces the pads of Indian stick insects produce *in vivo* and compared them to three models for viscoelastic tackiness, in the hopes of answering the key question surrounding insect adhesion: Do insects use a "wet" or a "dry" adhesive system.

3.5.1 Magnitude of the Measured Forces and Their Rate Dependence

The adhesive forces measured in this study fall within the same range as those previously measured for stick insects of similar sizes (Labonte and Federle, 2015a; Labonte et al., 2019). *Labonte et al.* measured the rate dependence of adhesive forces at room temperature, and the force and contact radius profiles were similar to those presented above, with a maximum peak load in the 0.1-0.6 mN range, and crack speeds ranging from 8 to 1500 μm/s (Labonte and Federle, 2015a). Despite the similarities in the contact radii profiles, the upper range of crack speeds determined in this study is slightly lower than the values reported by *Labonte et al.* for the same retraction speeds. This discrepancy can be explained by the stiffness of their cantilever beam, which was

2-3 times stiffer than the one I used here, presumably resulting in less beam deflection, and a faster peeling rate of the pad from the substrate. A stiffer beam is however preferable, as inertial effects of the cantilever could result in more pronounced adhesive peaks, especially at high retraction speeds. However, these effects were overshadowed by vibration noise generated by the 3D stage's motors, which which was considerably higher than any inertial effect. Furthermore, such oscillation noise was significantly reduced up until the last instant of contact between the pad and the coverslip, as a closed mechanical loop was maintained between the load cell, the pad, and the glass slide.

3.5.2 The Effect of Temperature

Temperature had no significant effect, neither on the magnitude of the adhesive forces, nor on the relation between crack speed and retraction speed. Much like for the contact angles and the surface tension of the secretion, as well as for the shift in the viscoelastic functions, a weak influence of temperature on the forces insects are capable of producing is biologically advantageous. Insects are presumably capable of adhering to surfaces spanning a range of temperatures typically encountered in nature (Colinet et al., 2015; Stark et al., 2018) with unaffected contact areas and dynamics of peeling. At first glance, it may be tempting to use the results in this chapter to question the role the secretion's viscosity plays on insects's attachment abilities, since as detailed in Chapter 1, it is exponentially dependent on temperature. One could argue that the weak temperature dependence of the capillary forces is in good agreement with the forces measured here, but capillary forces are rate independent by nature. These first insights must be treated carefully, and before making any conclusions on the function of the secretion, a rigorous analysis of the viscoelastic models detailed above must be carried out.

The insects considered in this work were all adults and had similar body mass, but several studies have focussed on the effects of scale on insect adhesion (Gorb et al., 2001; Kaimaki et al., 2022; Labonte and Federle, 2015b; Labonte et al., 2019). An insect's mass m will typically scale with its volume, or equivalently with the cube of a characteristic length L: $m \propto L^3$. The pad surface area A available to sustain such mass scales with the square of said length: $A \propto L^2$. Thus, the larger the insect, the larger the adhesive strength per surface area σ required to maintain a constant "safety factor". Similarly, insects of decreasing size face the inverse issue, where σ must

decrease or else they might get stuck on surfaces they attach to, as the adhesive force their pads produce will significantly exceed their body weight (Labonte and Federle, 2015b; Labonte et al., 2019). *Labonte et al.* demonstrated that shear forces are crucial in achieving size-independent scaling, where stick insects use the sliding motion of their pad to make up for the predicted adhesive performance loss as body size increases (Labonte et al., 2019). In light of the data presented in this study, it is thus likely that insects of different sizes use similar mechanisms to produce strong and controllable adhesive forces across temperatures by utilising friction-controlled adhesion. The exact scaling of friction forces at different temperature however goes beyond the goal of this study, and thus constitutes an interesting future avenue to explore the temperature and size (in)dependence of adhesion at the microscopic scale.

3.5.3 An Empirical Power Law is Consistent with Detachment Dynamics

The power law dictating the rate dependence of the strain energy release rate fits the data well (See Figure 3.5 and Table 3.4). *Labonte et al.* used the same fitting function, and found a characteristic velocity in the $37 < v^\star < 136\,\mu$m/s range, with an associated power coefficient $0.49 < n < 0.77$. The measurements presented here are in excellent agreement with these parameters at all temperatures, where I found $51 < v^\star < 102\,\mu$m/s and $0.46 < n < 0.83$. It must be noted that the variation in these factors stems from the temperature range explored in this study, while the estimate provided by *Labonte et al.* was based on two models (flat punch and spherical indenter). After verifying the insignificance of temperature on the measured forces, the fitting coefficients became $v^\star = 69.7$ and $n = 0.58$. These values, similarly to *Labonte et al.*, are in agreement with those typically found for soft elastomers, for which $n \approx 0.6$ (Ahn and Shull, 1998; Barquins and Maugis, 1981; Feng et al., 2007; Labonte and Federle, 2015a; Maugis and Barquins, 1980; Shull, 2002). Following the reasoning detailed by *Labonte et al.*, the coefficient n acts as a source of dissipation in the material, where a typical elastic behaviour with a constant strain energy release rate is obtained for $n = 0$ (Labonte and Federle, 2015a). The magnitude of said dissipation, still according to *Labonte et al.*, is modulated by the factor $v^\star$ (Labonte and Federle, 2015a). One may expect from a linear viscoelastic solid a decrease in the characteristic velocity $v^\star$ with increasing temperatures (Lakes, 2009). Observing the fitted power laws at different temperatures, this trend is existent, albeit statistically insignificant. Overall,

the power law utilised in this study seems to capture accurately the behaviour of the viscoelastic pads.

3.5.4 Contact Theory Predicts the Pull-off Forces

Predictive laws for the strain energy release rate are particularly useful when trying to determine the exact dynamics of a material's tackiness. The system of equations described by *Barquins et al.* allows predicting the contact radius, crack speed, and force profiles of a viscoelastic material being pulled off a stiff substrate by means of a cantilever beam indenter. These equations only require assumptions about the geometry and material properties of the system – namely, the pad is assumed to be a sphere, and a spring constant is attributed to the cantilever – as well as a specific shape of the strain energy release rate (Barquins and Maugis, 1981; Maugis and Barquins, 1980). Using the power law in Equation (3.17) provides load and contact radius curves that match those obtained for insect pads, at least for low retraction speeds. At higher speeds, the peak loads are overestimated ($P_{\max} = 0.6\,\mathrm{mN}$ from simulations, versus $P_{\max} = 0.38 \pm 0.08\,\mathrm{mN}$ for insect pads). This discrepancy likely arises from the difference in the derivative of the simulated contact radius at all times, which corresponds to the crack speed (See Figure 3.6C). At peak adhesion, the crack speed predicted from theory exceeds the experimentally observed speed at least by a factor of two (See Figure 3.4B). This discrepancy is seemingly the result of assuming that the pad – which has a bean shape – resembles a sphere. When being peeled off a substrate, spheres presumably exhibit a much faster rate of decrease of the contact area than a flatter geometry due to their convexity. When estimating the strain energy release rate from the peak adhesive forces obtained with the *Barquins et al.* model, the overestimation of the crack speeds leads to a horizontal dilation of the curves (See Figure 3.6D). All things considered, the *Barquins et al.* model reasonably predicts peak adhesive forces, but is perhaps not well suited to represent the dynamics of separation for non-spherical geometries.

3.5.5 Viscoelastic Tackiness Predicts Rate and Temperature Effects

Persson's theory is developed from first principles and thus does not require the use of empirical approximations. According to this predictive model, the range of values the strain energy release rate can take during crack opening is bound by the viscoelastic

ratio: $E_0/E_\infty = \mathcal{G}(v_c \to \infty)/\mathcal{G}_0$, which for insect pads is $E_0/E_\infty = 3.2$ (See Chapter 2). Thus, when determining the theoretical adhesive bounds of a viscoelastic material, the low and high frequency behaviour of its dynamic modulus approximated by a *Prony* series are of higher relative importance than the time constants governing the frequency transition. The ratio between the strain energy release rate at low and high speeds was 3.51 ± 0.72, close to the viscoelastic ratio of the pad $E_0/E_\infty = 3.2$. The strain energy release rate predictions using a one-term *Prony* series in Equation (3.12) thus approximate the data for insect pads well (See Figure 3.7 and Table 3.4).

Over the investigated range, increasing temperatures induce shifts of the strain energy release rate towards higher crack speeds, modulated by the *WLF* factor a_T determined in Chapter 2. The relatively minor range of these transitions suggests that the magnitude of $\mathcal{G}$ (or equivalently, the adhesive force produced by a pad) does not drastically change. Similarly, the crack speeds at which the strain energy release rate reaches a value greater than $\mathcal{G}_0$ might be lower for higher temperatures. This trend was not observed in the data presented here, however the strain energy release rate ratio $\mathcal{G}(v_c \to \infty)/\mathcal{G}_0 = 3.51 \pm 0.72$ calculated for insect pads has a standard deviation of comparable magnitude to the predicted shift resulting from changing temperatures (See Figure 3.7B). In fact, this standard deviation is also of similar order of magnitude as the RMSEs obtained for the *Persson* model investigated here. Thus, the weak temperature dependence this model predicts is likely not represented in the natural variation of the peak adhesive forces measured in this study.

It must be noted the strain energy release rate at the highest crack speed is underestimated by the viscoelastic tackiness model (See Figure 3.7B). Nonetheless, this discrepancy is again within the bounds of the standard deviation of $\mathcal{G}(v_c \to \infty)/\mathcal{G}_0$. The data collected on insect pads was also compared to a less recent theory from *Persson et al.* (Persson and Brener, 2005). The latter was written considering the spectral density of a viscoelastic material following the *Rouse* model (Doi and Edwards, 1986; Persson and Brener, 2005), and predicts the high-speed behaviour of $\mathcal{G}$ (Persson, 2021; Persson and Brener, 2005). This model fits the high crack speed data well, with a total RMSE slightly higher to the those obtained for the power law and *Persson*'s most recent theory (See Table 3.4). This earlier theory, however, must be treated carefully for finite adhesive systems. Specifically, *Ciavarella et al.* discuss in recent literature the first theory developed by *Persson et al.*, and particularly the *controversial** topic

*Their words, not mine!

of relative interface dimensions (Ciavarella and Papangelo, 2021; Persson and Brener, 2005). In fact, for a viscoelastic adhesive system of finite thickness L (Roughly 500-1000 μm for insect pads Bennemann et al., 2014), a deviation from theory at high crack speeds is expected for low values of the L/a_0 ratio. The latter is of order 10^{-1} for the adhesive system considered here, thus violating the infinite half-space assumption made by *Persson et al.* in their 2005 paper (Ciavarella and Papangelo, 2021; Persson and Brener, 2005). Fortunately, *Persson*'s most recent theory (Equation (3.12), from their 2021 paper) does not suffer from such limitations, since according to the authors, the strain energy release rate model for a finite material is equivalent to the semi-infinite case (Ciavarella and Papangelo, 2021; Persson, 2021).

Altogether, *Persson*'s viscoelastic model, as well as the other models of viscoelastic tackiness presented above, not only provide a reasonable approximation of the adhesive performance of insect pads; they also allow predicting the dynamics of detachment of said pads, over multiple retraction velocities and temperatures.

3.5.6 Wet or Dry Adhesion? The Functional Significance of the Pad Secretion

From the data presented herein, and their good agreement with the multiple models presented above, I suggest that the viscoelasticity of the pad is likely to be at the origin of reversible surface attachment in insects. I put forward "dry" models as a valid interpretation of the observed forces arising from insects's pads for two reasons: the rate dependence of the adhesive forces, and their weak variation with temperature. While viscous forces arising from fluid-film deformation would also be rate dependent, the lack of significant – or even further, exponential – temperature variation of the single pad adhesive forces exclude viscosity as a main effect. Surface tension and contact angle on the other hand are relatively stable over the 20-50°C temperature range, but since capillary forces are static by nature, they cannot be invoked to explain the rate dependence of the strain energy release rate observed in this study (See Chapter 1). In fact, the consistencies of single pad force measurements with "dry" models is not enough to draw conclusions on the main mechanism of adhesion. It is rather the inconsistency of "wet" models with rate dependence and stability over biological temperatures that is key in casting doubt over their significance.

Nonetheless, despite the statistical insignificance of the effect of temperature, it is insightful to observe the difference between the strain energy release rate at different temperatures towards higher crack speeds. In fact, the peak adhesive forces obtained with the highest retraction speed considered in this study present the most substantial changes with temperature (See Figure 3.7). Considering the sharp decrease of the secretion's viscosity with increasing temperatures, and the rate dependence of viscous forces explored in Chapter 1, it would be natural for the highest viscous forces to occur at the highest retraction speeds and at the lowest temperatures. The viscosity might thus give rise to an additional force contribution to the overall adhesive performance of the pad, with the viscoelastic tack as the main contributor to adhesion. While a decrease in viscous forces is consistent with increasing temperatures, so is the model for viscoelastic tackiness described above (Barquins and Maugis, 1981; Bates, 1976; Counsell and Whitehouse, 1977). In fact, increasing temperatures horizontally shift the strain energy release rate, resulting in higher crack speeds at equal energy (See Figure 3.7). This phenomenon might seem counter-intuitive, but finds its origin in the region around the crack tip, which dissipates less energy as temperature increases (Barquins and Maugis, 1981; Bates, 1976; Counsell and Whitehouse, 1977). As a result, a greater proportion of "useful" energy is utilised to break bonds at the interface, resulting in a lower tack force (Barquins and Maugis, 1981; Bates, 1976; Counsell and Whitehouse, 1977). This effect is however weak, since the range of possible values for the normalised strain energy release rate is bound by the material's viscoelastic ratio (Persson, 2021). Using *Persson*'s viscoelastic tack model (Equation (3.12)) for a constant crack speed ($v_c = 129\,\mu$m/s, the second highest measured in this study, see Table 3.3), and the *WLF* shift factor a_T established in Chapter 2, I estimate the relative decrease in the strain energy release to be around 30% over the 25-45°C temperature range, a value comparable to the standard deviation of the force measurements presented here (See Figure 3.8). On the other hand, the exponential decrease of the viscosity coefficient with temperature is more significant; Using the exponential law and activation energy determined in Chapter 1, I predict a decrease of 80% for the viscous forces over the temperature range investigated in this study (See Figure 3.8). The modes of variation of viscous and viscoelastic effects with temperature are hence distinct. Viscoelastic tackiness thus seems to be a better fitting explanation for the weak temperature dependence of the adhesive forces, where the increasing temperatures result in changes below the standard deviation of the forces measured here.

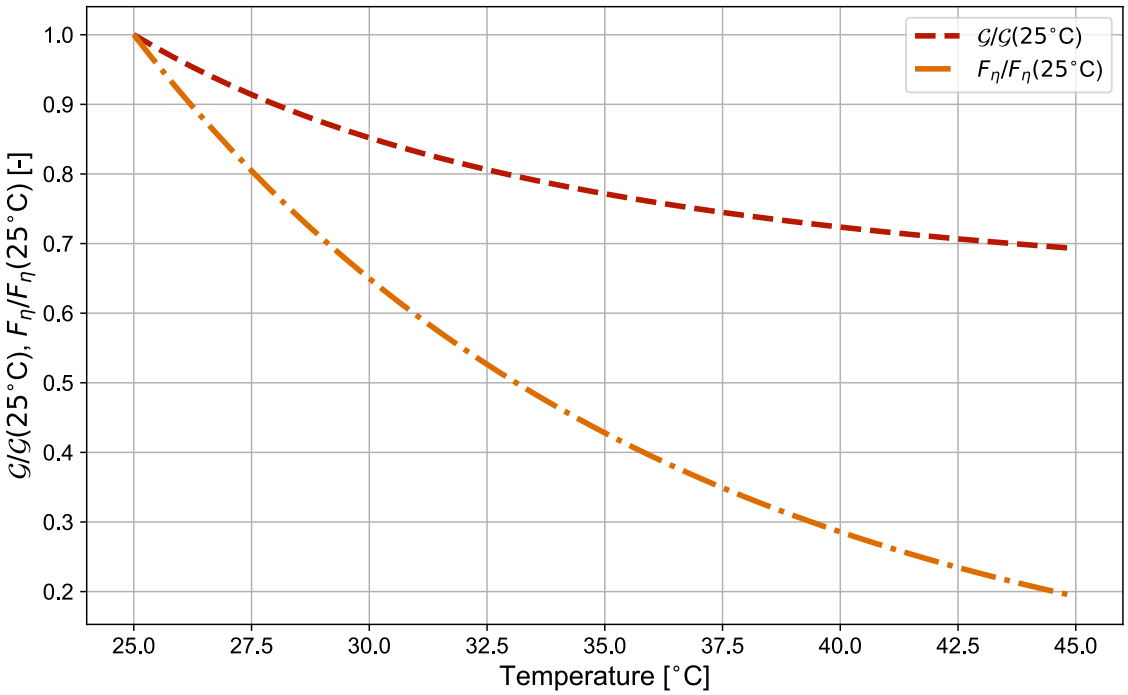


Figure 3.8 The viscous force (F_η) induced by the secretion and the viscoelastic tack induced by the pad (expressed through its strain energy release rate $\mathcal{G}$) should both decrease with increasing temperatures. I used *Persson*'s viscoelastic tack model (Equation (3.12)), and the *WLF* shift factor a_T established in Chapter 2 to estimate the magnitude of the decrease in the viscoelastic forces over the 25-45°C temperature range (dashed line) at a crack speed of $v_c = 129\,\mu$m/s. The viscous forces induced by the secretion follow a exponential decrease with temperature, as determined in Chapter 1. The extent of this decrease over the same temperature range (dash dotted line) is thus more consequential than the decrease in the viscoelastic tack.

These considerations highlight an important element of discussion: Typically, contacts are never fully wet or dry, but are rather dependent on the proportion of dry to wet contact. Boundary lubrication regimes such as elasto-hydrodynamic lubrication (EHL) or even visco-elasto-hydrodynamic lubrication (VEHL) are well established in the literature, and allow insights into the contribution of the liquid film and its temperature dependence (Dowson and Higginson, 1977; Lugt and Morales-Espejel, 2011; Putignano and Dini, 2017; Wu et al., 2020). Typically, a higher sliding velocity results in an decrease in dry contacts, until hydrodynamic lubrication governs friction completely (Israelachvili, 1992; Putignano and Dini, 2017). Recent work by *Putignano*

et al. tackled the problem of friction in a liquid mediated contact on a viscoelastic solid, and found that varying the time constants used to parametrise the viscoelastic material changes the shape of the corresponding *Stribeck* curve (Putignano and Dini, 2017). In fact, viscoelastic materials add dissipation to frictional systems, and the transition to higher forces can be obtained at lower velocities than for a traditional elastic solid (Putignano and Dini, 2017).

Incidentally, frictional forces during pad sliding can be also explained by "dry" adhesion. *Labonte et al.* interpreted the sliding process of a viscoelastic material as the simultaneous opening and closing of cracks in the sliding plane as the pad is displaced (Labonte and Federle, 2015a). The energy required to create or break bonds over a characteristic molecular distance corresponds to an advancing and receding strain energy release rate, which have different magnitudes (Labonte and Federle, 2015a; Persson, 2021). This hysteresis is hence a source of dry sliding friction, and *Labonte et al.* argue that since the energy required by sliding pads depends on a molecular distance, friction can be considerably larger than adhesion which scales with a much larger contact radius.

Hence, the role of the secretion might not be to directly contribute to adhesion or friction. Instead, following the reasoning detailed by *Labonte et al.*, the secretion's viscosity might be so high that the thin film is clamped during detachment, allowing most of the deformation to occur within the pad (Labonte and Federle, 2015a). The authors also suggested that the secretion might act as a "release layer", providing segmental mobility to the region around the crack tip, where dry contacts typically rupture (Ahn and Shull, 1998; Labonte and Federle, 2015a). The presence of a secretion covering insects's pads is in fact unlikely to be coincidental, and might serve multiple other functions. The mechanical properties of the pad, and in particular its viscoelasticity, appear to be crucial to an insect's adhesion capacities. Since the mechanical properties of insect cuticle are majorly influenced by their hydration (Klocke and Schmitz, 2011), the primary function of the secretion might thus be to act as a protective layer, providing resistance to evaporation (a crucial issue for animals with a large area to volume ratio Abou et al., 2010), as well as self-cleaning properties (Clemente et al., 2010; Federle, 2006). In fact, such functions are desirable for the entirety of an insect's body, which might be the reason tarsal secretions have not been found to significantly differ from the lipid layer found on the rest of insects's bodies (Geiselhardt et al., 2011, 2010, 2009; Speidel et al., 2017; Votsch et al., 2002).

The viscoelastic models presented here, combined with the capillary and viscous models described in previous chapters, thus constitute a powerful set of predictive tools, which allow simplifying a complex interface into its key components and their different dependencies on external parameters such as rate and temperature.

Concluding Remarks

During the course of this thesis, I discussed findings regarding insect adhesion dating back almost 200 years. This is how long insects's capabilities have amazed scientists and engineers, who have attempted to provide a physical explanation to the performance of their adhesive system. Given the environmental constraints they face, insects require a versatile and robust adhesive system. In addition to strong attachment, fast detachment is also indispensable in the daily life of an insect. With these constraints and considerations in mind, I investigated the liquid properties of the secretion found under their pads, and the mechanical properties of the material they are made of using state of the art microtechnological investigative techniques. Perhaps more consequentially than determining the magnitude of these physical properties, determining their variation with respect to rate and temperature proved to be an essential and missing piece of information to answering a centuries old question. Towards the end of this thesis, I measured *in vivo* adhesive forces produced by insects, and compared them with the predictive models built from the knowledge of the secretion's surface tension, contact angle, viscosity, the pad's viscoelastic functions, and their variance (and invariance) with the two key parameters discussed throughout.

To conclude on these findings, I find it interesting to follow a reverse train of thought than that presented in this thesis. Beginning from estimating the forces insects are capable of producing, their weak variation with temperature is a quite striking observation. Biologically speaking, it is reasonable for a living organism to benefit from an attachment system which has been optimised to operating under the conditions it typically encounters. However, the observed rate dependence of the adhesive forces produced by insects could at first glance tell a different story: By their nature, the two sources of rate dependence considered in this interface are viscosity and viscoelasticity, both well documented to be influenced by temperature. If insects's adhesive organs are not hindered by temperature changes, the question evolves from wondering which part of the interface is influenced by temperature, to determining how significant this influence is.

The results presented here indicated that the viscosity of the secretion is exponentially affected by temperature. If insects truly made use of the rheological behaviour of their pad's secretion, one would expect adhesive forces to also vary exponentially. Such a dependence on environmental factors would be a significantly detrimental feature of an adhesive system which some insects need to rely on through daily temperature changes. The surface tension of the secretion did not suffer from such pronounced variability, and proved to excel at wetting all surfaces considered in this work. The wetting properties of the secretion even predicted affinity on a large range of natural surfaces, due to the dispersive nature of the surface tension. However, the latter lacks a key aspect discussed above and throughout this thesis: controllability. Capillary forces are by nature static, and unless the contacting area, contact angle, or surface tension of the liquid can be rapidly changed, they are not likely to be responsible for the astonishing striding paces insects are capable of.

This brings us to the viscoelastic properties of the pad, which according to my results, are a plausible mechanism for producing controllable adhesive forces. The storage and loss moduli of the pad were affected by rate, changing by almost an order of magnitude over short frequency ranges. They also followed a weak *Williams-Landel-Ferry* model, and were hence weakly affected by temperature, and consequently so was the energy required to propagate a crack at the interface between the pad and a substrate on which it sticks. Much like the adhesive forces investigated in this study, the magnitude of the change in the detachment dynamics induced by temperature seems to be lesser than the changes related to time. The latter thus offers a level of control on the bonding strength between pad and substrate over a biologically significant temperature range.

My thesis brought to light different elements of understanding regarding the different components of the stick insect's adhesive system, thus investigating the physical properties of the solid and liquid interfaces composing it. While previous studies had already provided estimates for the contact angle, surface tension, and viscosity of the secretion, their sensitivity to temperature was unclear. My work filled this knowledge gap, while improving the methodology that had been used thus far for reconstructing IRM profiles. Further work on the investigation of the secretion's properties should, in my view, be focused on the two following aspects. First, a complete optical theory capable of reconstructing 2D light intensity profiles of 3D droplets is still missing due to the complexity associated with convex interfaces, the interference between different light polarisations, and multi-reflections across interfaces. Second, in most studies

focused on the mechanical properties of the secretion, its solid lipids were largely ignored (as an illustrative example,in this work, droplets containing solid components were excluded from the data analysis). It is however likely that their mechanical properties are relevant to the rheology of the secretion, and further work should be aimed at assessing their contribution and their occurrence, particularly at lower temperatures. One could, for example, conduct nano-indentation experiments on isolated solid lipids, and consider them as a sparse interface within the secretion.

The viscoelastic properties of the pad had been investigated through nano indentation before, but a complete reconstruction of the dynamic modulus and its shifting behaviour with temperature had, to my knowledge, not been provided. My research employed a state of the art indenter, and combined contact theory and viscoelastic first principles to derive all the relevant viscoelastic functions of the pad. I believe that the scope of this specific aspect of my work is broad, as most indentation systems (including the one used here) provide purely elastic data analysis tools for trapezoidal loading experiments. For viscoelastic materials, dynamic mechanical analysis is often employed to directly measure the storage and loss moduli, but clear technological limitations were found with the sensitivity of closed-loop control for material such as insects's pads, or any soft and tacky materials. Modern indentation tools could thus benefit from including models for linearly viscoelastic materials such as the one described in this work, since they allow reconstructing the dynamic moduli of a material with creep and relaxation experiments. This improvement is of course not limited to the model system studied here, but also ranges across fields and applications.

During the course of my experiments, it became apparent that my analysis of the mechanical properties of the pad could benefit from being expanded to lower temperatures, thus further reaching into the high-frequency behaviour of the pad's material. Similarly, there is a clear interest in expanding the range of forces and control times tested in both creep and relaxation, perhaps further validating the assumption of linear viscoelasticity, or determining under which circumstances it breaks down. Finally, more rigorous TTS models could be considered and applied directly on the creep curves obtained from indentation; those will certainly be a key part of further analyses of the presented data.

The forces produced by single pads had once again been the focus of previous literature, but a comprehensive study of their variation with temperature and rate, together with their correlation with the two aforementioned liquid and solid interfaces is perhaps my

most fundamental contribution to the field. So far, the importance of the viscoelastic properties of the pad had remained speculative, and inconclusive in the discrimination between "wet" and "dry" adhesion models. My thesis shed new light on this question, using a fully custom-built set-up and data analysis tools. Similar to the viscoelastic properties of the pad, it would be valuable to investigate single pad adhesive forces at lower temperatures, in an effort to observe the transition point for low velocities as predicted by *Persson et al.* Furthermore, the fracture mechanics models utilised in this work are relatively recent, but still under constant development and improvement. I look forward to seeing further progress on local crack theories and their variation with scale, and how such models apply to the adhesive system considered here.

While I observed relatively little inter-individual variation across the experiments carried out in my thesis, there are of course many other insect species to be considered. Thus, the most important future consideration is certainly the influence of an insect's size on the secretion's properties, the viscoelasticity of the pad, and the forces it can produce. Scale remains one of the main unanswered questions surrounding insect adhesion, and is likely to be a focal point for understanding how insects of extremely variable sizes are capable of scalable adhesion. Answering this question in turn would enable the development of bio-inspired tools capable of gripping and releasing a wide variety of surfaces.

To conclude, I argue that viscous dissipation interpreted in the context of fracture mechanics offers a viable answer to the old question and source of wonder that is insect adhesion. There are of course other factors to be considered, such as the influence of shear forces and the proportion of wet versus dry contact under an insect's pad, but I maintain that the key role of the secretion might not be to directly aid attachment, but rather to facilitate detachment, as well as to preserve the deformability and time-response of the pad.



My thesis brought together multiple elements of discussion, and investigated a biological system by breaking it down into fundamental physical models, demonstrating that the variation of key parameters with physical factors such as temperature and time is essential in gaining insight into complex interfaces.

I find personal satisfaction in the answer being time. Per the *Deborah* number; All things flow, and all things have an end, at length by the passage of time.

"But he that is infinite has been pleased to decree immutably that all things have an end. Thus my love, which was more fervent than any other love, my love which no resolve, no advice, no evident shame, no risk of danger could ever break or bend, at length by the passage of time diminished of itself, and now has left within my soul that delight which love is wont to grant those who do not adventure too far upon its dark seas."

– *Giovanni Boccaccio, The Decameron.*

References

Abou, B., Cyprien, G., Bastien, L., Olivier, C., Dagmar, V., Henrik, P., and Stanislav, G. (2010). Extensive collection of femtolitre pad secretion droplets in the beetle Leptinotarsa decemlineata allows nanolitre microrheology. *J. R. Soc. Interface*, 7(April):1745–1752.

Adderley, C. (1984). Adhesive Bonding. *Materials and Design*, 9(5):287–293.

Ahn, D. and Shull, K. R. (1998). Effects of methylation and neutralization of carboxylated poly(n-butyl acrylate) on the interfacial and bulk contributions to adhesion. *Langmuir*, 14(13):3637–3645.

Ajami, E. and Aguey-Zinsou, K. F. (2011). Formation of OTS self-assembled monolayers at chemically treated titanium surfaces. *Journal of Materials Science: Materials in Medicine*, 22(8):1813–1824.

Arzoumanidis, G. A. and Liechti, K. M. (2003). Linear viscoelastic property measurement and its significance for some nonlinear viscoelasticity models. *Mechanics Time-Dependent Materials*, 7(3-4):209–250.

Asbeck, A. T., Kim, S., Cutkosky, M. R., Provancher, W. R., and Lanzetta, M. (2006). Scaling hard vertical surfaces with compliant microspine arrays. *International Journal of Robotics Research*, 25(12):1165–1179.

Attipoe, A. E. (2018). *Microrheology of sub-nanolitre samples : Study and characterisation of Insect adhesive secretions*. Master's thesis, Université de Liège.

Autumn, K., Sitti, M., Liang, Y. A., Peattie, A. M., Hansen, W. R., Sponberg, S., Kenny, T. W., Fearing, R., Israelachvili, J. N., and Full, R. J. (2002). Evidence for van der Waals adhesion in gecko setae. *PNAS*, 99(19):12252–12256.

Bae, J. E., Cho, K. S., Seo, K. H., and Kang, D. G. (2011). Application of geometric algorithm of time-temperature superposition to linear viscoelasticity of rubber compounds. *Korea Australia Rheology Journal*, 23(2):81–87.

Barnes, W. J. P. (2007). Functional Morphology and Design Constraints of Smooth Adhesive Pads Introduction : From Climbing. *MRS Bulletin*, 32:479–485.

Barnes, W. J. P., Oines, C., and Smith, J. M. (2006). Whole animal measurements of shear and adhesive forces in adult tree frogs: Insights into underlying mechanisms

of adhesion obtained from studying the effects of size and scale. *Journal of Comparative Physiology A: Neuroethology, Sensory, Neural, and Behavioral Physiology*, 192(11):1179–1191.

Barnes, W. J. P., Perez Goodwyn, P. J., Nokhbatolfoghahai, M., and Gorb, S. N. (2011). Elastic modulus of tree frog adhesive toe pads. *J Comp Physiol A*, 197:969–978.

Barquins, M. and Maugis, D. (1981). Tackiness of elastomers. *The Journal of Adhesion*, 13:53–65.

Bates, R. (1976). Studies in the Nature of Adhesive Tack. *Journal of Applied Polymer Science*, 20:2941–2954.

Baumgart, L., Wittke, M., Morsbach, S., Abou, B., and Menzel, F. (2022). Why do ants differ in acclimatory ability? Biophysical mechanisms behind cuticular hydrocarbon acclimation across species. *The Journal of experimental biology*, 225(16).

Beauregard, B. (2021). Arduino PID Library (pid_v2).

Bennemann, M., Backhaus, S., Scholz, I., Park, D., and Mayer, J. (2014). Determination of the Young ' s modulus of the epicuticle of the smooth adhesive organs of Carausius morosus using tensile testing. *The Journal of Experimental Biology*, 217:3677–3687.

Bennemann, M., Scholz, I., and Baumgartner, W. (2011). Functional morphology of the adhesive organs of stick insects (Carausius morosus). *Bioinspiration, Biomimetics, and Bioreplication*, 7975:79751A.

Berger, O., Battistella, C., Chen, Y., Oktawiec, J., Siwicka, Z. E., Tullman-Ercek, D., Wang, M., and Gianneschi, N. C. (2022). Mussel Adhesive-Inspired Proteomimetic Polymer. *Journal of the American Chemical Society*, 144(10):4383–4392.

Betz, O. (2002). Performance and adaptive value of tarsal morphology in rove beetles of the genus Stenus (Coleoptera, Staphylinidae). *Journal of Experimental Biology*, 205(8):1097–1113.

Betz, O. (2003). Structure of the tarsi in some Stenus species (Coleoptera, Staphylinidae): External morphology, ultrastructure, and tarsal secretion. *Journal of Morphology*, 255(1):24–43.

Betz, O. (2010). *Adhesive Exocrine Glands in Insects: Morphology, Ultrastructure, and Adhesive Secretion.* Springer, Vienna, Vienna, byern, j., edition.

Betz, O., Maurer, A., Verheyden, A. N., Schmitt, C., Kowalik, T., Braun, J., Grunwald, I., Hartwig, A., and Neuenfeldt, M. (2016). First protein and peptide characterization of the tarsal adhesive secretions in the desert locust, Schistocerca gregaria, and the Madagascar hissing cockroach, Gromphadorhina portentosa. *Insect molecular biology*, 25(5):541–549.

Beutel, R. G. and Gorb, S. N. (2001). Ultrastructure of attachment specializations of hexapods (Arthropoda): Evolutionary patterns inferred from a revised ordinal phylogeny. *Journal of Zoological Systematics and Evolutionary Research*, 39(4):177–207.

Birkhead, T., Lee, K., and Young, P. (1987). Downloaded from Brill.com11/09/2020 12:08:38PM via free access. *Behaviour*, 106:112–118.

Bitter, R., Mohiuddin, T., and Nawrocki, M. (2007). *LabView: Advanced Programming Techniques*. CRC Press, Boca Raton, 2nd editio edition.

Blackwall, J. (1833). Letter adressed to the secretary. *Extracts from the Minute-Book of the Linnean Society*, 21:767.

Blumm, J. and Lindemann, A. (2013). Characterization of the thermophysical properties of molten polymers and liquids using the flash technique. *High Temperatures - High Pressures*, 35-36(6):627–632.

Bohn, H., Thornham, G. D. T., and Federle, W. (2012). Ants swimming in pitcher plants : kinematics of aquatic and terrestrial locomotion in Camponotus schmitzi. *J Comp Physiol A*, 198(6):465–476.

Brugnara, M. (2004). Contact Angle.

Bullock, J. M. and Federle, W. (2011a). The effect of surface roughness on claw and adhesive hair performance in the dock beetle Gastrophysa viridula. *Insect Science*, 18(3):298–304.

Bullock, J. M. R., Drechsler, P., and Federle, W. (2008). Comparison of smooth and hairy attachment pads in insects : friction , adhesion and mechanisms for direction-dependence. *The Journal of Experimental Biology*, 211:3333–3343.

Bullock, J. M. R. and Federle, W. (2009). Division of labour and sex differences between fibrillar , tarsal adhesive pads in beetles : effective elastic modulus and attachment performance. *The Journal of Experimental Biology*, (212):1876–1888.

Bullock, J. M. R. and Federle, W. (2011b). Beetle adhesive hairs differ in stiffness and stickiness : in vivo adhesion measurements on individual setae. *Naturwissenschaften*, 98:381–387.

Burack, J., Gorb, S. N., and Büscher, T. H. (2022). Attachment Performance of Stick Insects (Phasmatodea) on Plant Leaves with Different Surface Characteristics. *Insects*, 13(10).

Büscher, T. H., Becker, M., and Gorb, S. N. (2020). Attachment performance of stick insects (Phasmatodea) on convex substrates. *Journal of Experimental Biology*, 223(17).

Büscher, T. H., Buckley, T. R., Grohmann, C., Gorb, S. N., and Bradler, S. (2018). The evolution of tarsal adhesive microstructures in stick and leaf insects (Phasmatodea). *Frontiers in Ecology and Evolution*, 6(MAY):1–11.

Bush, A. W., Gibson, R. D., and Thomas, T. R. (1975). The elastic contact of a rough surface. *Wear*, 35(1):87–111.

Butler, M., Box, F., Robert, T., and Vella, D. (2019). Elasto-capillary adhesion: The effect of deformability on adhesion strength and detachment. *Phys. Rev. Fluids*, 4:033601.

Butt, H. J., Barnes, W. J. P., Del Campo, A., Kappl, M., and Schönfeld, F. (2010). Capillary forces between soft, elastic spheres. *Soft Matter*, 6(23):5930–5936.

Byern, J. and Grunwald, I. (2010). *Biological Adhesive Systems: From Nature to Technical and Medical Application*. Springer, Vienna, Vienna.

Cassie, A. and Baxter, S. (1944). Wettability of porous surfaces. *Transaction of the Faraday Society*, 40:546–551.

Chan, R. W. (2001). Estimation of viscoelastic shear properties of vocal-fold tissues based on time–temperature superposition. *The Journal of the Acoustical Society of America*, 110(3):1548–1561.

Chan, T. S. and Carlson, A. (2019). Physics of adhesive organs in animals. *Eur. Phys. J. Special Topics*, 227:2501–2512.

Chang, E. P. (1997). Viscoelastic properties of pressure-sensitive adhesives. *Journal of Adhesion*, 60(1-4):233–248.

Cho, H., Wu, G., Jolly, J. C., Fortoul, N., He, Z., Gao, Y., Jagota, A., and Yang, S. (2019). Intrinsically reversible superglues via shape adaptation inspired by snail epiphragm. *Proceedings of the National Academy of Sciences of the United States of America*, 116(28):13774–13779.

Ciavarella, M. and Papangelo, A. (2021). Effects of finite thickness on crack propagation in viscoelastic materials. *Engineering Fracture Mechanics*, 248(January):107703.

Clemente, C. J., Bullock, J. M., Beale, A., and Federle, W. (2010). Evidence for self-cleaning in fluid-based smooth and hairy adhesive systems of insects. *Journal of Experimental Biology*, 213(4):635–642.

Clemente, C. J. and Federle, W. (2008). Pushing versus pulling: Division of labour between tarsal attachment pads in cockroaches. *Proceedings of the Royal Society B: Biological Sciences*, 275(1640):1329–1336.

Clemente, C. J. and Federle, W. (2012). Mechanisms of self-cleaning in fluid-based smooth adhesive pads of insects. *Bioinspiration and Biomimetics*, 7(4).

Cohen, S. R. and Kalfon-Cohen, E. (2013). Dynamic nanoindentation by instrumented nanoindentation and force microscopy: A comparative review. *Beilstein Journal of Nanotechnology*, 4(1):815–833.

Colinet, H., Sinclair, B. J., Vernon, P., and Renault, D. (2015). Insects in fluctuating thermal environments. *Annual Review of Entomology*, 60:123–140.

Contreras-naranjo, J. C., Silas, J. A., and Ugaz, V. M. (2010). Reflection interference contrast microscopy of arbitrary convex surfaces. *Applied Optics*, 49(19):3701–3712.

Costa, M. F. P. and Ribeiro, C. (2011). Parameter estimation of viscoelastic materials: A test case with different optimization strategies. *AIP Conference Proceedings*, 1389:771–774.

Counsell, P. and Whitehouse, R. (1977). *Developments in Adhesives*. Appl. Sci. Publ. Ltd, London, UK, vol. 1 edition.

Coupland, J. M. and Lobera, J. (2010). Measurement of Steep Surfaces Using White Light Interferometry. *Strain*, 46(1):69–78.

Creton, C. (2003). Pressure-Sensitive Adhesives : An Introductory Course. *MRS Bulletin*, 28(6):434–439.

Creton, C. and Leibler, L. (1996). How does tack depend on time of contact and contact pressure? *Journal of Polymer Science, Part B: Polymer Physics*, 34(3):545–554.

Cruse, H. and Bartling, C. (1995). Movement of joint angles in the legs of a walking insect, Carausius morosus. *Journal of Insect Physiology*, 41(9):761–771.

Curro, J. G. and Salazar, E. A. (1975). Physical and chemical stress relaxation of elastomers. *Journal of Applied Polymer Science*, 19(9):2571–2581.

Dahlquist, C. A. (1966). *Adhesion Fundamentals and Practice,*. McLaren and Sons Ltd., London, UK.

Dai, Z., Gorb, S. N., and Schwarz, U. (2002). Roughness-dependent friction force of the tarsal claw system in the beetle Pachnoda marginata (Coleoptera, Scarabaeidae). *Journal of Experimental Biology*, 205(16):2479–2488.

Darwin, C. (1859). *On the Origin of Species by Means of Natural Selection, or the Preservation of Favoured Races in the Struggle for Life*. John Murray, London.

de Gennes, P.-G., Brochard-Wyart, F., and Quere, D. (2003). *Capillarity and Wetting Phenomena*. Springer, New York.

de Sinéty, R. (1901). *Recherches sur la Biologie et l'Anatomie des Phasmes*. Joseph Van In & Cie, Lierre.

Devarajan, K. (2016). The antsy social network: Determinants of nest structure and arrangement in Asian weaver ants. *PLoS ONE*, 11(6):1–15.

Diaz, M. E., Savage, M. D., and Cerro, R. L. (2017). The effect of temperature on contact angles and wetting transitions for n-alkanes on PTFE. *Journal of Colloid and Interface Science*, 503:159–167.

Dirks, J.-H. (2009). *Mechanisms of fluid-based adhesion in insects*. Ph.d thesis, University of Cambridge.

Dirks, J.-H. (2014). Physical principles of fluid-mediated insect attachment - Shouldn't insects slip? *Beilstein J. Nanotechnol.*, 5:1160–1166.

Dirks, J. H., Clemente, C. J., and Federle, W. (2010). Insect tricks: Two-phasic foot pad secretion prevents slipping. *Journal of the Royal Society Interface*, 7(45):587–593.

Dirks, J. H. and Federle, W. (2011a). Fluid-based adhesion in insects - Principles and challenges. *Soft Matter*, 7(23):11047–11053.

Dirks, J.-h. and Federle, W. (2011b). Mechanisms of fluid production in smooth adhesive pads of insects. *J. R. Soc. Interface*, 8:952–960.

Dixon, A. F. G., Croghan, P., and Gowing, R. (1990). The mechanism by which aphids adhere to smooth surfaces. *J Exp Biol*, 152:243–253.

Doi, M. and Edwards, S. (1986). *The Theory of Polymer Dynamics*. Oxford University Press, Oxford, UK.

Dowson, D. and Higginson, G. (1977). *Elasto-hydrodynamic Lubrication*. Pergamon Press, Oxford, UK, si edition edition.

Drechsler, P. and Federle, W. (2006). Biomechanics of smooth adhesive pads in insects : influence of tarsal secretion on attachment performance. *J Comp Physiol A*, 192:1213–1222.

Eimüller, T., Guttmann, P., and Gorb, S. N. (2008). Terminal contact elements of insect attachment devices studied by transmission X-ray microscopy. *Journal of Experimental Biology*, 211(12):1958–1963.

Eisner, T. and Aneshansley, D. J. (2000). Defense by foot adhesion in a beetle (Hemisphaerota cyanea). *Proceedings of the National Academy of Sciences of the United States of America*, 97(12):6568–6573.

Emerson, S. B. and Diehl, D. (1980). Toe pad morphology and mechanisms of sticking in frogs. *Biological Journal of the Linnean Society*, 13(3):199–216.

Endlein, T. and Federle, W. (2008). Walking on smooth or rough ground: Passive control of pretarsal attachment in ants. *Journal of Comparative Physiology A: Neuroethology, Sensory, Neural, and Behavioral Physiology*, 194(1):49–60.

Endlein, T. and Federle, W. (2013). Rapid preflexes in smooth adhesive pads of insects prevent sudden detachment. *Proceedings of the Royal Society B: Biological Sciences*, 280(1757):1–5.

Endlein, T. and Federle, W. (2015). On heels and toes: How ants climb with adhesive pads and tarsal friction hair arrays. *PLoS ONE*, 10(11):1–16.

Endlein, T., Ji, A., Samuel, D., Yao, N., Wang, Z., Jon, W., Federle, W., Kappl, M., and Dai, Z. (2013). Sticking like sticky tape: Tree frogs use friction forces to enhance attachment on overhanging surfaces. *Journal of the Royal Society Interface*, 10(80).

Eötvös, R. (1886). Ueber den Zusammenhang der Oberflächenspannung der Flüssigkeiten mit ihrem Molecularvolumen. *Annalen Der Physik Und Chemie*, 263(3):448–459.

Fasina, O. O., Hallman, H., Craig-Schmidt, M., and Clements, C. (2006). Predicting temperature-dependence viscosity of vegetable oils from fatty acid composition. *JAOCS, Journal of the American Oil Chemists' Society*, 83(10):899–903.

Favi, P. M. F., Yi, S. Y., Lenaghan, S. C., Xia, L., and Zhang, M. (2014). Inspiration from the natural world : From bio-adhesives to bio-inspired adhesives. *Journal ofAdhesion Science and Technology*, 28:290–319.

Féat, A., Federle, W., Kamperman, M., and van der Gucht, J. (2019). Coatings preventing insect adhesion: An overview. *Progress in Organic Coatings*, 134(March):349–359.

Federle, W. (2006). Why are so many adhesive pads hairy ? *The Journal of Experimental Biology*, 209:2611–2621.

Federle, W., Barnes, W. J. P., Baumgartner, W., Drechsler, P., and Smith, J. M. (2006). Wet but not slippery : boundary friction in tree frog adhesive toe pads. *J. R. Soc. Interface*, 3(May):689–697.

Federle, W., Baumgartner, W., and Hölldobler, B. (2004). Biomechanics of ant adhesive pads : frictional forces are rate- and temperature- dependent. *The Journal of Experimental Biology*, 206:67–74.

Federle, W. and Labonte, D. (2019). Dynamic biological adhesion: Mechanisms for controlling attachment during locomotion. *Philosophical Transactions of the Royal Society B: Biological Sciences*, 374(1784).

Federle, W., Riehle, M., Curtis, A. S., and Full, R. J. (2002). An Integrative Study of Insect Adhesion: Mechanics and Wet Adhesion of Pretarsal Pads in Ants. *Integrative and Comparative Biology*, 42(6):1100–1106.

Feng, X., Meitl, M. A., Bowen, A. M., Huang, Y., Nuzzo, R. G., and Rogers, J. A. (2007). Competing fracture in kinetically controlled transfer printing. *Langmuir*, 23(25):12555–12560.

Fernández, V. and Khayet, M. (2015). Evaluation of the surface free energy of plant surfaces: Toward standardizing the procedure. *Frontiers in Plant Science*, 6:510.

Fogden, A. and White, L. R. (1990). Contact elasticity in the presence of capillary condensation. I. The nonadhesive Hertz problem. *Journal of Colloid And Interface Science*, 138(2):414–430.

Fowkes, F. M. (1964). Attractive Forces At Interfaces. *Industrial and Engineering Chemistry*, 56(12):40–52.

Gao, H. and Yao, H. (2004). Shape insensitive optimal adhesion of nanoscale fibrillar structures. *Proceedings of the National Academy of Sciences of the United States of America*, 101(21):7851–7856.

Geiselhardt, S. F., Geiselhardt, S., and Peschke, K. (2011). Congruence of epicuticular hydrocarbons and tarsal secretions as a principle in beetles. *Chemoecology*, 21(3):181–186.

Geiselhardt, S. F., Lamm, S., Gack, C., and Peschke, K. (2010). Interaction of liquid epicuticular hydrocarbons and tarsal adhesive secretion in Leptinotarsa decemlineata Say (Coleoptera: Chrysomelidae). *J Comp Physiol A*, 196:369–378.

Geiselhardt, S. F., Sven, G., and Peschke, K. (2009). Comparison of tarsal and cuticular chemistry in the leaf beetle Gastrophysa viridula (Coleoptera: Chrysomelidae) and an evaluation of solid-phase microextraction and solvent extraction techniques. *Chemoecology*, 19:185–193.

Gere, J. (2012). *Mechanics of Materials*. Cengage Learning, Boston, USA, 8th editio edition.

Gerhardt, H., Betz, O., Albert, K., and Lämmerhofer, M. (2016). Insect Adhesion Secretions: Similarities and Dissimilarities in Hydrocarbon Profiles of Tarsi and Corresponding Tibiae. *Journal of Chemical Ecology*, 42(8):725–738.

Gernay, S., Federle, W., Lambert, P., and Gilet, T. (2016). Elasto-capillarity in insect fibrillar adhesion. *Journal of the Royal Society Interface*, 13(121).

Gernay, S. M., Labousse, S., Lambert, P., Compère, P., and Gilet, T. (2017). Multi-scale tarsal adhesion kinematics of freely-walking dock beetles. *Journal of the Royal Society Interface*, 14(136).

Gilet, T., Heepe, L., Lambert, P., Compère, P., and Gorb, S. N. (2018). Liquid secretion and setal compliance: the beetle's winning combination for a robust and reversible adhesion. *Current Opinion in Insect Science*, 30(August):19–25.

Gillett, J. and Wigglesworth, V. (1932). The Climbing Organ of an Insect, Rhodnius prolixus (Hemiptera; Reduviidae). *Proceedings of the Royal Society B: Biological Sciences*, 111:364–376.

Goodman, J. M., Kirby, P. D., and Haustedt, L. O. (2000). Some calculations for organic chemists: Boiling point variation, Boltzmann factors and the Eyring equation. *Tetrahedron Letters*, 41(50):9879–9882.

Gorb, S. (2001). *Attachment Devices of The Insect Cuticle*. Kluwer Academics Publishers.

Gorb, S., Gorb, E., and Kastner, V. (2001). Scale effects on the attachment pads and friction forces in syrphid flies (Diptera, Syrphidae). *Journal of Experimental Biology*, 204(8):1421–1431.

Gorb, S., Jiao, Y., and Scherge, M. (2000). Ultrastructural architecture and mechanical properties of attachment pads in Tettigonia viridissima (Orthoptera Tettigoniidae). *J Comp Physiol A*, 186:821–831.

Gorb, S. N. (1998). The design of the fly adhesive pad: Distal tenent setae are adapted to the delivery of an adhesive secretion. *Proceedings of the Royal Society B: Biological Sciences*, 265(1398):747–752.

Gorb, S. N. (2007). *Smooth Attachment Devices in Insects: Functional Morphology and Biomechanics*, volume 34. Academic Press.

Gorb, S. N., Sinha, M., Peressadko, A., Daltorio, K. A., and Quinn, R. D. (2007). Insects did it first: A micropatterned adhesive tape for robotic applications. *Bioinspiration and Biomimetics*, 2(4).

Gravish, N., Wilkinson, M., and Autumn, K. (2008). Frictional and elastic energy in gecko adhesive detachment. *Journal of the Royal Society Interface*, 5(20):339–348.

Greenwood, J. A. and Johnson, K. L. (1981). The mechanics of adhesion of viscoelastic solids. *Philosophical Magazine A: Physics of Condensed Matter, Structure, Defects and Mechanical Properties*, 43(3):697–711.

Greenwood, J. A. and Williamson, J. B. P. (1966). Contact of nominally flat surfaces. *Proceedings of the Royal Society of London. Series A. Mathematical and Physical Sciences*, 295(1442):300–319.

Griffith, A. A. (1921). The phenomena of rupture and flow in solids. *Philosophical Transactions of the Royal Society A*, 221:163–198.

Grimaldi, D. and Engel, M. (2005). *Evolution of the Insects*. Cambridge University Press, Cambridge.

Haj-kacem, R. B., Ouerfelli, N., Herráez, J. V., Guettari, M., Hamda, H., and Dallel, M. (2014). Fluid Phase Equilibria Contribution to modeling the viscosity Arrhenius-type equation for some solvents by statistical correlations analysis. *Fluid Phase Equilibria*, 383:11–20.

Halsch, C. A., Shapiro, A. M., Fordyce, J. A., Nice, C. C., Thorne, J. H., Waetjen, D. P., and Forister, M. L. (2021). Insects and recent climate change. *Proceedings of the National Academy of Sciences of the United States of America*, 118(2):1–9.

Han, L., Yan, L., Wang, K., Fang, L., Zhang, H., Tang, Y., Ding, Y., Weng, L. T., Xu, J., Weng, J., Liu, Y., Ren, F., and Lu, X. (2017). Tough, self-healable and tissue-adhesive hydrogel with tunable multifunctionality. *NPG Asia Materials*, 9(4).

Hanna, G. and Barnes, W. J. (1991). Adhesion and detachment of the toe pads of tree frogs. *Journal of Experimental Biology*, 155:103–125.

Hasenfuss, I. (1999). The adhesive devices in larvae of Lepidoptera (Insecta, Pterygota). *Zoomorphology*, 119(3):143–162.

Herrmann, V., Unseld, K., Fuchs, H.-B., and Blumich, B. (2002). Molecular dynamics of elastomers investigated by DMTA and the NMR-MOUSE. *Colloid Polym Sci*, 280:758–764.

Hertz, H. and Lenard, P. (1896). On the contact of rigid elastic solids and on hardness. In *Miscellaneous Papers*, chapter Chapter VI, pages 163–183. Macmillan, London.

Hirano, D., Tanishima, N., Bylard, A., and Chen, T. G. (2020). Underactuated Gecko Adhesive Gripper for Simple and Versatile Grasp. *Proceedings - IEEE International Conference on Robotics and Automation*, pages 8964–8969.

Horcas, I., Fernández, R., Gómez-Rodríguez, J. M., Colchero, J., Gómez-Herrero, J., and Baro, A. M. (2007). WSXM: A software for scanning probe microscopy and a tool for nanotechnology. *Review of Scientific Instruments*, 78(1).

Horowitz, P. and Hill, W. (2015). *The Art of Electronics*. Cambridge University Press, Cambridge, 3rd editio edition.

Hosoda, N., Nakamoto, M., Suga, T., and Gorb, S. N. (2021). Evidence for intermolecular forces involved in ladybird beetle tarsal setae adhesion. *Scientific Reports*, 11(1):1–9.

Huber, G., Mantz, H., Spolenak, R., Mecke, K., Jacobs, K., Gorb, S. N., and Arzt, E. (2005). Evidence for capillarity contributions to gecko adhesion from single spatula nanomechanical measurements. *Proceedings of the National Academy of Sciences of the United States of America*, 102(45):16293–16296.

Huey, R. B., Crill, W. D., Kingsolver, J. G., and Weber, K. E. (1992). A Method for Rapid Measurement of Heat or Cold Resistance of Small Insects. *Functional Ecology*, 6(4):489.

Hui, C. Y., Lin, Y. Y., and Baney, J. M. (2000). The mechanics of tack: Viscoelastic contact on a rough surface. *Journal of Polymer Science Part B: Polymer Physics*, 38(11):1485–1495.

Hutchings, I. M. (2009). The contributions of David Tabor to the science of indentation hardness. *Journal of Materials Research*, 24(3):581–589.

Iazzolino, A., Cerkvenik, U., Tourtit, Y., Ladang, A., Compère, P., and Gilet, T. (2020). Liquid dispensing in the adhesive hairy pads of dock beetles. *Journal of the Royal Society Interface*, 17(166).

Islam, M. R. and Oyen, M. L. (2021). A poroelastic master curve for time-dependent and multiscale mechanics of hydrogels. *Journal of Materials Research*, 36(12):2582–2590.

Israelachvili, J. (1992). Interfacial Forces. *Journal of Vacuum Science and Technology A*, 10(2961):1650–1661.

Jagota, A. and Hui, C. Y. (2011). Adhesion, friction, and compliance of bio-mimetic and bio-inspired structured interfaces. *Materials Science and Engineering R: Reports*, 72(12):253–292.

Janczuk, B., Wojcik, W., and Zdziennicka, A. (1993). Determination of the components of the surface tension of some liquids from interfacial liquid-liquid tension measurements. *Journal of Colloid and Interface Sc*, 157:384–393.

Jiao, Y., Gorb, S., and Scherge, M. (2000). Adhesion measured on the attachment pads of Tettigonia viridissima (Orthoptera, Insecta). *Journal of Experimental Biology*, 203(12):1887–1895.

Johnson, K. L. (1985). *Contact Mechanics*. Cambridge University Press.

Johnson, K. L., Kendall, K., and Roberts, A. D. (1971). Surface Energy and the Contact of Elastic Solids. *Proc. R. Soc. Lond*, 324:301–313.

Jönsson, U., Olofsson, G., Malmqvist, M., and Rönnberg, I. (1985). Chemical vapour deposition of silanes. *Thin Solid Films*, 124(2):117–123.

Kaelble, D. H. (1970). Dispersion-Polar Surface Tension Properties of Organic Solids. *The Journal of Adhesion*, 2(2):66–81.

Kaimaki, D. M., Andrew, C. N., Attipoe, A. E., and Labonte, D. (2022). The physical properties of the stick insect pad secretion are independent of body size. *Journal of the Royal Society, Interface*, 19(191):20220212.

Kaimaki, D. M., Smith, B. E., and Durkan, C. (2018). On the use of nanomechanical atomic force microscopy to characterise oil-exposed surfaces. *RSC Advances*, 8(12):6680–6689.

Kendall, M. D. (1970). The Anatomy of the Tarsi of Schistocerca gregaria Forskål. *Zeitschrift für Zellforschung und Mikroskopische Anatomie*, 109(1):112–137.

Klein, T., Yan, S., Cui, J., Magee, J. W., Kroenlein, K., Rausch, M. H., Koller, T. M., and Fröba, A. P. (2019). Liquid Viscosity and Surface Tension of n-Hexane, n-Octane, n-Decane, and n-Hexadecane up to 573 K by Surface Light Scattering. *Journal of Chemical and Engineering Data*, 64(9):4116–4131.

Klocke, D. and Schmitz, H. (2011). Water as a major modulator of the mechanical properties of insect cuticle. *Acta Biomaterialia*, 7(7):2935–2942.

Koerner, L., Gorb, S. N., and Betz, O. (2012). Functional morphology and adhesive performance of the stick-capture apparatus of the rove beetles Stenus spp. (Coleoptera, Staphylinidae). *Zoology*, 115(2):117–127.

Koller, T. M., Klein, T., Giraudet, C., Chen, J., Kalantar, A., Van Der Laan, G. P., Rausch, M. H., and Fröba, A. P. (2017). Liquid Viscosity and Surface Tension of n-Dodecane, n-Octacosane, Their Mixtures, and a Wax between 323 and 573 K by Surface Light Scattering. *Journal of Chemical and Engineering Data*, 62(10):3319–3333.

Kosaki, A. and Yamaoka, R. (1996). Chemical Composition of Footprints and Cuticula Lipids of Three Species of Lady Beetles. *Japanese Journal of Applied Entomology and Zoology*, 40:47–53.

Krahn, J., Sameoto, D., and Menon, C. (2011). Controllable biomimetic adhesion using embedded phase change material. *Smart Materials and Structures*, 20(1).

Krajina, B. A., Tropini, C., Zhu, A., Digiacomo, P., Sonnenburg, J. L., Heilshorn, S. C., and Spakowitz, A. J. (2017). Dynamic Light Scattering Microrheology Reveals Multiscale Viscoelasticity of Polymer Gels and Precious Biological Materials. *ACS Central Science*, 3(12):1294–1303.

Labonte, D. (2010). *Biomechanics of attachment in insects - The influence of surface energy.* Phd thesis, Hochschule Bremen.

Labonte, D. (2015). *Biomechanics of controllable attachment in insects.* Phd, University of Cambridge.

Labonte, D. and Federle, W. (2013). Functionally Different Pads on the Same Foot Allow Control of Attachment : Stick Insects Have Load-Sensitive " Heel " Pads for Friction and Shear-Sensitive " Toe " Pads for Adhesion. *PLoS ONE*, 8(12).

Labonte, D. and Federle, W. (2015a). Rate-dependence of 'wet' biological adhesives and the function of the pad secretion in insects. *Soft Matter*, 11:8661–8673.

Labonte, D. and Federle, W. (2015b). Scaling and biomechanics of surface attachment in climbing animals. *Philosophical Transactions of the Royal Society B: Biological Sciences*, 370(1661).

Labonte, D. and Federle, W. (2016). Biomechanics of shear-sensitive adhesion in climbing animals : peeling , pre-tension and sliding-induced changes in interface strength. *J. R. Soc. Interface*, 13:20160373.

Labonte, D., Lenz, A.-k., and Oyen, M. L. (2017). Acta Biomaterialia On the relationship between indentation hardness and modulus , and the damage resistance of biological materials. *Acta Biomaterialia*, 57:373–383.

Labonte, D., Struecker, M. Y., Birn-Jeffery, A. V., and Federle, W. (2019). Shear-sensitive adhesion enables size-independent adhesive performance in stick insects. *Proceedings of the Royal Society B: Biological Sciences*, 286(1913).

Labonte, D., Williams, J. A., and Federle, W. (2014). Surface contact and design of fibrillar ' friction pads ' in stick insects (Carausius morosus): mechanisms for large friction coefficients and negligible adhesion. *J. R. Soc. Interface*, 11:20140034.

Lakes, R. (2009). *Viscoelastic Materials*. Cambridge University Press.

Landau, L. D. and Lifshits, E. M. (1987). *Fluid Mechanics*. Pergamon Press, Oxford, second edi edition.

Langer, M. G., Ruppersberg, J. P., and Gorb, S. (2004). Adhesion forces measured at the level of a terminal plate of the fly's seta. *Proceedings of the Royal Society B: Biological Sciences*, 271(1554):2209–2215.

Laplace, P. (1806). Sur l'Action Capillaire. *Journal de Physique*, 63.

Lee, E. H. and Radok, J. R. M. (1960). The Contact Problem for Visooelastiac Bodies. *J. Appl. Mech.*, 27(3):438–444.

Lees, A. and Hardie, J. (1988). The organs of adhesion in the aphid Megoura viciae. *Journal of Experimental Biology*, 136:209–228.

Leong, Y. C., Lee, L. M. S., and Gan, S. N. (2003). The viscoelastic properties of natural rubber pressure-sensitive adhesive using acrylic resin as a tackifier. *Journal of Applied Polymer Science*, 88(8):2118–2123.

Liang, Y., He, J., and Guo, B. (2021). Functional Hydrogels as Wound Dressing to Enhance Wound Healing. *ACS Nano*, 15(8):12687–12722.

López-Guerra, E. A. and Solares, S. D. (2014). Modeling viscoelasticity through spring-dashpot models in intermittent-contact atomic force microscopy. *Beilstein Journal of Nanotechnology*, 5(1):2149–2163.

Lugt, P. M. and Morales-Espejel, G. E. (2011). A review of elasto-hydrodynamic lubrication theory. *Tribology Transactions*, 54(3):470–496.

MacBride, E. and Jackson, A. (1915). The Inheritance o f Colour in the Stick-Insect, Carausius morosus. *Proc. R. Soc. Lond. B*, 89:109–118.

Maginnis, T. L. (2008). Autotomy in a stick insect (Insecta: Phasmida): Predation versus molting. *Florida Entomologist*, 91(1):126–127.

Mann, J. Y., Pell, R. A., Jones, R., and Heller, M. (1985). Reducing the effects of rivet holes on fatigue life by adhesive bonding. *Theoretical and Applied Fracture Mechanics*, 3(2):113–124.

Martina, D., Creton, C., Damman, P., Jeusette, M., and Lindner, A. (2012). Adhesion of soft viscoelastic adhesives on periodic rough surfaces. *Soft Matter*, 8(19):5350–5357.

Mattice, J. M., Lau, A. G., Oyen, M. L., and Kent, R. W. (2006). Spherical indentation load-relaxation of soft biological tissues. *Journal of Materials Research*, 21(8):2003–2010.

Maugis, D. and Barquins, M. (1980). *Fracture Mechanics and Adherence of Viscoelastic Solids In: Lee, LH. (eds) Adhesion and Adsorption of Polymers. Polymer Science and Technology*. Springer, Boston, USA, vol. 12 edition.

McQuarrie, D. A. and Simon, J. D. (2008). *Mathematics for Physical Chemistry.* University Science Books, Sausalito, California.

Menzel, F., Morsbach, S., Martens, J. H., Räder, P., Hadjaje, S., Poizat, M., and Abou, B. (2019). Communication versus waterproofing: The physics of insect cuticular hydrocarbons. *Journal of Experimental Biology*, 22(23).

Messaâdi, A., Dhouibi, N., Hamda, H., Belgacem, F. B. M., Adbelkader, Y. H., Ouerfelli, N., and Hamzaoui, A. H. (2015). A New Equation Relating the Viscosity Arrhenius Temperature and the Activation Energy for Some Newtonian Classical Solvents. *Journal of Chemistry*, 2015:7–10.

Müser, M. H. and Persson, B. N. (2022). Crack and pull-off dynamics of adhesive, viscoelastic solids. *EPL*, 137(3).

Nalam, P. C., Gosvami, N. N., Caporizzo, M. A., Composto, R. J., and Carpick, R. W. (2015). Soft Matter Nano-rheology of hydrogels using direct drive force modulation atomic force microscopy. *Soft Matter*, 11:1–3.

Niederegger, S. and Gorb, S. (2003). Tarsal movements in flies during leg attachment and detachment on a smooth substrate. *Journal of Insect Physiology*, 49(6):611–620.

Nikitin, E. D. and Popov, A. P. (2014). Critical temperatures and pressures of C40, C44, and C60 normal alkanes measured by the pulse-heating technique. *Fluid Phase Equilibria*, 379:191–195.

Owens, D. and Wendt, R. (1969). Estimation of Estimation of. *Journal of Applied Polymer Science*, 13:1741–1747.

Oyen, M. L. (2005). Spherical indentation creep following ramp loading. *J. Mater. Res.*, 20:2094–2100.

Oyen, M. L. (2006). Analytical techniques for indentation of viscoelastic materials. *Philosophical Magazine*, 86:5625–5641 Analytical.

Palit, S. R. (1956). Thermodynamic Interpretation of the Eötvös Constant. *Nature*, 177(4521):1180.

Pandey, N., Soto-Garcia, L., Liao, J., Zimmern, P., and Hong, Y. (2020). Mussel-Inspired Bioadhesives in Healthcare: Design Parameters, Current Trends, and Future Perspectives. *Biomater. Sci.*, 8(5):1240–1255.

Peattie, A. M., Dirks, J. H., Henriques, S., and Federle, W. (2011). Arachnids secrete a fluid over their adhesive pads. *PLoS ONE*, 6(5):2–7.

Peisker, H., Heepe, L., Kovalev, A. E., and Gorb, S. N. (2014). Comparative study of the fluid viscosity in tarsal hairy attachment systems of flies and beetles. *J. R. Soc. Interface*, 11:20140752.

Peisker, H., Michels, J., and Gorb, S. N. (2013). Evidence for a material gradient in the adhesive tarsal setae of the ladybird beetle Coccinella septempunctata. *Nature Communications*, 4:1607–1608.

Perez Goodwyn, P., Peressadko, A., Schwarz, H., Kastner, V., and Gorb, S. (2006). Material structure , stiffness , and adhesion : why attachment pads of the grasshopper (Tettigonia viridissima) adhere more strongly than those of the locust (Locusta migratoria) (Insecta : Orthoptera). *J Comp Physiol A*, pages 1233–1243.

Persson, B. N. (2001). Elastoplastic contact between randomly rough surfaces. *Physical Review Letters*, 87(11):116101–1–116101–4.

Persson, B. N. (2021). A simple model for viscoelastic crack propagation. *European Physical Journal E*, 44(1):1–10.

Persson, B. N., Albohr, O., Creton, C., and Peveri, V. (2004). Contact area between a viscoelastic solid and a hard, randomly rough, substrate. *Journal of Chemical Physics*, 120(18):8779–8793.

Persson, B. N., Albohr, O., Tartaglino, U., Volokitin, A. I., and Tosatti, E. (2005). On the nature of surface roughness with application to contact mechanics, sealing, rubber friction and adhesion. *Journal of Physics Condensed Matter*, 17(1).

Persson, B. N. and Tosatti, E. (2001). The effect of surface roughness on the adhesion of elastic solids. *Journal of Chemical Physics*, 115(12):5597–5610.

Persson, B. N. J. and Brener, E. A. (2005). Crack propagation in viscoelastic solids. *Physical Review E*, 71(January):1–8.

Plum, F. and Labonte, D. (2021). scAnt — An open-source platform for the creation of 3D models of arthropods (and other small objects). *PeerJ*, 9:e11155.

Prowse, M. S., Wilkinson, M., Puthoff, J. B., Mayer, G., and Autumn, K. (2011). Effects of humidity on the mechanical properties of gecko setae. *Acta Biomaterialia*, 7(2):733–738.

Püffel, F., Pouget, A., Liu, X., Zuber, M., Van De Kamp, T., Roces, F., and Labonte, D. (2021). Morphological determinants of bite force capacity in insects: A biomechanical analysis of polymorphic leaf-cutter ants. *Journal of the Royal Society Interface*, 18(182).

Puthoff, J. B., Holbrook, M., Wilkinson, M. J., Jin, K., Pesika, N. S., and Autumn, K. (2013). Dynamic friction in natural and synthetic gecko setal arrays. *Soft Matter*, 9(19):4855–4863.

Puthoff, J. B., Prowse, M. S., Wilkinson, M., and Autumn, K. (2010). Changes in materials properties explain the effects of humidity on gecko adhesion. *Journal of Experimental Biology*, 213(21):3699–3704.

Putignano, C. and Dini, D. (2017). Soft Matter Lubrication: Does Solid Viscoelasticity Matter? *ACS Applied Materials and Interfaces*, 9(48):42287–42295.

Qian, L. and Zhao, H. (2018). Nanoindentation of Soft Biological Materials. *Micromachines*, 9(654).

R Core Team (2020). *R: A Language and Environment for Statistical Computing*. R Foundation for Statistical Computing, Vienna, Austria.

Rajan, S., Sutton, M. A., Fuerte, R., and Emri, I. (2018). Time Temperature Superposition and Prony Series Coefficients of Asphalt Roof Shingle Material from Viscoelastic Creep Testing. *Challenges in Mechanics of Time Dependent Materials*, 2:79–86.

Redon, C., Brochard-Wyart, F., and Rondelez, F. (1991). Dynamics of Dewetting. *Physical Review Letters*, 66(6):715–718.

Reid, C. R., Lutz, M. J., Powell, S., Kao, A. B., Couzin, I. D., and Garnier, S. (2015). Army ants dynamically adjust living bridges in response to a costbenefit trade-off. *Proceedings of the National Academy of Sciences of the United States of America*, 112(49):15113–15118.

Reiter, G. (1993). Unstable Thin Polymer Films : Rupture and Dewetting Processes. *Langmuir*, 9:1344–1351.

Reitz, M., Gerhardt, H., Schmitt, C., Betz, O., Albert, K., and Lämmerhofer, M. (2015). Analytica Chimica Acta Analysis of chemical profiles of insect adhesion secretions by gas chromatography – mass spectrometry. *Analytica Chimica Acta*, 854:47–60.

Romero-Martínez, A. and Trejo, A. (1998). Surface tension of pure hydrocarbons. *International Journal of Thermophysics*, 19(6):1605–1614.

Roth, L. M. and Willis, E. R. (1952). Tarsal structure and climbing ability of cockroaches. *Journal of Experimental Zoology*, 119(3):483–517.

Rudawska, A. and Jacniacka, E. (2009). Analysis for determining surface free energy uncertainty by the Owen-Wendt method. *International Journal of Adhesion and Adhesives*, 29(4):451–457.

Ruotolo, W., Brouwer, D., and Cutkosky, M. R. (2021). From grasping to manipulation with gecko-inspired adhesives on a multifinger gripper. *Science Robotics*, 6(61):1–14.

Sahasrabudhe, S. N., Rodriguez-Martinez, V., O'Meara, M., and Farkas, B. E. (2017). Density, viscosity, and surface tension of five vegetable oils at elevated temperatures: Measurement and modeling. *International Journal of Food Properties*, 20(2):1965–1981.

Sakai, M. (2002). Time-dependent viscoelastic relation between load and penetration for an axisymmetric indenter. *Philosophical Magazine A*, 82(January 2014):1841–1849.

Schindelin, J., Arganda-Carreras, I., Frise, E., Kaynig, V., Longair, M., Pietzsch, T., Preibisch, S., Rueden, C., Saalfeld, S., Schmid, B., Tinevez, J. Y., White, D. J., Hartenstein, V., Eliceiri, K., Tomancak, P., and Cardona, A. (2012). Fiji: An open-source platform for biological-image analysis. *Nature Methods*, 9(7):676–682.

Schmitt, M., Büscher, T. H., Gorb, S. N., and Rajabi, H. (2018). How does a slender tibia resist buckling? Effect of material, structural and geometric characteristics on buckling behaviour of the hindleg tibia in stick insect postembryonic development. *Journal of Experimental Biology*, 221(4).

Scholz, I., Baumgartner, Æ. W., and Federle, W. (2008). Micromechanics of smooth adhesive organs in stick insects : pads are mechanically anisotropic and softer towards the adhesive surface. *J Comp Physiol A*, 194:373–384.

Seabold, S. and Perktold, J. (2010). Statsmodels: Econometric and Statistical Modeling with Python. *Proceedings of the 9th Python in Science Conference*, Scipy 2010:92–96.

Shangguan, Y., Chen, F., Jia, E., Lin, Y., Hu, J., and Zheng, Q. (2017). New insight into Time-Temperature correlation for polymer relaxations ranging from secondary relaxation to terminal flow: Application of a Universal and developed WLF equation. *Polymers*, 9(11).

Shull, K. R. (2002). Contact mechanics and the adhesion of soft solids. *Materials Science and Engineering: R: Reports*, 36(1):1–45.

Sinclair, B. J., Vernon, P., Klok, C. J., and Chown, S. L. (2003). Insects at low temperatures: An ecological perspective. *Trends in Ecology and Evolution*, 18(5):257–262.

Smith, A. M. (2002). The structure and function of adhesive gels from invertebrates. *Integrative and Comparative Biology*, 42(6):1164–1171.

Song, Y., Dai, Z., Wang, Z., Ji, A., and Gorb, S. N. (2016). The synergy between the insect-inspired claws and adhesive pads increases the attachment ability on various rough surfaces. *Scientific Reports*, 6(April):1–9.

Speidel, M. W., Kleemeier, M., Hartwig, A., Rischka, K., Ellermann, A., Daniels, R., and Betz, O. (2017). Structural and tribometric characterization of biomimetically inspired synthetic " insect adhesives ". *Beilstein J. Nanotechnol.*, 8:45–63.

Stark, A. Y., Arstingstall, K., and Yanoviak, S. P. (2018). Adhesive performance of tropical arboreal ants varies with substrate temperature. *Journal of Experimental Biology*, 221(1).

Stark, A. Y., Badge, I., Wucinich, N. A., Sullivan, T. W., Niewiarowski, P. H., and Dhinojwala, A. (2013). Surface wettability plays a significant role in gecko adhesion underwater. *Proceedings of the National Academy of Sciences of the United States of America*, 110(16):6340–6345.

Stark, A. Y. and Yanoviak, S. P. (2018). Adhesion and running speed of a tropical arboreal ant (Cephalotes atratus) on wet substrates. *R. Soc. open sci.*, 5:181540.

Stefan, J. (1875). Versuche über die scheinbare Adhäsion. *Annalen der Physik*, 230(2):161–320.

Stork, N. (1980). A scanning electron microscope study of tarsal adhesive setae in the Coleoptera. *Zoological Journal of the Linnean Society*, 68(3):173–306.

Stork, N. (1983). How does the housefly hold on to your window? *Antenna*, 7:20–23.

Stork, N. (2018). How Many Species of Insects and Other Terrestrial Arthropods Are There on Earth ? *Annual Review of Entomology*, 63:31–45.

Stoukidi, M. (2019). *Temperature-regulated Viscosity Measurements in Stick Insects' Pads Secretions*. Master's thesis, Imperial College London.

Sudersan, P., Kappl, M., Pinchasik, B. E., Butt, H. J., and Endlein, T. (2021). Wetting of the tarsal adhesive fluid determines underwater adhesion in ladybird beetles. *Journal of Experimental Biology*, 224(20).

Tabor, D. (1951). *The Hardness of Metals*. Clarendon Press, Oxford, UK.

Tassieri, M., Laurati, M., Curtis, D. J., Auhl, D. W., Coppola, S., Scalfati, A., Hawkins, K., Williams, P. R., and Cooper, J. M. (2016). i-Rheo: Measuring the materials' linear viscoelastic properties "in a step"! *Journal of Rheology*, 60(4):649–660.

Theodoly, O., Huang, Z. H., and Valignat, M. P. (2010). New modeling of reflection interference contrast microscopy including polarization and numerical aperture effects: Application to nanometric distance measurements and object profile reconstruction. *Langmuir*, 26(3):1940–1948.

Thomson, G. W. (1946). The Antoine Equation for Vapor-Pressure Data. *Chemical Reviews*, 38(1):1–29.

Tóth, T. I. and Daun, S. (2019). A kinematic model of stick-insect walking. *Physiological Reports*, 7(8):1–26.

Uran, S. and Safaric, R. (2017). Reliable and Accurate Release of Micro-Sized Objects with a Gripper that Uses the Capillary-Force Method. *Micromachines*, 8(182).

Van Rossum, G. and Drake, F. L. (2009). *Python 3 Reference Manual*. CreateSpace, Scotts Valley, CA.

Vincent, J. F. V. and Wegst, U. G. K. (2004). Design and mechanical properties of insect cuticle. *Arthropod Structure and Development*, 33:187–199.

Virtanen, P., Gommers, R., Olipha'nt, T. E., Haberland, M., Reddy, T., Cournapeau, D., Burovski, E., Peterson, P., Weckesser, W., Bright, J., van der Walt, S. J., Brett, M., Wilson, J., Millman, K. J., Mayorov, N., Nelson, A. R., Jones, E., Kern, R., Larson, E., Carey, C. J., Polat, I., Feng, Y., Moore, E. W., VanderPlas, J., Laxalde, D., Perktold, J., Cimrman, R., Henriksen, I., Quintero, E. A., Harris, C. R., Archibald, A. M., Ribeiro, A. H., Pedregosa, F., van Mulbregt, P., Vijaykumar, A., Bardelli, A. P., Rothberg, A., Hilboll, A., Kloeckner, A., Scopatz, A., Lee, A., Rokem, A., Woods, C. N., Fulton, C., Masson, C., Häggström, C., Fitzgerald, C., Nicholson, D. A., Hagen, D. R., Pasechnik, D. V., Olivetti, E., Martin, E., Wieser, E., Silva, F., Lenders, F., Wilhelm, F., Young, G., Price, G. A., Ingold, G. L., Allen, G. E., Lee, G. R., Audren, H., Probst, I., Dietrich, J. P., Silterra, J., Webber, J. T., Slavič, J., Nothman, J., Buchner, J., Kulick, J., Schönberger, J. L., de Miranda Cardoso, J. V., Reimer, J., Harrington, J., Rodríguez, J. L. C., Nunez-Iglesias, J., Kuczynski, J., Tritz, K., Thoma, M., Newville, M., Kümmerer, M., Bolingbroke, M., Tartre, M., Pak, M., Smith, N. J., Nowaczyk, N., Shebanov, N., Pavlyk, O., Brodtkorb, P. A., Lee, P., McGibbon, R. T., Feldbauer, R., Lewis, S., Tygier, S., Sievert, S., Vigna, S., Peterson, S., More, S., Pudlik, T., Oshima, T., Pingel, T. J., Robitaille, T. P., Spura, T., Jones, T. R., Cera, T., Leslie, T., Zito, T., Krauss, T., Upadhyay, U., Halchenko, Y. O., and Vázquez-Baeza, Y. (2020). SciPy 1.0: fundamental algorithms for scientific computing in Python. *Nature Methods*, 17(3):261–272.

Voigt, D., Schuppert, J. M., Dattinger, S., and Gorb, S. N. (2008). Sexual dimorphism in the attachment ability of the Colorado potato beetle Leptinotarsa decemlineata (Coleoptera: Chrysomelidae) to rough substrates. *Journal of Insect Physiology*, 54(5):765–776.

Voigt, D., Schuppert, J. M., Dattinger, S., and Gorb, S. N. (2010). Temporary stay at various environmental humidities affects attachment ability of Colorado potato beetles Leptinotarsa decemlineata (Coleoptera, Chrysomelidae). *Journal of Zoology*, 281(4):227–231.

Votsch, W., Nicholson, G., Müller, R., Stierhof, Y.-D., Gorb, S., and Schwarz, U. (2002). Chemical composition of the attachment pad secretion of the locust Locusta migratoria. *Insect Biochemistry and Molecular Biology*, 32:1605–1613.

Walker, G. (1993). Adhesion to smooth surfaces by insects a review. *Int J Adhes Adhes*, 13(1):6–10.

Walker, G., Yulf, A. B., and Ratcliffe, J. (1985). The adhesive organ of the blowfly, Calliphora vomitoria: a functional approach (Diptera: Calliphoridae). *Journal of Zoology*, 205(2):297–307.

Wang, H., Shi, H., Li, Y., and Wang, Y. (2014). The effects of leaf roughness, surface free energy and work of adhesion on leaf water drop adhesion. *PLoS ONE*, 9(9).

Wenzel, R. N. (1936). Resistance of solid surfaces to wetting by water. *Industrial and Engineering Chemistry*, 28:988–994.

West, T. (1862). The Foot of the Fly; Its Structure and Action: elucidated by comparison with the feet of other Insects. *Trans. Linn. Soc. Lond*, 23:393–421.

Wiegand, G., Jaworek, T., Wegner, G., and Sackmann, E. (1997). Studies of Structure and Local Wetting Properties on Heterogeneous, Micropatterned Solid Surfaces by Microinterferometry. *Journal of Colloid and Interface Science*, 196:299–312.

Wiegand, G., Neumaier, K. R., and Sackmann, E. (1998). Microinterferometry: three-dimensional reconstruction of surface microtopography for thin-film and wetting studies by reflection interference contrast microscopy (RICM). *Applied Optics*, 37(29):6892–6905.

Wigglesworth, V. B. (1987). How does a fly cling to the under surface of a glass sheet? *Journal of Experimental Biology*, Vol. 129:373–376.

Williams, M. L., Landel, R. F., and Ferry, J. D. (1955). The Temperature Dependence of Relaxation Mechanisms in Amorphous Polymers and Other Glass-forming Liquids. *Journal of the American Chemical Society*, 77(14):3701–3707.

Wolff, J. O. and Gorb, S. N. (2011). The influence of humidity on the attachment ability of the spider Philodromus dispar (Araneae, Philodromidae). *Proceedings of the Royal Society B: Biological Sciences*, 279(1726):139–143.

Wu, H., Moyle, N., Jagota, A., and Hui, C. Y. (2020). Lubricated steady sliding of a rigid sphere on a soft elastic substrate: Hydrodynamic friction in the Hertz limit. *Soft Matter*, 16(11):2760–2773.

Xu, B., Li, H., and Zhang, Y. (2013). Understanding the viscoelastic behavior of collagen matrices through relaxation time distribution spectrum. *Biomatter*, 3(3):e24651.

Xu, D., Harvey, T., Begiristain, E., Domínguez, C., Sánchez-Abella, L., Browne, M., and Cook, R. B. (2022). Measuring the elastic modulus of soft biomaterials using nanoindentation. *Journal of the Mechanical Behavior of Biomedical Materials*, 133(June).

Yadav, A. R., Sriram, R., Carter, J. A., and Miller, B. L. (2014). Comparative study of solution-phase and vapor-phase deposition of aminosilanes on silicon dioxide surfaces. *Materials Science and Engineering C*, 35(1):283–290.

Yang, J., Wu, J., and Bi, S. (2021). Surface Tension Measurements by Pendant Drop Method of 10 Pure Long-Chain Alkanes and Alcohols for Temperatures up to 573.15 K. *Journal of Chemical and Engineering Data*, 66(6):2615–2628.

Yang, S. C., Huang, K. S., and Lin, Y. C. (2007). Optimization of a pulsed carbon dioxide snow jet for cleaning CMOS image sensors by using the Taguchi method. *Sensors and Actuators, A: Physical*, 139(1-2 SPEC. ISS.):265–271.

Yoo, S. H., Kim, M., Park, H. J., Lee, G. I., Lee, S. H., and Kwak, M. K. (2023). Vacuum-powered soft actuator with oblique air chambers for easy detachment of artificial dry adhesive by coupled contraction and twisting. *Science and Technology of Advanced Materials*, 24(1).

Young, T. (1805). An essay on the cohesion of fluids. *Philosophical Transactions of the Royal Society of London*, 95(65-87).

Yu, Z. and Wachs, A. (2007). A fictitious domain method for dynamic simulation of particle sedimentation in Bingham fluids. *Journal of Non-Newtonian Fluid Mechanics*, 145(2-3):78–91.

Zenkiewicz, M. (2007). Comparative study on the surface free energy of a solid calculated by different methods. *Polymer Testing*, 26(1):14–19.

Zhou, Y., Robinson, A., Steiner, U., and Federle, W. (2014). Insect adhesion on rough surfaces: Analysis of adhesive contact of smooth and hairy pads on transparent microstructured substrates. *Journal of the Royal Society Interface*, 11(98).

Appendix A

Contact Angles and IRM

Spherical Cap Fitting

In Chapter 1, I compared the differences between fitting spherical caps and lines to Interference Reflection Microscopy (IRM) fringes to measure contact angles.

When determining the contact angle of a droplet reconstructed with IRM, fitting a line through the first few fringes can underestimate the contact angle, especially for shallow droplets with a small number of fringes (See Figure A.1A). I ran simulations, using the illumination wavelength and INA utilised in this study, for droplet heights $\in [0.25, 3.0]\mu$m and contact angles $\in [10, 30]^\circ$. I then calculated the "line fit" contact angle θ_l and compared it to the real contact angle θ (See Figure A.1B). The error becomes as high as 62% for shallower droplets.

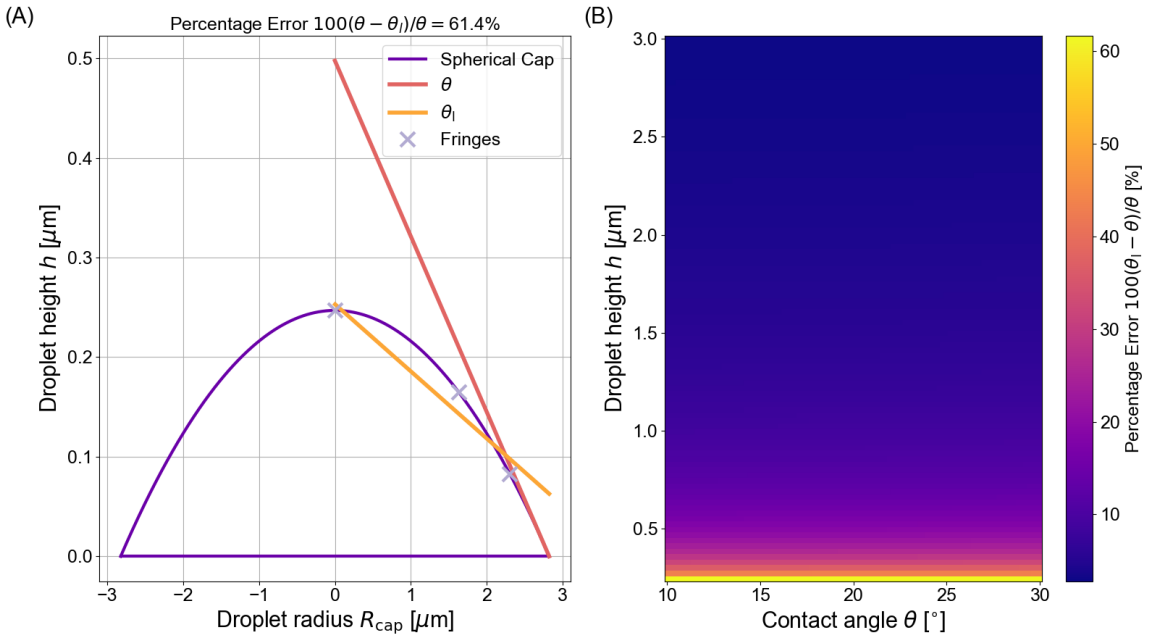


Figure A.1 (A) Schematic representation of the error introduced by the "line fit". This increases for shallower droplet geometries. (B) The percentage error of the "line" fit error can be as high as 62%.

I verified the accuracy of the spherical cap fitting procedure was robust to the outliers appearing on light intensity profiles. I ran simulations on the same height and contact angle ranges, this time introducing outliers at the edge of the droplets with an occurrence probability of $P_{out} = 0.01$, together with outliers on the most central fringe with variable

occurrence probabilities. In all cases, the spherical cap fitting has a systematically lower error than the line fit.

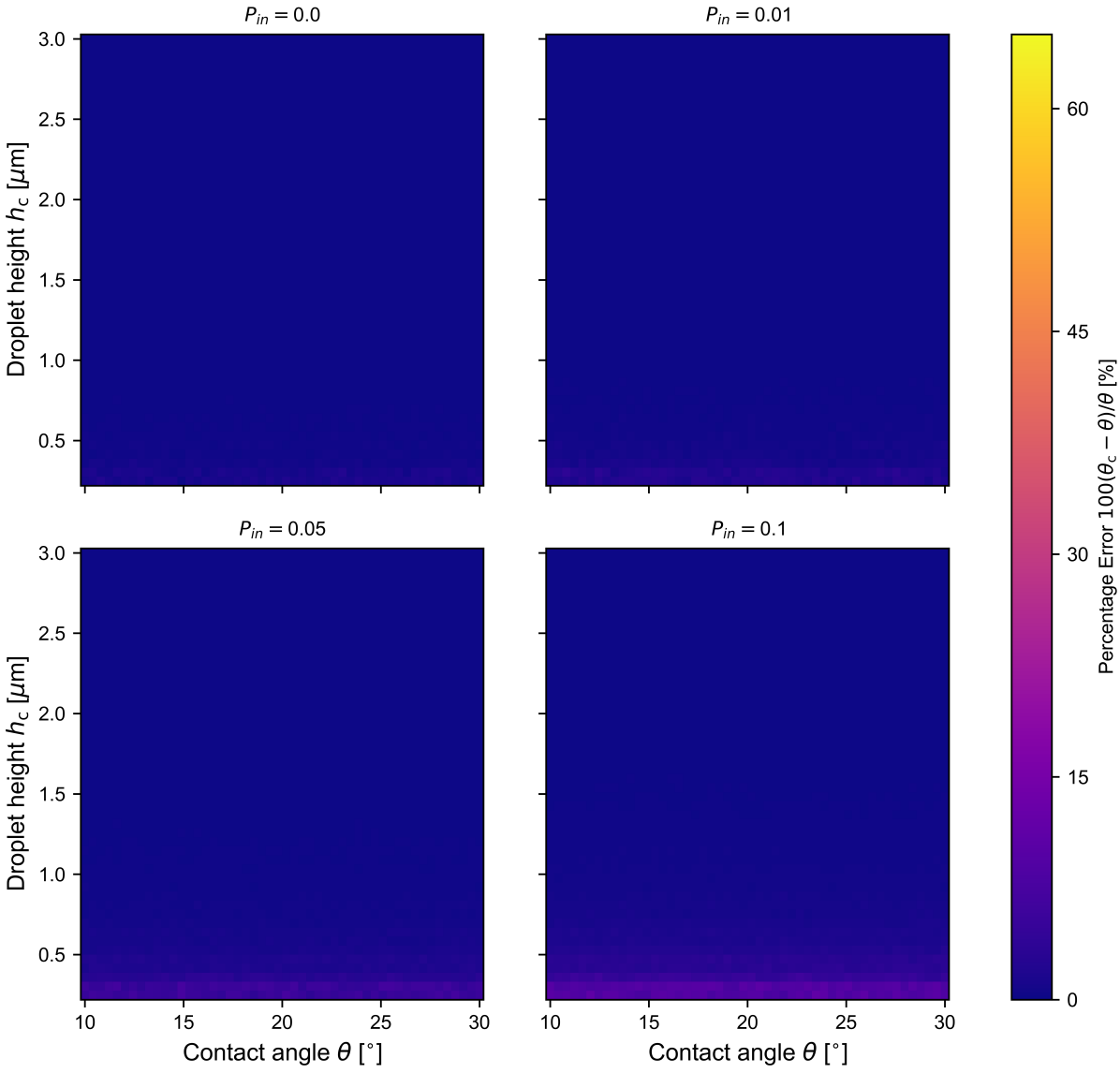


Figure A.2 The percentage error introduced by the spherical cap fitting procedure on simulated droplets for $P_{\text{out}} = 0.01$ and variable P_{in} is similar for different droplet geometries. The error remains below 15% in all cases.

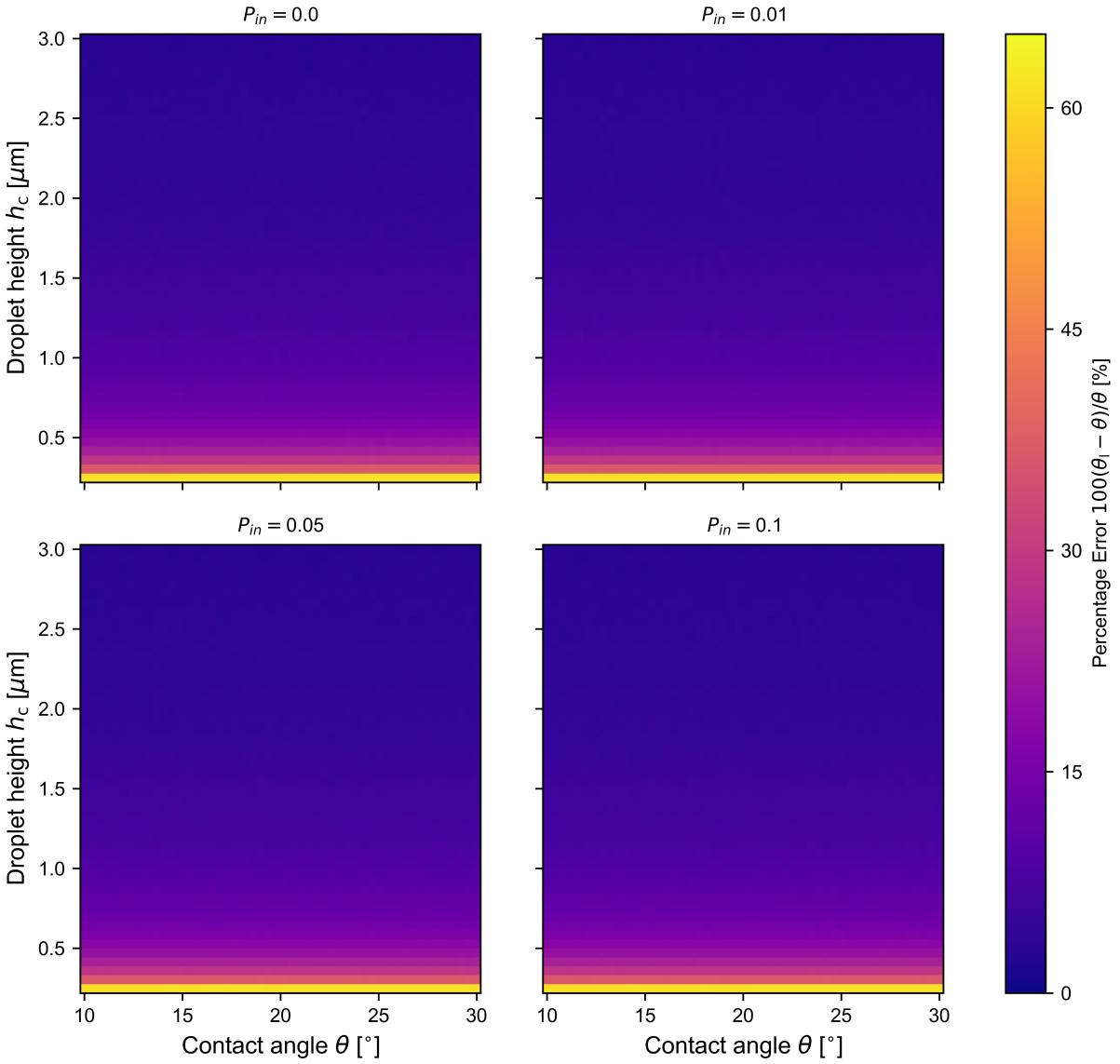


Figure A.3 The percentage error committed by the line fitting procedure on simulated droplets for $P_{\text{out}} = 0.01$ and variable P_{in} increases for small droplets. The error can be as high as 65%.

Simulating Interference Patterns under IRM

In Chapter 1, I produced a correction factor predicting the difference in slopes between a "real" wedge, and its reconstruction from Interference Reflection Microscopy (IRM) imaging. This entire section is a reproduction and rephrasing of the theories detailed by *Wiegand et al.* (Wiegand et al., 1997, 1998).

Electromagnetic Theory

The images obtained under an Interference Reflection Microscope are the result of multiple monochromatic light rays of wavelength λ and bandwidth $\delta\lambda$ coinciding at every (x,y) point in the imaging plane. Each of these rays contribute to the total electric field $\vec{E}$, whose time averaged square corresponds to the local light intensity $I(x,y)$ through:

$$I(x,y) = \langle \vec{E}^2 \rangle_t \tag{A.1}$$

where $\vec{E}$ is a complex number providing the magnitude and direction $\vec{E_0}$, phase shift kx and angular frequency ω of the electric field through $\vec{E} = \vec{E_0} \exp(ikx) \exp(i\omega t)$.

Each ray striking the observation point $B(x,y)$ does so with an orientation defined by the two spherical coordinate angles (ϕ, θ). For incoherent light, the time average can be integrated into an addition of intensities:

$$I(x,y) = \frac{\int_0^{2\pi} \int_0^{\theta} \vec{E} * \vec{E} \sin\theta \, d\theta d\phi}{\int_0^{2\pi} \int_0^{\theta} \sin\theta \, d\theta d\phi} \tag{A.2}$$

The local electric field $\vec{E}(x,y)$ is the sum of all electric fields reflected at the interfaces of the observed multi-layered system and ultimately reaching point $B(x,y)$ in the imaging plane.

Wedge Geometry

The systems considered here are made of three layers: a substrate L_0, a thin film covering it L_1 and the ambient medium L_2 (See Figure A.4). In such scenarios, the

rays (respectively in blue and red in Figure A.4) reaching point B are reflected by either of the two interfaces separating these media, IF_{01} or IF_{12}.

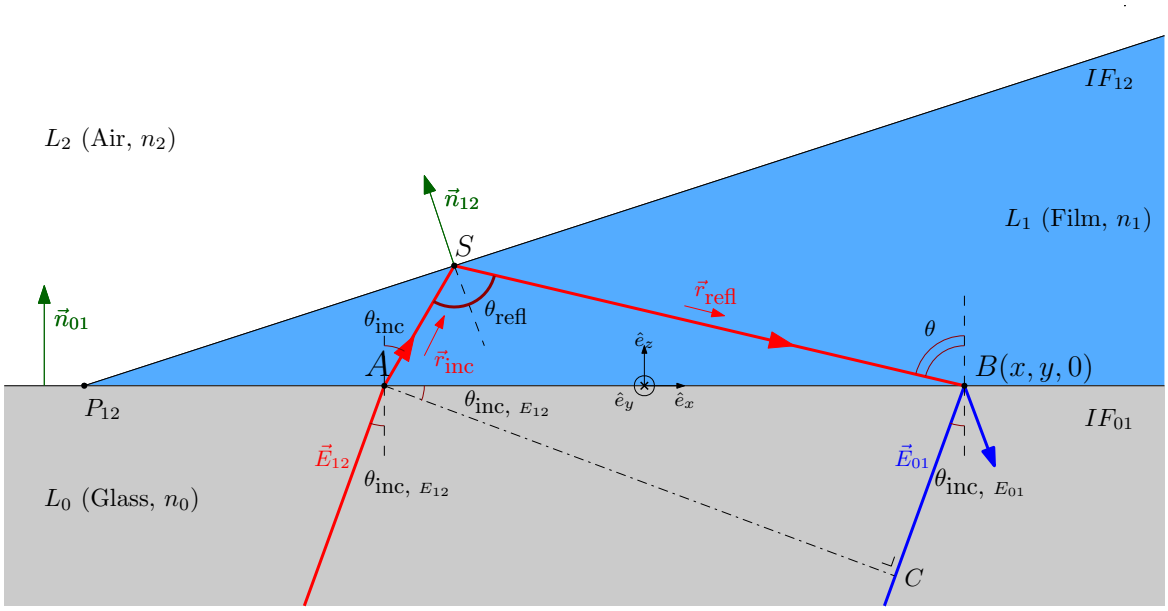


Figure A.4 Schematic figure representing the light path of incident and reflected rays under IRM imaging, for a wedge geometry.

The total electric field hence is:

$$\vec{E} = \vec{E}_{01} + \vec{E}_{12} = r_{01}^{s/p}\vec{E}_i + t_{01}^{s/p}\, r_{12}^{s/p}\, t_{10}^{s/p}\vec{E}_i \exp(-ik\Delta_1) \tag{A.3}$$

where $\vec{E}_i$ is the incident electric field, $\vec{E}_{01}$ is the local electric field reflected by the IF_{01} interface, and $\vec{E}_{12}$ is transmitted through IF_{01}, reflected by IF_{12} and ultimately transmitted trough IF_{01}, which results in a phase delay related to the additional distance Δ_1 the ray underwent in layer L_1. The wave number $k = 2\pi/\lambda$ was introduced, and the coefficients r_{ij} and t_{ij} are the reflection and transmission coefficients at the IF_{ij} interface obtained through the *Fresnel* equations for s and p polarised light:

$$\begin{cases} r_{ij}^{s}(\theta_i) = \dfrac{n_i\cos\theta_i - n_j\cos\theta_j}{n_i\cos\theta_i + n_j\cos\theta_j} \\ r_{ij}^{p}(\theta_i) = \dfrac{n_j\cos\theta_i - n_i\cos\theta_j}{n_j\cos\theta_i + n_i\cos\theta_j} \\ t_{ij}^{s/p}(\theta_i) = \sqrt{1 - (r_{ij}^{s/p})^2} \end{cases} \tag{A.4}$$

The angles $\theta_{i/j}$ are the incident angles on either side of IF_{ij}, and are related through *Snell*'s law:

$$n_i \sin\theta_i = n_j \sin\theta_j, \tag{A.5}$$

and hence the reflection and transmission coefficients are a function of a single incident angle, and the refractive indices of the interfaces. Note that in the case of total reflection (when either angle reaches a critical value $\theta_i \geq \arcsin n_j/n_i$), then $\theta_j = \pi/2$ and no light is transmitted.

Equation A.3 can be rewritten to highlight $\vec{E}_i$, from which all rays originate, considering separate cases for s and p polarised light since they can not interfere together:

$$\vec{E}^{s/p} = \mathcal{R}^{s/p}(\theta,\phi)\vec{E}_i^{\,s/p}$$

where for a three-layer system, $\mathcal{R}^{s/p}(\theta,\phi)$ is a complex function of the optical properties of the media and the incident angles of the two interfering rays at each interface:

$$\mathcal{R}^{s/p}(\theta,\phi) = r_{01}^{s/p}(\theta_{\text{inc, }E_{01}}) + t_{01}^{s/p}(\theta_{\text{inc, }E_{12}})\, r_{12}^{s/p}(\theta_{\text{refl}})\, t_{10}^{s/p}(\theta)\, \exp(-ik\Delta_1) \tag{A.6}$$

where the angles specified are the incident angles before interface IF_{ij}.

Equation A.2 now becomes:

$$I(x,y) = I^s + I^p$$

$$I^{s/p}(x,y) = \frac{\int_0^{2\pi}\int_0^{\theta} \mathcal{R}^{s/p}(\theta,\phi) * \mathcal{R}^{s/p}(\theta,\phi) E_i^{s/p}(\theta)^2 \sin\theta\, d\theta d\phi}{\int_0^{2\pi}\int_0^{\theta} \sin\theta\, d\theta d\phi}$$

$$= \frac{\int_0^{2\pi}\int_0^{\theta} |\mathcal{R}^{s/p}(\theta,\phi)|^2 E_i^{s/p}(\theta)^2 \sin\theta\, d\theta d\phi}{\int_0^{2\pi}\int_0^{\theta} \sin\theta\, d\theta d\phi}$$

The incident electric field $E_i^{s/p}(\theta)$ is dependent on the light source. Considering circularly polarised light, for which the intensity is equally split between polarisations:

$$E_i^{s/p}(\theta) = \begin{cases} \sqrt{I_0/2} & \text{if } \theta \leq \alpha_{\text{ill}}, \\ 0 & \text{otherwise.} \end{cases} \tag{A.7}$$

where $\alpha_{\text{ill}} = \left(\frac{\text{NA}_{\text{ill}}}{n_0}\right)$ is the maximum aperture angle of the illumination source of numerical aperture NA_{ill}, and I_0 is the incident light intensity.

The light intensity becomes:

$$I^{s/p}(x,y) = \frac{I_0}{2\zeta(\alpha_{\text{ill}})} \int_0^{2\pi} \int_0^{\theta} |\mathcal{R}^{s/p}(\theta,\phi)|^2 \sin\theta \, d\theta d\phi \tag{A.8}$$

with $\zeta(\theta) = \int_0^{2\pi} \int_0^{\theta} \sin\theta \, d\theta d\phi = 2\pi(1-\cos\theta)$. Since the objective of a microscope set-up also has a finite numerical aperture NA_{obj}, only the rays whose azimuthal coordinate θ is below the maximum detectable angle $\alpha_{\text{obj}} = \arcsin\left(\frac{\text{NA}_{\text{obj}}}{n_1}\right)$ can be resolved. Ultimately, the light intensity at any given point $B(x,y)$ is the result of rays coming from multiple directions and interfering after being reflected at either interfaces:

$$I^{s/p}(x,y) = \frac{I_0}{2\zeta(\alpha_{\text{ill}})} \int_0^{2\pi} \int_0^{\alpha_{\text{obj}}} |\mathcal{R}^{s/p}(\theta,\phi)|^2 \sin\theta \, d\theta d\phi. \tag{A.9}$$

These equations allows determining the intensity profile of an IRM image, provided that $\mathcal{R}^{s/p}(\theta,\phi)$ can be determined for every possible orientation (θ,ϕ). Since it is entirely defined by the rays' incident angles and the phase delay Δ_1, this quantity is purely determined by the geometry of the system.

Here, the system is made of a flat glass slide covered by a liquid wedge of constant slope β in ambient air. Let us consider first rays that have been transmitted through IF_{01}, reflected at IF_{12} and then transmitted to the objective. At any observation point $B(x,y)$, such rays may exist for any observable orientation (θ,ϕ). One can hence back-calculate the origin of a potential ray observed after being reflected from the interface IF_{12} by determining the positive intersection between a line of origin $\mathbf{B}$ $(x,y,0)$ and orientation $\vec{r}_{refl}$ defined by the two polar coordinates (θ,ϕ):

$$\vec{r}_{\text{refl}} = -\left(\sin\theta\cos\phi,\ \sin\theta\sin\phi,\ \cos\theta\right) \tag{A.10}$$

where all points belonging to the ray obey:

$$\mathbf{X} = \mathbf{B} + \lambda_{\mathrm{w}} \vec{r}_{\mathrm{refl}} \tag{A.11}$$

and the plane IF_{12}, defined by any point $\mathbf{P}_{12}$ belonging to it and its normal vector:

$$\vec{n}_{12} = (-\sin\beta, 0, \cos\beta) \tag{A.12}$$

All points $\mathbf{X}$ belonging to the IF_{12} plane hence obey:

$$(\mathbf{X} - \mathbf{P}_{12}) \cdot \vec{n}_{12} = \mathbf{0} \tag{A.13}$$

If an intersection exists between the wedge and the ray at point S, one can determine λ_{w}, whose absolute value is the distance $SB = |\lambda_{\mathrm{w}}|$ and the reflection angle between the normal direction $\vec{n}_{12}$ to the wedge at S and the reflected ray $\vec{r}_{\mathrm{refl}}$, which corresponds to the reflection angle θ_{refl} through:

$$\lambda_{\mathrm{w}} = \frac{(\mathbf{P}_{12} - \mathbf{B}) \cdot \vec{n}_{12}}{\vec{r}_{\mathrm{refl}} \cdot \vec{n}_{12}} \tag{A.14}$$

and

$$\theta_{\mathrm{refl}} = \arccos\left(-\vec{r}_{\mathrm{refl}} \cdot \vec{n}_{12}\right) \tag{A.15}$$

Three case scenarios can occur here:

- $\lambda_{\mathrm{w}} \leq 0$ and the ray is reflected by IF_{12}
- $\lambda_{\mathrm{w}} > 0$ and the ray is below the imaging plane and does not contribute to the light intensity.
- $\lambda_{\mathrm{w}} \to \infty$ and the intersection does not exist.

Similarly, the distance SA can be determined by calculating the intersection between the incident ray $\vec{r}_{\mathrm{inc}}$ and the plane IF_{01} through:

$$\vec{r}_{\mathrm{inc}} = \vec{r}_{\mathrm{refl}} + 2\cos\theta_{\mathrm{refl}} \vec{n}_{12} \tag{A.16}$$

$$\mathbf{X} = \mathbf{S} + \eta_{\mathrm{w}} \vec{r}_{\mathrm{inc}} \tag{A.17}$$

providing the direction of the incident ray to point S, and:

$$\vec{n}_{01} = (0, 0, 1) \tag{A.18}$$

$$(\mathbf{X} - \mathbf{0}) \cdot \vec{n}_{01} = \mathbf{0} \tag{A.19}$$

defining the imaging plane.

From determining the reflection angle θ_{refl}, one can then backtrace the origin point A of the ray in L_0 through the intersection:

$$\eta_{\mathrm{w}} = \frac{(\mathbf{0} - \mathbf{S}) \cdot \vec{n}_{01}}{\vec{r}_{\mathrm{inc}} \cdot \vec{n}_{01}} \tag{A.20}$$

and

$$\theta_{\mathrm{inc}} = \arccos\left(\vec{r}_{\mathrm{inc}} \cdot \vec{n}_{01}\right) \tag{A.21}$$

where $SA = |\eta_{\mathrm{w}}|$. Again, only those rays for which $\eta_{\mathrm{w}} \leq 0$ correspond to a valid intersection and are hence considered in the evaluation of $\mathcal{R}^{s/p}(\theta, \phi)$. The remaining distance CB can be obtained by evaluating the angle $\theta_{\mathrm{inc},\, E_1 2}$ through *Snell*'s law A.5:

$$CB = AB \sin \theta_{\mathrm{inc}, E_{12}} = \sqrt{SA^2 + SB^2} \frac{n_1}{n_0} \sin \theta_{\mathrm{inc}} \tag{A.22}$$

The total phase delay is hence:

$$\Delta_1 = n_1(SA + SB) - n_0 CB \tag{A.23}$$

where the contribution CB is accounted for as negative, since ray $\vec{E}_{12}$ undergoes a shorter distance in L_0 comparatively to $\vec{E}_{01}$.

Finally, the angles $\theta_{\text{inc},\ E_{01}}$ and $\theta_{\text{inc},\ E_{12}}$ are obtained through *Snell*'s law:

$$\theta_{\text{inc},\ E_{01},\ E_{12}} = \frac{n_1}{n_0} \sin \theta_{\text{inc}} \tag{A.24}$$

provided that the existence criteria for ray $\vec{E}_{12}$ imposed by λ_{w} and η_{w} are satisfied. If they are not, then ray $\vec{E}_{12}$ does not exist, and the second term in Equation (A.6) is set to null. In that case, since ray $\vec{E}_{01}$ still exists, the incident angle $\theta_{\text{inc},\ E_{01}}$ is equal to θ. The reflected ray term in $\mathcal{R}^{s/p}$ is also set to zero if Δ_1 is greater than the coherence length of the illuminating source $\Delta_{\text{ill}} = \lambda^2/(n_1 \delta\lambda)$, or if point A lands out of the imaging field. A last ray exclusion criteria is due to the limited aperture of the objective, where the second or first term in Equation (A.6) are set to zero if $\theta_{\text{inc},\ E_{01}}$ or $\theta_{\text{inc},\ E_{12}}$ are greater than α_{obj}, respectively, since they could not be resolved by the finite aperture objective.

Spherical Cap Geometry

I extended the theory presented by *Wiegand et al.* to similar geometric conditions (Wiegand et al., 1997, 1998), this time using a spherical cap instead of a wedge (See Figure A.5. The distance $SB = |\lambda_{\text{s}}|$ is obtained by finding the intersection between ray r_{refl} and a spherical cap defined by a cap radius r_{cap}, and contact angle β_{cap}.

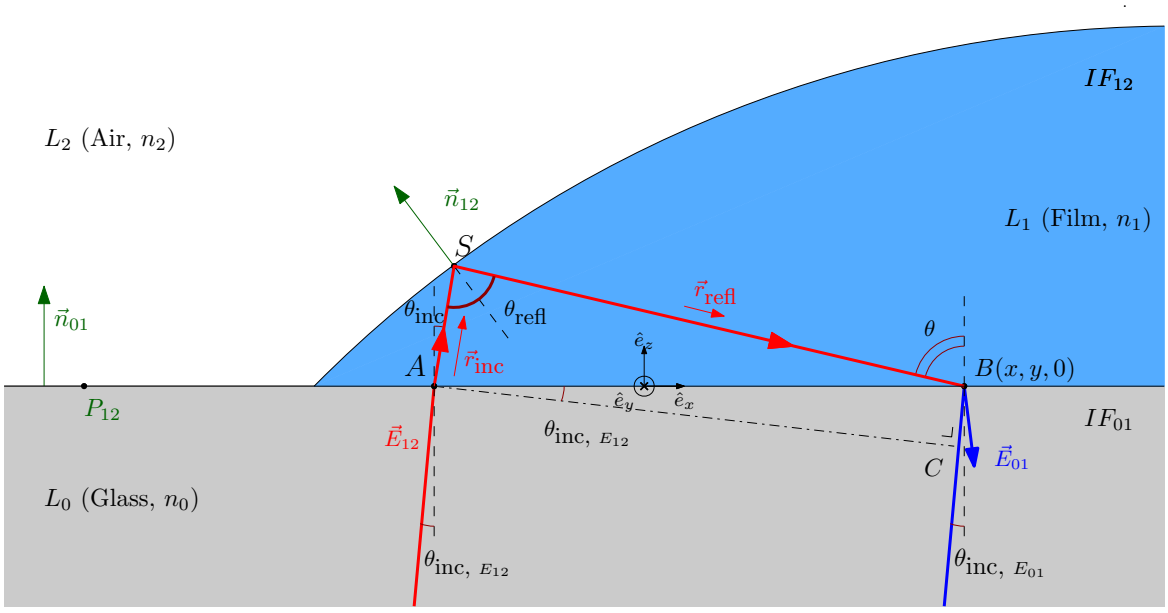


Figure A.5 Schematic figure representing the light path of incident and reflected rays under IRM imaging, for a spherical geometry.

The cap originates from a sphere of radius:

$$r_{\text{sphere}} = \frac{r_{\text{cap}}}{\sin \beta_{\text{cap}}} \tag{A.25}$$

The height of the cap is then $h_{\text{cap}} = r_{\text{sphere}}(1 - \cos \beta_{\text{cap}})$, and hence the center of the sphere $\mathbf{C}_{\text{s}}$ is located at:

$$\mathbf{C}_{\text{s}} = (0, 0, h_{\text{cap}} - r_{\text{sphere}}) \tag{A.26}$$

Hence, λ_{s} is given by the intersection:

$$\lambda_{\text{s}} = \vec{r}_{\text{refl}} \cdot (\mathbf{C}_{\text{s}} - \mathbf{B}) + \sqrt{\rho} \tag{A.27}$$

with

$$\rho = [-\vec{r}_{\text{refl}} \cdot (\mathbf{B} - \mathbf{C}_{\text{s}})]^2 - |\mathbf{B} - \mathbf{C}_{\text{s}}|^2 + r_{\text{sphere}}^2 \tag{A.28}$$

Appendix B

Nanoindentation Validation

Validation with a Known Material

In Chapter 2, I assumed I indented an isotropic homogenous elastic half space, which is certainly not the case for heterogeneous insect pads (Scholz et al., 2008). However the theory fits the data well, so suggesting that an effective modulus approach is reasonable. In fact, the elastic moduli are in good agreement with literature values detailed above, and so the complex moduli analysis provides an insight into the losses occurring in the pad when deforming.

To validate the nanoindentation method developed here, I used the indentation protocol described above to measure the material properties of a known material: a collagen hydrogel sold under the brand name *Petrisoft* (Cell Guidance Systems LLC, USA. Elastic modulus: 25 kPa, as specified by the manufacturer). The force-indentation curves are in accordance with a mostly elastic (low creep) material and follow *Hertz*'s law (See Figure B.1). The average values for the instantaneous and relaxed moduli extracted from fitted two constants *Prony* series were: $E_0 = 25.6 \pm 5.8\,\text{kPa}$ and $E_\infty = 13 \pm 0.4\,\text{kPa}$ (n=5, mean ± std.). The average of the viscoelastic ratios E_0/E_∞ was 1.96 ± 0.39. These values are in good agreement with the manufacturer's specifications, and with literature values ($E_0 \approx 12.5\,\text{kPa}$, $E_\infty \approx 9\,\text{kPa}$, $E_0/E_\infty \approx 1.4$. Islam and Oyen, 2021; Xu et al., 2013, 2022).

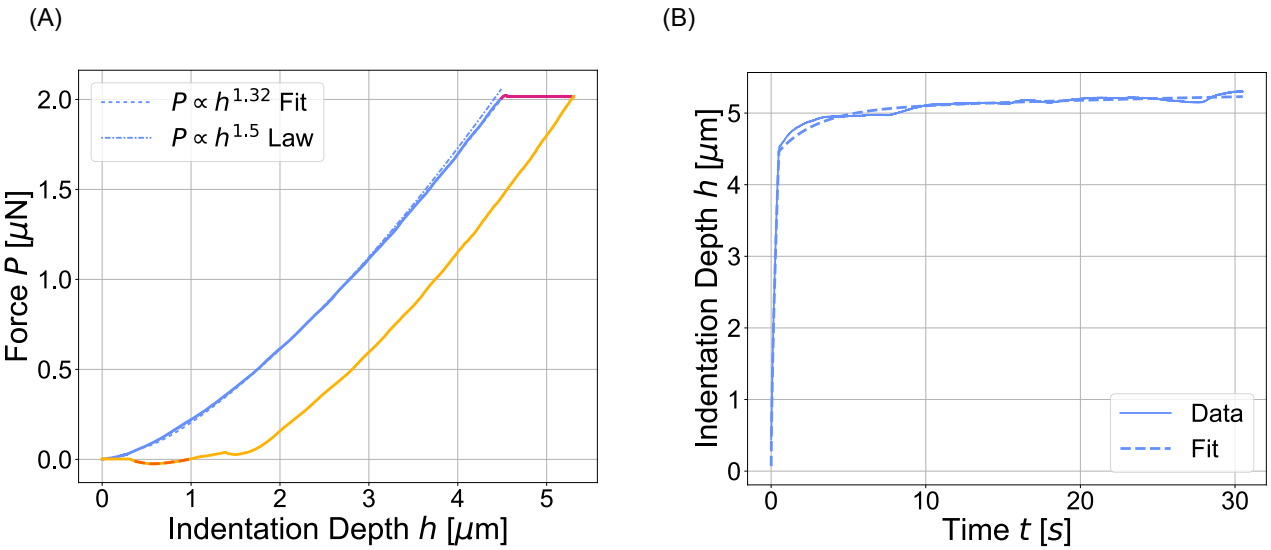


Figure B.1 (A) Example of a force-displacement curve resulting from the indentation of collagen, characterised by three segments: Loading (blue), creep (pink), unloading (yellow). The dashed and dotted lines show the fit of a simple power law compared to the prediction from *Hertz* theory. (B) Characteristic Displacement-Time data (solid) and theoretical fit (dashed) for collagen.

Force and Displacement Profiles over Time

The indentation profiles typically obtained with the *Chiaro* are typical of a viscoelastic material undergoing creep (See Figure B.2).

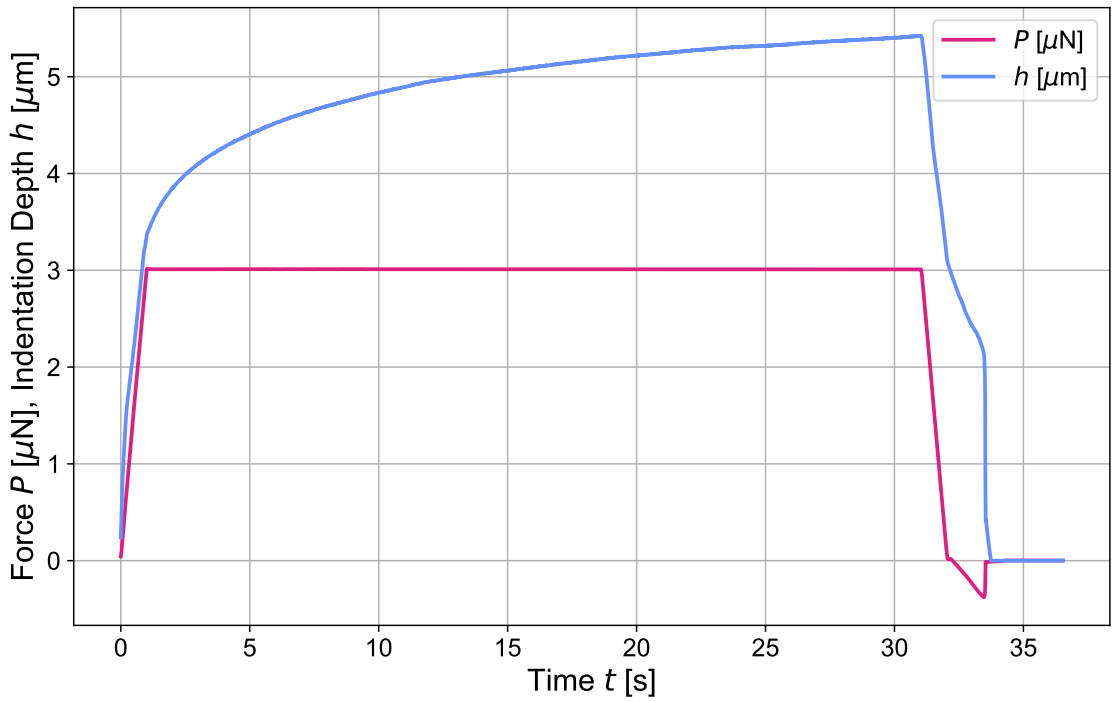


Figure B.2 Example curves of the force (P) and displacement h profiles obtained during the indentation of a stick insect's pad. The material's creep becomes apparent during the force profile's holding phase, followed by the probe's retraction and subsequent adhesion.

Creep Compliance Function

The interpretation of creep data through *Fourier* transforms detailed in this work hence provides a complete characterisation of the viscoelastic pad cuticle, through multiple viscoelastic functions and their variation with respect to rate and temperature. The bulk creep compliance $J(t)$, parametrised as a *Prony series* relates such changes in rate and temperature (See Figure B.3).

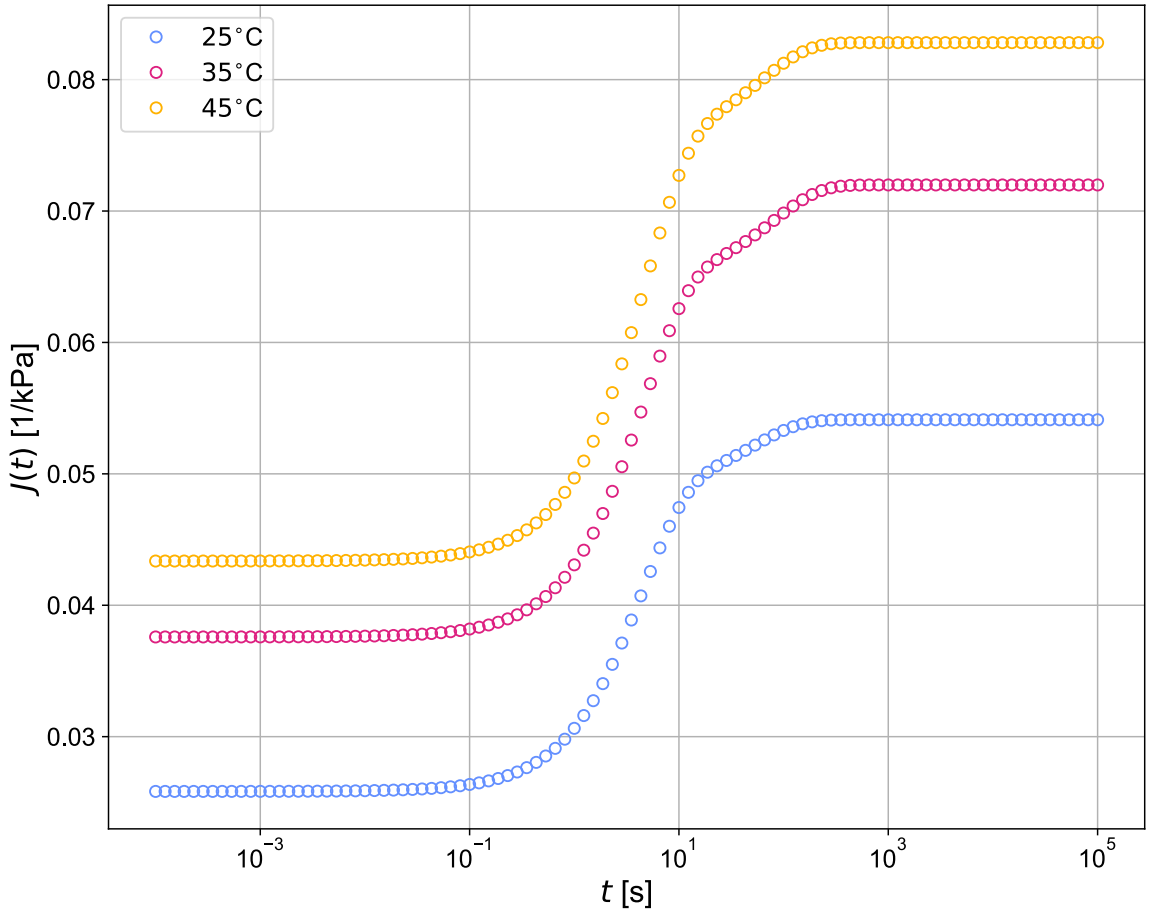


Figure B.3 The time-space creep compliance function $J(t)$ is obtained by fitting *Prony* series to the creep data at different temperatures. The creep function increases in magnitude with increasing temperatures.

Appendix C

Force Sensor Calibration

Beam Theory and Calibration

In Chapter 3, I used a custom built force transducer based on a fibre optic sensor and a cantilever beam to determine the forces produced by the adhesive pads of insects. In order to determine the relationship between the deflection of the cantilever beam read by the fibre optic sensor and the forces applied on the glass slides, different calibration weights in the 2-500 mg range were hung at two lever arms, separated by a 1.5 mm distance (See Figure C.1A). The beam theory formula for the deflection d of a beam resulting from an applied load P concentrated at a distance a from the beam's clamp is (Gere, 2012):

$$d = \frac{P l_{\text{obs}}^2}{6EI}(3a - l_{\text{obs}}) = \mathcal{C}P(3a - l_{\text{obs}}), \tag{C.1}$$

where $l_{\text{obs}} = 16$ mm is the distance at which the fibre optic sensor was placed on the beam, E is the elastic modulus of the beam, and I its moment of inertia. Thus, a least squares algorithm ($R^2 = 1.0$) was used to fit a line through the linear relationship between the load adjusted by the lever arm and the cantilever deflection, providing the calibration constant $\mathcal{C}$ (See Figure C.1B). The force sensor was calibrated for this procedure each time the glass coverslips were replaced.

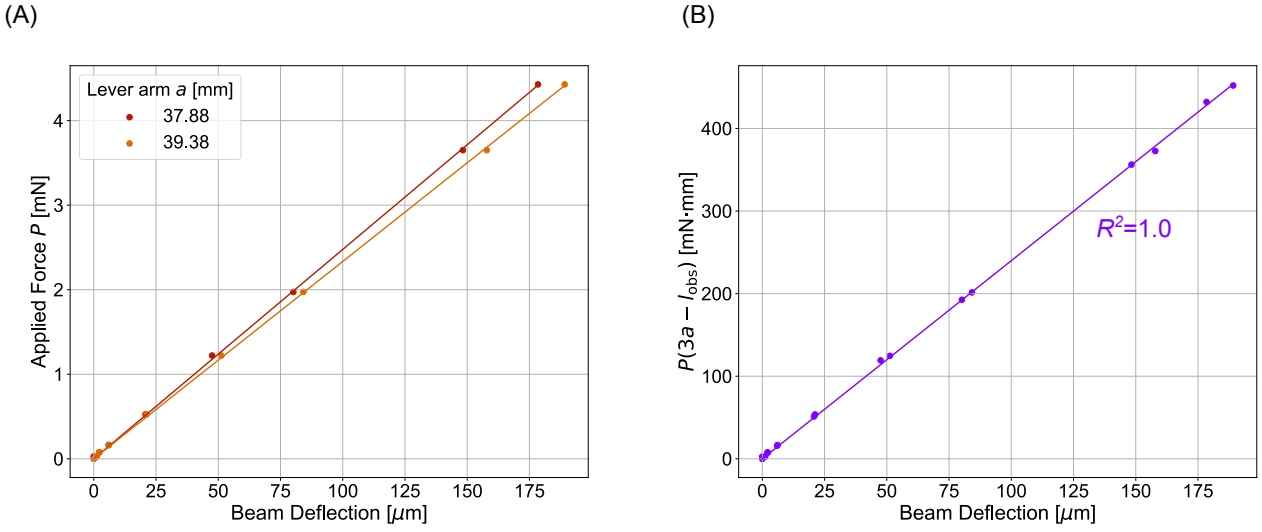


Figure C.1 (A) The relationship between the deflection of the cantilever beam read by the sensors and the forces applied on the coverslips was determined by hanging different calibration weights in the 2-500 mg range at two lever arms a. (B) The difference in lever arms was adjusted using Equation (C.1). The slope of the resulting curve was used as the multi-lever arm calibration factor $\mathcal{C}$.